UNIVERSITÀ DEGLI STUDI DI PAVIA

DOTTORATO IN SCIENZE CHIMICHE E FARMACEUTICHE

XXX CICLO

Coordinatore: Chiar.mo Prof. Mauro Freccero

"Molecular receptors and devices from

macrocyclic chemistry"

Tutore   **Tesi di Dottorato di**

Chiar.mo Prof. Maurizio Licchelli   **MICHELE INVERNICI**

a.a. 2016- 2017

Contents

3

1 Thesis abstract

The present thesis, entitled "molecular receptors and devices from macrocyclic chemistry", is focused on two main topics, anion recognition and carbon dioxide reduction electrocatalysis. The subjects of my study are represented by Ni^{II} and Cu^{II} complexes of mono- (**1**) and bis- (**2**) azamacrocyclic ligands. These complexes are able to act as synthetic receptors for anions and as catalysts for the CO_2 reduction. The dimetallic complexes, $[M^{II}_2(\mathbf{2})]^{4+}$, consist of two *trans*-III $[M(dimethyl\text{-}cyclam)]^{2+}$ subunits, bridged by an ortho-xylyl group. Both methyl groups of each cyclam ring are in the equatorial position with respect to the chair conformation of the six membered chelate rings, causing an axial orientation of the xylylene group and consequently favoring a face-to-face arrangement of the two macrocyclic subunits. The equivalent monometallic complexes, $[M^{II}(\mathbf{1})]^{2+}$, consist of an analogous *trans*-III $[M(dimethyl\text{-}cyclam)]^{2+}$functionalized by a benzyl group.
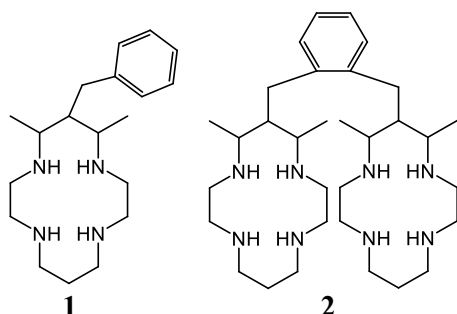
Compared to other systems consisting of one or more tetramine units (e.g., tren and trien), the great advantage of these cyclam-like systems is their inertia toward demetallation, even under severe conditions.

The dimetallic complexes, $[M^{II}_2(\mathbf{2})]^{4+}$, are particularly suitable as small anions receptors, due to their face-to-face conformation and short M(II) - M(II) distances. The first part of the anion recognition chapter deals with the study of the interaction of $[Ni^{II}_2(\mathbf{2})]^{4+}$ with halides (Cl^-, Br^-, I^-) and pseudohalides (NCO^-, NCS^-, N_3^-) in DMSO and the determination of the corresponding stepwise binding constants through spectrophotometric titration experiments. Moreover, the crystal and

molecular structure of the dinuclear complex $[Ni^{II}_2(\mathbf{2})(\mu\text{-NCO})(NCO)_2]^+$, containing two high-spin Ni^{II} centers has been determined, and the Ni^{II}-to-Ni^{III} oxidation potential has been investigated through voltammetric techniques, in the absence and in the presence of different anions (Cl^-, NCO^-, N_3^- and NO_3^-), to evaluate the capability of the $[Ni^{II}_2(\mathbf{2})]^{4+}$ receptor to act as an electrochemical anion sensor. Finally, in order to verify the existence of cooperative effects in the solution behavior of $[Ni^{II}_2(\mathbf{2})]^{4+}$, analogous spectrophotometric and voltammetric studies have been carried out on the mononuclear complex $[Ni^{II}(\mathbf{1})]^{2+}$, under the same experimental conditions.

The presence of a $[Ni_2^{II}(\mathbf{2})]^{4+}$ advantage over $[Ni^{II}(\mathbf{1})]^{2+}$ in halides binding, due to their coordination inside the $[Ni_2^{II}(\mathbf{2})]^{4+}$ intermetallic cavity, pushed us to perform further studies on the nature of this particular "bimacrocyclic effect". Therefore, the second part of the anion recognition chapter describe the interaction of $[Cu_2^{II}(\mathbf{2})]^{4+}$ with halides (Cl^-, Br^-, I^-), pseudohalides (NCO^-, NCS^-, N_3^-) and oxyanions (CH_3COO^-, NO_3^-, HSO_4^-) in a DMSO solution and the corresponding stepwise binding constants, enthalpy and entropy changes have been determined through isothermal titration calorimetry. The comparison with the related monometallic complex $[Cu^{II}(\mathbf{1})]^{2+}$ permitted us to better understand the nature of the "bimacrocyclic effect". The leading position of copper(II) in the Irving-Williams series makes the interaction with anionic ligands stronger than that expected for other metal ions, allowing the study of the bimacrocyclic effect even in water. Comparison of the EPR spectra of the two copper (II) complexes further confirmed the existence of the bimacrocyclic effect. In the presence of bridging anions, $[Cu_2(\mathbf{2})]^{4+}$ favors delocalization of the unpaired electrons between its two copper centers, resulting in a simple method to distinguish between bridging and non-bridging anions. Moreover, $[Cu_2(\mathbf{2})]^{4+}$ showed an exceptionally high affinity for HSO_4^- in DMSO. The same anion is only poorly coordinated by the related monometallic $[Cu^{II}(\mathbf{1})]^{2+}$. The X-ray crystal structure of $[Cu^{II}_2(\mathbf{2})(\mu\text{-}HSO_4)(HSO_4)_2]^{4+}$, show the presence of a bridged HSO_4^-, strongly bound to the receptor thanks to the simultaneous presence of coordinative and hydrogen bonds.

The last chapter of the present thesis deal with the reduction of CO_2 catalyzed by the M^{II} complexes of the same ligands, along with the *meta*-xylylene and *para*-xylylene isomers of complex $[Ni_2(\mathbf{2})]^{4+}$. Their catalytic efficiency has been compared with that of the analogous M^{II} complexes of cyclam (cyclam = 1,4,8,11tetraazacyclotetradecane), where the nickel complex, $[Ni^{II}(cyclam)]^{2+}$, is one of the most famous homogeneous catalyst for the CO_2 reduction to CO in water. Different type of electrodes have been tested (mercury, bismuth, glassy carbon), since the electrode itself plays a key role for the CO_2 reduction to CO, facilitating the CO release from the catalyst. Due to the importance of proton donors in the CO_2 reduction and considering that the competitive reduction of H^+ to H_2

could also be catalyzed by these complexes, the effect of pH on the reaction has also been investigated. Moreover, HCO_3^- and CO_3^{2-} reductions were also investigated. All of the experiments were performed by using the cyclic voltammetry technique.

All the catalysts under study resulted active for the CO_2 reduction, each with its own catalytic efficiency. Interestingly, when using an Hg electrode, all the catalysts except $[Cu^{II}(cyclam)]^{2+}$, are also capable of catalyzing the HCO_3^- reduction, while reduction of CO_3^{2-} was observed only in the presence of $[Ni_2^{II}(2)]^{4+}$, possibly as a result of the bismacrocyclic effect. $[Ni^{II}(1)]^{2+}$ has been found to be a better catalyst than $[Ni^{II}(cyclam)]^{2+}$, exhibiting an higher catalytic activity, lower overpotential and higher selectivity for CO_2 reduction over H^+ reduction. $[Ni_2^{II}(2)]^{4+}$ is not as active as the analogous monometallic complex, especially when catalyst adsorption on electrode surface is involved. Finally, the most active electrode has been observed to be mercury, whereas glassy carbon showed only a poor activity. Bismuth electrode achieved intermediate results and considering its non-toxicity and its ability to lower the CO_2 overpotential, it could be a good alternative to the mercury electrode.

2 Introduction

2.1 Macrocyclic ligand

Macrocyclic ligand are synthetic or natural polydentate ligands, containing their donor atoms incorporated in a cyclic backbone or in substituents attached to it. They contain at least three donor atoms and the ring contains a minimum of nine atoms (including all hetero atoms).[1] The earliest known examples of macrocyclic ligands were observed in natural substances, such as the porphyrin ring (figure 1a) of the iron-containing heme proteins, the related (partially reduced) chlorin ring (figure 1b) of chlorophyll (a magnesium complex), or the corrin ring of vitamin B12 (a cobalt complex), and in some synthetic highly conjugated phthalocyanines (figure 1c), used mainly as dyes or pigments.[1–3]
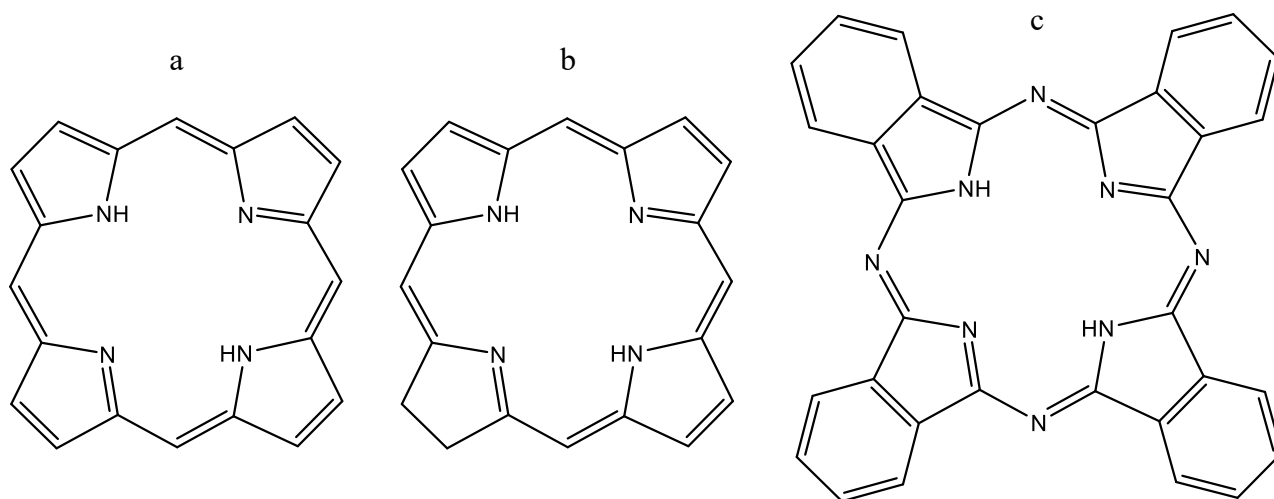
Figure 1. Earliest example of macrocyclic ligands: (a) porphyrin ring, (b) chlorin ring, (c) phthalocyanine.

The discovery in 1964 that certain naturally occurring antibiotic ionophores such as valinomycin, nonactin, monensin, and others, exhibiting alkali specificity, were capable of active transport of metal ions across membranes, was a starting point for many studies of alkali and alkaline-earth cations selectivity of biological and model systems. The intense interest on macrocyclic compounds was related to their unusual affinity for certain metal ions, their ability to bind selectively some cations in preference to others, the inertia to decomposition of some complexes, and the capacity of some of those ligands to solubilize inorganic salts in non-aqueous media.[4] Macrocyclic ligands typically contain central hydrophilic cavities with electronegative or electropositive binding atoms and an exterior flexible skeleton exhibiting a

hydrophobic behaviour. Their hydrophobic exteriors allow them to solubilize ionic substances in non-aqueous solvents and in membrane media. The era of synthetic macrocycles started in 1967 with the Pederson's work on crown-ethers.[4] Pederson reported syntheses of over 50 cyclic polyethers where the size of the rings, the number of oxygen atoms, and the number and type of substituent groups are varied (some examples are shown in figure 2). In the history of organic chemistry, crown ethers emerged as the first subclass of synthetic macrocycles that offered a clear relationship between structure and function. The cyclic polyether 18-crown-6, represented in the center of figure 2, possesses micromolar affinity for potassium ions in methanol. To date, crown ethers exemplify an intuitively clear consequence of molecular-level organization of electron-donating oxygen atoms on a useful property – metal ion recognition.[5] After that, a fast progress ensued in the following decades, not only for crown ethers, but also for macrocycles containing all kind of donor atoms (mainly nitrogen, but also sulphur, phosphorus, and mixed donor atoms).

Figure 2. Some example of cyclic polyethers, the so called "crown ethers".

2.2 Why macrocyclic ligands?

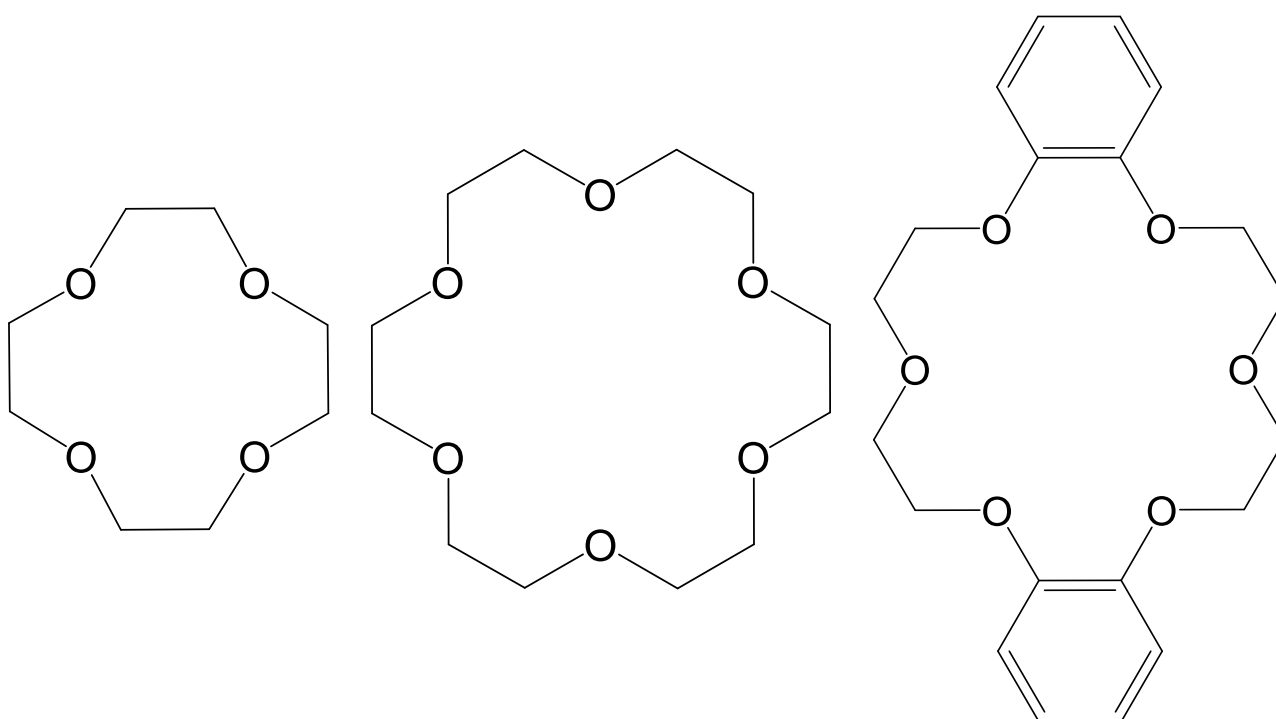Nature chooses metal-ion macrocyclic ligand systems in several important biological systems that include chlorophyll, hemoglobin and vitamin B12. In such species, the metal ion is held firmly in the macrocyclic cavity such that the biological role of these species is not impaired by, for example, competing demetallation reactions. Such stability is typical of many synthetic macrocyclic complexes which also often show enhanced resistance to degradation, high thermal stabilities and inertness to acids and alkalis when compared with their metal-containing open-chain analogues. Over the past half century, there has been a remarkable growth in synthetic macrocyclic chemistry, in part associated with mimicking the unusual spectral, redox, kinetic and/or thermodynamic behavior commonly displayed by Nature's macrocycles but also for the development of new macrocyclic systems for use in medicine, metal-ion discrimination, metal-ion catalysis, organic syntheses and analytical processes. The enhanced kinetic and thermodynamic stabilities of macrocyclic ligand complexes – collectively known as the macrocyclic effect – often make such complexes ideal components for use in metallo-supramolecular chemistry. Indeed, the inherent stability of macrocyclic systems coupled with their usually well-defined geometry tends to simplify the design process when such systems are being considered for use as supramolecular building blocks for the construction of molecular assemblies. Moreover, in such products the other ''special'' properties of macrocyclic complex species such as unusual spectral, magnetic, redox (including stabilization of less common oxidation states) and catalytic properties are commonly maintained in the final assemblies – usually in modified form – and frequently giving rise to new materials displaying a range of interesting and potentially useful attributes.[6]

2.3 Polyaza Macrocycles

Poly-aza macrocycles, are macrocycles contains nitrogen donor atoms. In general, they form extremely stable complexes with transition metals ions, but show reduced affinity for alkali and alkaline earth metal ions compared to the oxa-macrocycles.

2.4 The most studied tetra-aza-macrocylic ligand: cyclam

Synthetic tetraaza macrocycles have attracted a great deal of attention because they can be used as models for more intricate biological macrocyclic systems: metalloporphyrins (hemoglobin, myoglobin, cytochromes, chlorophylls). Since the observation of Curtis[7] in 1968 of the high acid stability of the condensation products of acetone with $[Ni(en)_3]^{2+}$, the chemistry of macrocyclic transition metal complexes has seen unprecedented growth and the trend continues even today. Of the ligands, the saturated 14-membered macrocycle cyclam (1,4,8,11-tetraazatetradecane) (Figure 3) has been used more extensively than any other cyclic systems for the complexation of transition metal ions.
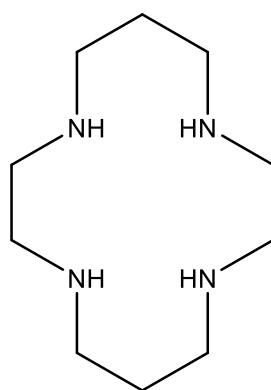
Figure 3. The 14-membered macrocycle cyclam (1,4,8,11-tetraazatetradecane): cyclam.

It was synthetized for the first time in 1936 by the chemist Jan van Alphen, by the reaction shown in figure 4, but only in 1965 Bosnich, Poon and Tobe, reported the first complexes of 1,4,7,11-tetra-aza-cyclo-tetradecane, which they named cyclam (from cycl[ic] [tetr]am[ine]).[8]
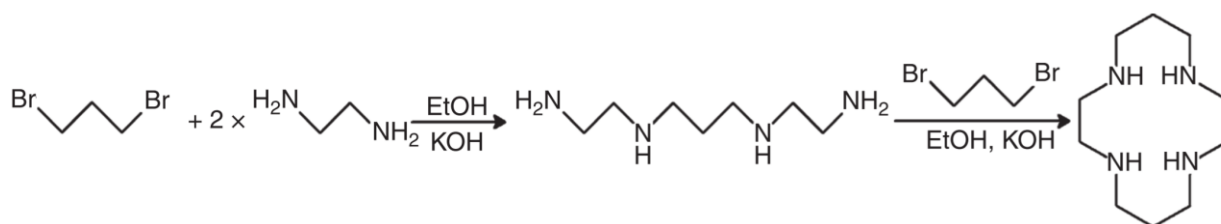
Figure 4. Van Alphen's synthetic route to 2·3·2-tet,[9] and to cyclam.[10]

They took the view that each nitrogen in the cyclam molecule, when coordinated, represents an asymmetric center, thus giving rise to five distinct configurational isomers, which they indicated as *trans*-I –*trans*-V. Then, based on a qualitative analysis made with Dreiding stereomodels, they concluded that the most stable configurations should be *trans*-I and *trans*-

III, whose arrangements are shown in Figure 5. Indeed, the first structure of a cyclam complex, [Ni^{II}(cyclam)Cl$_2$] (see Figure 6),[11] showing a *trans*-dichloro-octahedral geometry, exhibited the *trans*-III configuration, which hundreds of X-rays determined crystal and molecular structures have later demonstrated to be the most common arrangement in metal cyclam complexes. It has been also shown, through crystallographic studies, that the *trans*-I configuration prevails in metal complexes of tetra-*N*-alkyl substituted cyclam derivatives.[12]
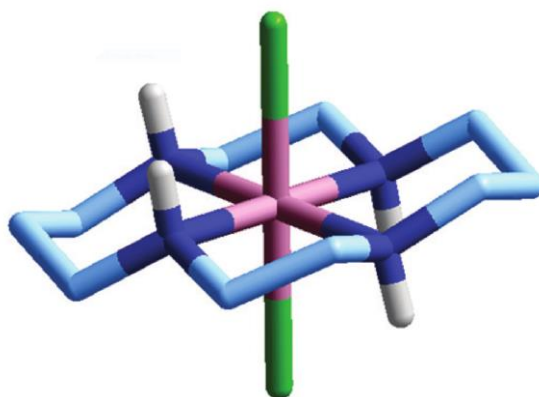
Figure 6. The first crystal and molecular structure of a cyclam metal complex: [Ni^{II}(cyclam)Cl$_2$].[11] The complex is octahedral, paramagnetic for two unpaired electrons and exhibits a trans-III configuration.

The purely organic lengthy procedure, the recommended high-dilution technique (to minimize polymerization), the low overall yield discouraged from the synthesis of cyclam by inorganic chemists, but in 1972 E. Kent Barefield, reported a very convenient metal template synthesis of cyclam, illustrated in figure 7.[13]

Trans-I
R, S, R, S
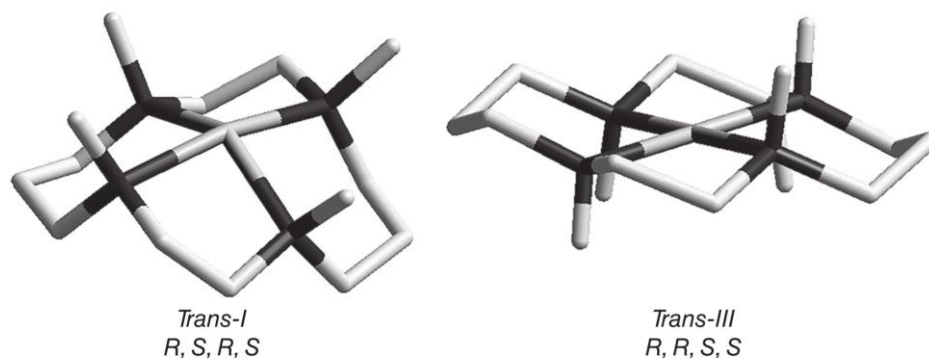
Trans-III
R, R, S, S

Figure 5. The trans-I configuration of a metal-cyclam complex, in which all the N − H fragments (or N − R) point on the same side of the plane of nitrogen atoms. In the trans-III isomers, the two N − H fragments linked by one trimethylenic chain point above the plane, the other two points below. R and S descriptors have been assigned according to CIP rules.

The templating role was exerted by Ni(II), which, in an aqueous solution, formed a stable complex with the open chain tetramine (3·2·3-tet), positioning the four nitrogen atoms at the corners of a square. In this way, the two primary amine groups of 3·2·3-tet were in the right positions to undergo Schiff base condensation with one molecule of glyoxal, thus giving the diene macrocyclic complex. The two C=N double bonds were reduced by catalytic hydrogenation on nickel Raney, the metal was removed from the $[Ni^{II}(cyclam)]^{2+}$ complex by treatment with boiling cyanide in the presence of NaOH and the ligand was extracted in $CHCl_3$ from the aqueous solution. All the process was carried out in the same solution at a very high concentration (0.25 M). The overall yield was quite low (20%), but the procedure was one-pot and involved cheap reagents with water as a solvent.
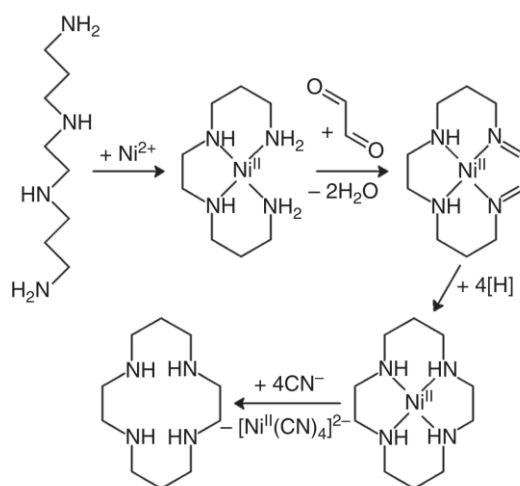
Figure 7. The Ni(II) template synthesis of cyclam.[13]

2.5 Thermodynamic aspects

2.5.1 Macrocyclic effect

Macrocyclic ligands – ligands that form a large, continuous ring around a metal ion – form extremely robust complexes because of the macrocyclic effect.[14] This effect has both thermodynamic and kinetic origins. The thermodynamic macrocyclic effect refers to the higher binding constant ($\log \beta$) for a macrocyclic ligand compared to an analogous open-chain ligand (Eq. (1)):

$$\text{Macrocyclic effect} = \Delta \log \beta = \log \beta_{\text{macrocycle}} - \log \beta_{\text{open-chain}} \tag{1}$$

Because the macrocyclic ring lacks a "free end," stepwise removal of the donor atoms is exceedingly difficult. This feature results in very slow dissociation rates of macrocyclic ligands from their complexes: the *kinetic macrocyclic effect* (fig. 8b). In 1969, Dale W. Margerum, of Purdue University, West Lafayette, reported the first investigation of the thermodynamic stability of metal macrocyclic complexes. They demonstrated that macrocyclic complexes are more stable than their open chain analogue. In particular they compared the affinity constants, the enthalpy and the entropy changes of the formation of the complex $[Ni^{II}(2\cdot3\cdot2\text{-tet})]^{2+}$ and the analogue cyclic complex $[Ni^{II}(\text{cyclam})]^{2+}$. They demonstrated that the complexation of the Ni(II) with cyclam is much more exergonic than with the $2\cdot3\cdot2$-tet linear ligand and the macrocyclic effect is totally driven by an extremely favorable enthalpy change and moderately disfavored by the entropy contribution. The interpretation suggested by Margerum was based exclusively on the different hydration of the uncomplexed ligands $2\cdot3\cdot2$-tet and cyclam. In particular, it was considered that the open-chain tetramine in the primary hydration shell interacted with four water molecules, whereas the macrocycle, due to its closed arrangement, could establish hydrogen bonds at most with two H_2O molecules.

The energetic basis for the macrocyclic effect can be understood by comparing the relative stabilities of unbound macrocyclic ligands to open-chain ligands as illustrated in Fig. 8a.[15,16] As indicated in the figures, a free macrocyclic ligand in solution is less stable than its open-chain analog because of reduced flexibility and the resulting loss of configurational entropy. Macrocycles also have less solvent-accessible surface area and cannot be as efficiently stabilized by interactions with solvent molecules. This solvent interaction is especially important for nitrogen macrocycles in aqueous solution, where the free open-chain ligand can extend, and the nitrogen atoms can accept hydrogen bonds from the solvent. By contrast, macrocyclic nitrogen ligands are conformationally restricted, and the nitrogen atoms are not as accessible for hydrogen bonding, resulting in poor stabilization of the free macrocycle. Because of this, the macrocyclic effect in nitrogen ligands is especially large (up to log $\beta \sim 10$).[17] Macrocyclic oxygen ligands (crown ethers), which bind electrostatically to alkali metals and other cations, show smaller macrocyclic effects (log $\beta \sim 3$–4),[18] which are primarily attributed to enthalpic contributions. Macrocyclic sulfur ligands show an even smaller macrocyclic effect (log $\beta \sim 2$).[19]
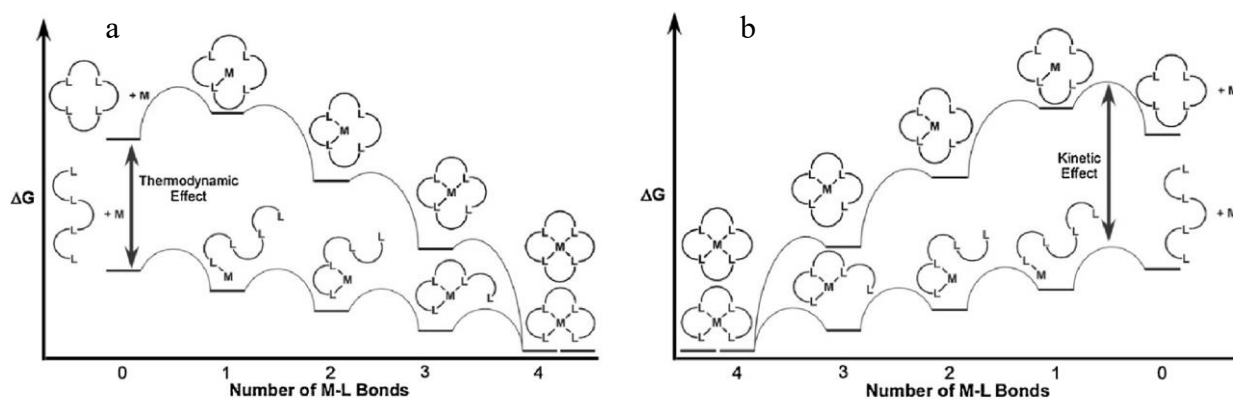
Figure 8. (a) Origin of the thermodynamic macrocyclic effect, (b) origin of the kinetic macrocyclic effect.

In 1973, Fabbrizzi and coworkers discovered a linear correlation between the enthalpy of complex formation in aqueous solution (determined calorimetrically) and the energy of the d–d absorption band for a series of copper(II) tetramine and bis-diamine complexes, illustrated in Figure 9.[20] The energy of the band expresses the intensity of the in-plane interaction, thus giving a measure of the energy of the bonds established by Cu(II) with the four amine nitrogen atoms. It seems therefore reasonable to assume a correlation of the wavenumber of the absorption band with the enthalpy of complex formation, which includes as a main contribution the energy of the Cu^{II}– N coordinative interaction. They demonstrated that the macrocyclic effect is also due to the increased energy of the metal-ligand coordinative interaction, moving from linear to cyclic ligand.
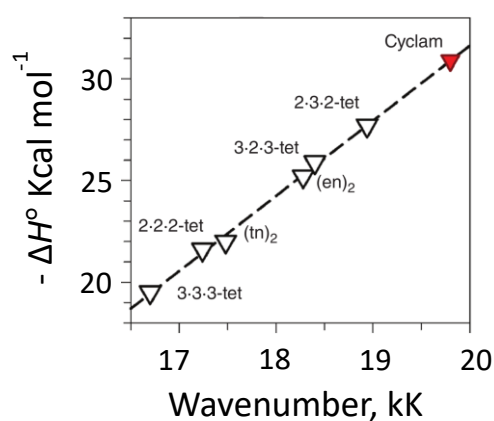
Figure 9. Linear correlation between the enthalpy of complex formation in aqueous solution and the energy of the d–d absorption band for a series of copper(II) tetramine and bis-diamine complexes.[20]

2.5.2   Selectivity

Ring size selectivity had been observed in the complexation of alkaline metal ions by crown ethers and cryptands. A similar behavior can be observed between Cu(II) and tetramine macrocycles with different atomicity (figure 10).
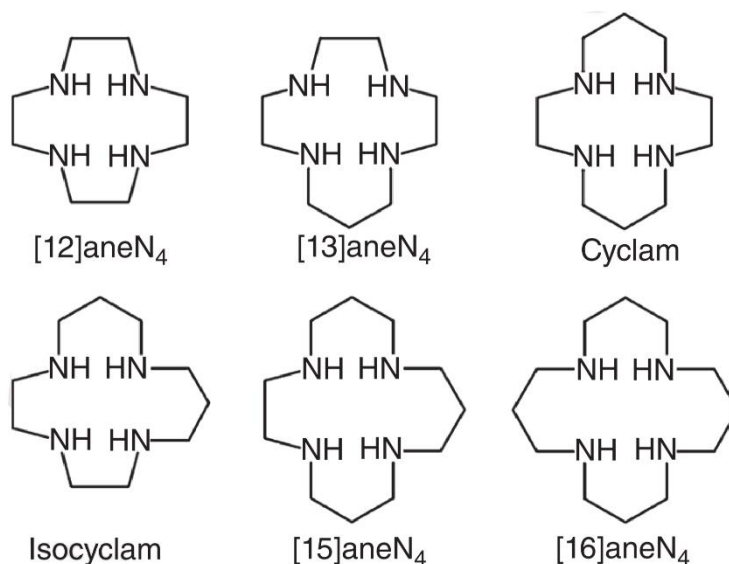
Figure 10. Tetramine macrocycles with different atomicity.

The enthalpy changes associate to the formation of the corresponding copper(II) complexes, in aqueous solution, at 25°C, are displayed in Figure 11, which highlights the selectivity for 14-membered macrocycle (cyclam).[21] Either expansion or contraction of the macrocyclic cavity induces a drastic reduction of the heat of complex formation. Noticeably, the same ring-size dependence is observed for the energy of the d–d band (wavenumber, kK, open circles in Figure 10), which suggests that the enthalpy selectivity is strictly related to the capability of the macrocycle to establish more or less intense in-plane metal–ligand interaction. Anyway, the enthalpic selectivity of copper(II) tetra-aza-macrocyclic complexes is not a simple matter of ring size. This is demonstrated by the behavior of the "other" 14-membered macrocycle in addition to cyclam: the so-called isocyclam.[22] $\Delta H°$ for the formation of $[Cu^{II}(isocyclam)]^{2+}$ is -27.8 kcal mol-1, i.e. 4.6 kcal less exothermic than for $[Cu^{II}(cyclam)]^{2+}$. Figure 11 shows the structure of the two complexes $[Cu^{II}(cyclam)]^{2+}$,[23] and $[Cu^{II}(isocyclam)]^{2+}$,[24] both crystallized as perchlorate salts.
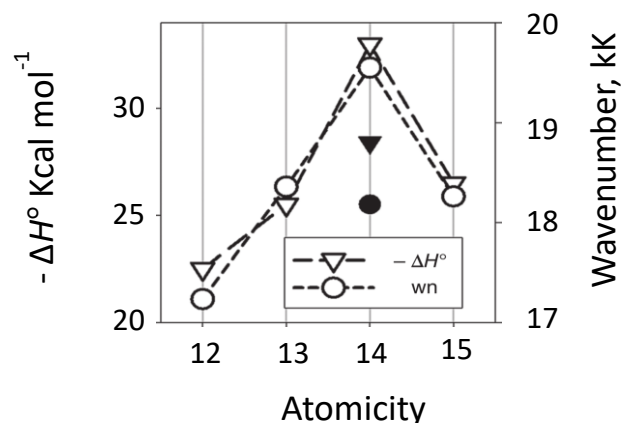
Figure 11. Enthalpy changes and wavenumber associate to the formation of the complexes between copper(II) and tetramine macrocycles of vary atomicity.[21] Triangles: $\Delta H°$ in aqueous solution at 25°C; circles: energy of the d-d band. Filled symbols refer to the copper(II) complex of isocyclam.

The nitrogen atoms of each macrocycle have been linked with a red dotted straight segment, to define a quadrilateral. The quadrilateral of $[Cu^{II}(cyclam)]^{2+}$ is an almost regular square with four right angles, a circumstance which allows a substantial overlap of the nitrogen lone pairs with the empty dx^2-y^2 metal orbital and affords a strong binding interaction. On the other hand, $[Cu^{II}(isocyclam)]^{2+}$ gives a kite-like quadrilateral, to which a poor lone pair/orbital overlap should correspond. This accounts for the distinctly less negative enthalpy change and for the lower energy of the d–d band (18.18 kK). Noticeably, the uncomplexed cyclam, whose structure is shown in Figure 12,[25] shows a quite regular square of nitrogen atoms, whose edges are close to those observed in the $[Cu^{II}(cyclam)]^{2+}$ complex. Cyclam forms especially stable complexes because it is perfectly preorganized and preoriented for including and establishing strong interactions with those 3d metals that experience the highest ligand field stabilization from a tetragonal coordination geometry. Such a macrocyclic advantage diminishes or vanishes when the ligand's structure deviates from that of cyclam.
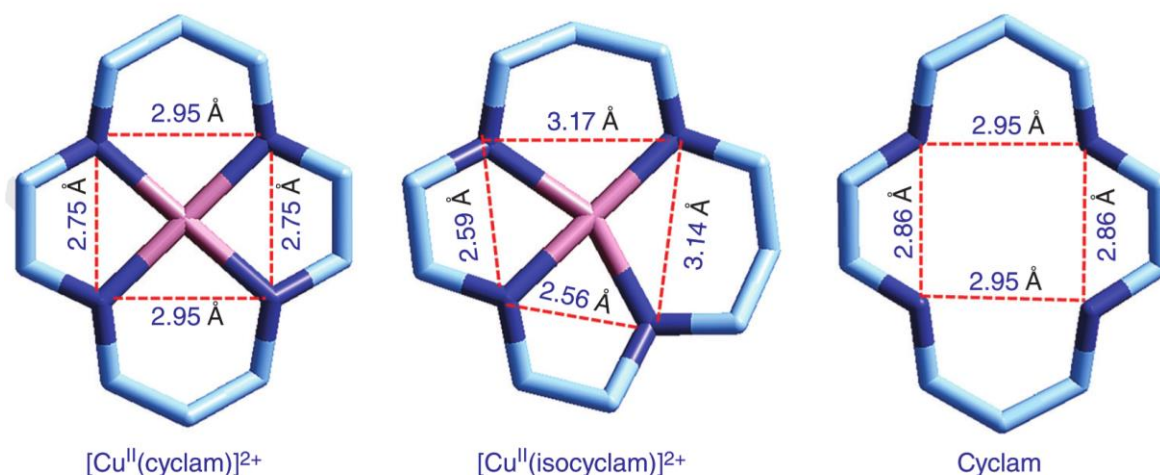
Figure 12. The molecular structure of the complexes $[Cu^{II}(cyclam)]^{2+}$,[23] and $[Cu^{II}(isocyclam)]^{2+}$,[24] and of the uncomplexed cyclam. Red dotted lines define a quadrilateral whose vertices are the nitrogen atoms. Complexes are both crystallized as perchlorate salts.

2.6 Bimacrocyclic complexes

In the intervening years, clever synthetic chemists have continued to produce more, and more azamacrocycles with important applications alone and/or in their metal ion complexes. A still difficult task to carry out is to join two azamacrocycles together. Architectures produced by joining rings (Fig. 13) include (1) fused ring systems—those in which one or more atom belongs to two or more of the rings; (2) mechanically interlocked multi-ring systems, commonly called catenanes; and (3) linked ring systems—here defined as those not mechanically bonded and having no atoms belonging to more than one macrocyclic ring.[26]
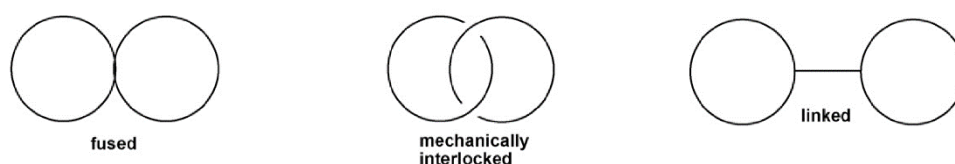
Figure 13. Types of architectures produced by joining rings. This thesis will focus on the linked systems.

Two macrocyclic ligands can be linked through a variety of bridges involving donor atoms (mainly nitrogen), or directly through a C-C bond linking the carbon framework of each tetraaza macrocycle, and many of these bis(macrocycles) (2–5) based on cyclam have been studied. Depending upon the mode of connection and the nature of the bridging group, two aspects of their structures influence the chemistry of these systems. They are (i) the inter-metal ion distance and (ii) the relative

orientation of the macrocyclic rings with respect to each other. Electrostatic and steric effects also play a role, which is controlled by these structural factors.[27]
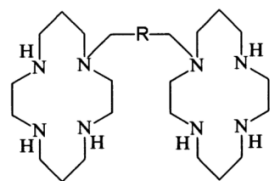
2, N,N'-bis(cyclam)
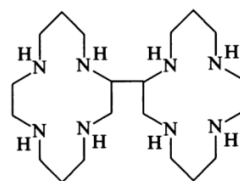
3, 2,2'-bi(cyclam)
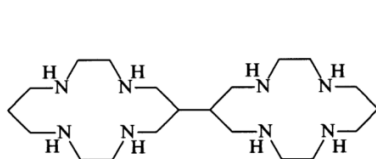
4, 6,6'-bi(cyclam)
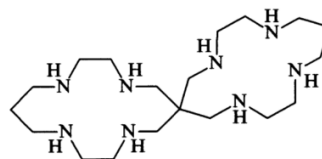
5, 6,6'-C-spirobi(cyclam)

The preset thesis will focus on C-C linked synthetic azamacrocycles, where all donor atoms are nitrogen. One of the main propriety of the C-C linked bimacrocycles compared to the N-N linked bimacrocycles is to maintain unaltered the around coordination of the metal center.

2.7   Application of azamacrocycle

Azamacrocycle complexes and ligands have very useful applications, in different area of interest, such as medical imaging (magnetic resonance imaging, luminescence, radiolabeling), molecular recognition (anion, cation and neutral molecule recognition), catalysis (ester cleavage, catalytic disproportion of H_2O_2, catalytic CO_2 reduction) and medicinal chemistry (CXCR4 antagonists). The present thesis is focused on anion recognition and catalytic CO_2 reduction.[26]

3 Anion recognition

3.1 Introduction

Anions have an enormous impact upon our lives. They carry genetic information (DNA is a polyanion) and the majority of enzyme substrates and co-factors are Anionic (ATP). Amongst the halides, chloride is found extensively in extracellular fluid, with its misregulation being linked to diseases such as cystic fibrosis, iodide is required for the biosynthesis of hormones by the thyroid gland, while fluoride is considered essential for healthy bone and teeth growth, which has led to the (sometimes controversial) artificial fluoridation of water supplies. In the case of other anions, it is well-established that bicarbonate is vital in the maintenance of pH levels in the body, whereas cyanide is highly toxic. Certain anions have an adverse effect on the environment around us. Nitrate and sulfate are key components in the production of acid rain. Excessive use of phosphates and nitrates in fertilizers has led to eutrophication in waterways. Pertechnetate (a by-product of nuclear fuel reprocessing) and perchlorate (arising from the manufacture of explosives) are two further examples of anthropogenic pollutants, while arsenate is an example of a naturally occurring one. In short, there has been, and still is, considerable motivation for investigating the binding and sensing of anionic species.[28]

Given a molecular substrate (either neutral or electrically charged), its receptor, i.e. a system capable of establishing selective interactions, can be designed by taking into account three basic parameters: shape, size and energy. In particular, the receptor should provide a concave portion of space (the cavity), whose shape is complementary with that of the substrate. Moreover, the size of the cavity should be comparable with that of the substrate, so that the receptor framework does not have to undergo any endergonic rearrangement (either expansion or contraction) in order to conform with the required bond distances. Finally, the energy of the receptor substrate interaction has to be high enough to be able to more than compensate the endergonic terms related to desolvation (both of the receptor and of the substrate). The latter issue is especially significant for the recognition of ionic analytes in an aqueous medium.[29]

3.2 Anion recognition by cyclam-like macrocyclic complexes[30]

Cyclam complexes can be considered as ideal subjects for the study of metal–anion interaction for two main reasons: (i) they offer plenty of space to the incoming anion along the z axis, and (ii) thanks to their inertness, they cannot be demetallated even on addition of a large excess of anion. In 1984, Hancock studied, through spectrophotometric titrations, the interaction of $Cu(cyclam)^{2+}$ with anions in an aqueous solution ($\mu = 0.1$ M, 25 ° C). Very weak interactions were observed, and no reliable binding constants could be measured for F^- and Cl^- ions at the 10^{-2} M concentration scale (which indicates a binding constant with log $K < 1$). Appreciable interaction was observed for polyatomic anions as N_3^- (log $K = 2.1$) and NCS^- (log $K = 1.8$). The intrinsically low magnitude of the binding constants has to be mainly ascribed to the endothermic anion dehydration, very high for monoatomic anions, less significant for polyatomic anions, in which the negative charge is spread over three atoms. Fig. 14 shows the molecular structure of the $[Cu^{II}(cyclam)NCS]^+$, and $[Cu^{II}(cyclam)N_3]^+$, ternary complexes.
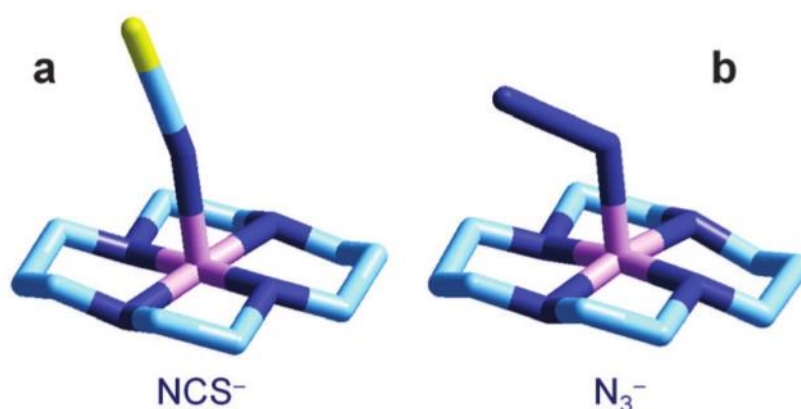
Figure 14. Crystal structures of (a) $[Cu^{II}(cyclam)NCS]^+$; displacement of Cu^{II} from the N4 plane: 0.04 Å, Cu–N(amine) distance 2.01 ± 0.01 Å, Cu–N(NCS^-) distance 2.43 Å; (b) $[Cu^{II}(cyclam)N_3]^+$; displacement of Cu^{II} from the N4 plane: 0.16 Å, Cu–N(amine) distance 2.02 ± 0.01 Å, Cu–N(N_3^-) distance 2.31 Å. Hydrogens and counteranions omitted for clarity.

Both complexes show a regular square pyramidal geometry, with the anion occupying the apical position. The Cu^{II} center is only slightly displaced from the plane of four amine nitrogen atoms ($[Cu^{II}(cyclam)NCS]^+$: 0.04Å; $[Cu^{II}(cyclam)N_3]^+$: 0.16Å). Cyclam can be permethylated at the amine nitrogen atoms to give 1,4,8,11-tetramethyl-1,4,8,11-tetraazacyclotetradecan ($Me_4cyclam$), which, on reaction with transition metal salts, gives complexes of trans-I configuration (R,S,R,S). The crystal and molecular structures of some divalent 3d metal complexes of $Me_4cyclam$ are shown in Fig. 15. All the complexes show a square pyramidal geometry, with the four amine nitrogen atoms

positioned at the corners of the square and an apically bound anion, as observed for $Cu^{II}(cyclam)^{2+}$ complexes shown in Fig. 14. However, in the present cases, the metal lies well above the plane of nitrogen atoms, on the side of methyl substituents. In particular, the displacement from the N plane is expected to favor the interaction with the anion. In this connection, one should observe that in the case of Co^{II} ((ii) and (iv) in Fig. 15) and Ni^{II} complexes (iii) the metal-anion distance is especially small, smaller than the average M^{II}-N(amine) distance. The opposite occurs with the Cu^{II} complex (i), for which the length of the apical bond is larger than that of the Cu^{II}-N(amine) bond (see values reported in Fig. 15). On these bases, one should anticipate that $Co^{II}(Me_4cyclam)^{2+}$ and $Ni^{II}(Me_4cyclam)^{2+}$ should be inclined to form with a given anion more stable ternary complexes than $Cu^{II}(Me_4cyclam)^{2+}$. The interaction of the rod-like triatomic anions N_3^-, NCO^- and NCS^- with Co^{II}, Ni^{II} and Cu^{II} complexes of $Me_4cyclam$ in water has been investigated by Kaden and Paoletti in 1982 through spectrophotometric titration experiments. Log K values for the equilibria of formation of ternary complexes are shown in Fig. 16a. As a general behavior, Co^{II} and Ni^{II} complexes form more stable ternary species than the Cu^{II} analogue, which may reflect the formation of more intense metal–anion interactions, as expected on the basis of structural data.
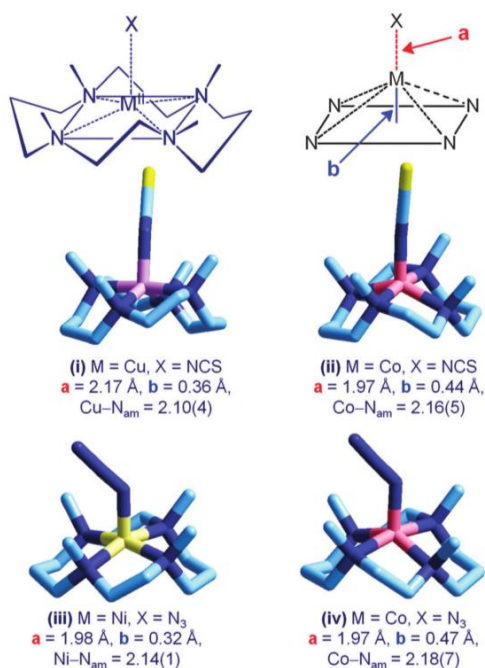
Figure 15. The crystal and molecular structures of $[M^{II}(Me_4cyclam)X]^+$ complexes (M = Cu^{II}, Co^{II}, Ni^{II}), with relevant geometrical parameters (a): distance between the anion donor atom and the metal ion; (b) distance of the metal ion from the plane of the four amine nitrogen atoms; M–N_{am}, average distance between the metal ion and the nitrogen atoms of $Me_4cyclam$. Not coordinated counter-anions and hydrogen atoms have been omitted for clarity. $[Cu^{II}(Me_4cyclam)NCS]^+$; $[Co^{II}(Me_4cyclam)NCS]^+$; $[Ni^{II}(Me_4cyclam)N_3]^+$; $Co^{II}(Me_4cyclam)N_3]^+$.

Moreover, calorimetric studies showed that the stability of the ternary complexes of formula $[M^{II}(Me_4cyclam)X]^+$ results from both favorable $\Delta H°$ and $T\Delta S°$ contributions. As an example, Fig. 15b shows the thermodynamic quantities for the equilibria involving the N_3^- anion. It appears that anion desolvation plays, also in the present systems, a determining role: (i) it makes the entropy change distinctly positive and (ii) it reduces the exothermicity associated the formation of the metal–anion coordinative bond. In particular, in the $Cu^{II}(Me_4cyclam)^{2+}/N_3^-$ system, the exothermic effect of the Cu^{II}-N_3 and the endothermic effect of azide dehydration balance exactly, thus making complexation athermic and solely driven by the entropy term. Fig. 15b reports also, as green bars, the $\Delta G°$ values associated to the equilibria $M^{2+} + NCO^- \rightarrow [M(NCO)]^+$ in water. These values are of the same order of magnitude of those referring to $Me_4cyclam$ complexes. In particular, in the case of Co^{II} and Ni^{II}, the interaction of the $[M^{II}(Me_4cyclam)]^{2+}$ complex with NCO^- is favored with respect to the corresponding aquaions, whereas for Cu^{II} the reverse behavior is observed. Pre-coordination by $Me_4cyclam$ is especially favorable, as it eliminates the endothermic dehydration of the uncomplexed aqueous ion and it prearranges the metal to the interaction with the anion. $Me_4cyclam$ and cyclam complexes, as well as any other monometallic polyamine complex, do not form very stable ternary complexes with anions and do not provide any defined selectivity with respect to anion binding. In classical coordination chemistry, when a metal does not form a stable complex with a given unidentate ligand (e.g. ammonia), it is convenient to move to the corresponding bidentate ligand (e.g. ethylenediamine), in order to profit from the chelate effect. In the same way, in the case of anion binding, in order to have more stable ternary complexes, it seems convenient to profit from the chelate effect, thus designing polyamine complexes containing two (or even more) coordinatively unsaturated metal centers. As an additional benefit, steric constraints possibly present in the polyamine framework can generate a pronounced geometrical selectivity with respect to anion binding.
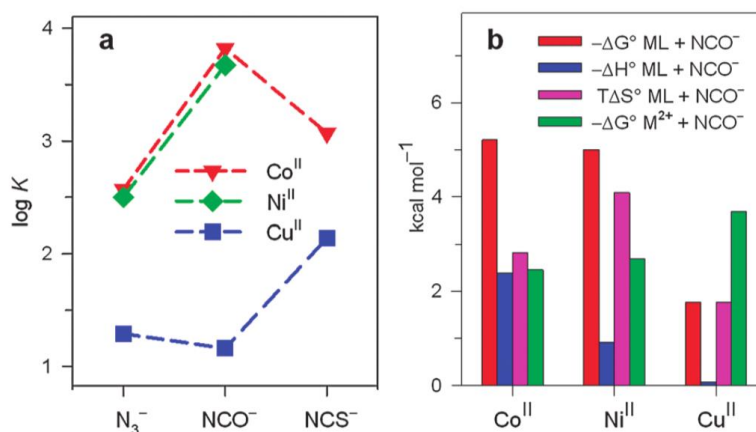
Figure 16. (a) Log K values for the equilibria $M^{II}(Me_4cyclam)^{2+} + X^- \leftrightarrows [M^{II}(Me_4cyclam)X]^+$, in water at 25 °C (M = Cu^{II}, Co^{II}, Ni^{II}; X^- = N_3^-, NCO^-, NCS^-); (b) thermodynamic quantities for he equilibria $M^{II}(Me_4cyclam)^{2+} + NCO^- \leftrightarrows M^{II}(Me_4cyclam)NCO]^+$, in water at 25 °C.

3.3   Anion recognition by bimacrocyclic complexes

In terms of receptor design, a common approach to improve the anion recognition ability is the chelating strategy illustrated in figure 17, where an organic scaffold with coordinating atoms (typically nitrogens) holds two metal centers at a specific distance, so they can be bridged by a target anion. In terms of the recognition mechanism, there are two limiting cases to consider. In one case, the scaffold binds the metal cations so strongly that the complex can be considered as a single molecular unit with two Lewis acidic sites whose separation is controlled by the length and rigidity of the scaffold. The alterative mechanism is when the scaffold has an inherently weak affinity for one or both metal cations. However, the presence of a suitable bridging anion induces a three-component assembly to occur that brings together the scaffold, metal cations, and bridging anion.[31]
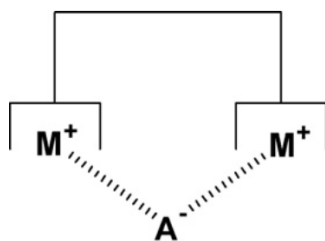
Figure 17. Anion recognition by a dimetallic coordination complex. The organic scaffold may also be a macrocycle.

The present thesis is focused on the first recognition mechanism, since the chelating subunit of the complexes under study are macrocycles, which strongly bind the metal centers.

A prominent metal-containing building blocks are zinc(II) complexes of 1,4,7,10-tetraazadodecane (cyclen) ligand. It has been studied extensively in the Kimura group.[32] Examples are ditopic receptor 6 and tritopic receptor 7. Receptors 6 and 7 both interact with p-nitrophenylphosphate in slightly acidic aqueous solution (pH < 6) with an affinity log K of 4.0 and 5.8, respectively. This increase in complex stability is attributed to the cooperative binding of all three zinc(II)–cyclen units in 7 to the three oxygen atoms of the guest. Phosphate affinity seems to parallel the basicity of the substrate as p-nitrophenyl phosphate (pK_a = 5.2; log K = 5.8), phenyl phosphate (pK_a = 5.8; log K = 6.6), and phenyl phosphonate (pK_a = 7.0; log K = 7.9) are bound increasingly more strongly. In a basic solution, phosphate is displaced by hydroxide ions from the metal centers in these receptors.

6   **7**   **8**
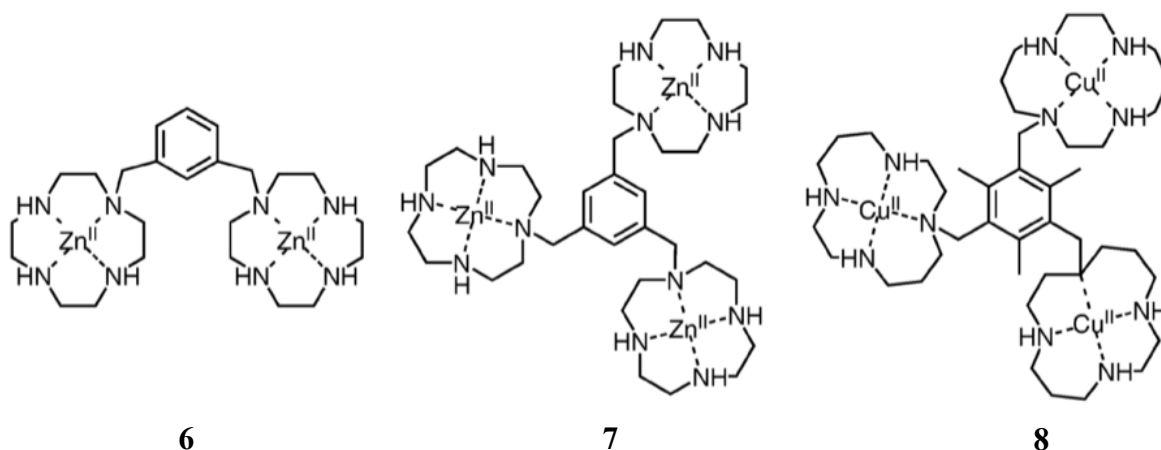
In a related approach, the tris(copper(II)–cyclam) receptor 8 was shown to interact with carboxylates in aqueous solution (10 mM HEPES buffer, pH 7).[33] Binding was visualized by the recovery of the fluorescence emission of the indicator 5-carboxy-fluorescein upon its displacement from the receptor by suitable substrates. Binding is strongest for tricarboxylates, the citrate complex, for example, has a log K of 5.59. Receptor affinity for dicarboxylates is ca. one order of magnitude lower while monocarboxylates are bound even less efficiently. Moreover, it is capable of discriminating citrate from competing analytes present in beverages. No demetallation of 8 was observed even in the presence of a large excess of substrate.

4   Anion Binding by Dimetallic Nickel(II) and Nickel(III) Complexes of a Face-to-face Bicyclam: Looking for a Bimacrocyclic Effect[34]

ABSTRACT: The dinickel(II) complex of the face-to-face bicyclam ligand α,α'-bis(5,7-dimethyl-l,4,8,l1-tetraazacyclotetradecan-6-yl)-o-xylene (L∩L) in a DMSO solution exists as a mixture of high- and low-spin forms and uptakes up to three halide and pseudohalide ions (X$^-$), according to stepwise equilibria, whose constants were determined through spectrophotometric titration experiments. In the case of halides, the first anion goes into the intermetallic cavity, whereas pseudohalides first coordinate the metal center from outside. Comparison with equilibrium data for the complex with the macrocycle 5,7-dimethyl-1,4,8,11-tetraazacyclotetradecane (L), shows that the dinuclear complex [Ni$^{II}_2$(L∩L)]$^{4+}$ displays an affinity for the first halide distinctly higher than the mononuclear complex [Ni^{II}(L)]$^{2+}$, thus disclosing the existence of a *bimacrocyclic effect* for anion binding. Differential Pulse Voltammetry studies typically showed a three-peak profile: the most anodic pertaining to the [Ni$^{II}_2$(L∩L)]$^{4+}$ → Ni$^{III}_2$(L∩L)]$^{6+}$ two-electron process, then one originating from the [Ni$^{II}_2$(L∩L)X]$^{3+}$ → Ni$^{III}_2$(L∩L)X]$^{5+}$ two-electron process, and one deriving from the two two-electron half reactions [Ni$^{II}_2$(L∩L)X$_2$]$^{2+}$ → Ni$^{III}_2$(L∩L)X$_2$]$^{4+}$ and [Ni$^{II}_2$(L∩L)X$_3$]$^+$ → Ni$^{III}_2$(L∩L)X$_3$]$^{3+}$, taking place at nearly the same potential. The crystal and molecular structure of the [Ni$^{II}_2$(L∩L)(μ-NCO)(NCO)$_2$]ClO$_4$ complex salt showed a caterpillar arrangement of the three metal bound cyanate ions.
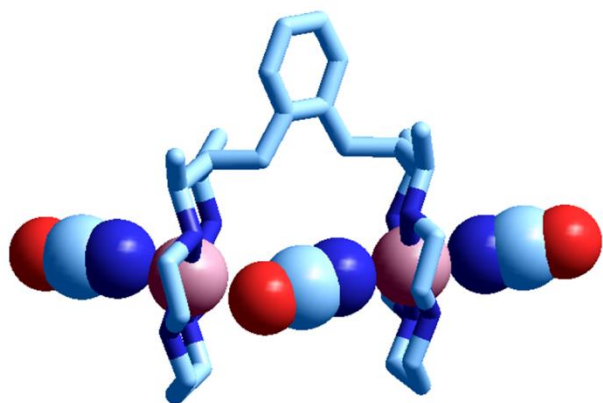
4.1   Introduction

Anion recognition results from the selective interaction with a given receptor, possibly of a concave shape, whose structural features fulfil the geometrical requirements of the anion.[35] Most anion receptors operate through electrostatic interactions, including hydrogen bonding. These interactions are not very energetic and the formation of stable complexes requires the design of highly preorganized receptors, whose positively charged binding points are strategically positioned inside the cavity.[36] On the other hand, coordinatively unsaturated metal complexes establish rather intense

interactions with anions and can behave as efficient receptors for anions, operating in solvent of high polarity including water.[37] This is the case of complexes of labile metal ions (e.g. Cu[II]) with *tetramines*: branched (tren), linear (trien), cyclic (cyclam).[30] In general, the intensity of the metal-anion interaction varies according to the spectrochemical series, a circumstance which limits any design of selectivity.
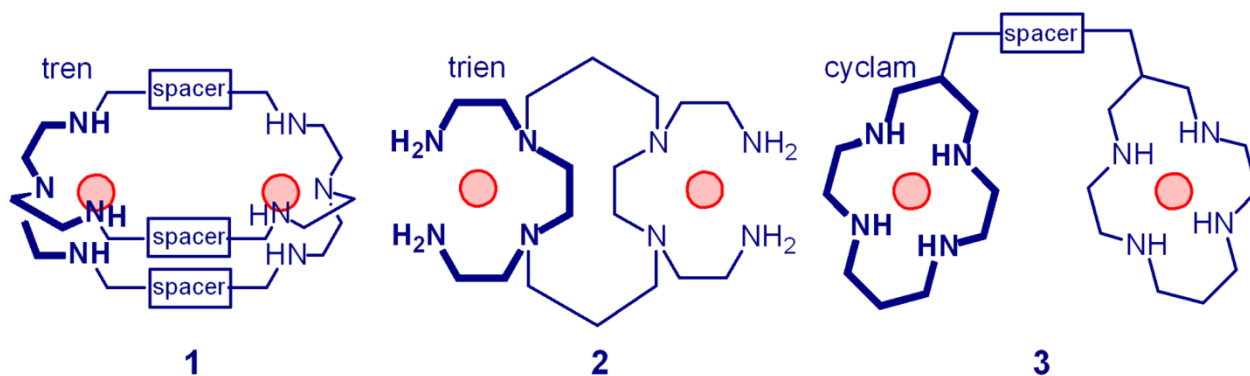
Scheme 1. Octamine ligands consisting of two distinct tetramine subunits, each capable to bind one metal center. Dimetallic complexes of the three tetramines can bind a single anion capable to bridge the two coordinatively unsaturated metal centers.

However, geometrical selectivity can be achieved through the design of *octamine* systems, consisting of two distinct *tetramine* subunits, each interacting with a metal center, which should remain coordinatively unsaturated. Three different types of octamine dinucleating ligands are shown in Scheme 1. The most investigated systems of this class are those of type **1** (*bistrens*), in which two tren subunits have been covalently linked by a variety of spacers.[38] The length of the spacer provides selectivity. For instance, when the spacer is 1,3-dimethylbenzene, the corresponding dicopper(II) bistren complex encapsulates polyatomic ambidentate anions capable of bridging the two metal centers, according to a selectivity based on the *bite length* (i.e. the distance of two consecutive donor atoms of the anion): the azide ion, among inorganic anions, forms the most stable inclusion complex.[39] The octamine **2**, bearing two trien subunits, shows a higher flexibility than **1** and its dicopper(II) complex is able to coordinate both mono- and poly-atomic anions bridging the two metals.[40] Notice that the tetramine subunits of octamines **1** and **2** forms with metal ions (e.g. Cu[II]) *labile* complexes and are subject to demetallation in the presence of an excess of anion or under acidic conditions (due to the protonation of the amine groups). A further route to the design of dimetallic octamine receptors involves the covalent linking of two cyclam subunits (*bicyclams*, **3**).[41] In particular, the corresponding dimetallic complexes contain two *inert* metallocyclam moieties and will not undergo demetallation even under severe conditions. Moreover, if the two metallocyclam subunits

are made to converge by an appropriate spacer, they can firmly include one anion, possibly establishing selective interactions.

4   **5**
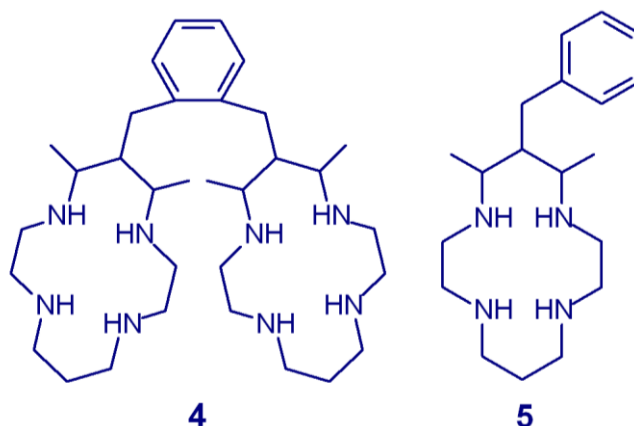
The bicyclam ligand **4** belongs to this family: it consists of two dimethylcyclam subunits bridged at the carbon center with an *ortho*-xylyl group, thus providing a face-to-face arrangement of the two macrocycles. A dinuclear complex of **4** is expected to include an ambidentate anion capable of encompassing the two metal centers, as sketched in formula **6**.

6
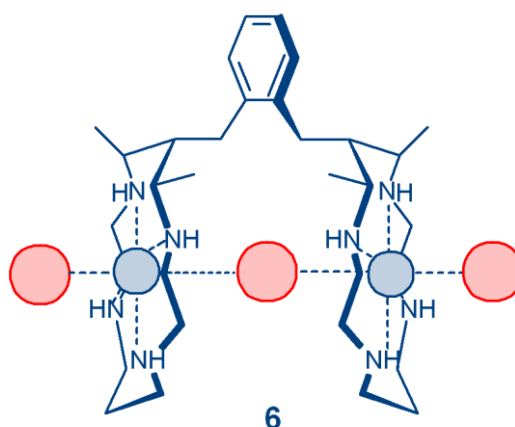
Ito *et al.* in 1993 reported the crystal structure, taken at room temperature, of the Ni^{II}_2(**4**)$Br_4 \cdot H_2O$ salt, in which the dimetallic complex [Ni^{II}_2(**4**)(μ-Br)Br_2]$^+$ contained three bromide ions, one in the cavity between the two metal centers, and two external ones.[42] The Br$^-$ ion in the middle was located at two disordered positions and the distance between each Ni^{II} center and the closest Br$^-$ position was 2.57 Å. On the other hand, the distance of each Ni^{II} center from the external bromide ion was rather long (2.88 Å), indicating a very weak interaction. The Authors suggested that 'each Ni^{II} ion is, therefore, in a square-planar four-coordinate geometry at 50% probability and in a five-coordinated square pyramidal environment at 50%.'[9] The puzzling point was that the Ni^{II}–N distance in both

macrocyclic subunits was 2.01 ± 0.01 Å, a value intermediate between that expected for low-spin square-planar Ni^{II} (1.90−1.95 Å) and that expected for high-spin octahedral Ni^{II} (2.07−2.10 Å).
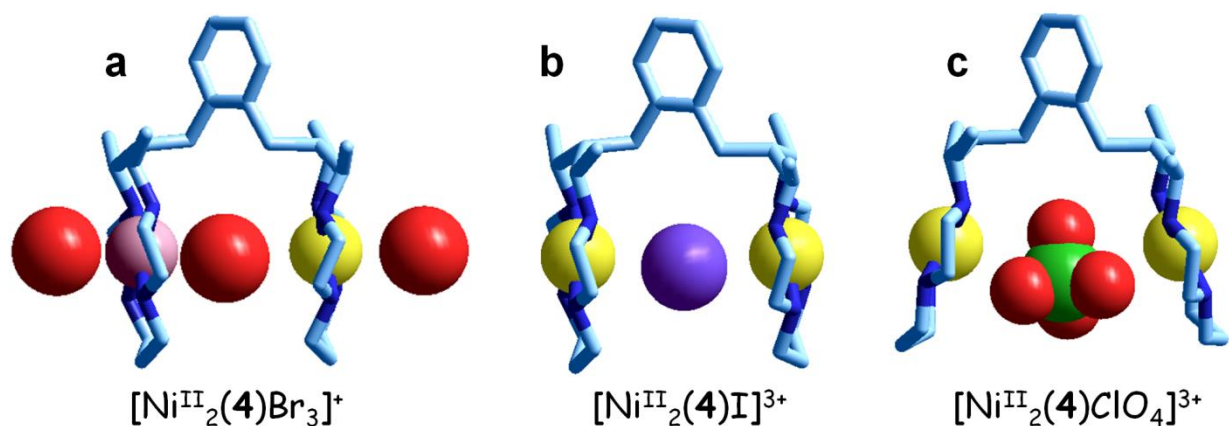
Figure 1. Crystal and molecular structures of (a) $[Ni^{II}_2(\mathbf{4})(\mu\text{-Br})Br_2]^+$ (taken at 100 K); (b) $Ni^{II}_2(\mathbf{4})(\mu\text{-I})]^{3+}$ (room temperature); (c) $[Ni^{II}_2(\mathbf{4})(\mu\text{-ClO}_4)]^{3+}$ (room temperature), all from ref 10. Color of the spheres in the metallocyclam subunits indicates the spin state of Ni^{II}: yellow, low-spin; blue-violet, high-spin.

In 2005, Endicott *et al.* made clear the point determining the X-ray structure of $[Ni^{II}_2(\mathbf{4})(\mu\text{-}Br)Br_2]ClO_4$ salt at 100 K.[43] The structure, reported in Figure 1a, showed the presence of one high-spin Ni^{II} (blue-violet sphere) with long Ni^{II}–N bonds (2.07 Å) and of one low-spin Ni^{II} (yellow sphere) with short Ni^{II}–N bonds (1.96 Å). Moreover, the high-spin Ni^{II} established two short bonds with Br^- (2.62 Å inside the dimer, 2.71 Å outside), whereas long Ni^{II}–Br distances were observed for the low-spin metal center (3.32 Å inside, 3.07 Å outside). The $Ni^{II}\cdots Ni^{II}$ distance was 5.80 Å.

Furthermore, the Authors demonstrated that nickel(II) complexes of **4** showed an extreme versatility in the electronic behavior, depending upon the nature of the anion enclosed between the two facing metallocyclam subunits. Figure 1b shows the room temperature structure of the complex salt $[Ni^{II}_2(\mathbf{4})(\mu\text{-I})](ClO_4)_3$. Both Ni^{II} ions (yellow spheres) are low-spin and the iodide ion in the middle is weakly coordinated. The $Ni^{II}\cdots Ni^{II}$ distance is 6.38 Å. The complex in Figure 1c, $[Ni^{II}_2(\mathbf{4})(\mu\text{-}ClO_4)]^{3+}$ (from the salt $[Ni^{II}_2(\mathbf{4})(\mu\text{-ClO}_4)](ClO_4)_3\cdot C_2H_5OH\cdot H_2O$ exhibits a quite similar structure, with a perchlorate ion included between two low-spin Ni^{II} ions (yellow spheres, $Ni^{II}\cdots Ni^{II}$ distance 7.20 Å).

We considered that the behavior of the $[Ni^{II}_2(\mathbf{4})]^{4+}$ complex as an anion receptor in solution could deserve an investigation. The present study has been addressed to the interaction of $[Ni^{II}_2(\mathbf{4})]^{4+}$ with halides and pseudohalides (NCO^-, NCS^-, N_3^-) in a DMSO solution and the corresponding stepwise binding constants have been determined through spectrophotometric titration experiments. Moreover, the crystal and molecular structure of the dinuclear complex $[Ni^{II}_2(\mathbf{4})(\mu\text{-NCO})(NCO)_2]^+$, containing

two high-spin Ni^{II} centers, has been determined, and the Ni^{II}-to-Ni^{III} oxidation process in DMSO has been investigated through voltammetric techniques, in the absence and in the presence of poorly reducing anions: Cl^-, NCO^-, N_3^- and NO_3^-, to evaluate the capability of the $[Ni^{II}_2(\mathbf{4})]^{4+}$ receptor to act as an electrochemical anion sensor. Finally, in order to verify the existence of cooperative effects in the solution behavior of $[Ni^{II}_2(\mathbf{4})]^{4+}$, if any, comparative spectrophotometric and voltammetric studies have been carried out on the mononuclear complex $[Ni^{II}(\mathbf{5})]^{2+}$, under the same conditions.

4.2 Results and discussion

4.2.1 Nature of the mononuclear $[Ni^{II}(5)]^{2+}$ and dinuclear $[Ni^{II}_2(4)]^{4+}$ complexes in DMSO solution

Nickel(II) complexes with cyclam and cyclam-like macrocycles exist in solution as an equilibrium mixture of two species: a high-spin complex of octahedrically elongated geometry and a low-spin complex of square planar geometry,[44] as illustrated in Figure 2.
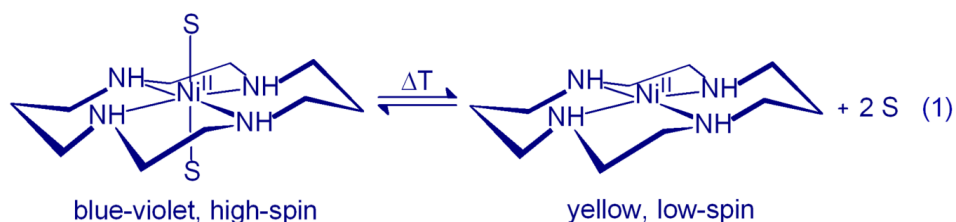
Figure 2. The blue-to-yellow conversion in nickel(II) complexes of cyclam and cyclam-like macrocycles. The position of the equilibrium depends upon the coordinating tendencies of the solvent S: the more coordinating S, the higher the concentration of the high-spin complex.

Two solvent molecules participate in the equilibrium, as they occupy the axial positions of the elongated octahedral high-spin complex. It derives that coordinating solvents favor the formation of the octahedral species and displace the equilibrium (1) to the left side. For instance, in the case of cyclam, the high-spin complex is present at 29% in water and at 78% in the more coordinating solvent MeCN.[45]
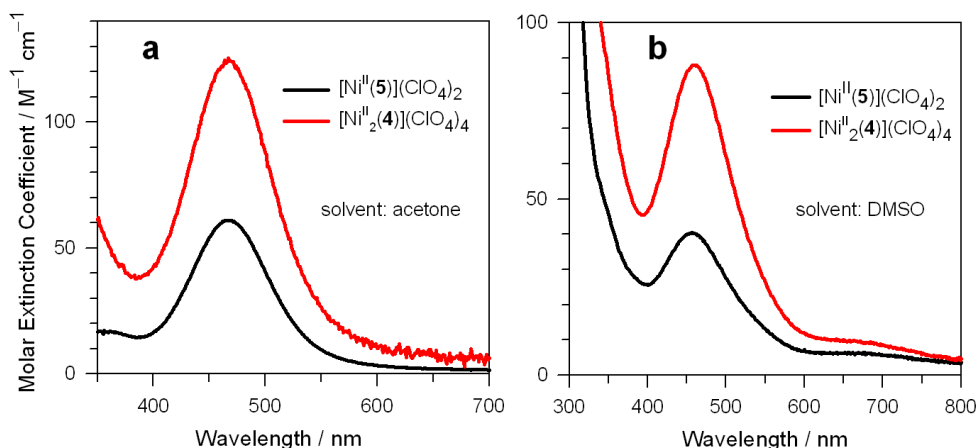
Figure 3. (a) spectra in acetone solution of $[Ni^{II}_2(\textbf{4})](ClO_4)_4$ (red line) and of $[Ni^{II}(\textbf{5})](ClO_4)$ (black line); (b) spectra in DMSO solution of $[Ni^{II}(\textbf{4})](ClO_4)_2$ (red line) and of $[Ni^{II}(\textbf{5})](ClO_4)_2$ (black line).

Acetone is a typically non-coordinating solvent and promotes the formation of 100% of the square planar complex. Figure 3a compares the spectra in acetone of the $[Ni^{II}_2(\textbf{4})]^{4+}$ dinuclear complex and of the corresponding mononuclear species $[Ni^{II}(\textbf{5})]^{2+}$. Both complexes present a band centered at 468 nm, corresponding to a low-spin square planar chromophore. Noticeably, the molar extinction coefficient ε for the dinuclear complex (124 M^{-1} cm^{-1}) is twice that observed for the mononuclear complex $[Ni^{II}(\textbf{5})]^{2+}$ (62 M^{-1} cm^{-1}). On the other hand, the solvent used in this study, DMSO, is a coordinating medium and is expected to favor the formation of the octahedral high-spin complex. Both mononuclear and dinuclear complexes in DMSO show bands centered at 460 nm ($\varepsilon = 40$ and 93 M^{-1} cm^{-1}, respectively), which are distinctly less intense than in acetone, thus suggesting the occurrence of a blue-to-yellow equilibrium. Notice that the intense absorption band centered at 460 nm obscures the bands of the high-spin octahedral form of both mono- and di-nuclear complexes. Thus, only a weak band at $\sim$ 700 nm can be observed.

On tentatively assuming that the ε value of the band of the yellow complex is the same in acetone and in DMSO (a quite reasonable assumption for *d-d* transitions), $\varepsilon_{DMSO}/\varepsilon_{acetone} \times 100 = 65\%$ should give an approximate value of the concentration of the square planar form of the mononuclear complex $[Ni^{II}(\textbf{5})]^{2+}$. Also, the spectrum of the dinuclear complex in DMSO (red line in Figure 3b) indicates a dominating presence of the low-spin yellow chromophore. From the expression $\varepsilon_{DMSO}/\varepsilon_{acetone} \times 100$, a concentration of the yellow square chromophore of 75% can be calculated. It is suggested that the spin conversion equilibrium involves a dinuclear complex containing a high-spin metallocyclam and a low-spin metallocyclam on the left side (**a**) and a dinuclear complex with two low-spin metallocyclam on the right side (**b**), as tentatively sketched in Figure 4.
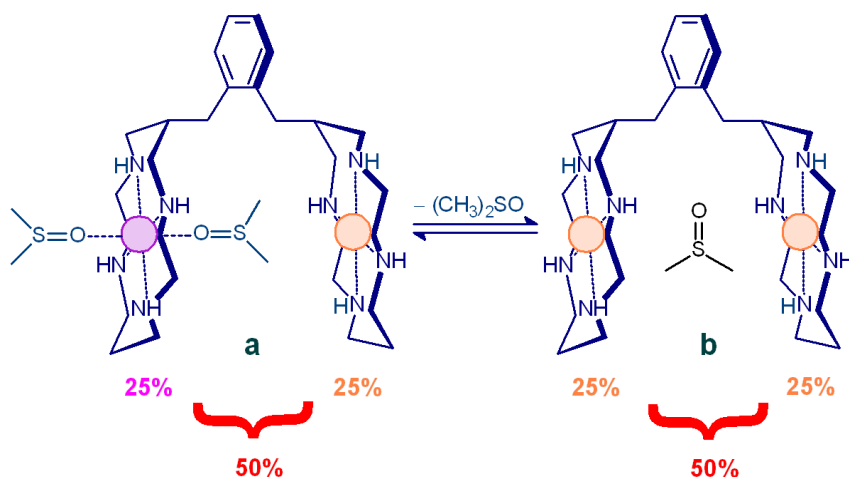
Figure 4. The hypothesized spin conversion equilibrium involving complex **a** (one high-spin octahedral subunit and one low-spin square-planar subunit) and complex **b** (two low-spin square-planar subunits).

The value of $\varepsilon_{DMSO}/\varepsilon_{acetone} \times 100 = 75\%$ should therefore result from the presence in solution of 50% of the complex **a** (mixed spin state) and 50% of the complex **b** (all low-spin state). The presence of the high-spin complex alone cannot be excluded in principle, but in such a complex *two* coordinated DMSO molecules should be probably present in the space between the two metallocyclam subunits, a circumstance highly disfavored by sterical repulsions.

4.2.2 Crystal and molecular structure of the $[Ni^{II}_2(4)(\mu\text{-}NCO)(NCO)_2]ClO_4 \cdot 2.5(H_2O)$ complex salt

Figure 5 shows the molecular structure of the $[Ni^{II}_2(4)(\mu\text{-}NCO)(NCO)_2]ClO_4 \cdot 2.5H_2O$ complex salt.
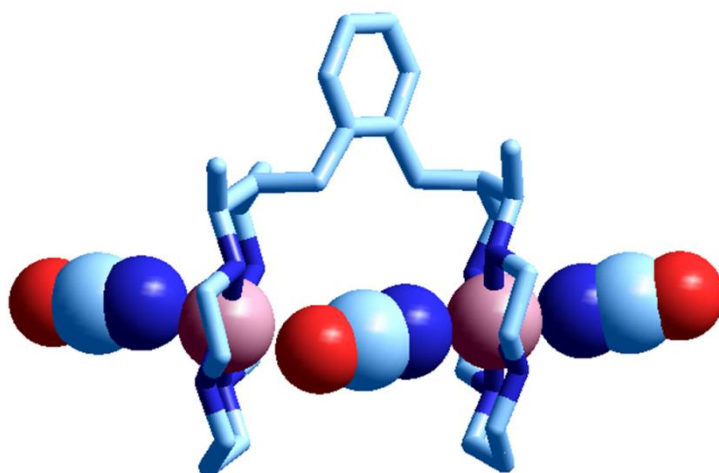
Figure 5. The crystal and molecular structure of the $[Ni^{II}_2(4)(\mu\text{-}NCO)(NCO)_2]ClO_4 \cdot 2.5H_2O$ complex salt. The perchlorate anion as well as the water molecules and hydrogen atoms have been omitted for clarity.

Each nickel(II) ion is coplanarly chelated by the cyclam macrocycle, arranged in a *trans*-III configuration,[8] the most common conformational arrangement found in Ni^{II}-cyclam complexes.[46] The Ni^{II}–N_{amine} distances observed for both metallocyclam subunits (2.07−2.08 Å) are those expected for a high-spin center.[47]
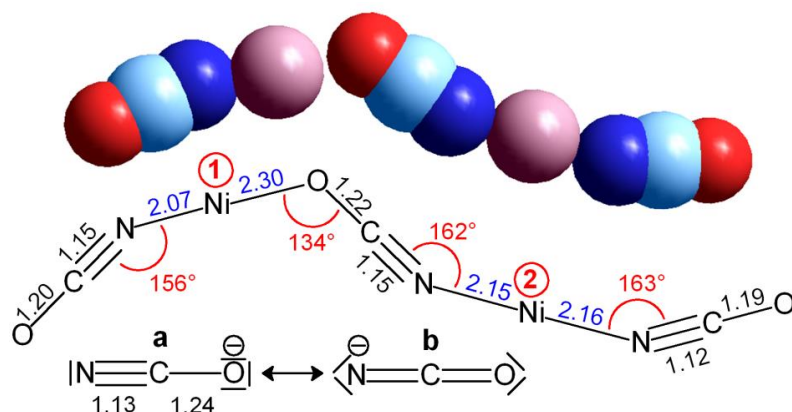
Figure 6. Bond distances (Å) and bond angles in the chain of Ni^{II} and cyanate ions in the $[Ni^{II}_2(\mathbf{4})(\mu\text{-}NCO)(NCO)_2]^+$ complex, whose complete structure is shown in Figure 5. The N−C and C−O distances in the ionic NCO^- is shown at the bottom of the Figure.

Geometrical aspects of the coordination of cyanate to the Ni^{II} ions are illustrated in Figure 6. Both Ni^{II} ions experience a distorted octahedral geometry with, however, quite different features. The metal center labeled with ② in the structural formula in Figure 6 is axially coordinated to the nitrogen atoms of the two cyanate ions with similar Ni^{II}–N distances of 2.15 and 2.16 Å, to give rise to an axially elongated octahedron. On the other hand, the Ni^{II} ion labeled with ① is bound to the nitrogen atom of an NCO^- ion with a relatively short distance (2.07 Å, the same as the Ni^{II}–N_{amine} bond), but is loosely bound to the oxygen atom of NCO^- (Ni^{II}①−O distance 2.30 Å), originating an uniaxially elongated octahedron. Ni^{II} and NCO^- ions are arranged according to a caterpillar-like shape, which results from the different hybridization of the nitrogen and oxygen atoms of the cyanate ion. Bonding in NCO^- can be described by the resonance diagram shown at the bottom of Figure 6. Canonical form **a** is the major contributor because the negative charge is located on the more electronegative atom, which agrees with the experimentally determined bond distances (d(N≡C) appreciably shorter than d(C−O), see Figure 6). Thus, the nitrogen atom should have a prevailing *sp* character and the oxygen atom a dominant *sp³* nature. This may account for the fact that the C−O−Ni^{II}① angle (134°) is distinctly smaller than the C−N−Ni^{II}① angle (156°) and C−N−Ni^{II}② angles (162° and 163°). The Ni^{II}①···Ni^{II}② distance is 6.43 Å, intermediate between those observed for the $[Ni^{II}_2(\mathbf{4}))(\mu\text{-}Br)Br_2]^+$

complex (5.80 Å) and the $[Ni^{II}_2(\mathbf{4})(\mu\text{-}ClO_4)]^{3+}$ complex (7.20 Å). Thus, it appears that there is no steric impediment to a closer approach of the two cyclam subunits, which could favor the formation of a strong Ni^{II}–O bond. This suggests that the long $Ni^{II}①$–O distance has to be ascribed to an intrinsically low affinity of the metal center for the NCO⁻ oxygen atom.

Many examples have been reported of sequences of three or more thiocyanate anions interfaced by two transition metal cations (including Co^{II}, Ni^{II} and Cu^{II}). The described complex is the first example of three NCO⁻ anions interfaced by two Ni metal cations with the sequence: O–C≡N–Ni–O–C≡N–Ni–N≡C–O. A similar caterpillar-like arrangement occurs only for the bis(3-aminopyridine)-di-cyanate-copper(II) complex,[48] where square-planar Cu^{II} centers establish two additional and very weak axial interactions with the oxygens of adjacent CNO⁻ ions (Cu–O = 2.66 Å) originating infinite chains of the type: –Cu–O–C≡N–Cu–N≡C–O–Cu–O–C≡N–Cu–. These chains exhibit C–N–Cu^{II} and C–O–Cu^{II} angles of 161° and 119°, respectively, to be compared with the values observed in the Ni^{II} complex reported here: 163°, 162°, and 156° for C–N–Ni^{II} and 134° for C–O–Ni^{II}.

4.2.3   Anion uptake by the mononuclear $[Ni^{II}(\mathbf{5})]^{2+}$ and dinuclear $[Ni^{II}_2(\mathbf{4})]^{4+}$ complexes in DMSO solution

The affinity toward anions of the envisaged nickel(II) complexes was investigated through spectro-photometric titration experiments in DMSO solution. In a typical experiment, a solution of the metal complex perchlorate salt (either mono- or di-nuclear) was titrated with a solution of the tetrabutyl-ammonium salt of the chosen anion (halide, pseudohalide). Spectrophotometric data were processed by a non-linear least-squares program,[49] in order to single out species present at the equilibrium and to determine their association constants. Figure 7a shows the spectra taken over the course of the titration of a solution 5×10^{-3} M in the mononuclear complex salt $[Ni^{II}(\mathbf{5})](ClO_4)_2$ with a solution of $[Bu_4N]I$.

Figure 7. (a) Spectra taken over the course of the titration of a DMSO solution 5×10^{-3} M in [Ni^{II}(**5**)](ClO$_4$)$_2$ with [Bu$_4$N]I, at 25 °C; (b) symbols: Molar Extinction Coefficients (ε) taken at a selected wavelength; lines: concentration profiles of the complex species at the equilibrium over the course of the titration (L = **5**).

On addition of iodide, the band centered at 455 nm, pertinent to the square-planar low-spin complex, present at the equilibrium at 65%, undergoes a slight increase in intensity and a moderate red-shift. Best fitting of the titration data was obtained by assuming the occurrence of a single equilibrium, eq. (2), to which a binding constant log $K = 1.87 \pm 0.02$ corresponded.

$$[Ni^{II}L]^{2+} + I^- \leftrightarrows [Ni^{II}L(I)]^+ \qquad (2)$$
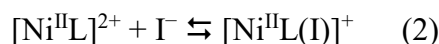
It is suggested that the [Ni^{II}L(I)]$^+$ species exhibits a square-pyramidal geometry: the apically bound iodide does not exert a coordinative interaction strong enough to induce a complete spin-crossover and the mixture of the five-coordinated low-spin and high-spin forms is maintained. This explains the minor modification of the spectral features. The geometrical aspects of eq.(1) are pictorially illustrated in Figure 8b.
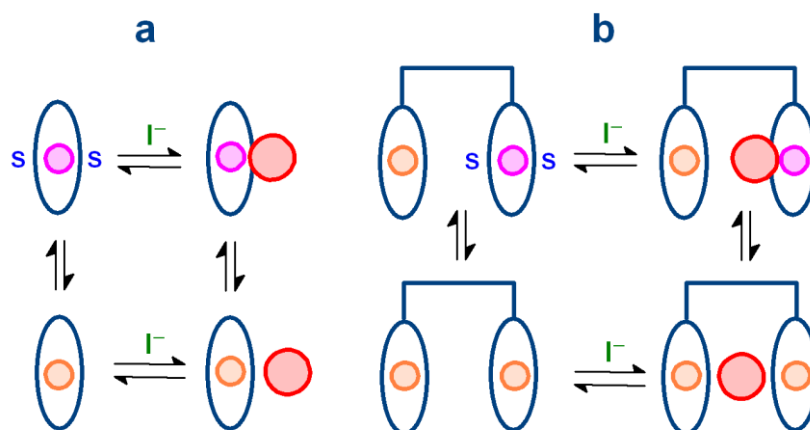
Figure 8. Pictorial description of the interaction of iodide with: (a) [Ni^{II}(**5**)]$^{2+}$ and (b) [Ni^{II}$_2$(**4**)]$^{4+}$.

Notice that the $[Ni^{II}L(I)]^+$ complex is poorly stable and, even on addition of a large excess of I^- (~ 13 equiv.) it forms only at $\sim 75\%$ (see Figure 8a).
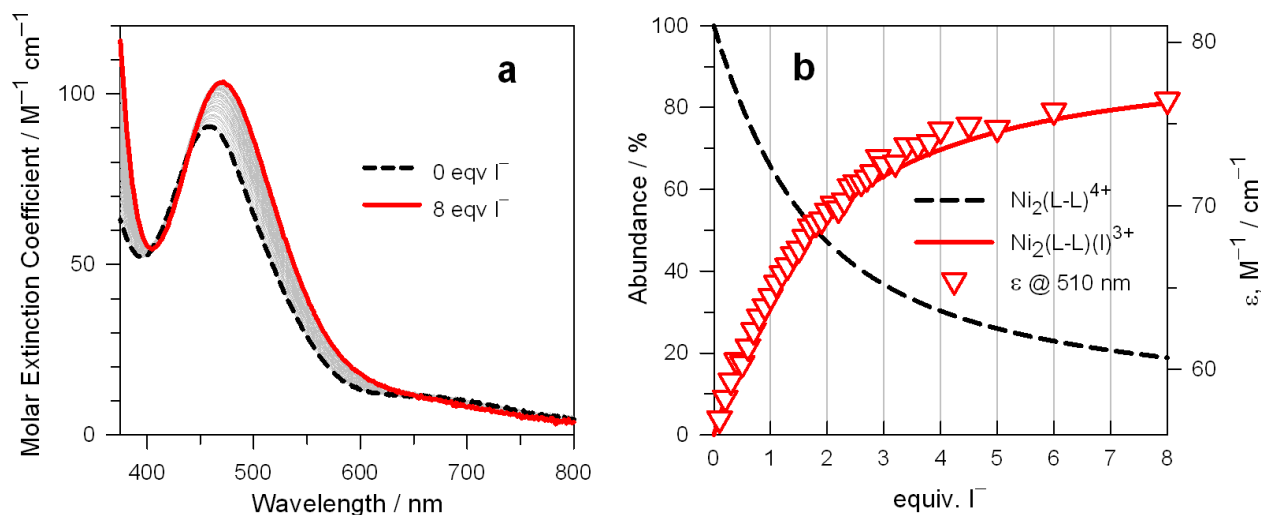
Figure 9. (a) Family of spectra taken over the course of the titration of a DMSO solution 5.10×10^{-4} M in $[Ni^{II}_2(\mathbf{4})](ClO_4)_4$ with $[Bu_4N]I$, at 25 °C; (b) symbols: Molar Extinction Coefficients (ε) taken at selected wavelengths; lines: concentration profiles of the complex species at the equilibrium over the course of the titration (L∩L = **4**).

Figure 9 shows the spectra taken over the course of the titration of a solution 5×10^{-3} M in the dinuclear complex salt $[Ni^{II}_2(\mathbf{4})](ClO_4)_4$ with $[Bu_4N]I$, at 25 °C. The spectral pattern is similar to that observed for the mononuclear analogue, involving a moderate increase and red-shift of the absorption band of the yellow chromophore. Best fitting of titration data was obtained by assuming the occurrence of eq.(3), to which a log $K = 2.22 \pm 0.02$ corresponded (L∩L = **4**).

$$[Ni^{II}_2L∩L]^{2+} + I^- \leftrightarrows [Ni^{II}_2L∩L(I)]^+ \quad (3)$$
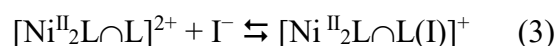
The hypothesized structural features of eq.(3) are illustrated in Figure 8b. It is suggested that the I^- ion is included between the two metallocyclam subunits, according to the arrangement observed in the solid state (Figure 1b). Also in the present case, iodide binding does not substantially modify the the concentration of the high-spin and low-spin forms. In any case, the weak coordinative interaction of I^- with the two Ni^{II} ions may account for the slightly higher value of log K of $[Ni^{II}_2(\mathbf{4})]^{4+}$ with respect to $[Ni^{II}(\mathbf{5})]^{2+}$, which establishes only one interaction (0.3 log units). The behavior of iodide is unique among the investigated halides. Figure 10 shows the spectra taken during the titration with chloride of a solution of the mononuclear complex $[Ni^{II}(\mathbf{5})]^{2+}$.
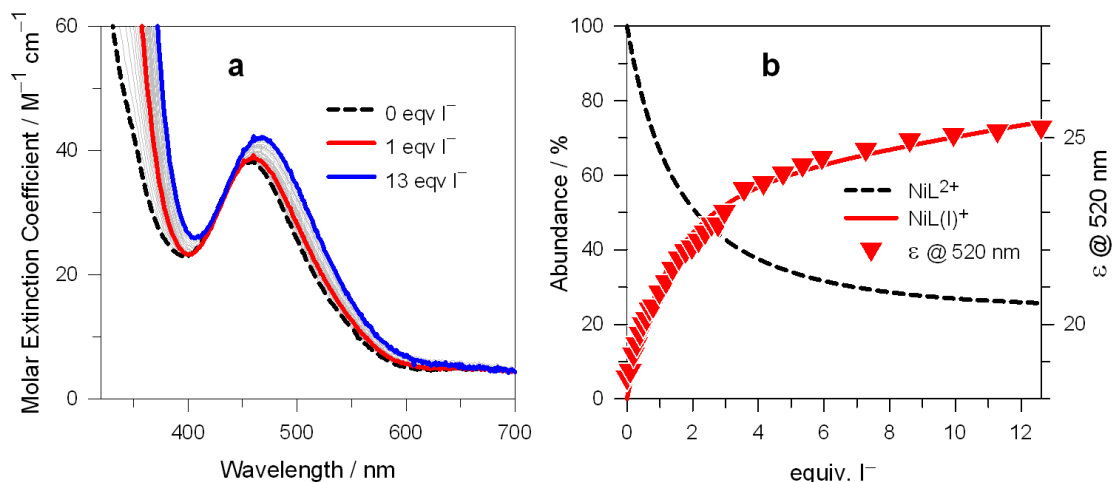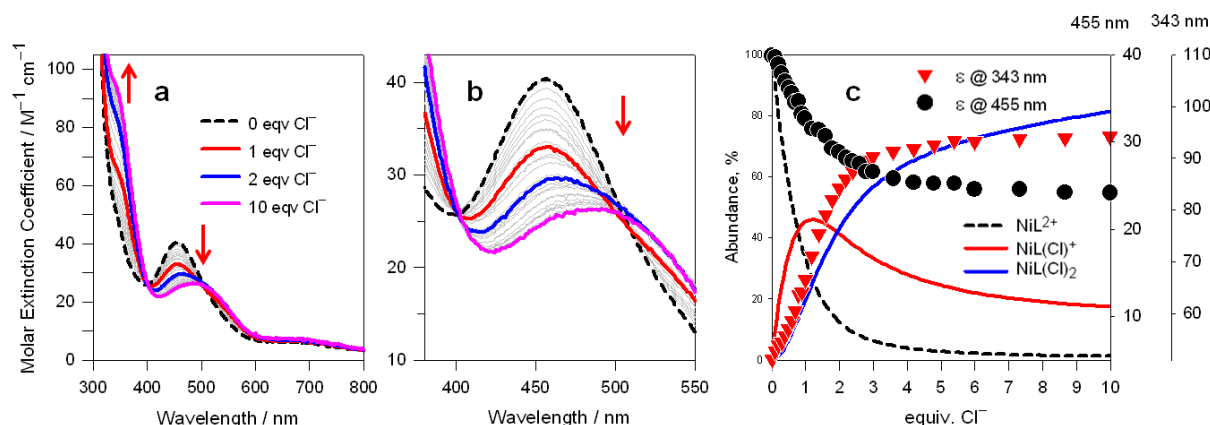
Figure 10. (a) Spectra taken over the course of the titration of a DMSO solution 5.0×10^{-4} M in $[Ni^{II}(\mathbf{5})](ClO_4)_2$ with $[Bu_4N]Cl$, at 25 °C; (b) spectra taken in the visible region (c) symbols: Molar Extinction Coefficients (ε) taken at selected wavelengths; lines: concentration profiles of the complex species at the equilibrium over the course of the titration.

It is observed (Figure 10a) that, on chloride addition, the band at 455 nm, pertinent to the low-spin species, decreases substantially and undergoes a red-shift, whereas the bands at 700 nm and, in particular, at 330 nm, pertinent to the high-spin complex, develop. However, even on addition of a 10-fold excess of anion, the band of the yellow chromophore does not disappear, but reaches a steady value (see filled circles in Figure 10c). This indicates that diamagnetic species are present at the equilibrium in substantial concentration over the entire titration. Best fitting of the titration data was obtained by assuming the occurrence of the two following stepwise equilibria:

$$[Ni^{II}L]^{2+} + Cl^- \rightleftarrows [Ni^{II}L(Cl)]^+ \qquad (4)$$

$$[Ni^{II}L(Cl)]^+ + Cl^- \rightleftarrows [Ni^{II}L(Cl)_2] \qquad (5)$$
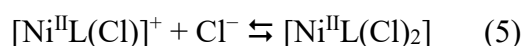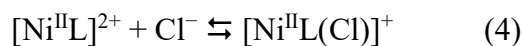
to which the following stepwise constants correspond: $\log K_1 = 2.7 \pm 0.1$ and $\log K_2 = 2.2 \pm 0.3$. Structural changes associated to eq.(4) and eq(5) are tentatively illustrated in Figure 11.
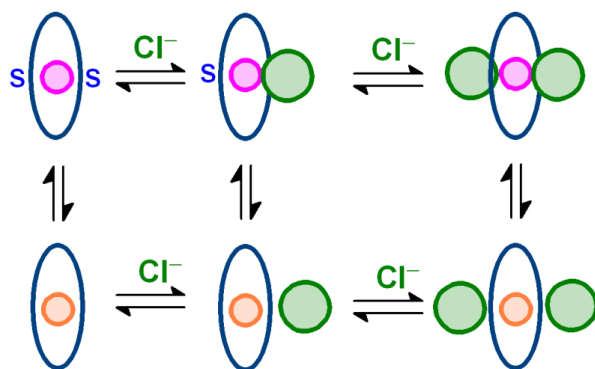
Figure 11. Hypothesized changes in the coordination sphere of the $[Ni^{II}(\mathbf{5})]^{2+}$ complex on titration with Cl^-.

In particular, it is assumed that the high/low-spin equilibrium is maintained during the stepwise addition of chloride ions, but the concentration of the high-spin form progressively prevails. For $[Ni^{II}L(Cl)_2]$ two octahedrically elongated complexes co-exist, whose spin state, whether high or low, is determined by the $Ni^{II}\cdots Cl$ distance, shorter for high-spin, longer for low-spin. Such a situation has been postulated to occur for complexes of the type $[Ni^{II}(macrocycle)(H_2O)_2]^{2+}$ in aqueous solution,[50] but it has been not observed yet in the presence of coordinating anions in non-aqueous solutions.

Figure 12 shows the spectra taken over the course of the titration of a solution 5×10^{-3} M in the dinuclear complex salt $[Ni^{II}_2(\mathbf{4})](ClO_4)_4$ with $[Bu_4N]Cl$, at 25 °C. The spectral pattern is analogous to that observed for the mononuclear counterpart, involving decrease, but not disappearance of the yellow chromophore. Moreover, a band at 350 nm, characteristic of the blue-violet chromophore distinctly develops on chloride addition.

Figure 12. (a) Spectra taken over the course of the titration of a DMSO solution VALUE $\times 10^{-4}$ M in $[Ni^{II}_2(\mathbf{4})](ClO_4)_4$ with $[Bu_4N]Cl$, at 25 °C; (b) symbols: Molar Extinction Coefficients (ε) taken at selected wavelengths; lines: concentration profiles of the complex species at the equilibrium over the course of the titration.

Best fitting of the titration data was obtained by assuming the occurrence of three stepwise equilibria, to which the following constants corresponded: $\log K_1 = 4.20 \pm 0.01$, $\log K_2 = 2.48 \pm 0.02$, $\log K_3 = 1.46 \pm 0.04$.

$$[Ni^{II}_2(L \cap L)]^{4+} + Cl^- \leftrightarrows [Ni^{II}_2(L \cap L)Cl]^{3+} \qquad (6)$$

$$[Ni^{II}_2(L \cap L)Cl]^{3+} + Cl^- \leftrightarrows [Ni^{II}_2(L \cap L)Cl_2]^{2+} \qquad (7)$$

$$[Ni^{II}_2(L \cap L)Cl_2]^{3+} + Cl^- \leftrightarrows [Ni^{II}_2(L \cap L)Cl_3]^+ \qquad (8)$$

There is no way, from spectrophotometric data, to assess where the first Cl- ion goes (eq. (6)), whether in the intermetallic cavity or in one of the two external positions. The crystal structure of the

dinuclear complex salt $[Ni^{II}_2(\mathbf{5})(\mu\text{-}Cl)(ClO_4)](ClO_4)_2 \cdot H_2O$, shown in Figure 13, suggests that the first Cl^- prefers to occupy the inter-metallocyclam space. In solution, the external perchlorate ion of the crystalline complex, would be probably replaced by a DMSO molecule.
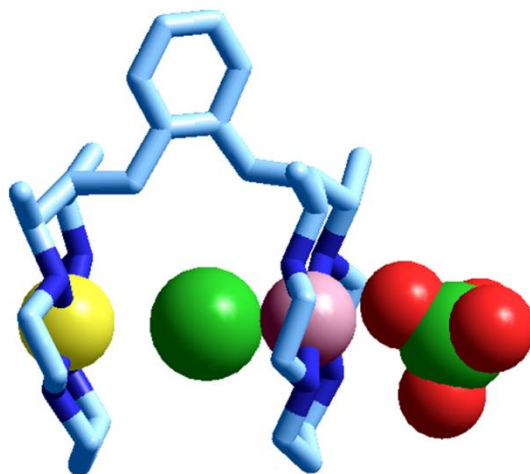
Figure 13. The crystal and molecular structure of the complex salt $[Ni^{II}_2(\mathbf{5})(\mu\text{-}Cl)(ClO_4)](ClO_4)_2 \cdot H_2O$. Hydrogen atoms of the ligand, the two uncoordinated ClO_4^- ions and the solvational water molecule have been omitted for clarity.

Moreover, persistence of the absorption band of the yellow chromophore even in the presence of excess chloride suggests that in each step of the anion complexation a mixture of high- and low-spin forms exists. On these bases, coordinative and geometrical aspects of the three stepwise equilibria are pictorially illustrated in Figure 14.
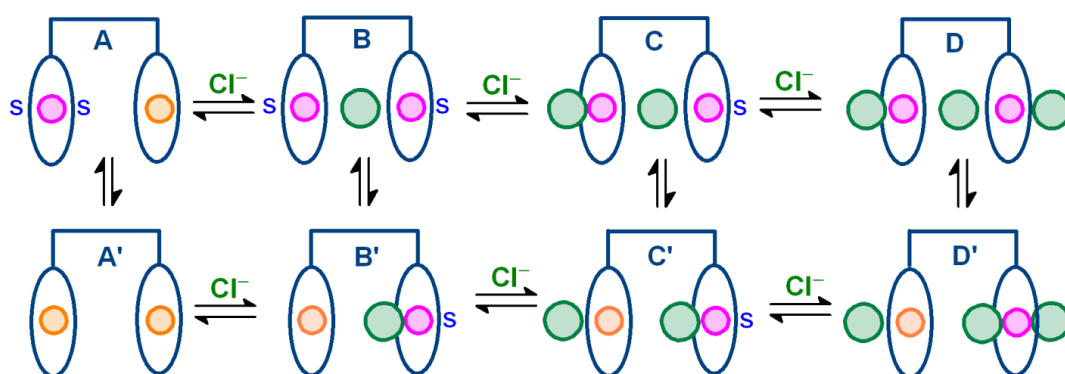
Figure 14. Hypothesized structural changes in the $[Ni_2^{II}(\mathbf{4})]^{4+}$ complex during titration with Cl^-.

In particular, the μ-Cl complex should exist as an equilibrium mixture of a fully paramagnetic species (B) and a mixed-valence form (B'). In the following steps, the concentration of the paramagnetic forms increase, to reach a steady value. Whether in the fully paramagnetic species B,

C and D the intermetallic chloride ion lies at the same distance from the two metal centers or is closer to one of them is only matter of speculation, in the absence of specific structural data.

It has to be noticed that K_1 for the dinuclear complex $[Ni_2^{II}(4)]^{4+}$ is 32-fold higher than that observed for the mononuclear complex $[Ni^{II}(5)]^{2+}$ ($\Delta \log K_1 = 1.5$), pointing out to the existence of a *bimacrocyclic effect*. The corresponding energy advantage (8.6 kJ mol^{-1}) roughly reflects the additional contribution of the interaction of Cl$^-$ included in the inter-ring cavity with the facing low-spin Ni^{II} ion.
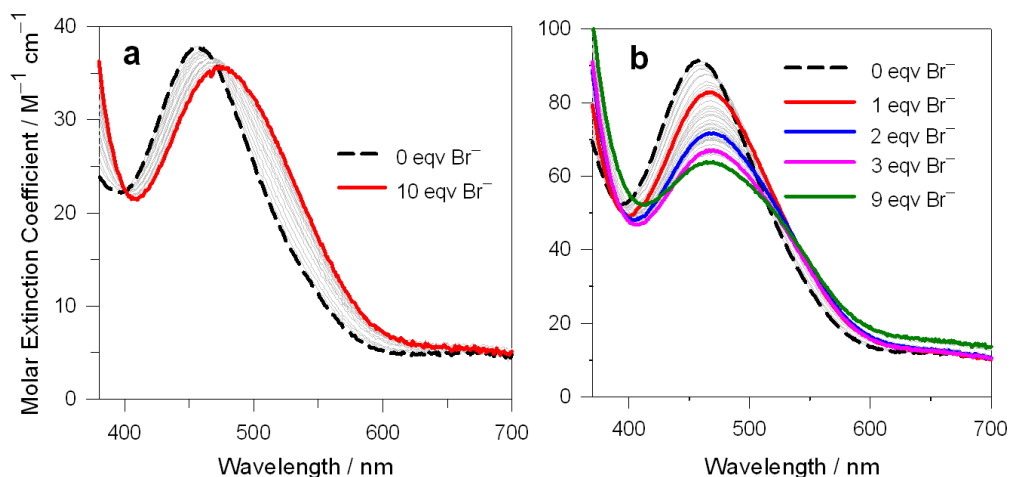
Figure 15. Spectra taken over the course of the titration with [Bu$_4$N]Br of a DMSO solution (a) of [Ni^{II}(**5**)](ClO$_4$)$_2$, and (b) of [Ni^{II}$_2$(**4**)](ClO$_4$)$_4$, at 25 °C.

The mode of interaction of bromide with mono- and di-nuclear receptors is peculiar, as shown by the spectra shown in Figure 15. The monometallic complex $[Ni^{II}(5)]^{2+}$ interacts with Br$^-$ in the same way as with iodide: (i) red-shift of the band of the yellow chromophore (see Figure 15a), which maintains its intensity; (ii) formation of a single receptor-anion complex, of 1:1 stoichiometry, whose association constant is reported in Table 1. The five-coordinate, probably square-pyramidal, complex, exists as an equilibrium mixture of the high- and low-spin form. On the other hand, the behavior of the dimetallic complex $[Ni_2^{II}(4)]^{4+}$ is similar to that observed with chloride: (i) the absorption band centered at 455 nm undergoes a red-shift and a pronounced decrease in intensity (see Figure 15b); (ii) the best fitting of the titration data was obtained by assuming the stepwise formation of three complexes: $[Ni_2L \cap LX]^{3+}$, $[Ni_2L \cap LX_2]^{2+}$ and $[Ni_2L \cap LX_3]^+$. The corresponding equilibrium constants are reported in Table 1.

Table 1. Log K values associated to the stepwise association equilibria of complexes $[Ni^{II}(\mathbf{5})]^{2+}$ and $[Ni_2^{II}(\mathbf{4})]^{4+}$ with halides and pseudohalides, in DMSO at 25° C. In parentheses the standard deviation on the last figure.

L = **5**	Cl^-	Br^-	I^-	NCO^-	NCS^-	N_3^-
$[NiL]^{2+} + X^- \leftrightarrows [NiLX]^+$	2.7(1)	2.34(2)	1.87(2)	4.51(1)	3.5(1)	2.54(6)
$[NiLX]^+ + X^- \leftrightarrows [NiLX_2]$	2.2(4)			4.2(3)	1.1(3)	2.6(1)
L∩L = **4**	$Cl-$	$Br-$	$I-$	$NCO-$	$NCS-$	$N3-$
$[Ni_2L{\cap}L]4+ + X- \leftrightarrows [Ni_2L{\cap}LX]3+$	4.20(7)	3.05(4)	2.22(1)	4.51(2)	3.9(1)	2.7(1)
$[Ni_2L{\cap}LX]3+ + X- \leftrightarrows [Ni_2L{\cap}LX_2]2+$	2.5(1)	2.70(6)		4.07(5)	3.2(2)	2.1(3)
$[Ni_2L{\cap}LX_2]2+ + X- \leftrightarrows [Ni_2L{\cap}LX_3]+$	1.5(2)	2.56(9)		3.31(8)	2.1(3)	1.2(3)

It is therefore suggested that the stepwise interaction of $[Ni_2^{II}(\mathbf{4})]^{4+}$ with bromide proceeds according to the scheme illustrated in Figure 14. A moderate bimacrocyclic effect exists ($\Delta\log K_1 = 0.7$), to which an energy contribution of 4 kJ mol^{-1} corresponds.

Pseudohalides display a different behavior from halides when interacting with both mononuclear $[Ni^{II}(\mathbf{5})]^{2+}$ and dinuclear $[Ni_2^{II}(\mathbf{4})]^{4+}$ complexes. Figure 16a shows the spectra taken over the course of the titration of a DMSO solution of $[Ni^{II}(\mathbf{5})](ClO_4)_2$ with $[Bu_4N]NCO$.
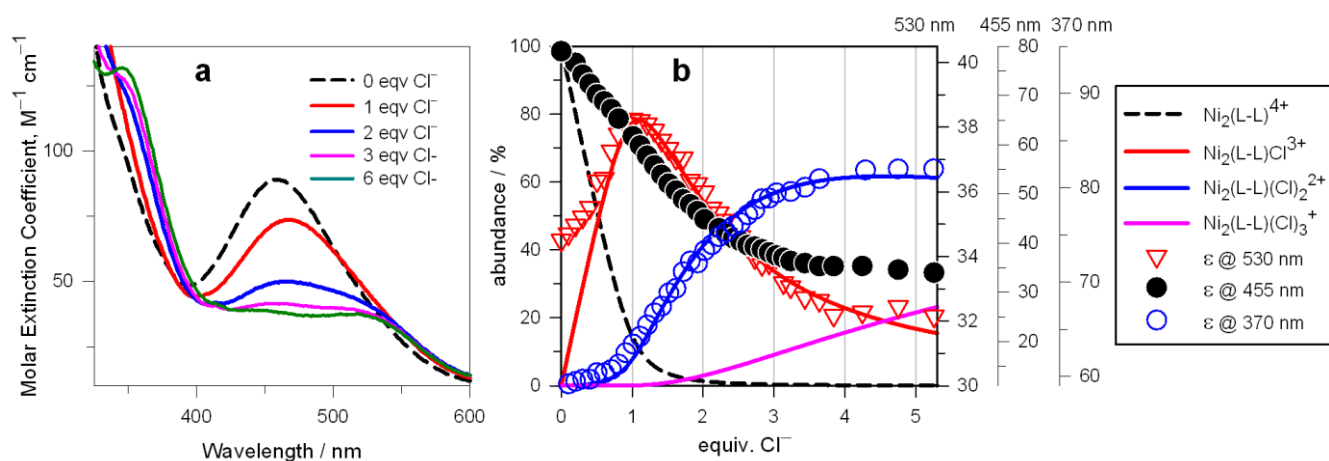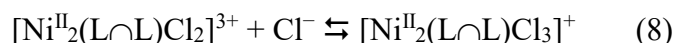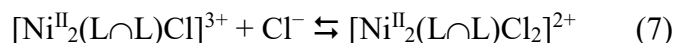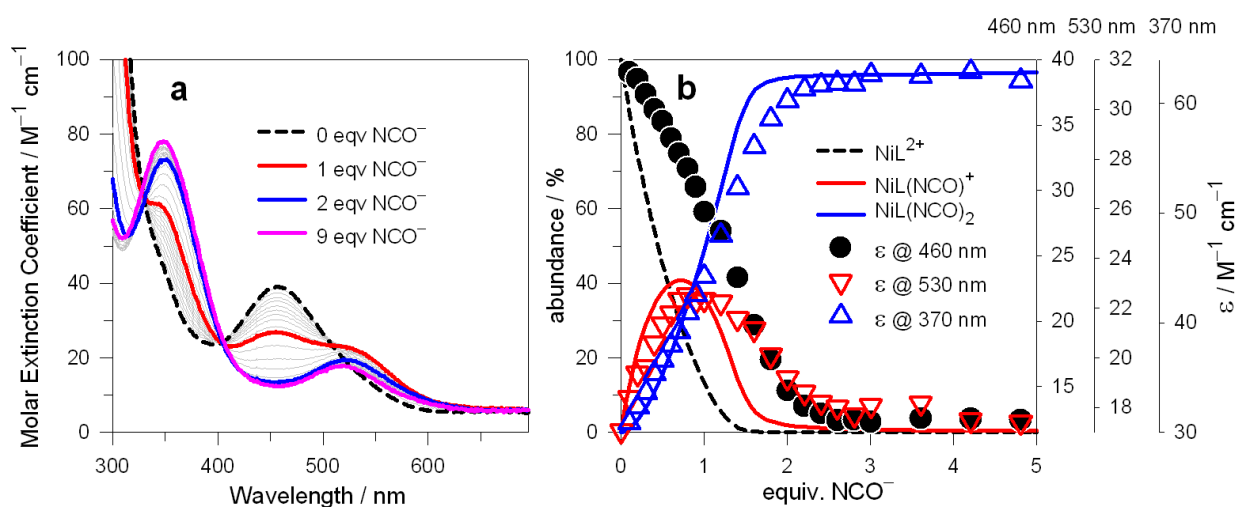

Figure 16. (a) Spectra taken over the course of the titration of a DMSO solution 5×10^{-3} M in $[Ni^{II}(\mathbf{5})](ClO_4)_2$ with $[Bu_4N]NCO$, at 25 °C; (b) symbols: Molar Extinction Coefficients (ε) taken at selected wavelengths; lines: concentration profiles of the complex species at the equilibrium over the course of the titration.

On cyanate addition, the band at 455 nm of the low-spin complex decreases, while new bands, pertinent to the high-spin form, develop at 370 nm and 530 nm, a behavior observed also on titration with chloride. However, on addition of 2 and more equiv. of NCO⁻, the absorption of the yellow chromophore completely disappears. On these bases, $[Ni^{II}(\mathbf{5})]^{2+}$/NCO⁻ interaction can be described by the scheme in Figure 17.
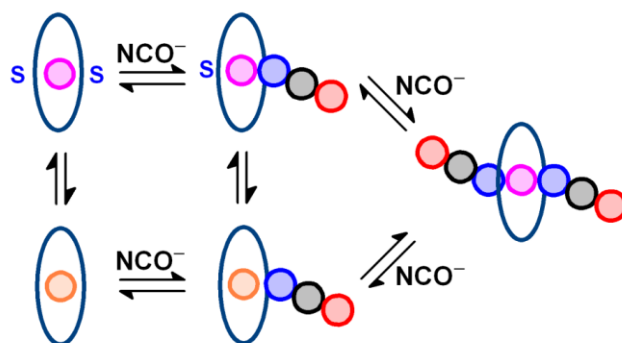
Figure 17. Hypothesized structural changes in the $[Ni^{II}(\mathbf{5})]^{2+}$ complex on titration with NCO^-.

In particular, on addition of the first equivalent of cyanate both a high-spin octahedral species and a low-spin five- or six-coordinate species forms, with the spin equilibrium displaced towards the high-spin complex. On addition of the second equiv. of NCO^-, the high-spin octahedral complex $[Ni^{II}(\mathbf{5})(NCO)_2]$ forms, which is present at 100%.

Figure 18a reports the spectra obtained on titration with NCO^- of a solution of the dinuclear complex $[Ni^{II}_2(\mathbf{4})](ClO_4)_4$.
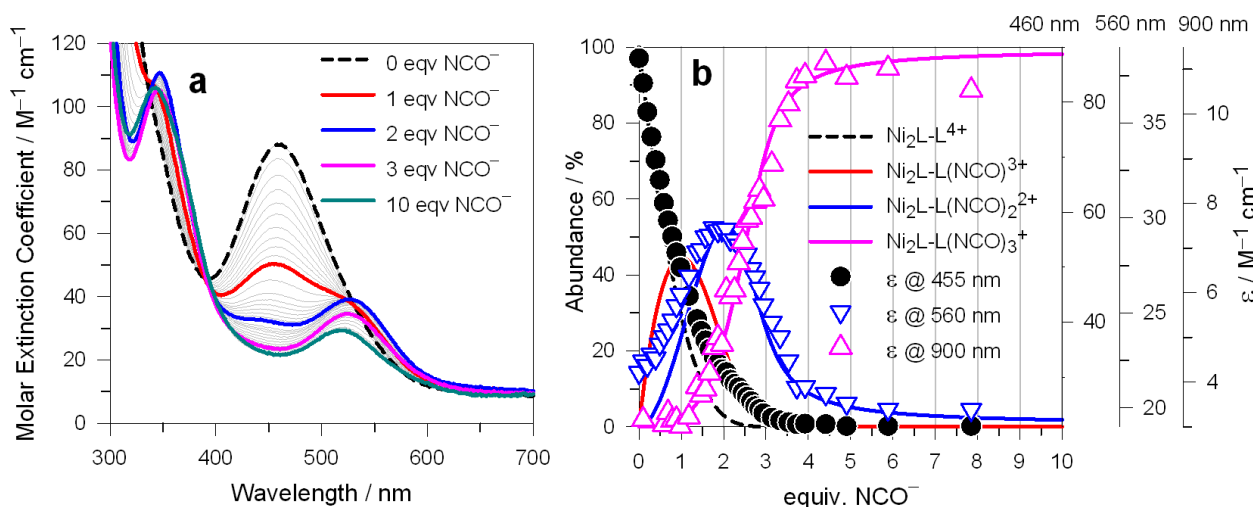
Figure 18. (a) Spectra taken over the course of the titration of a DMSO solution 5×10^{-3} M in $[Ni^{II}_2(\mathbf{4})](ClO_4)_4$ with $[Bu_4N]NCO$, at 25 °C; (b) symbols: Molar Extinction Coefficients (ε) taken at selected wavelengths; lines: concentration profiles of the complex species at the equilibrium over the course of the titration.

The spectral pattern is similar to that observed for the mononuclear complex, with a drastic decrease of the band of the yellow chromophore and the definite development of the bands of the blue-violet chromophore at 350 and 530 nm. In particular, on addition of 2 equiv. of NCO^- or more the band at 455 nm (filled circles in Figure 18b) disappears and only high-spin species are present in solution. Best fitting of the titration data was obtained on assuming the presence at the equilibrium of three

species: $[Ni^{II}_2(L \cap L)NCO]^{3+}$, $[Ni^{II}_2(L \cap L)(NCO)_2]^{2+}$ and $[Ni^{II}_2(L \cap L)(NCO)_3]^{+}$. The corresponding log K values are reported in Table 1.

Also in this case, absorption spectra alone do not give definite information on the coordination site of the first anion, whether inner or outer with respect to the inter-ring cavity of the dinuclear complex. On the other hand, the only crystal structure available for complexes of **4**, $[Ni^{II}_2(\mathbf{4})(\mu\text{-}NCO)(NCO)_2]^{+}$ (this work) refers to 1:3 receptor/anion complex (see Figures 5 and 6). The absence of a bimacrocyclic effect (log K_1 values are the same for both mono- and di-nuclear complexes) would suggest external coordination of the first cyanate ion. More convincing information will be provided by voltammetric studies, described in the next Section.

Titrations with thiocyanate and azide of both $[Ni^{II}(\mathbf{5})](ClO_4)_2$ and $[Ni^{II}_2(\mathbf{4})](ClO_4)_4$ showed the same spectral features observed with cyanate (see pertinent spectra in Supplementary Information: Figures S3-S4). Corresponding log K values are reported in Table 1.

4.2.4 The Ni^{II}/Ni^{III} redox change in the absence and in the presence of coordinating and poorly reducing anions: electrochemical anion sensing.

Encircling by cyclam of transition metal favors the attainment of unusually high oxidation states (Ni^{III},[51,52] Cu^{III},[53,54] Ag^{II},[55] Ag^{III},[56] and also Hg^{III}, as a red transient). Such a feature results from the capability of the 14-membered tetra-aza macrocycle to exert strong in-plane interactions, which raise the energy of the metal centered, essentially antibonding orbital, from which the electron is removed on oxidation. In particular, the Ni^{II}-to-Ni^{III} oxidation process can be carried out both chemically and electrochemically, in an acidic aqueous solution or in media resistant to oxidation (MeCN, DMSO). The $[Ni^{III}(cyclam)]^{3+}$ complex which forms typically shows an elongated octahedral coordination geometry, with two solvent molecules or two anions occupying the axial positions of the distorted octahedron. The formation of an authentic Ni^{III} complex (d^7, low-spin) has been confirmed in solution by ESR investigations.[57] The crystal structure of the complex salt $[Ni^{III}(cyclam)(MeCN)_2](CF_3SO_3)_3$ has been reported.[58]

The black line in Figure 20 shows the differential pulse voltammetry (DPV) profile obtained at a platinum microsphere working electrode for a DMSO solution 10^{-3} M in $[Ni^{II}(\mathbf{5})](ClO_4)_2$ and 0.1 M in $[Bu_4N]PF_6$ (black line).
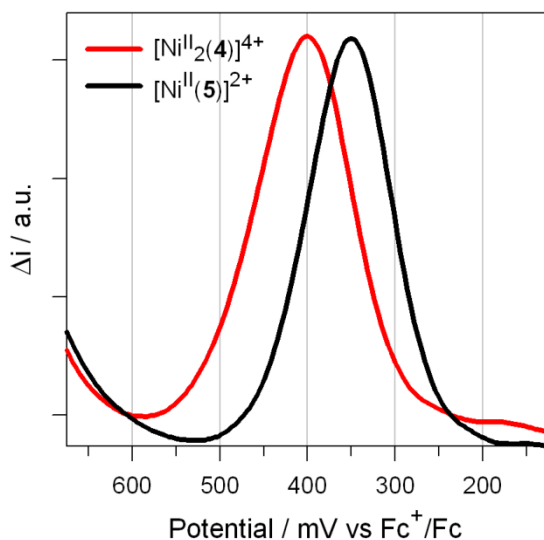
Figure 20. DPV profiles obtained at a platinum microsphere working electrode for a DMSO solution 0.1 M in [Bu$_4$N]PF$_6$ (pulse amplitude 20 mV). Black line: solution 10^{-3} M in [Ni^{II}(**5**)](ClO$_4$)$_2$; red line: solution 10^{-3} M in [Ni^{II}$_2$(**4**)](ClO$_4$)$_4$. Potential scan from less positive to more positive potentials (←). The intensities of the two profiles have been arbitrarily adjusted.

The oxidation peak ($E_{1/2}$ = 400 mV vs the internal Fc$^+$/Fc reference couple) shows a width at half maximum (δ) of 104 mV. The value expected for a fully electrochemically reversible one-electron redox change at 25 °C is 91 mV.[59] On the other hand, the red line in Figure 20 refers to the oxidation behavior of the dinuclear complex salt [Ni^{II}$_2$(**4**)](ClO$_4$)$_4$. The observed single peak must be considered the convolution of two distinct peaks corresponding to the two stepwise one-electron oxidation processes:

$$[Ni^{II}-Ni^{II}(L \cap L)]^{4+} \leftrightarrows [Ni^{II}-Ni^{III}(L \cap L)]^{5+} + e^- \qquad (9)$$

$$[Ni^{II}-Ni^{III}(L \cap L)]^{4+} \leftrightarrows [Ni^{III}-Ni^{III}(L \cap L)]^{5+} + e^- \qquad (10)$$
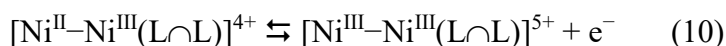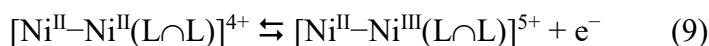
In the case of two non-interfering and independent one-electron processes a single peak with δ = 91 mV should be observed (for fully reversible electrochemical processes).[29] This corresponds to a $\Delta E_{1/2}$ = $E_{1/2}(2)$ – $E_{1/2}(1)$ difference of 36 mV (resulting from a purely statistical effect). Two peaks can be experimentally discerned in the DPV profile when $\Delta E_{1/2} \geq 80$ mV. In the present case, a δ value of 126 mV is observed, which, assuming full electrochemical reversibility, would give $\Delta E_{1/2}$ = 60 mV and, admitting a reversibility comparable to that of the mononuclear complex, $\Delta E_{1/2} \sim 50$ mV. Such a value should reflect a moderate electrostatic repulsion between the two positively charged metal centers. The existence of a minor repulsive effect is also demonstrated by the fact that the peak potential observed for the [Ni^{II}(**5**)]$^{2+}$ complex (350 mV vs Fc$^+$/Fc) is distinctly less positive than the peak potential for the [Ni^{II}$_2$(**4**)]$^{4+}$ complex (400 mV). In particular, the charge increase of each of the

43

two Ni^{II} ions of the dinuclear complex is made slightly more difficult by the presence of a proximate positive charge.

Further, voltammetric studies have been carried out on DMSO solutions of $[Ni^{II}(5)](ClO_4)_2$ and of $[Ni^{II}_2(4)](ClO_4)_4$ (0.1 M in $[Bu_4N]PF_6$, 25 °C), in the presence of poorly reducing anions (Cl^-, NCO^-, N_3^-). Figure 21a shows the DPV profiles obtained over the course of the titration of a 10^{-3} M solution of the mononuclear complex salt $[Ni^{II}(5)](ClO_4)_2$ with $[Bu_4N]Cl$.
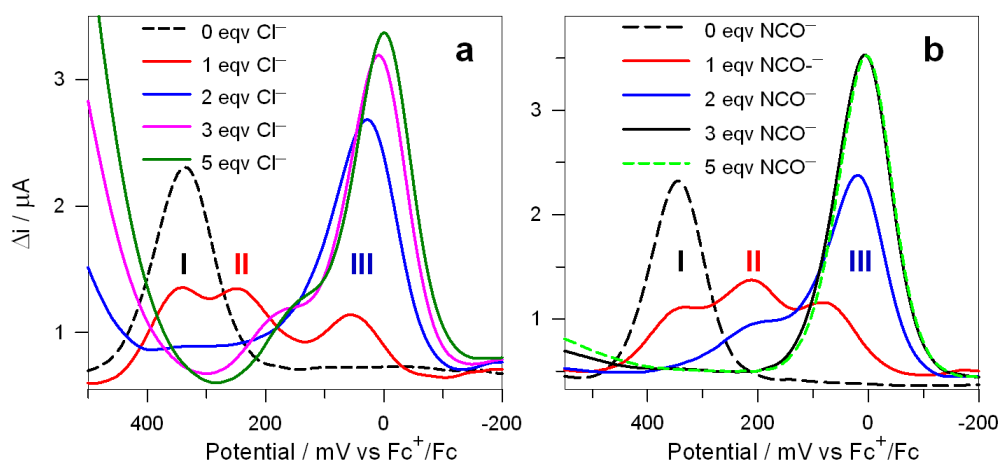
Figure 21. DPV profiles obtained at a platinum microsphere working electrode for a DMSO solution 10^{-3} M in $[Ni^{II}(5)](ClO_4)_2$ and 0.1 M in $[Bu_4N]PF_6$ (pulse amplitude 10 mV), to which up to 5 equiv. of $[Bu_4N]Cl$ (**a**) and $[Bu_4N]NCO$ (**b**) were added; potential scan from less positive to more positive potentials ($\leftarrow$).

The development of the DPV profiles during titration can be interpreted on assuming the occurrence of the three stepwise half-reactions ($X^- = Cl^-$):

$$[Ni^{II}(L)]^{2+} \leftrightarrows [Ni^{III}(L)]^{3+} + e^- \qquad (11)$$

$$[Ni^{II}(L)X]^+ \leftrightarrows [Ni^{III}(L)X]^{2+} + e^- \qquad (12)$$

$$[Ni^{II}(L)X_2] \leftrightarrows [Ni^{III}(L)X_2]^+ + e^- \qquad (13)$$
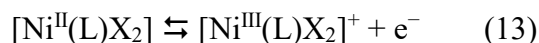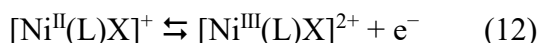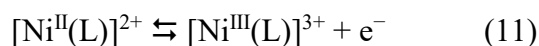
It is observed that on addition of 1 equiv. of Cl^- (red line) a three-peak profile develops, due to the sequential occurrence of all three processes: (11) to which peak **I** corresponds, (12) ($\rightarrow$ **II**), and (13) ($\rightarrow$ **III**). On addition of further aliquots of chloride, peaks **I** and **II** progressively disappear, while peak **III** strengthens, according to a pattern roughly reproducing the change of concentration of the Ni^{II} complexes undergoing oxidation. The high intensity peak developing at more anodic potentials on addition of excess of anion refers to the oxidation of free Cl^-.

Figure 21b displays the DPV profiles obtained on titration of $[Ni^{II}(5)](ClO_4)_2$ with $[Bu_4N]NCO$. The pattern is similar to that observed with chloride and, also in this case, the three oxidation peaks

can be associated to eq. (11-13). Totally similar behavior was observed on titration of a solution of $[Ni^{II}(\mathbf{5})](ClO_4)_2$ with $[Bu_4N]N_3$.

Figure 22a shows the DPV profiles obtained over the course of the titration of a 10^{-3} M solution of the dinuclear complex salt $[Ni^{II}_2(\mathbf{4})](ClO_4)_4$ with $[Bu_4N]Cl$.

Figure 22. DPV profiles obtained at a platinum microsphere working electrode for a DMSO solution 10^{-3} M in $[Ni^{II}_2(\mathbf{4})](ClO_4)_4$ and 0.1 M in $[Bu_4N]BF_4$ (pulse amplitude 10 mV), to which up to 5 equiv. of $[Bu_4N]Cl$ (**a**) and $[Bu_4N]NCO$ (**b**) were added; potential scan from less positive to more positive potentials.

The DPV pattern consists of three peaks, a circumstance which seems inconsistent with the occurrence of the expected four half-reactions reported below ($X^- = Cl^-$):

$$[Ni^{II}_2(L\cap L)]^{4+} \leftrightarrows [Ni^{III}_2(L\cap L)]^{6+} + 2e^- \qquad (14)$$

$$[Ni^{II}_2(L\cap L)X]^{3+} \leftrightarrows [Ni^{III}_2(L\cap L)X]^{5+} + 2e^- \qquad (15)$$

$$[Ni^{II}_2(L\cap L)(X)_2]^{2+} \leftrightarrows [Ni^{III}_2(L\cap L)(X)_2]^{4+} + 2e^- \qquad (16)$$

$$[Ni^{II}_2(L\cap L)(X)_3]^{+} \leftrightarrows [Ni^{III}_2(L\cap L)(X)_3]^{3+} + 2e^- \qquad (17)$$

The apparent paradox can be cleared on assuming that: (i) peak **I** corresponds to eq. (14), in which the two Ni^{II} centers (belonging to the forms **A** and **A'**, see Figure 13) are oxidized at nearly the same potential; (ii) peak **II** corresponds to eq. (15), in which the $[Ni^{II}_2(L\cap L)\mu\text{-}Cl]^{3+}$ complex (**B** and **B'** in Figure 13) undergoes a two-electron oxidation; (iii) peak **III** is the convolution of the two peaks corresponding to the half-reactions (16) and (17): the two equilibria refer to the concurring oxidation of complexes with a rather similar coordinative array (**C** and **C'**, then **D** and **D'** in Figure 13) and should be characterized by not too different $E_{1/2}$ values.

Figure 22b shows the family of DPV profiles obtained on voltammetric titration of the dinuclear complex with cyanate ion, which show a three-peak behavior as observed for titration with chloride. However, the pattern for NCO^- is not exactly the same as for Cl^-. In particular, for Cl^- peak **III** develops significantly since the addition of the second equiv. of anion (blue line in Figure 22a). On the other hand, in the case of cyanate, peak **III** grows significantly only on addition of the fourth equiv. of anion and fully develops with the fifth equiv. (brown line in Figure 22b). Such a different behavior can be interpreted on assuming that: (i) first, the oxidation of the complexes $[Ni^{II}_2(L \cap L)NCO]^{3+}$ (**B** in Figure 23) and $[Ni^{II}_2(L \cap L)(NCO)_2]^{2+}$ (**C** in Figure 23), in which cyanate ions are externally coordinated to the two Ni^{II} centers, takes place; therefore, peak **II** should be considered the convolution of two peaks with very similar $E_{1/2}$ values; (ii) then, it is the turn for the oxidation of the $[Ni^{II}_2(L \cap L)(\mu\text{-}NCO)(NCO)_2]^+$ complex (**D** in Figure 23), in which the third NCO^- ion occupies the intermetallic cavity, a process producing peak **III**. Thus, voltammetric titration enables us to propose a sound mechanistic sequence for the stepwise uptake of three cyanate ions by the dinuclear receptor $[Ni^{II}_2(\mathbf{4})]^{4+}$ in DMSO, which is pictorially illustrated in Figure 23.
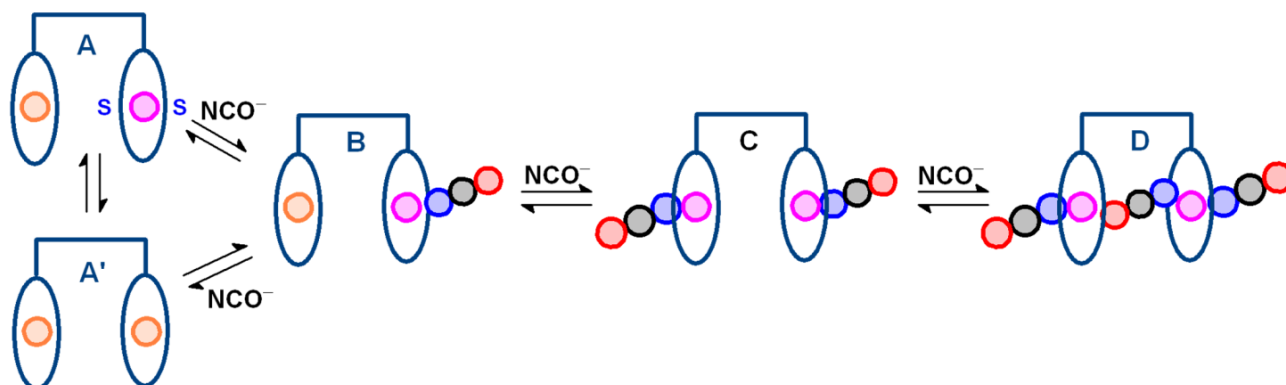
Figure 23. Hypothesized structural changes in the $[Ni^{II}_2(\mathbf{4})]^{4+}$ complex during titration with NCO^-.

The failure of the first cyanate ion to occupy the intermetallic cavity should be ascribed to two main factors: (i) the intrinsic difficulty of the triatomic anion to fit the inter-ring cavity and to fulfil the geometrical requirements associated to the hybridization of terminal donor atoms; (ii) the less pronounced coordinating tendency of the terminal oxygen atom of NCO^- with respect to terminal nitrogen atom. Such a feature is confirmed by the large $Ni^{II}-O$ distance (2.30 Å) compared to $Ni^{II}-N$ (2.15 Å). As a consequence, the first and second NCO^- choose to bind the Ni^{II} ions externally, thus profiting by the coordination of nitrogen atoms according to a geometrical arrangement free of steric constraints.

The model illustrated in Figure 23 can be proposed also for the interaction of $[Ni^{II}_2(4)]^{4+}$ with N_3^-, for which a pattern of voltammetric profiles similar to that of NCO^- was observed (see Figure S8 in Supplementary Information). Moreover, the scheme in Figure 23 should be valid also for the interaction of $[Ni^{II}_2(4)]^{4+}$ with NCS^-, which was spectrophotometrically, but not voltammetrically investigated, due to the poor resistance of thiocyanate to oxidation at platinum electrode.

Further information on the oxidation mechanism can be obtained by considering that the separation of each couple of DPV peaks ΔE is expressed by the following equation:

$$\Delta E \text{ (mV)} = \frac{59.16}{n} \times \log \frac{K_i(Ni^{III})}{K_i(Ni^{II})} \qquad (18)$$

where $K_i(Ni^{II})$ is the equilibrium constant for the ith step of complexation for the Ni^{II} complex: $[Ni^{II}LX_i]^{(2-i)+} + X^- \leftrightarrows [Ni^{II}LX_{1+i}]^{(1-i)+}$, and $K_i(Ni^{III})$ is the equilibrium constant for the ith step of complexation for the Ni^{III} complex: $[Ni^{III}LX_i]^{(3-i)+} + X^- \leftrightarrows [Ni^{III}LX_{1+i}]^{(2-i)+}$ (i = 1, 2). N is the number of electrons involved in the redox process. The ratio $K_i(Ni^{III})/K_i(Ni^{II})$ is called Enhancement Factor (EF) and defines the effect of complexation (e.g. by Cl^-) on the stabilization of the Ni^{III} state.[60] The larger the peak separation, the higher the stability of the complex of the oxidised receptor with respect to the reduced one. Values of ΔE for the complexation of the mono- and di-nuclear complexes by Cl^- and NCO^- can be visually evaluated in the diagram in Figure 24.
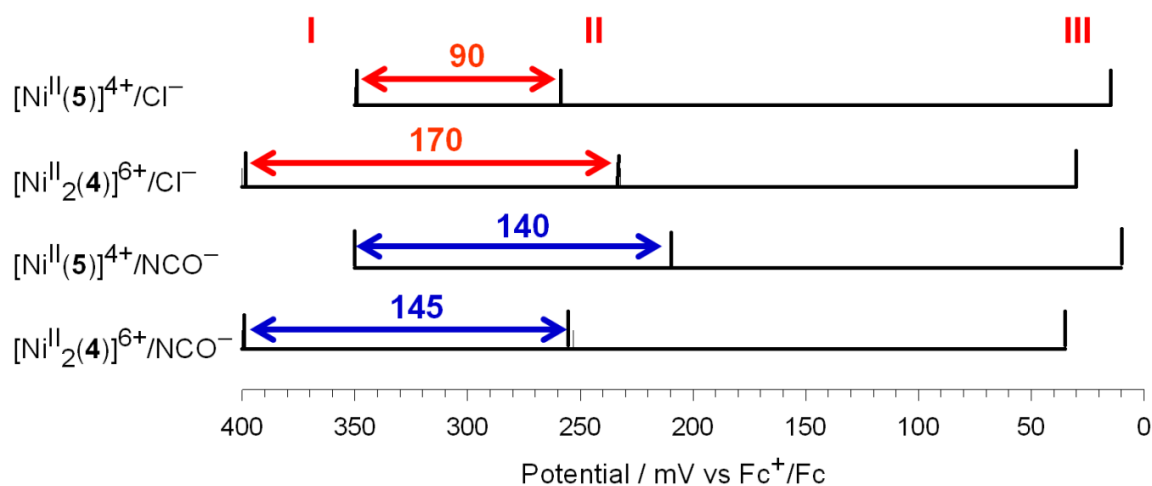
Figure 24. Linear representation of peak potentials determined over the course of the DPV titrations of $[Ni^{II}(5)]^{2+}$ and $[Ni_2^{II}(4)]^{4+}$ with Cl^- and NCO^-. The larger the peak separation, the higher the stability of the complex of the oxidised receptor (Ni^{III}) with respect to the reduced one (Ni^{II}).

As far ΔE(I-II) differences are concerned, the following features are observed:

1. for NCO$^-$, ΔE(I-II) values are nearly the same for both the the mononuclear and dinuclear complexes, as well as EF values (232 and 282). This is consistent with the fact that in the two complexes the first NCO$^-$ interacts with only one metal center, thus exerting the same stabilization effect on the trivalent state, of mere ligand field origin (the tripositive metal ion experiences a Ligand Field Stabilization Energy higher than the dipositive one).

2. For Cl$^-$, ΔE(I-II) for the dinuclear complex is remarkably larger than for the mononuclear complex (170 and 90 mV, respectively, to which EF values of 750 and 33 correspond)). The huge stabilization results from the additional contribution due to the shielding of the intermetallic electrostatic repulsion by the first chloride ion occupying the inner compartment of the dinuclear receptor.

4.2.5 Strange case of NO₃$^-$, which binds only Ni^{III} in a bicyclam arrangement.

Titration of DMSO solutions of $[Ni^{II}(5)]^{2+}$ and of $[Ni^{II}_2(4)]^{4+}$ with $[Bu_4N]NO_3$ did of not cause any modification of the absorption spectra, indicating no interaction of the anion with the divalent metal. Moreover, the DPV profile of the $[Ni^{II}(5)]^{2+}$ complex was not altered following the addition of nitrate, which demonstrated that also the trivalent mononuclear complex does not shows any affinity towards NO₃$^-$. On the other hand, when $[Bu_4N]NO_3$ was added to a DMSO solution of $[Ni^{II}_2(4)]^{4+}$, the DPV peak at 400 mV, progressively moved towards less positive potentials (see Figure 25a).
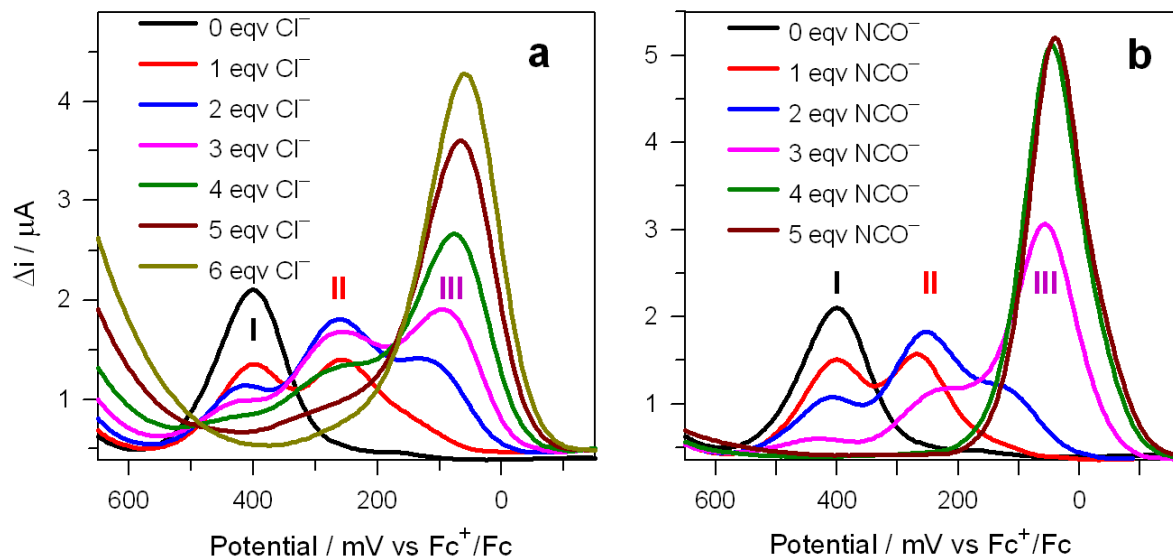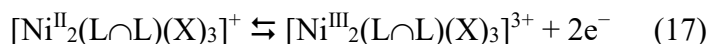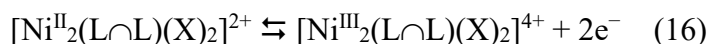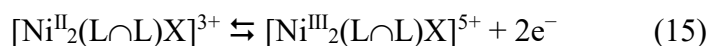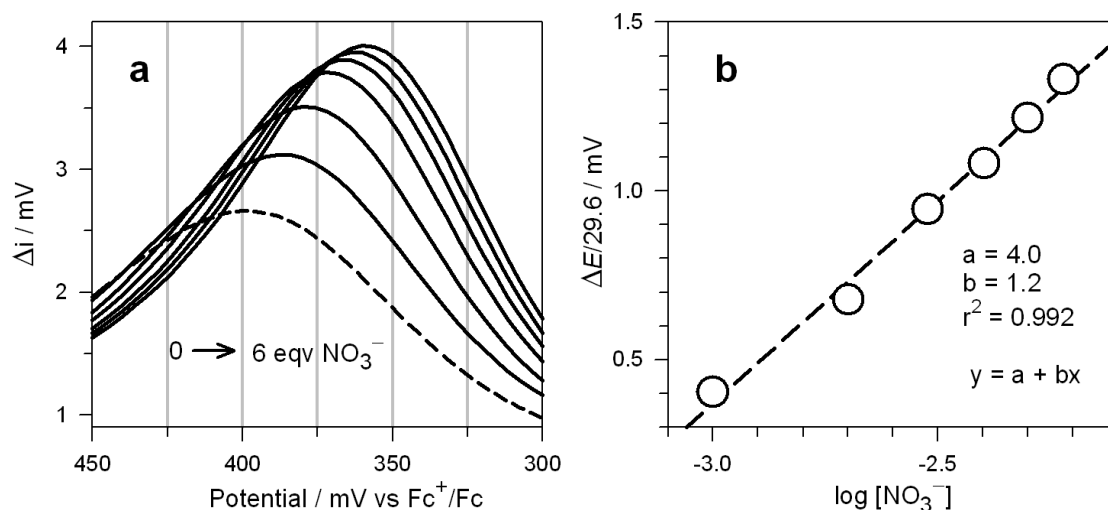

Figure 25. (a) DPV profiles obtained at a platinum microsphere working electrode for a DMSO solution 10^{-3} M in $[Ni^{II}_2(4)](CF_3SO_3)_4$ and 0.1 M in $[Bu_4N]PF_6$ (pulse amplitude 20 mV), to which 1, 2, 3, 4, 5, 6 equiv. of $[Bu_4N]NO_3$ were added; (b) plot of $\Delta E/29.6$ vs log[NO₃$^-$] disclosing a linear correlation which roughly corresponds to the equation: $\Delta E/29.6 = K(III) + log[NO_3^-]$. K(III) is the association constant of the 1:1 complex $[Ni^{III}_2(4)(NO_3)]^{5+}$.

Such a behavior is expected for a redox system M^+/M in which only the oxidized form M^+ interacts with X^-, according to the equilibrium $M^+ + X^- \leftrightarrows [MX]$, whose constant is K^+. In particular, the difference of the peak potential in the absence (ΔE) and in the presence of X^- is related to the molar concentration $[X^-]$ according to the equation:[61,62]

$$\Delta E = \frac{59.16}{n} K^+ + 59.16 \log[X^-] \qquad (19)$$

Considering that we are in the presence of a two-electron process ($n = 2$), equation (18) must be rearranged to

$$\frac{\Delta E}{59.16} = K^+ + \log[X^-] \qquad (20)$$

Indeed, plotting of $\Delta E(\text{mV})/29.6$ vs $\log[X^-]$ gives a straight line (Figure 25b), whose slope reasonably approaches unity and whose intercept (4.0) is K^+ (i.e. the constant of the equilibrium: $[\text{Ni}^{III}_2(\textbf{4})]^{6+} + \text{NO}_3^- \leftrightarrows [\text{Ni}^{III}_2(\textbf{4})(\text{NO}_3)]^{5+}$).

The fact that the $[\text{Ni}^{II}(\textbf{5})]^{2+}/[\text{Ni}^{III}(\textbf{5})]^{3+}$ couple does not sense NO_3^- and the $[\text{Ni}^{II}_2(\textbf{4})]^{4+}/[\text{Ni}^{III}_2(\textbf{4})]^{6+}$ does indicate that the poorly coordinating nitrate ion is not able to bind any Ni^{III}-cyclam subunit externally. It is therefore suggested that NO_3^- goes into the inner cavity of $[\text{Ni}^{III}_2(\textbf{4})]^{6+}$ to profit from the interaction with the two metallocyclam subunits, a further evidence of the *bimacrocyclic effect*.

4.3 Conclusion

In the absence of serious steric constraints, receptors containing unsaturated metal centers uptake anions according to an affinity sequence which reflects the spectrochemical series, i.e. the ligand field effect exerted by each anion. This is surely the case of the mononuclear $[\text{Ni}^{II}(\textbf{5})]^{2+}$ complex, for which K_1 decreases along the series: $\text{NCO}^- > \text{Cl}^- > \text{N}_3^- > \text{Br}^- > \text{NCS}^- > \text{I}^-$. The same trend is observed for the dinuclear $[\text{Ni}_2^{II}(\textbf{4})]^{4+}$, but the ligand field effect varies with the nature of the anion.

In Figure 26 we have plotted $\log K_1$ for the dinuclear complex vs. $\log K_1$ value for the mononuclear complex.
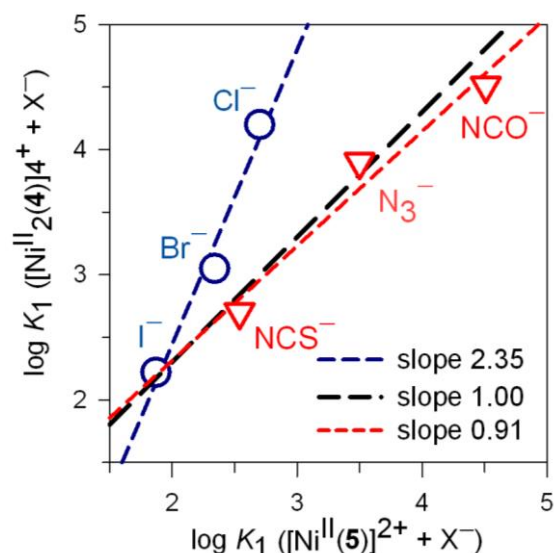
Figure 26. Plot of log K_1 for $[Ni_2^{II}(4)]^{4+}$ vs. log K_1 value for the $[Ni^{II}(5)]^{2+}$. Black dashed line refers to an ideal behavior in which ligand field effects are the same for both mononuclear and dinuclear complexes, in the absence of steric constraints: log $K_1([Ni_2^{II}(4)]^{4+})$ = 2.3 + log $K_1([Ni^{II}(5)]^{2+})$

If the anion affinity were the same for both receptors, values should lie on the same straight line with slope = 1.00. We observe that pseudohalides lie on a straight line whose slope (0.91) is very close to unity, whereas halides lie on a straight-line of much greater slope (2.35). Such a behavior seems to agree with the structural hypotheses put forward for the interaction of the receptor with the first anion: (i) pseudohalides profit from coordination to the same extent whether they bind the metal center of the mononuclear complex or the dinuclear complex (which takes place outside the intermetallic cavity); (ii) halides profit from coordination to a greater extent when binding the dinuclear receptor because they are included in the intermetallic cavity and interact with two metal centers.

Most metal-based receptors contain copper(II) in view of several convenient features of the metal ion: (i) geometrical versatility, (ii) leading position in the Irving-Williams series,[63] (iii) relatively high molar extinction coefficient (ε) of its complexes (e.g. with polyamines, ε > 100 M^{-1} cm^{-1}). The Ni^{II} ion does not show similar favorable characteristics and, in particular, forms weakly colored polyamine complexes (ε < 10). The metallocyclam subunit of $[Ni_2^{II}(4)]^{4+}$ is different, due to the coexistence in solution of a light-blue form (ε < 10 for bands in the visible region) and of a bright yellow form (ε 50−100 M^{-1} cm^{-1}, at ~ 500 nm). In particular, the blue-to-yellow interconversion is highly sensitive to axial binding by exotic ligands and allows a convenient monitoring of anion binding. Moreover, when encircled by cyclam-like ligands, Ni^{II} displays a rich redox activity (e.g. easy oxidation to Ni^{III}), which is strongly affected by anion coordination, thus providing a second channel for analyte detection. Studies on the design of dinickel(II) complexes with bicyclam ligands with increased steric constraints are under way in our Laboratory.

4.4 Experimental section

4.4.1 General Procedures and Materials.

All reagents and solvents were supplied by Aldrich and used as received. UV−Vis spectra were recorded on a Varian CARY 50 spectrophotometer with quartz cuvette of 1 cm path length. UV-Vis titrations were carried out at 25 °C on 5×10^{-3} M solutions of $[Ni^{II}_2(\mathbf{4})](ClO_4)_4$ and $[Ni^{II}(\mathbf{5})](ClO_4)_2$ in DMSO, by adding aliquots of freshly prepared standard solutions (in DMSO) of $[Bu_4N]X$ (X = Cl, Br, I, NCO, NCS and N_3). Titration data were processed with the Hyperquad software to determine the equilibrium constants.[49] HySS programm was used to obtain the distribution diagrams of the species.[64]

Differential-pulse voltammetry (DPV) measurements were performed in a conventional three-electrode cell, using a PAR 273 potentiostat/galvanostat controlled by a PC and driven by dedicated software. A platinum microsphere and a platinum foil were used as working and counter electrodes, respectively, while an Ag/AgCl wire, dipped in a solution of $AgNO_3$ in DMSO, was the reference electrode. $[Bu_4N]PF_6$ (0.1 M) was used as a supporting electrolyte. Potential values were then referred to the potential of the Fc^+/Fc couple, whose $E_{1/2}$ value was measured at the end of each DPV titration, after the addition of ferrocene to the DMSO solution. The potential scan rate in the DPV experiments was 20 mV s^{-1}. DPV titrations were carried out by adding aliquots of freshly prepared standard solutions (in DMSO) of $[Bu_4N]X$ (X = Cl, Br, I, NCO, NCS and N_3 to DMSO solutions 10^{-3} M of $[Ni^{II}_2(\mathbf{4})](ClO_4)_4$ and $[Ni^{II}(\mathbf{5})](ClO_4)_2$, at 25 °C.

Mass spectra were acquired on a Thermo-Finnigan ion trap LCQ Advantage Max instrument, equipped with an ESI source. Elemental analyses were carried out using a Costech ECS 4010 instrument at the Department of Chemistry, Materials, and Chemical Engineering "G. Natta", Politecnico di Milano, Milan, Italy.

[(5,7-Dimethyl-6-benzyl-1,4,8,11-tetraazacyclotetradecane)-nickel(II)] *Perchlorate, [Ni^{II}(5)](ClO_4)_2.* The complex salt was prepared according to a previously described procedure.[65] Anal. Calcd for $C_{19}H_{34}Cl_2N_4NiO_8$ (PM = 576.09): C, 39.6; H, 5.9; N, 9.7. Found: C, 39.4; H, 6.0; N, 9.6.MS (CH_3OH, ESI): m/z 188.2 (100%; $[Ni^{II}(\mathbf{5})]^{2+}$), 475.4 (20% $[Ni^{II}(\mathbf{5}) +ClO_4^-]^+$). UV−vis [Acetone, λ_{max} nm (ε, M^{-1} cm^{-1})]: 468 (62).

α,α'-Bis[(5,7-dimethyl-1,4,8,11- tetraazacyclotetradecan-6-yl)-nickel(II)]-o-xylene Perchlorate, [Ni^{II}_2(4)](ClO_4)_4. The complex salt was prepared according to a previously described procedure,[43] and dried under vacuum at 50 °C. Anal. Calcd for $C_{32}H_{62}Cl_4N_8Ni_2O_{16}$ (PM = 1074.08): C, 35.8; H,

5.8; N, 10.4. Found: C, 35.6; H, 5.7; N, 10.1. MS (CH_3OH, ESI): m/z 336.4 (40%, $[Ni^{II}_2(\mathbf{4})\,\text{-}2H^+]^{2+}$), 386.3 (100%, $[Ni^{II}_2(\mathbf{4})\,\text{-}H^+ + ClO_4^-]^{2+}$. UV−vis [acetone] λ_{max} nm (ε, $M^{-1}\,cm^{-1}$)]: 468 (124)

Safety note! *Perchlorate salts of metal complexes are potentially explosive and should be handled with care. In particular, they should never be heated as solids.*

4.4.2   X-ray crystallographic studies

Diffraction data for $[Ni^{II}_2(\mathbf{4})(\mu\text{-NCO})(NCO)_2]ClO_4 \cdot 2.5H_2O$ (violet, $0.41 \times 0.12 \times 0.10$ mm^3) have been collected by means of a Bruker-Axs CCD-based three circle diffractometer, working at ambient temperature with graphite-monochromatized Mo Kα X-radiation ($\lambda = 0.71073$ Å). Data reduction was performed with the *SAINT* software, and intensities were corrected for Lorentz and polarization effects. Absorption effects were empirically evaluated by the *SADABS* software,[37] and absorption correction was applied to the data. Crystal structure was solved by direct methods (*SIR 97*)[66] and refined by full-matrix least-square procedures on F^2 using all reflections (*SHELXL 97*).[67] Anisotropic displacement parameters were refined for all non-hydrogen atoms. Hydrogens bonded to C atoms were placed at calculated positions with the appropriate AFIX instructions and refined using a riding model. Hydrogens bonded to secondary amines were located in the final ΔF maps and their positions were successively refined restraining the N-H distance to be 0.90 ± 0.01 Å. Positions for hydrogens belonging to water solvent molecules remained undetermined. Perchlorate counterion was disordered over two alternative positions having three O-atom positions in common. The remaining O and Cl atom positions were mutually exclusive, and half populated. A partly present water solvent molecule occurred in the half-populated O(3w) site when the Cl(1b) and O(7b) alternative atom positions were not populated.

Crystal data for $[Ni^{II}_2(\mathbf{4})(\mu\text{-NCO})(NCO)_2]ClO_4 \cdot 2.5H_2O$: $C_{35}H_{67}ClN_{11}Ni_2O_{9.5,}$ $M = 946.87$, monoclinic, $P\,2_1/n$ (no. 14), $a = 9.5464(5)$ Å, $b = 25.5845(12)$ Å, $c = 18.1421(9)$ Å, $\beta = 90.9118(9)°$, $V = 4430.5(4)$ Å^3, $Z = 4$, 46001 measured reflections, 9656 unique reflections (R_{int} 0.038), 6975 strong data [$I_O > 2\sigma(I_O)$], 0.0507 and 0.1314 $R1$ and $wR2$ for strong data, 0.0722 and 0.1483 $R1$ and $wR2$ for all data.

4.5 Supporting information
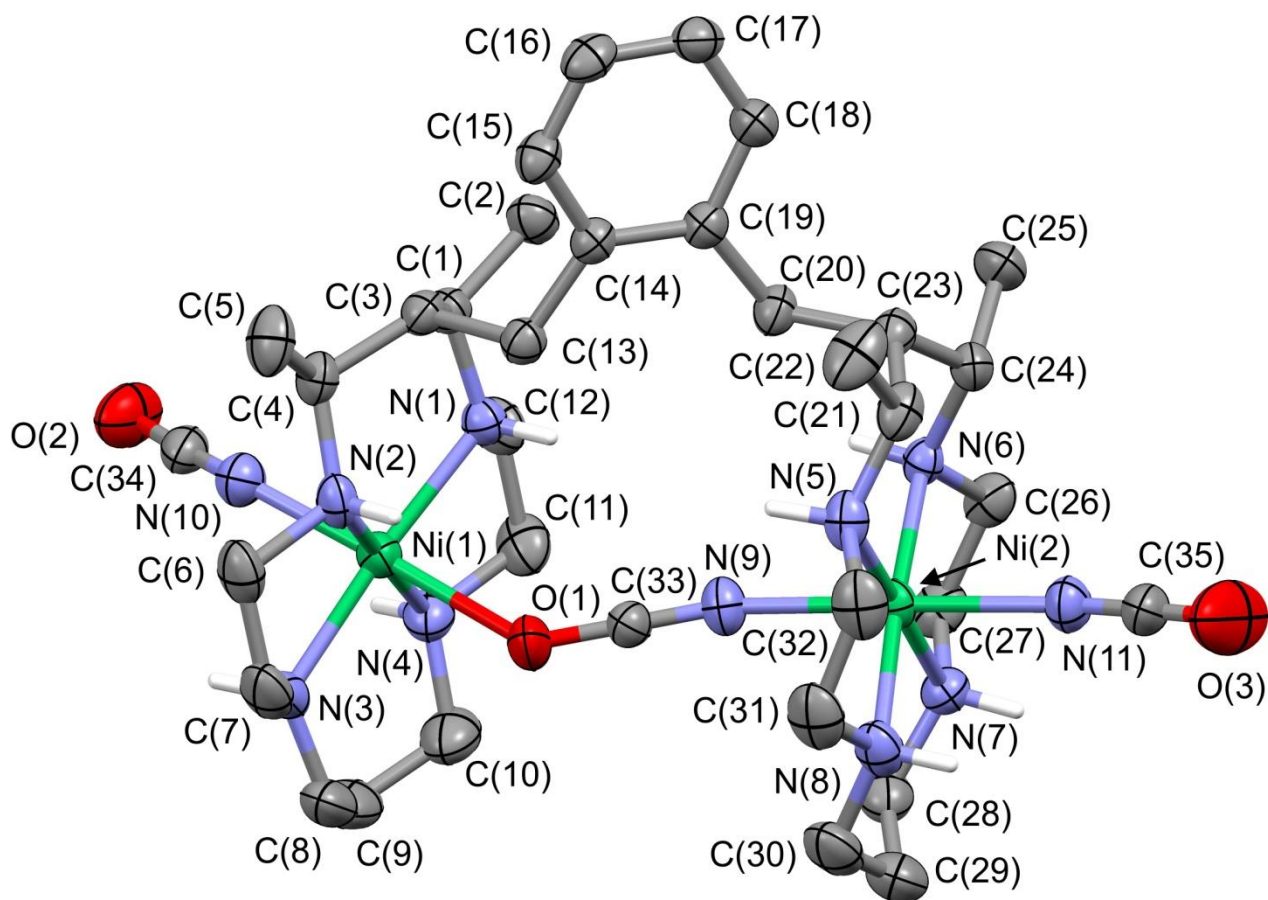
Figure S1. Plot showing thermal ellipsoids for the dinuclear complex $[Ni^{II}_2(\mathbf{4})(\mu\text{-NCO})(NCO)_2]^+$ occurring in the $[Ni^{II}_2(\mathbf{4})(\mu\text{-NCO})(NCO)_2]ClO_4 \cdot 2.5H_2O$ crystalline salt (ellipsoids are drawn at the 30% probability level, perchlorate counterions, water solvent molecules and H atoms not belonging to the amino groups were omitted for clarity). Geometrical features for the axially-elongated octahedral coordination of the metal centers are reported in Table S1.
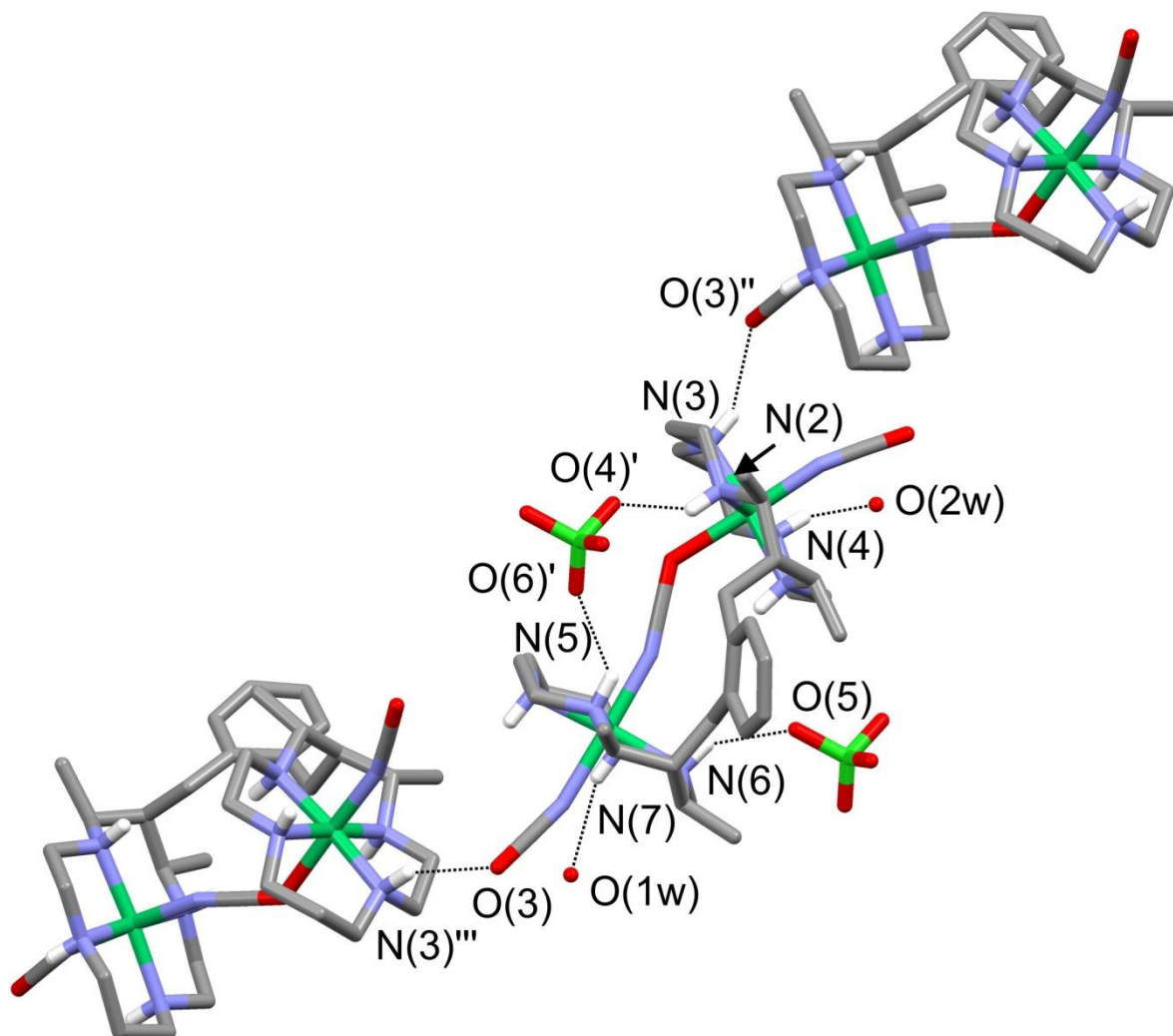
Figure S2. A simplified sketch of the H-bonds involving the dinuclear complex $[Ni^{II}_2(\mathbf{4})(\mu\text{-}NCO)(NCO)_2]^+$; complete H-bonds are drawn as dashed lines only for the dinuclear complex in the middle of the figure. Direct H-bond interactions occurring between the dinuclear complexes originate supramolecular chains extending along the **b** axis direction. These interactions involve the oxygen of the cyanate groups (H-acceptor) and the NH groups of the tetra-aza macrocyle (H-donor), whereas further indirect H-bond interactions, mediated by perchlorate ions and water solvent molecules, interconnect the supramolecular chains in the crystal.

Geometrical features for the H-bond interactions shown in figure are: N(2)⋯O(4)'3.01(1) Å, H(2N)⋯O(4)' 2.28(3) Å, N(2)-H(2N)⋯O(4)' 139.6(20)°; N(3)⋯O(3)" 3.26(1) Å, H(3N)⋯O(3)" 2.43(2) Å, N(3)-H(3N)⋯O(3)" 152.6(14)°;N(4)⋯O(2w) 3.02(1) Å, H(4N)⋯O(2w) 2.17(3) Å, N(4)-H(4N)⋯O(2w) 157.9(26)°;N(5)⋯O(6)' 3.31(1) Å, H(5N)⋯O(6)' 2.65(3) Å, N(5)-H(5N)⋯O(6)' 131.6(15)°; N(6)⋯O(5) 3.07(1) Å, H(6N)⋯O(5) 2.32(2) Å, N(6)-H(6N)⋯O(5) 141.5(12)°; N(7)⋯O(1w) 3.37(1) Å, H(7N)⋯O(1w) 2.53(2) Å, N(7)-H(7N)⋯O(1w) 157.7(12)°;symmetry code: (') = x-1, y, z; (") = -x+$^1/_2$, y-$^1/_2$, -z+$^1/_2$, ("') = -x+$^1/_2$, y+$^1/_2$, -z+$^1/_2$.

Table S1. Bond distances (Å) and bond angles (°) for the axially elongated octahedral coordination of the two metal centers in the dinuclear complex $[Ni^{II}_2(\textbf{4})(\mu\text{-NCO})(NCO)_2]^+$.

Ni(1)-N(1)	2.076(2)	Ni(2)-N(5)	2.078(3)
Ni(1)-N(2)	2.074(3)	Ni(2)-N(6)	2.082(2)
Ni(1)-N(3)	2.065(3)	Ni(2)-N(7)	2.077(3)
Ni(1)-N(4)	2.067(3)	Ni(2)-N(8)	2.076(3)
Ni(1)-N(10)	2.076(3)	Ni(2)-N(9)	2.146(3)
Ni(1)-O(1)	2.304(2)	Ni(2)-N(11)	2.156(3)
N(1)-Ni(1)-N(2)	95.07(10)	N(5)-Ni(2)-N(6)	96.46(10)
N(1)-Ni(1)-N(3)	175.32(11)	N(5)-Ni(2)-N(7)	178.55(11)
N(1)-Ni(1)-N(4)	85.34(11)	N(5)-Ni(2)-N(8)	85.46(12)
N(1)-Ni(1)-N(10)	94.03(10)	N(5)-Ni(2)-N(9)	87.62(10)
N(1)-Ni(1)-O(1)	87.75(9)	N(5)-Ni(2)-N(11)	91.94(11)
N(2)-Ni(1)-N(3)	85.53(12)	N(6)-Ni(2)-N(7)	84.98(10)
N(2)-Ni(1)-N(4)	176.33(11)	N(6)-Ni(2)-N(8)	176.45(10)
N(2)-Ni(1)-N(10)	93.00(11)	N(6)-Ni(2)-N(9)	90.55(10)
N(2)-Ni(1)-O(1)	86.96(10)	N(6)-Ni(2)-N(11)	90.82(10)
N(3)-Ni(1)-N(4)	93.77(13)	N(7)-Ni(2)-N(8)	93.09(11)
N(3)-Ni(1)-N(10)	90.58(11)	N(7)-Ni(2)-N(9)	92.52(10)
N(3)-Ni(1)-O(1)	87.65(10)	N(7)-Ni(2)-N(11)	87.89(11)
N(4)-Ni(1)-N(10)	90.61(12)	N(8)-Ni(2)-N(9)	92.52(11)
N(4)-Ni(1)-O(1)	89.41(11)	N(8)-Ni(2)-N(11)	86.12(11)
N(10)-Ni(1)-O(1)	178.22(10)	N(9)-Ni(2)-N(11)	178.60(10)
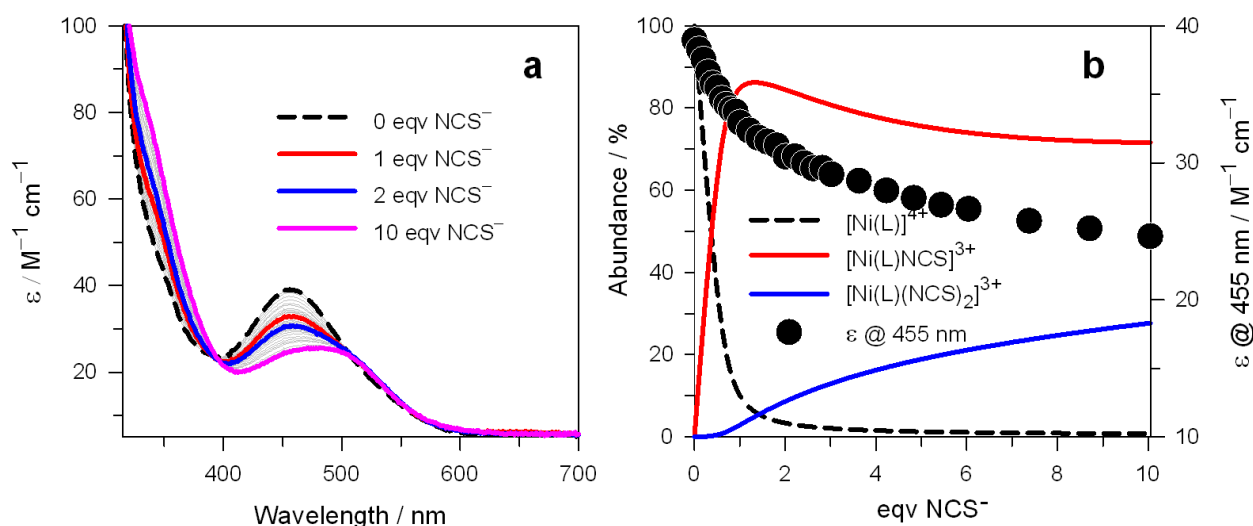
Figure S3. (a) Spectra taken over the course of the titration of a DMSO solution of 5.0×10^{-3} M $[Ni^{II}(\textbf{5})](ClO_4)_2$ with $[Bu_4N]NCS$, at 25 °C; (b) spectra taken in the visible region (c) symbols: Molar Extinction Coefficient

(ε) at 455 nm (monitoring the concentration of low-spin Ni^{II} complexes at the equilibrium); lines: concentration profiles of the complex species at the equilibrium over the course of the titration.
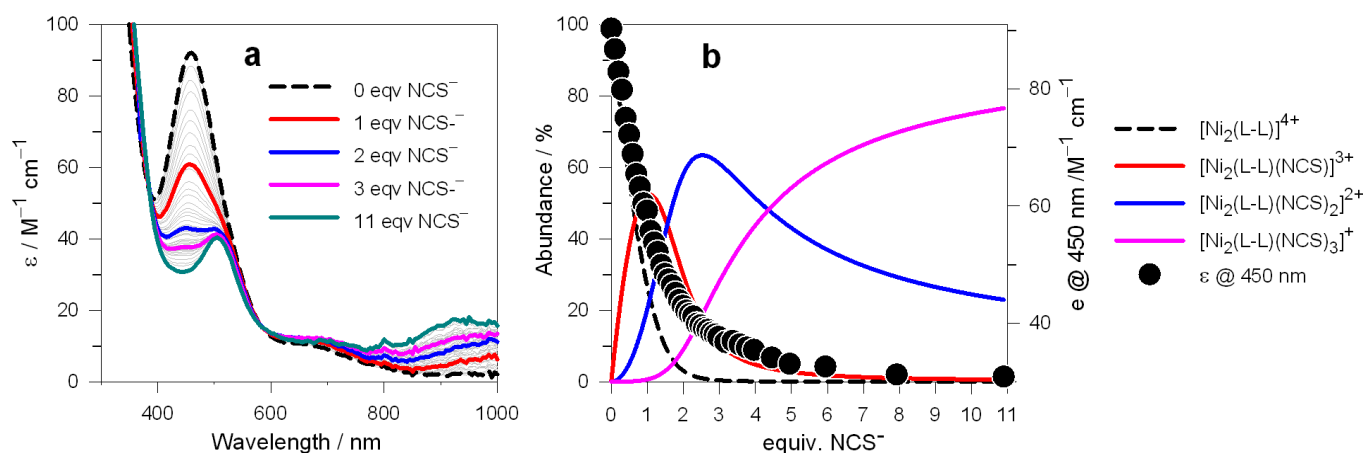
Figure S4. (a) Spectra taken over the course of the titration of a DMSO solution of 5×10^{-3} M [Ni$^{II}_2$(**4**)](ClO$_4$)$_4$ with [Bu$_4$N]NCS, at 25 °C; (b) symbols: Molar Extinction Coefficient (ε) taken at 450 nm, monitoring the concentration of low-spin Ni^{II} complexes at the equilibrium; lines: concentration profiles of the complex species at the equilibrium over the course of the titration.
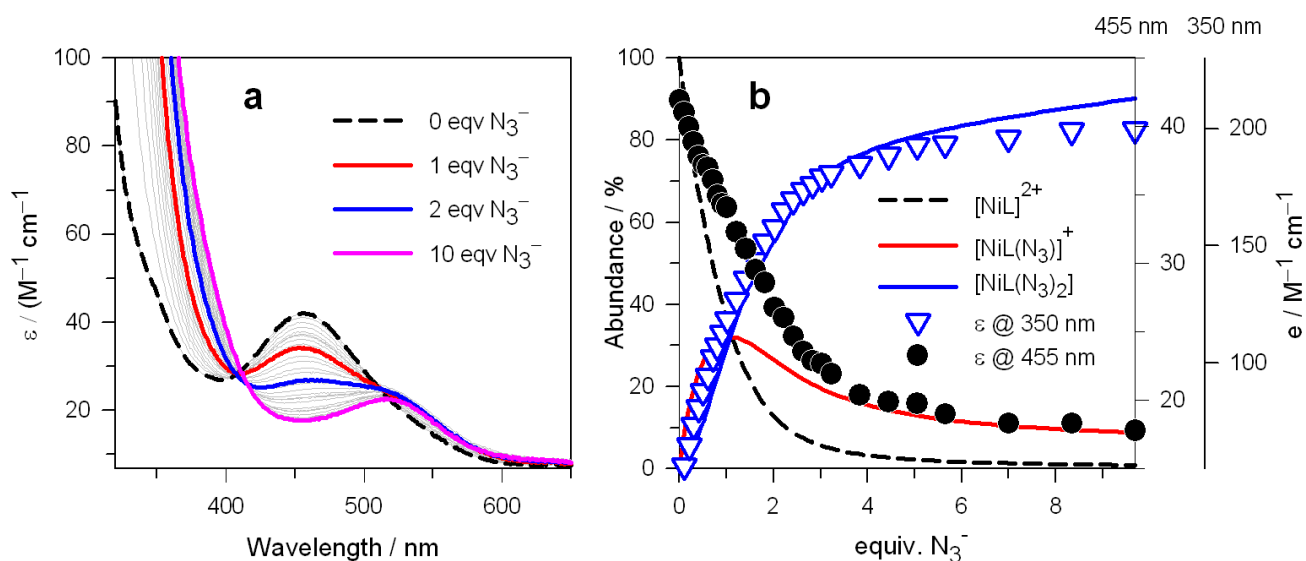
Figure S5. (a) Spectra taken over the course of the titration of a DMSO solution of 5.0×10^{-3} M [Ni^{II}(**5**)](ClO$_4$)$_2$ with [Bu$_4$N]N$_3$, at 25 °C; (b) spectra taken in the visible region (c) symbols: Molar Extinction Coefficient (ε) at selected wavelengths; lines: concentration profiles of the complex species at the equilibrium over the course of the titration.
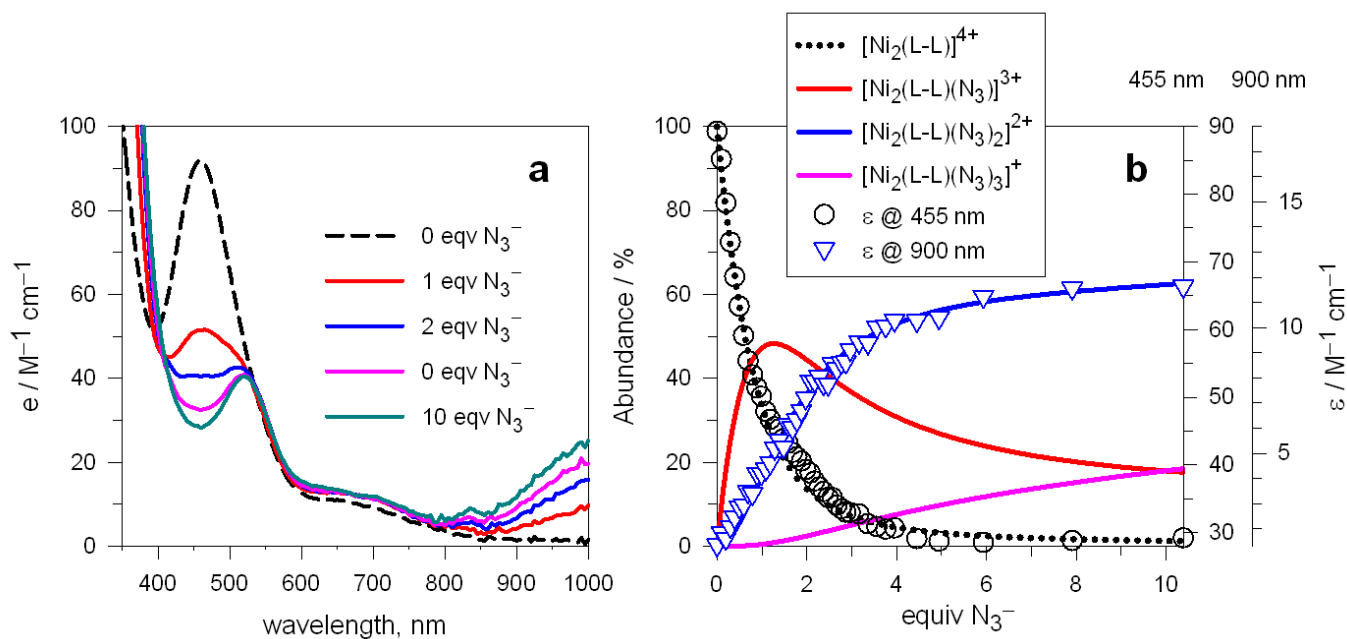
Figure S6. (a) Spectra taken over the course of the titration of a DMSO solution of 5×10^{-3} M [Ni^{II}_2(**4**)](ClO$_4$)$_4$ with [Bu$_4$N]N$_3$, at 25 °C; (b) symbols: Molar Extinction Coefficient (ε) taken at selected wavelengths; lines: concentration profiles of the complex species at the equilibrium over the course of the titration.
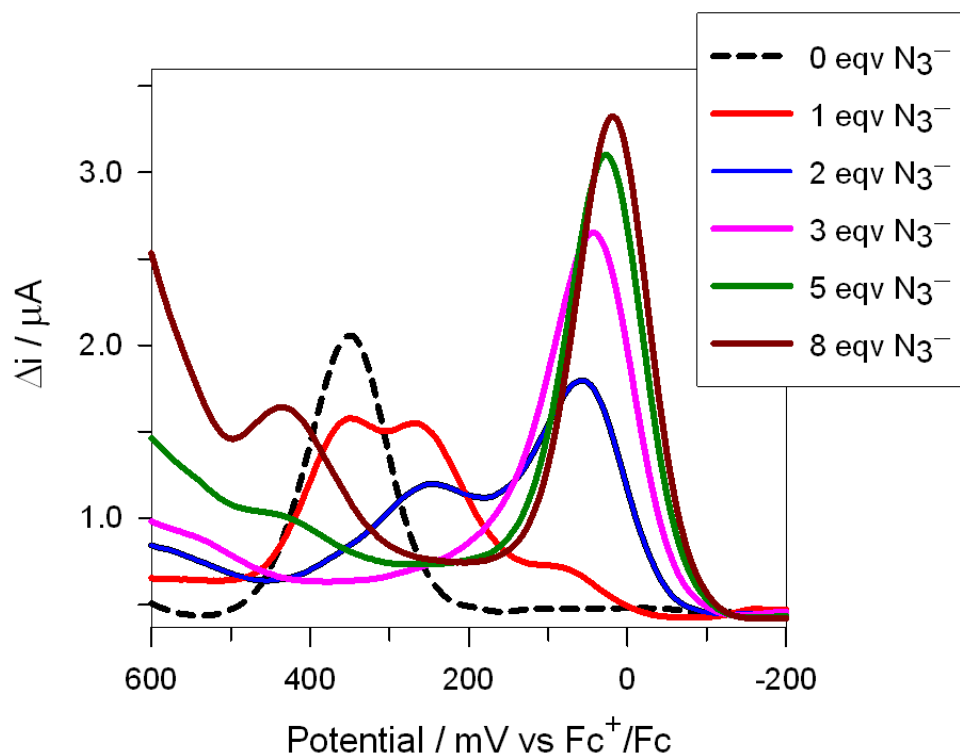
Figure S7. DPV profiles obtained at a platinum microsphere working electrode for a DMSO solution of 10^{-3} M [Ni^{II}(**5**)](ClO$_4$)$_2$ with 0.1 M [Bu$_4$N]PF$_6$ (pulse amplitude 10 mV), to which up to 8 equiv. of [Bu$_4$N]N$_3$ were added; potential scan from less positive to more positive potentials ($\leftarrow$).
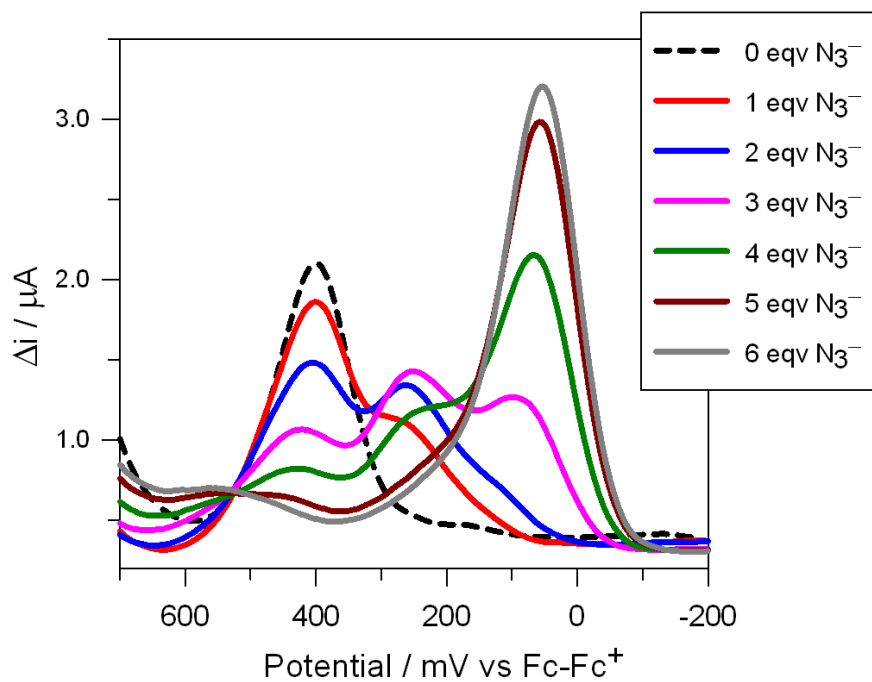
Figure S8. DPV profiles obtained at a platinum microsphere working electrode for a DMSO solution 10^{-3} M [Ni^{II}_2(**4**)](ClO_4)$_4$ with 0.1 M in [Bu_4N]PF_6 (pulse amplitude 20 mV), to which up to 6 equiv. of [Bu_4N]N_3; potential scan from less positive to more positive potentials ($\leftarrow$).

5 Anion chelation by a Copper(II) bis-macrocyclic complex

5.1 Introduction

The coordination chemistry of dinuclear complexes, particularly of systems containing two transition metal ions separated by a relatively short distance (3.5-7.0 Å), has attracted much interest along the last 30 years because of their involvement in a variety of biochemical and industrial processes.[68] The presence of two metal ions at a suitable distance can favor the coordination of small molecules, anions, and/or organic substrates, and grant a catalytic activity for certain reactions, e.g, reduction of CO_2,[69] and of O_2.[70]
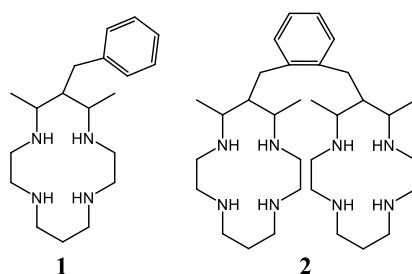
In particular, octaamine **2** represents an interesting example of bimacrocyclic ligand, consisting of two dimethyl-cyclam subunits in a *trans*-III conformation, bridged by an *ortho*-xylyl group. Both methyl groups on each cyclam ring are in the equatorial position with respect to the chair conformation of the six membered chelate rings, causing an axial orientation of the xylylene group and consequently favoring the face-to-face arrangement of the two macrocyclic subunits.[42] The corresponding bis-nuclear complexes are able to combine the high inertness toward demetallation of the cyclam-like analogues with the capability of the pincer-like structure to chelate anions between the two metal centers.
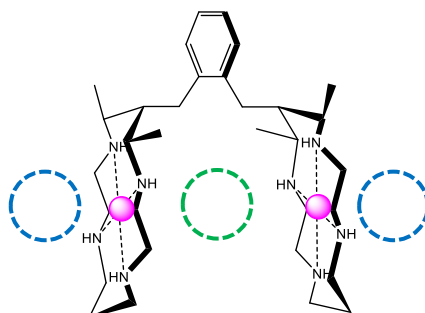
Figure 1. Schematic representation of the face-to-face structural arrangement adopted by dinuclear complexes of 2. Anions could be coordinated (i) simultaneously by two metal centers (inner position, green dashed circle) and/or by one metal ion (outer positions, blue dashed circles), in the same way as a mononuclear complex.

The di-nickel(II) complex of ligand **2** was studied in solid state by Endicott and co-workers,[43] who demonstrated that it shows an extreme versatility in the magnetic behavior, depending on the nature of the anion bound between the two facing metallocyclam subunits. Recently we have studied the interaction of $[Ni_2(\mathbf{2})]^{4+}$ with halides and pseudohalides in DMSO.[34] Figure 1 shows the possible positions where the anions can be coordinated by the dinuclear complex. Our spectrophotometric and voltammetric studies disclosed two main behaviors: (i) pseudohalides preferentially interact outside the intermetallic cavity of the bimacrocyclic complex, profiting from coordination to the metal ion of the dinuclear complex to the same extent as the analogous mononuclear species, $[Ni(\mathbf{1})]^{2+}$; (ii) halides profit from coordination to a greater extent when they bind the dinuclear complex because they are included in the intermetallic cavity and interact with two metal centers at the same time. We previously defined as "bimacrocyclic effect" the extra-stability displayed the complex-anion adduct in which the anionic guest occupies the room between the two macrocyclic subunits when compared to the adduct with the related mononuclear complex.[34] In order to confirm this particular type of chelate effect and to have a better insight on its nature, we investigated the interaction between the di-copper complex of the ligand **2**, $[Cu_2(\mathbf{2})]^{4+}$, and different anions, in comparison with the mononuclear analogous, $[Cu(\mathbf{1})]^{2+}$. In particular, the interaction was studied according to the receptor-substrate approach, by using different techniques i.e. electron paramagnetic resonance (EPR), isothermal titration calorimetry (ITC), UV-Vis spectrophotometry, and X-ray diffraction. Copper(II) complexes of ligands **1** and **2** were chosen for this study on the basis of the following considerations:

- the known preference of Cu^{2+} ion for the penta-coordination could favour the formation of 1:1 adduct between bimacrocyclic complex $[Cu_2(\mathbf{2})]^{4+}$ and bridged anions, limiting the possible access of further coordinating anions at the outer positions (see Fig. 1);

- the leading position of copper(II) in the Irving-Williams series[63] makes the interaction with anionic ligands stronger than that expected for other metal ions, allowing the study of bimacrocyclic effect even in very competitive solvents, including water;

- owing to copper(II) one-electron paramagnetism, complex $[Cu_2(\mathbf{2})]^{4+}$ could favor spin-spin coupling between its two copper centers in the presence of coordinated bridging anions, allowing the use of EPR technique to confirm the mechanism of the anion – di-nuclear complex interaction. Ligand-mediated spin-spin coupling processes have been previously investigated in different bimacrocyclic complexes.[71–76]

5.2 Results and discussion

5.2.1 EPR studies

EPR spectra were measured on frozen DMSO (117 K) solutions of $[Cu(\mathbf{1})](ClO_4)_2$ and $[Cu_2(\mathbf{2})](ClO_4)_4$ in the presence of increasing amount (0, 0.5, 1, 2, 7 equivalents) of different anions (chloride, bromide, iodide, azide, cyanate, and acetate). Collected data are resumed in Table 1.

Spectrum of $[Cu(\mathbf{1})]^{2+}$ shows the typical four-line pattern in the $g_{\parallel}$ (Figure 2a) expected for coupling of an electron with a single copper(II) nucleus (2NI + 1 = 4, where N is the number of equivalent nuclei felt by the electron and I is the nuclear spin quantum number, 3/2 for Cu). The spectrum of $[Cu_2(\mathbf{2})]^{4+}$ also displays a four-line pattern, as shown in Figure 2b and 2c, indicating that each unpaired electron feels only one copper center, resulting in two undistinguishable groups of 4 lines.
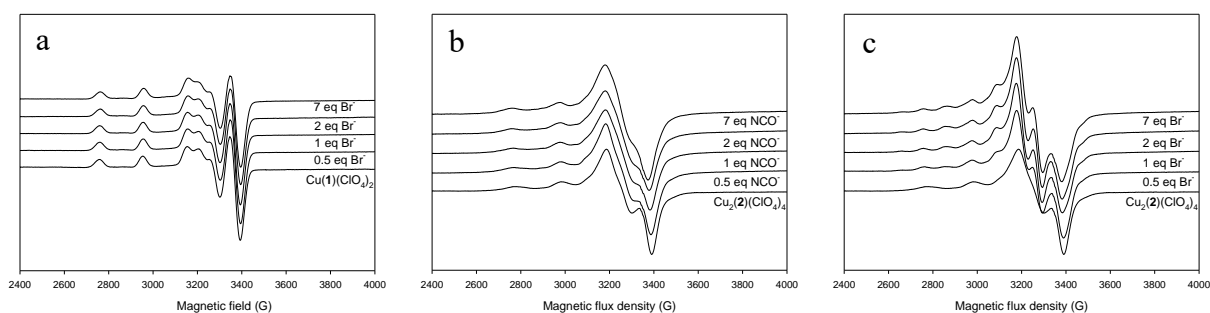
Figure 2. Experimental EPR spectra of: (a) a solution of $[Cu(\mathbf{1})](ClO_4)_2$ (5×10^{-4} M) with increasing amounts of Br⁻; (b) a solution of $[Cu_2(\mathbf{2})](ClO_4)_4$ (5×10^{-4} M) with increasing amounts of NCO⁻; c) a solution of $[Cu_2(\mathbf{2})](ClO_4)_4$ (5×10^{-4} M) with increasing amounts of Br⁻.

The mononuclear complex still displays the four-line pattern when increasing amounts (0.5, 1, 2, 7 equivalents) of any investigated anions are added. Spectra recorded on the solution of $[Cu(\mathbf{1})](ClO_4)_2$ with different amounts of bromide are shown in figure 3a, while analogous spectra families obtained with other anions are reported in Figure S1 (Supplementary Information). The di-nuclear complex displays similar spectra (*i.e.* $g_{\parallel}$ retains the four signals pattern) in the presence of cyanate and acetate (see Figures 2b and S2), while the addition of chloride, bromide, iodide, and azide results in profound spectral changes, easily attributed to the formation of a triplet state in which the two unpaired electron are delocalized on both copper centers. The interaction is evidenced by the larger number of peaks and the value of A_{II} (approximately half of that of the free dimeric receptor and analogous mononuclear complex), indicating a delocalization of the unpaired electrons (S = 1/2) over two equivalent copper centers. Spectra recorded on a frozen DMSO solution of $[Cu_2(\mathbf{2})]^{4+}$ with different amounts of bromide are shown in Figure 2c while spectra concerning other anions are reported in Figure S2. The

spectra of $[Cu_2(\mathbf{2})]^{4+}$ measured in the presence of anions that mediate the metal-metal interaction consist of two septuplets ($2NI + 1 = 2*2*3/2 + 1 = 7$), but due to a partial overlapping of the two septuplets just ten signals can be identified (figure 2c).

Table 1. EPR parameters for $[Cu(\mathbf{1})](ClO_4)_2$ and $[Cu_2(\mathbf{2})](ClO_4)_4$ determined in the presence of excess of anions in a frozen solution (DMSO, 117 K).

Anion	Complex	N. peaks[a]	Spin-Spin Coupling	g_{II}	A_{II} [$10^{-4}cm^{-1}$]	D_{II} [$10^{-4}cm^{-1}$]	Cu···Cu distance [Å]
Cl⁻	$[Cu(\mathbf{1})]^{2+}$	4	no	2.15	195	-	-
	$[Cu_2(\mathbf{2})]^{4+}$	10 [c]	yes	2.14	93	155	5.9
Br⁻	$[Cu(\mathbf{1})]^{2+}$	4	no	2.15	195	-	-
	$[Cu_2(\mathbf{2})]^{4+}$	10 [c]	yes	2.11	96	140	6.0
I⁻	$[Cu(\mathbf{1})]^{2+}$	4	no	2.15	195	-	-
	$[Cu_2(\mathbf{2})]^{4+}$	10 [c]	yes	2.2	96	92	7.0
N_3^-	$[Cu(\mathbf{1})]^{2+}$	4	no	2.15	195	-	-
	$[Cu_2(\mathbf{2})]^{4+}$	10 [c]	yes	2.14	94	147.5	6.0
NCO⁻	$[Cu(\mathbf{1})]^{2+}$	4	no	2.15	190	-	-
	$[Cu_2(\mathbf{2})]^{4+}$	4 [b]	no	2.13	212	-	-
CH_3COO^-	$[Cu(\mathbf{1})]^{2+}$	4	no	2.15	195	-	-
	$[Cu_2(\mathbf{2})]^{4+}$	4[b]	no	2.12	205	-	-

[a] Number of expected peaks = 2NI + 1 (N, number of equivalent nuclei felt by the electron; I, nuclear spin quantum number); [b] two group of four overlapped lines; [c] two group of seven lines where four of them are overlapped.

The barycenter of the two septuplets is separated by a value of $2D_{II}$. Assuming that the zero-field splitting is purely dipolar and using the equation $D_{II} = 0.65\ g_{II}^2/R^3$, values of R, and of Cu–Cu distances can be calculated, which are in good agreement with the values obtained from crystal structures.[72,77] It should be noted that the addition of 0.5 equivalent of chloride, bromide, or iodide, results in the simultaneous presence of both isolated and communicating Cu centers, indicating that the first anion is coordinated between the two metal centers, taking them closer and acting as a bridge. In the case of azide the coupling starts being noticed after the addition of two equivalents of anion, possibly due to a less strong interaction (see the next section for the stability constants of the bimacrocyclic complex-anion adducts). In the presence of a large excess of halides and azide (7 equivalents) the 10 lines are still visible in the EPR spectra, which indicates that the coordination of an anion inside the cavity, bridging the two Cu^{2+} centers, is strongly favored over the coordination of the maximum possible number of anions. Cyanate and acetate do not induce any relevant spectral change (see spectra in Figures 2b and S2, respectively), suggesting that they are more likely coordinated only at the external positions of the bimacrocyclic complex.

5.2.2 Calorimetric studies in DMSO

Studies of the anion-binding properties of complex species $[Cu(1)]^{2+}$ and $[Cu_2(2)]^{4+}$ in pure DMSO were performed by isothermal titration calorimetry (ITC). In a typical experiment, a solution of the envisaged complex in DMSO was titrated by a solution of the investigated anion dissolved in the same solvent as tetrabutilammonium (TBA$^+$) salt. (TBA)Cl, (TBA)Br, (TBA)I, (TBA)N$_3$, (TBA)NCO, (TBA)CH$_3$COO, (TBA)SCN, and (TBA)NO$_3$ were used as titrants. It should be noted that no heat effect was observed during the ITC titrations performed on both mono- and di-nuclear complexes with NCS$^-$ and NO$_3^-$, suggesting that the interaction with these anionic species is too weak to be detected. Figure 3 reports the thermograms and the ITC profiles (obtained by Affinimeter software, www.affinimeter.com) corresponding to the ITC titration of $[Cu(1)](ClO_4)_2$ with Cl$^-$, Br$^-$, N$_3^-$, and NCO$^-$ (data of titration with I$^-$ and CH$_3$COO$^-$ are shown in Figure S3).
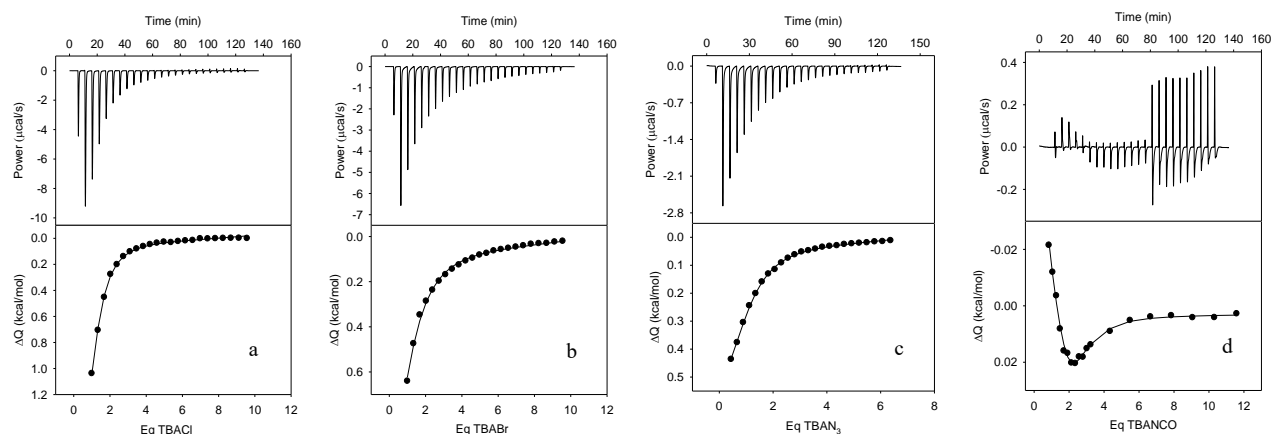
Figure 3. Thermograms and corresponding ITC profiles taken over the course of the titration experiments in DMSO: a) $[Cu(1)](ClO_4)_2$ (1 mM) titrated with (TBA)Cl (30 mM); b) $[Cu(1)](ClO_4)_2$ (5.087 mM) titrated with (TBA)Br (138.63 mM); c) $[Cu(1)](ClO_4)_2$ (5.8 mM) titrated with (TBA)N$_3$ (105.49 mM); d) $[Cu(1)](ClO_4)_2$ (5.8 mM) titrated with (TBA)NCO (112.59 mM); e) $[Cu(1)](ClO_4)_2$ (5.13 mM) titrated with (TBA)CH$_3$COO (120 mM). Circles: experimental data; line: fitting profile (sequential two site models for a, b, d and e; one site model for c; "receptor" complex in the cell); T = 25°C.

$[Cu(1)]^{2+}$ can coordinate the first equivalent of anion (1:1 adduct) according to a square pyramidal geometry, binding the anion in the axial position. Sequentially, the mononuclear complex can coordinate the second equivalent of anion (1:2 complex) exploiting an elongated octahedral geometry, with both anions in an axial position, one anion for each side (Figure S4). In the cases of Cl$^-$, Br$^-$, NCO$^-$, and CH$_3$COO$^-$ we obtained the best fitting by assuming the occurrence of two stepwise equilibria, corresponding to the formation of 1:1 (eq. 1) and 1:2 (eq. 2) complex/anion adducts.

$$[Cu(\mathbf{1})]^{2+} + X^- \rightleftharpoons [Cu(\mathbf{1})X]^+ \tag{1}$$

$$[Cu(\mathbf{1})X]^+ + X^- \rightleftharpoons [Cu(\mathbf{1})X_2] \tag{2}$$

(X$^-$ = Cl$^-$, Br$^-$, NCO$^-$, CH$_3$COO$^-$)

Concerning I$^-$ and N$_3^-$ the best fitting of the titration data was obtained by assuming the occurrence of only one equilibrium, corresponding to the formation of 1:1 complex species. Although the binding of 2 anions even for I$^-$ and N$_3^-$ cannot be ruled out at all, no experimental evidence was obtained for the formation of 1:2 adducts with these anions, i.e. the corresponding stability constant values could be too small to be experimentally determined.

Thermograms and ITC profiles corresponding to the titrations of [Cu$_2$(**2**)]$^{4+}$ with Cl$^-$, Br$^-$, N$_3^-$, and NCO$^-$ are reported in Figure 4, while data concerning titration with I$^-$ and CH$_3$COO$^-$ are reported in Figure S5.
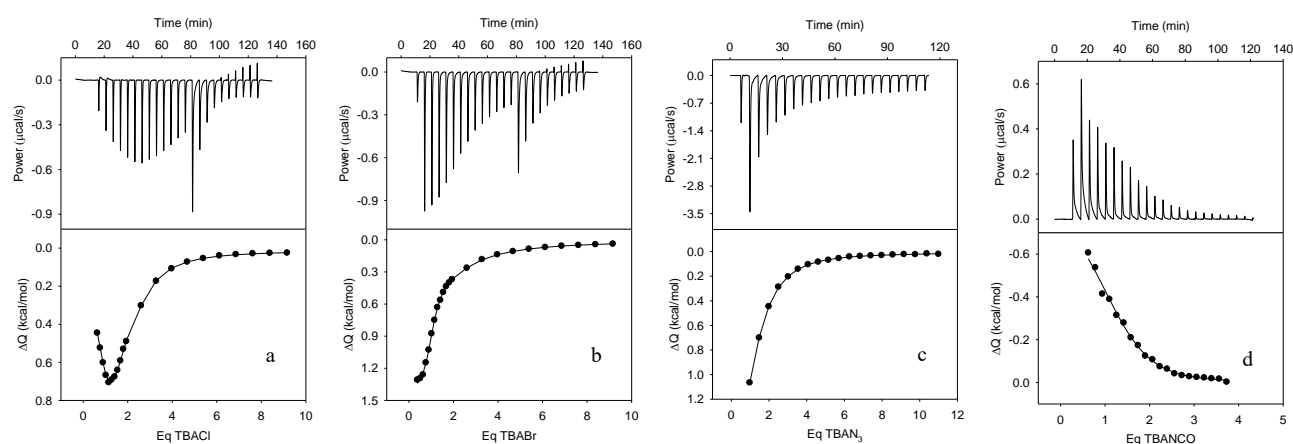
Figure 4. Thermograms and ITC profiles taken over the course of the titration of a solution of [Cu$_2$(**2**)](ClO$_4$)$_4$ (1 mM) in DMSO with a solution of: a) (TBA)Cl (30 mM); b) (TBA)Br (30 mM); c) (TBA)N$_3$ (50 mM); d) (TBA)NCO (37.07 mM). Circles: experimental data; line: fitting profile (sequential two site models for a, b, and d; one site model for c; "receptor" complex in the cell); T = 25°C.

Considering the titration of complex [Cu$_2$(**2**)]$^{2+}$ with (TBA)N$_3$ the best fitting of the data can be obtained by assuming the occurrence of one equilibrium corresponding to the formation of 1:1 complex. On the other hand, when the bis-macrocyclic complex is titrated with Cl$^-$, Br$^-$, I$^-$, NCO$^-$, and CH$_3$COO$^-$ the occurrence of two stepwise equilibria (eq. 3 and 4) has to be assumed in order to obtain the best fitting of the titration data.

$$[Cu_2(\mathbf{2})]^{4+} + X^- \rightleftharpoons [Cu_2(\mathbf{2})X]^{3+} \tag{3}$$

$$[Cu_2(\mathbf{2})X]^{3+} + X^- \rightleftharpoons [Cu_2(\mathbf{2})X_2]^{2+} \tag{4}$$

$(X^- = Cl^-, Br^-, I^-, NCO^-, CH_3COO^-)$

Differently from the behavior of the di-nickel complex $[Ni_2(\mathbf{2})]^{4+}$ that coordinates up to 3 equivalents of anion,[34] the analogous di-copper complex interacts in solution with no more than 2 equivalents of anionic ligands, likely due to the higher propensity of the Cu^{2+} for the penta-coordination.
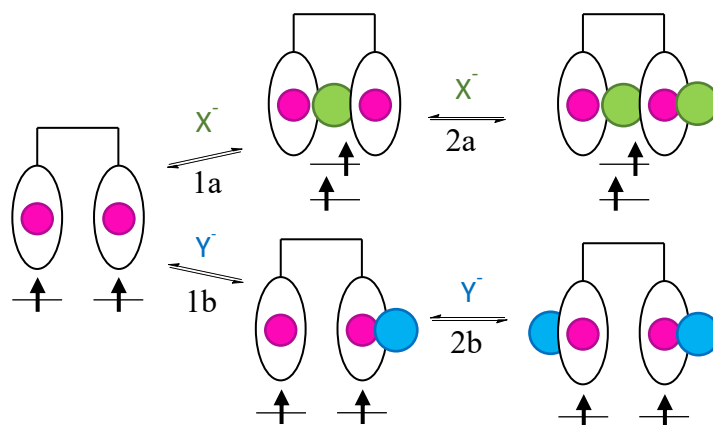
Figure 5. Schematic representation of the equilibria involved over the course of the titration of $[Cu_2(2)](ClO_4)_4$ with (i) bridging anions (X^-, green spheres = Cl^-, Br^-, I^-, N_3^-), which permit the spin-spin coupling between the two copper centers and (ii) non-bridging anions (Y^-, blue spheres = NCO^-, CH_3COO^-).

On the basis of EPR and ITC measurements the geometrical aspects of the equilibria taking place during the titrations of $[Cu_2(\mathbf{2})]^{4+}$ with the investigated anions in DMSO solution can be hypothesized. They are schematically resumed in Figure 5. The di-copper(II) complex can coordinate anionic species according to two distinct pathways:

(a) the first anion occupies the inner position between the two macrocyclic subunits, binding two metal centers at the same time (equilibrium 1a in Figure 5), giving rise to a square-pyramidal arrangement for both copper(II) ions, and providing a spin-spin coupling as shown by EPR measurements; then a second equivalent of anion can be coordinated at one of the two equivalent "external" positions of the dinuclear complex (equilibrium 1b in Figure 5), inducing one copper(II) ion to assume an elongated octahedral geometry and preserving the spin-spin coupling;

(b) both the first and the second equivalent of anion interacts with $[Cu_2(\mathbf{2})]^{4+}$ at the "external" positions (equilibria 2a and 2b in Figure 5); each metal ion assumes a square-pyramidal coordination geometry.

The interaction with a third equivalent of anion in solution (if any) has neither been observed by ITC, nor with other techniques used in this study (EPR and UV-vis, see next section). Taking into account the experimental data and referring to the equilibria depicted in Figure 5, azide interacts with $[Cu_2(\mathbf{2})]^{4+}$ according to equilibrium 1a, chloride, bromide and iodide according to equilibria 1a and 2a, cyanate and acetate according to equilibria 1b and 2b.

The thermodynamic quantities ($\log K$, ΔH, TΔS,) at 25°C obtained by fitting the data obtained during titrations of $[Cu(\mathbf{1})]^{2+}$ and $[Cu_2(\mathbf{2})]^{4+}$ with the considered anions are collected in Table 2. Log K_1 values determined for the interaction the mono-nuclear complex with the investigated anions (eq. 1) and related to the stability of $[Cu(\mathbf{1})X]^+$ species roughly fall in the 2.0 – 3.5 range. The experimental affinity sequence is the following: $Cl^- > CH_3COO^- > NCO^- > Br^- > N_3^- > I^- \gg SCN^-, NO_3^-$.

Table 2. Thermodynamic parameters at 25°C obtained by fitting ITC titration data of $[Cu(\mathbf{1})](ClO_4)_2$ and $[Cu_2(\mathbf{2})](ClO_4)_4$ in DMSO. In parentheses standard deviations on the last figures.

Anion	Complex	Fitting model	Log K_1	ΔH_1 [Kcal mol^{-1}]	TΔS_1 [Kcal mol^{-1}]	Log K_2	ΔH_2 [Kcal mol^{-1}]	-TΔS_2 [Kcal mol^{-1}]
Cl^-	$[Cu(\mathbf{1})]^{2+}$	1:2	3.42(4)	0.97(2)	5.64	1.8(1)	1.14(9)	3.58
	$[Cu_2(\mathbf{2})]^{4+}$	1:2	5.408(6)	0.360(9)	7.73	3.327(6)	1.11(2)	5.65
Br^-	$[Cu(\mathbf{1})]^{2+}$	1:2	2.76(6)	1.31(4)	5.07	1.2(1)	3.06(9)	4.66
	$[Cu_2(\mathbf{2})]^{4+}$	1:2	4.60(1)	1.27(1)	7.54	2.76(1)	1.21(3)	4.97
I^-	$[Cu(\mathbf{1})]^{2+}$	1:1	2.02(3)	2.5(2)	5.20	/	/	/
	$[Cu_2(\mathbf{2})]^{4+}$	1:2	3.8(2)	1.6(5)	6.73	<1(a)	a	a
N_3^-	$[Cu(\mathbf{1})]^{2+}$	1:1	2.54(2)	0.80(2)	4.27	/	/	/
	$[Cu_2(\mathbf{2})]^{4+}$	1:1	3.220(2)	2.543(4)	6.93	/	/	/
NCO^-	$[Cu(\mathbf{1})]^{2+}$	1:2	3.1(1)	-0.12(2)	4.18	2.9(2)	0.10(2)	4.10
	$[Cu_2(\mathbf{2})]^{4+}$	1:2	3.82(7)	-1.05(5)	4.16	3.4(4)	0.19(7)	4.77
CH_3COO^-	$[Cu(\mathbf{1})]^{2+}$	1:2	3.25(1)	-0.092(4)	4.33	2.18(2)	-1.51(1)	1.47
	$[Cu_2(\mathbf{2})]^{4+}$	1:2	3.9(1)	-1.6(9)	3.72	3.3(8)	a	a

^{a} reliable value cannot be calculated.

Compared to the mono-nuclear complex, the interactions between the di-nuclear complex and the same anionic species are characterized by higher equilibrium constants (log K_1 for eq.3). These larger values could be explained (i) on the basis of the larger positive charge of $[Cu_2(\mathbf{2})]^{4+}$ and (ii) also by taking into account also the statistical effect (i.e. number of binding sites) that is favorable to the di-copper(II) complex. Nevertheless, the variation of log K_1 between the two receptors strongly depends on the anion, being larger in the case of halides (about 2 order of magnitude) than for azide, acetate, and cyanate (about 0.6-0.7 log units, see Table 2). As a consequence, the affinity sequence of the di-nuclear complex significantly differs from that observed for the mono-nuclear analogue: $Cl^- > Br^- > I^- \sim CH_3COO^- \sim NCO^- > N_3^- \gg SCN^-, NO_3^-$.

In particular, all halides take the leading positions in the affinity sequence of $[Cu_2(\mathbf{2})]^{4+}$, with bromide overtaking acetate and cyanate and iodide surpassing azide. These relevant changes in the affinity of copper(II) bis-macrocyclic complex towards anions can be related to the ability of halides to interact with the di-nuclear species according to a bridging coordination mode, differently from acetate and cyanate. Therefore, the extra-stability displayed by the adducts formed by $[Cu_2(\mathbf{2})]^{4+}$ in the presence of Cl^-, Br^-, or I^-, can be explained on the basis of the anion advantage of occupying the room between the two metal centers, i.e. in terms of bimacrocyclic effect. Quite surprisingly, azide, that according to EPR data also interacts with $[Cu_2(\mathbf{2})]^{4+}$ by bridging the two copper(II) macrocyclic subunits, seems to not profit to the same extent as halides of the bimacrocyclic effect. In fact, the stability increase of $[Cu_2(\mathbf{2})N_3]^{3+}$ when compared to $[Cu(\mathbf{1})N_3]^+$ ($\Delta \log K_1 = 0.68$) is quite comparable to that observed for the analogue adducts of acetate and cyanate ($\Delta \log K_1 = 0.61$ and 0.72, respectively), which are bound only at the "external" coordination positions. It should be noted that when anions are bound between the two macrocyclic subunits a rearrangement of the receptor is needed in order to achieve the anion chelation. In the case of azide this rearrangement may require a more unfavorable energy contribution than halides, in order to have an inter-ring cavity fit for the triatomic guest and to fulfill the geometrical requirements associated with the hybridization of terminal donor atoms. As a consequence the overall stability of $[Cu_2(\mathbf{2})N_3]^{3+}$ is significantly reduced. Moreover, cyanate, which displays a similar geometry as N_3^- but is bit larger is not able to bind $[Cu_2(\mathbf{2})]^{4+}$ according to the bridging mode. These considerations support the important role of steric complementarity in the recognition of anionic guests by the di-copper complex.

When the interaction of $[Cu_2(\mathbf{2})X]^{3+}$ with a second equivalent of anion (eq. 4) is considered, interestingly, $\log K_2$ have similar (if not identical) values as $\log K_1$ found for the corresponding $[Cu(\mathbf{1})X]^+$ species. It is in agreement with the coordination mode of the second anion interacting with the di-copper(II) complex, which binds one metal center at an external position, similarly to the first anion interacting with the mononuclear complex.

All the interactions between the investigated anions and both copper(II) complexes are characterized by favourable entropy contributions (see Table 2). This result is explainable considering that the reagents are more solvated than the products, because the overall charge of the adducts decreases upon anion coordination (see eq. 1 and eq. 3) and, in addition, the complex-anion interaction decreases the surface available for the solvent interaction. In the case of anions that are coordinated according to a bridged mode (Cl^-, Br^-, I^-, and N_3^-) by $[Cu_2(\mathbf{2})]^{4+}$, $T\Delta S_1$ values are distinctly larger than the corresponding thermodynamic term obtained for the mono-nuclear complex. On the contrary,

equilibria involving acetate and cyanate are characterized by $T\Delta S_1$ values that are very similar both for mono- and di-nuclear complexes.

All enthalpy contributions concerning interactions of both complexes with chloride, bromide, iodide, and azide have positive values, suggesting that the endothermic desolvation prevails over the formation of exothermic coordination bonds. Moreover, an endothermic rearrangement of the bis-macrocyclic receptor toward a face-to-face structure should take place in order to interact with "bridging" anions. On the contrary, negative enthalpy changes were observed in the cases of cyanate and acetate, which are always coordinated at the "external" positions and do not require a particular rearrangement of the bis-macrocyclic complex.

Therefore, in the case of cyanate and acetate, the moderate stability increase of $[Cu_2(\mathbf{2})X]^{3+}$ when compared to $[Cu(\mathbf{1})X]^+$ has mainly an enthalpic nature, while the extra-stability that characterizes adducts formed by $[Cu_2(\mathbf{2})]^{4+}$ with "bridging anions" is especially due to a favorable entropy contribution. In particular, the nature of the bimacrocyclic effect in $[Cu_2(\mathbf{2})Br]^{3+}$ is exclusively entropic (di- and mono-copper complexes have the same ΔH_1, while $T\Delta S$ differs by 2.5 units) and it has both entropic and enthalpic origins in $[Cu_2(\mathbf{2})Cl]^{3+}$ and $[Cu_2(\mathbf{2})I]^{3+}$. The adduct of bimacrocyclic complex with azide also benefits from a favorable entropic effect but it is significantly mitigated by the enthalpic disadvantage, which could be due, as mentioned above, to a more difficult host rearrangement if compared to the analogous bridged halide species.

5.2.3   Spectrophotometric studies in DMSO

The affinity towards anions of both mono- and di-copper(II) complexes was also investigated through spectrophotometric titration experiments. Solutions of $[Cu(\mathbf{1})](ClO_4)_2$ and $[Cu_2(\mathbf{2})](ClO_4)_4$ in DMSO were titrated with standard solutions of the tetrabutylammonium (TBA^+) salts of the investigated anions (Cl^-, Br^-, I^-, N_3^-, NCO^-, CH_3COO^-, SCN^-, and NO_3^-). After each addition of sub-stoichiometric amounts of the anion, the UV-Vis spectrum of the solution was recorded. The titration data were fitted by means of a non-linear least-squares program,[49] in order to identify the species present at the equilibrium and to obtain the association constants (see Table 3). No significant spectral variations were observed upon the titration of both complexes with nitrate and thiocyanate, suggesting that weak interactions (if any) take place with these anions, as already observed during ITC experiments. As a consequence, no stability constants have been determined for the adducts with SCN^- and NO_3^-.

As an example, Figure 6 shows the UV-Vis spectra collected over the course of the titration of receptors $[Cu(\mathbf{1})]^{2+}$ and $[Cu_2(\mathbf{2})]^{4+}$ with TBABr, and the related distribution diagrams of species

present at the equilibrium (spectra and distribution diagrams obtained after titrations with (TBA)Cl, (TBA)I, (T BA)N$_3$, (TBA)NCO, and (TBA)CH$_3$COO are reported in Figure S6 of Supporting Information).

Table 3. Association constants (as logK values) for the interaction of [Cu(**1**)]$^{2+}$ and [Cu$_2$(**2**)]$^{4+}$ with anions (as TBA$^+$ salts) in pure DMSO at 25°C, determined by UV/Vis spectroscopy. Numbers in parentheses are standard deviations to the last significant figure.

Anion	Receptor	Fitting model	Log K_1[1]	Log K_2[2]
Cl$^-$	[Cu(**1**)]$^{2+}$	1:1	3.39(2)	/
	[Cu$_2$(**2**)]$^{4+}$	1:2	5.3(1)	3.0(3)
Br$^-$	[Cu(**1**)]$^{2+}$	1:1	2.94(3)	/
	[Cu$_2$(**2**)]$^{4+}$	1:2	4.8(2)	2.8(5)
I$^-$	[Cu(**1**)]$^{2+}$	1:1	2.12(2)	/
	[Cu$_2$(**2**)]$^{4+}$	1:2	3.89(4)	<1(a)
N$_3$$^-$	[Cu(**1**)]$^{2+}$	1:1	2.98(5)	/
	[Cu$_2$(**2**)]$^{4+}$	1:1	3.41(2)	/
NCO$^-$	[Cu(**1**)]$^{2+}$	1:1	3.67(3)	/
	[Cu$_2$(**2**)]$^{4+}$	a	a	a
CH$_3$COO$^-$	[Cu(**1**)]$^{2+}$	a	a	a
	[Cu$_2$(**2**)]$^{4+}$	a	a	a

[a] Reliable value cannot be calculated.

Both complexes display a band centered at 533 nm, due to the Cu(II) d-d transition. As expected, this band in the di-nuclear complex ($\varepsilon = 228$ M^{-1}cm^{-1}) is about twofold more intense than in the mono-nuclear analogue ($\varepsilon = 98$ M^{-1} cm^{-1}). In both complexes, the addition of Br$^-$ causes a redshift of the band, which also undergoes a slight intensity increase. In the case of [Cu(**1**)]$^{2+}$ the best fitting of the titration data are obtained by assuming the occurrence of only one equilibrium, corresponding to the formation of 1:1 adduct (eq. 2). The formation of [Cu(**1**)Br$_2$], which was observed in the corresponding ITC titrations, likely does not result in detectable spectral changes. A similar behavior was observed when [Cu(**1**)]$^{2+}$ was titrated with Cl$^-$, I$^-$, N$_3$$^-$, and NCO$^-$.

Considering the [Cu$_2$(**2**)]$^{4+}$ complex, data fitting indicates that two equilibria take place in the presence of bromide, corresponding to the formation of [Cu$_2$(**2**)Br]$^{3+}$ and [Cu$_2$(**2**)Br$_2$]$^{2+}$ species (see diagram of species distribution, Figure 6b). The occurrence of two analogous stepwise equilibria (eq. 3 and 4) is suggested also for the interaction of the di-copper complex with chloride and iodide, while only the formation of 1:1 adduct can be hypothesized in the case of azide. The results are coherent with the ITC experiments. It should be noted that titration data related to the interactions of NCO$^-$ with [Cu$_2$(**2**)]$^{4+}$ and of CH$_3$COO$^-$ with both complexes did not provide reliable fittings, not allowing determination of the corresponding stability constants.

The results obtained by UV-Vis titrations are in good agreement with those found by ITC experiments (see Tables 2 and 3), although some stability constants cannot be determined by spectrophotometric titrations due to the poorly intense corresponding spectral variations. In particular, the differences between $\log K_1$ values determined for $[Cu_2(2)]^{4+}$ and $[Cu(1)]^{2+}$ when interacting with "bridging" anions are similar to those obtained by ITC. It confirms that the di-copper(II) complex, thanks of its "chelating" ability, provides an extra-stability (bimacrocyclic effect) to the adducts with anionic guests that fit the room between the two macrocyclic subunits and coordinate the two copper(II) ions according to the bridging mode.
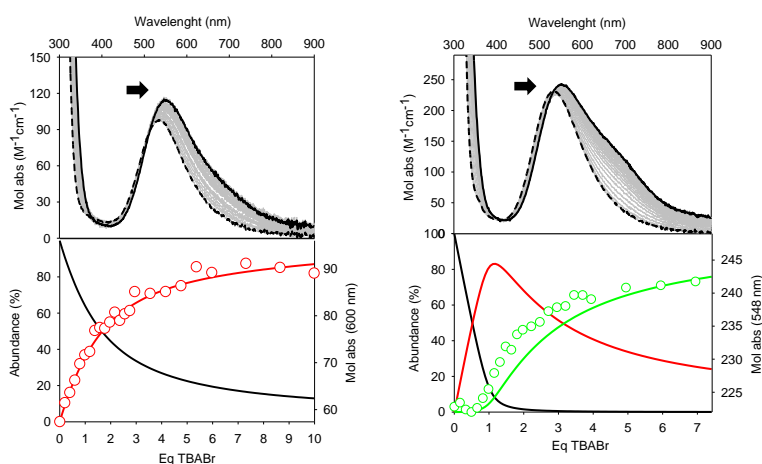
Figure 6. a) Absorption spectra taken over the course of the titration of $[Cu(1)](ClO_4)_2$ (1.02 mM in DMSO) with a solution of the (TBA)Br (0.5 mM in DMSO), and the related distribution diagram of species present at the equilibrium (black line: free $[Cu(1)]^{2+}$; red line: $[Cu(1)Br]^+$; red circles: superimposed plots of molar absorptivity (at 600 nm) versus the equivalent ratio Br⁻/complex, T = 25°C). b) Absorption spectra taken over the course of the titration of $[Cu_2(2)](ClO_4)_4$ (1.015 mM in DMSO) with a solution of the (TBA)Br (0.5 mM in DMSO), and the related distribution diagram of species present at the equilibrium (black line: free $[Cu_2(2)]^{4+}$; red line: $[Cu_2(2)Br]^{3+}$; Green line: $[Cu_2(2)Br_2]^{2+}$; circles: superimposed plots of molar absorptivity (at 548 nm) versus the equivalent ratio Br⁻/complex, T = 25°C).

5.2.4 Calorimetric and potentiometric studies in aqueous solution

Before studying the interaction between bimacrocyclic complex and anionic guests in water, we carried out potentiometric studies on $[Cu_2(2)]^{4+}$ in order to evaluate the possible competition of hydroxide anions for the Cu(II) binding sites. Potentiometric titration performed on $[Cu_2(2)](ClO_4)_4$ in water and further treatment of titration data with non-linear regression methods allowed determining the stability constants of species formed in the 2-14 pH range, and drawing the corresponding distribution diagram, in which the percentage of each species is plotted as a function of pH (Figure 7).

It should be noted that the di-copper(II) complex is stable toward demetallation even in distinctly acidic solutions due to the known inertness of macrocyclic complexes. On increasing pH from 2 to 12, two deprotonation processes can be observed, which are ascribed to the deprotonation of coordinated water molecules and provide the species $[Cu_2(\mathbf{2})OH]^{3+}$ (pKa = 9.41) and $[Cu_2(\mathbf{2})(OH)_2]^{2+}$ (pKa = 10.99). It can be reasonably postulated that the first deprotonation involves a H_2O molecule between the two macrocyclic subunits and, consequently, in $[Cu_2(\mathbf{2})OH]^{3+}$ hydroxide interacts with both metal centers.
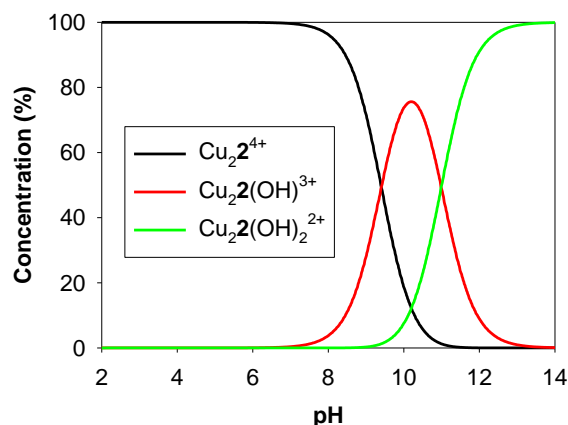
Figure 7. Distribution diagram of the species present at the equilibrium for a solution 5 x 10^{-3} M of $[Cu_2(\mathbf{2})](ClO_4)_4$, over the pH range 2-14, in H_2O at 25°C.

Based on the distribution diagram obtained by potentiometric titration data, $[Cu_2(\mathbf{2})]^{4+}$ is the main species at neutral pH values (99.0 % at pH = 7.4). Analogue experiments on the mono-nuclear complex showed that $[Cu(\mathbf{1})]^{2+}$ is the only species at pH values close to 7. Therefore, calorimetric studies in water have been performed in neutral buffered solution (pH = 6.8) of both mono- and di-nuclear complexes, in order to avoid any competition by coordinated hydroxide.

In a typical ITC experiment, a solution of the receptor in HEPES 0.05M was titrated by a solution of the sodium salt of the investigated anion, in the same solvent. NaCl, NaBr, NaI, NaN$_3$, NaNCO, NaHCO$_3$, NaCH$_3$COO, NaNO$_3$, NaH$_2$PO$_4$ and Na$_2$SO$_4$ have been used as titrants. The titrations with $[Cu(\mathbf{1})]^{2+}$ did not evidence any interaction (*i.e.* no heat variations could be detected), suggesting that in these conditions the $[Cu(\mathbf{1})]^{2+}$-anion association constants are excessively low. Calorimetric titration experiments also suggested that interactions between $[Cu_2(\mathbf{2})]^{4+}$ and HCO_3^-, CH_3COO^-, NO_3^-, and $H_2PO_4^-$ are too week in water to allow determination of logK values. Figure 8 reports the thermograms and the ITC profiles corresponding to the ITC titration of receptors $[Cu_2(\mathbf{2})]^{4+}$ with Br^-, and N_3^-, (data for Cl^-, I^-, NCO^- and SO_4^{2-} in Figure S7 of the Supporting Information). The best

fitting of the titration data was obtained in all cases by assuming the occurrence of one equilibria, corresponding to the formation of 1:1 adducts. The thermodynamic parameters (logK, ΔH, TΔS) determined by fitting of titrations curves in water are collected in Table 4.
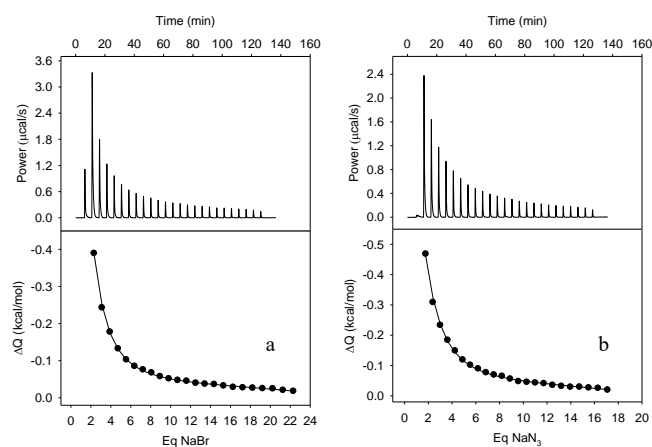
Figure 8. ITC profiles taken over the course of the titration of $[Cu_2(\mathbf{2})](ClO_4)_4$ (1.043 mM) in aqueous solution (HEPES 0.5 M) with aqueous solutions of: (a) NaBr (66.48 mM); (b) NaN_3 (50.99 mM). Circles: experimental data; line: fitting profile (one site model); receptor in the cell; T = 25°C.

The more competitive character of water, compared to DMSO, significantly affects the interaction between complexes and anions. In fact, the mono-nuclear complex does not interact (or interacts very weakly) with anionic species, *i.e.* the desolvation energy is excessively unfavorable for all of the considered anionic species. For the same reason interactions of the di-nuclear complex are considerably less strong in water than in DMSO. In particular, the formation of 1:1 adducts in water can be detected only with anions that were observed to coordinate according to the bridging mode, profiting from the bimacrocyclic effect, while 1:2 adducts were not detected in any titration experiment, differently from what observed in DMSO. Moreover, the stability constants, when determined, are considerably lower in water than in DMSO (for instance, log K_1 for chloride decreases by more than 2 log units).

Table 4. Thermodynamic parameters at 25°C obtained from fitting of ITC titration curves of $[Cu_2(\mathbf{2})](ClO_4)_4$ in aqueous solution (HEPES 0.05 M, pH = 6.8). Numbers in parentheses are standard deviations.

Anion	Log K_1	ΔH_1 [Kcal mol^{-1}]	$-T\Delta S_1$ [Kcal mol^{-1}]
Cl$^-$	3.15(2)	-0.79(1)	-3.53
Br$^-$	3.14(1)	-3.05(6)	-1.79
I$^-$	3.41(2)	-5.66(2)	1.01
N$_3^-$	2.88(1)	-2.55(5)	-1.95
NCO$^-$	2.30(1)	-1.28(3)	-1.85
HCO$_3^-$	<1(a)	a	a
CH$_3$COO$^-$	b	b	b
H$_2$PO$_4^-$	<1(a)	a	a
SO$_4^-$	3.10(1)	1.531(9)	-5.75

^{a} Reliable value cannot be calculated. ^{b} No heat effect was observed in the ITC measurements

On comparing thermodynamic quantities for the interaction of a given anion with the bimacrocyclic complex, whether in DMSO or in water (Table 3 and 4), we observe a quite surprising behavior. In DMSO complexation processes are in general endothermic and driven by a largely positive entropy change, whereas in water all processes are exothermic and characterized by moderately positive entropy contributions. This may seem paradoxical, if one considers that water is, generally speaking, a much more solvating medium than DMSO, thus anion complexation in an aqueous solution should be accompanied by a more significant desolvation of both anion and receptor, which should lead to a higher endothermicity than in DMSO. Uv-vis spectra of $[Cu_2(\mathbf{2})](ClO_4)_4$ measured in DMSO and in water display the d-d band maximum at 533 and 518 nm, respectively (see Figure S8). It has been observed that in five-coordinate complexes $[Cu^{II}(tetramine)X]^+$ the higher the Cu^{II}–X interaction, the more pronounced the red-shift of the absorption band.[30] This suggests that interaction of copper ions with apically coordinated solvent molecules is stronger in DMSO than in water. Therefore, the replacement of coordinated solvent molecules by anionic substrates at the apical positions is distinctly more endothermic in DMSO than in water and it is this term that makes anion complexation in DMSO endothermic and in water (Hepes 0.05M, pH = 6.8) exothermic. However, in spite of the exothermicity, complexation in water is less favored than in DMSO (log K values are smaller). This results from a more favorable balance of solvation and desolvation terms. In other words, DMSO is a more coordinating ligand than water (towards Cu^{II}), but it is a lower solvating medium.

The relevance of solvation/desolvation processes in the interaction between $[Cu_2(\mathbf{2})]^{4+}$ and anions can be pointed out for instance by considering the thermodynamic data corresponding to the halide series. In DMSO the stabilities of adducts $[Cu_2(\mathbf{2})X]^{3+}$ follow the sequence Cl$^-$ > Br$^-$ > I$^-$, while the

corresponding log K_1 determined in water indicate an almost opposite sequence ($I^- > Cl^-$, Br^-). This can be explained by taking into account that iodide has the lowest hydration enthalpy in the halide series and, as consequence, its coordination to the bimacrocyclic complex is the most exothermic (Table 4). The direct relationship between hydration enthalpy of halides and formation enthalpy of $[Cu_2(2)X]^{3+}$ ($X = Cl^-$, Br^-, I^-) is graphically represented in Figure 9.[78]
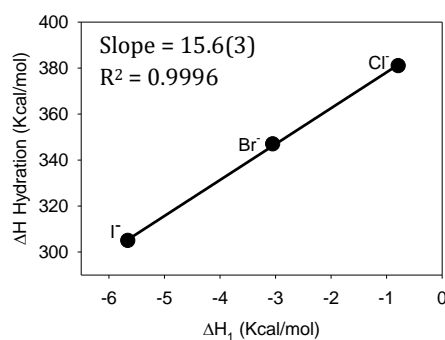
Figure 9. Correlation between the halide hydration enthalpy[78] and the enthalpy contribution determined for the $[Cu_2(2)]^{4+}$/halide interaction.

5.2.5 Unexpected case of bisulfate

The figure 10 shows the EPR spectra on frozen DMSO (117 K) solution of $[Cu(1)](ClO_4)_2$ and $[Cu_2(2)](ClO_4)_4$ in the presence of increasing amount (0, 0.5, 1, 2, 7 equivalents) of bisulfate. The spectra collected for $[Cu(1)]^{2+}$ show the typical four-line pattern in the g parallel region (Figure 11a) expected for coupling of electron with the 3/2 spin of a copper(II) nucleus. The Spectra of $[Cu_2(2)]^{4+}$ show, in presence of HSO_4^-, a two septuplets pattern in parallel region (figure 11b) analogous to the one observed for those anions (Cl^-, Br^-, I^-, N_3^-), that have been observed to bridge the two metal centers.
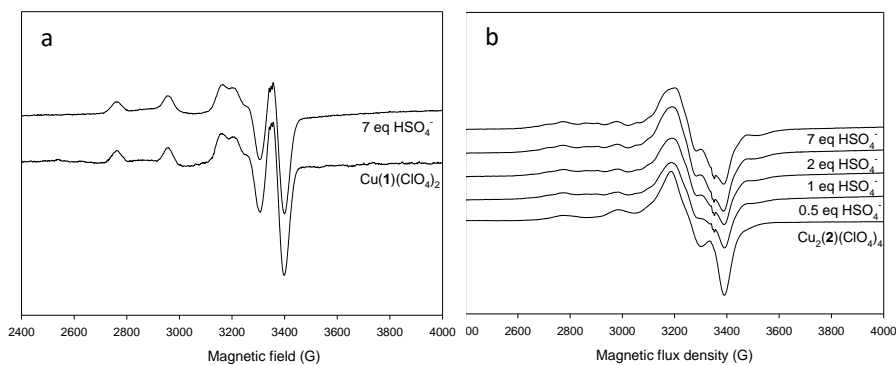
Figure 10. (a) Family of EPR spectra of the complex $[Cu(1)](ClO_4)_2$ with 0 and 7 equivalent of hydrogen sulfate, (b) family of EPR spectra of the complex $[Cu_2(2)](ClO_4)$ with 0, 0.5, 1, 2, and 7 equivalents of bisulfate.

A strong proof of the inner coordination of HSO_4^- between the two metal centers is given by the molecular crystal structure of $[Cu^{II}_2(2)(\mu_2\text{-}HSO_4)(HSO_4)_2]HSO_4 \cdot EtOH \cdot H_2O$, shown in figure 11. $[Cu_2(2)]^{4+}$ is able to accommodate a bisulfate anion between the facing cyclam units. The two HSO_4^- outside the cavity are coordinated very weakly to the copper centers with a bond length of 2.74 Å, whereas the one inside the cavity presents two donor oxygen atoms, forming two coordinative Cu-O interactions with a length of 2.38 Å. This latter short distance, indicate a strong receptor-anion interaction, favored by the good fitting between bisulfate bite length and cavity size. Furthermore, a third oxygen atom is placed between two NH groups of the cyclam rings, thus further favoring the coordination of this anion inside the cavity by forming hydrogen bond interactions with the receptor (see figure 11).

A more detailed discussion of the $[Cu^{II}_2(2)(\mu_2\text{-}HSO_4)(HSO_4)_2]HSO_4 \cdot EtOH \cdot H_2O$ crystal structure is described in the X-ray crystallographic section.
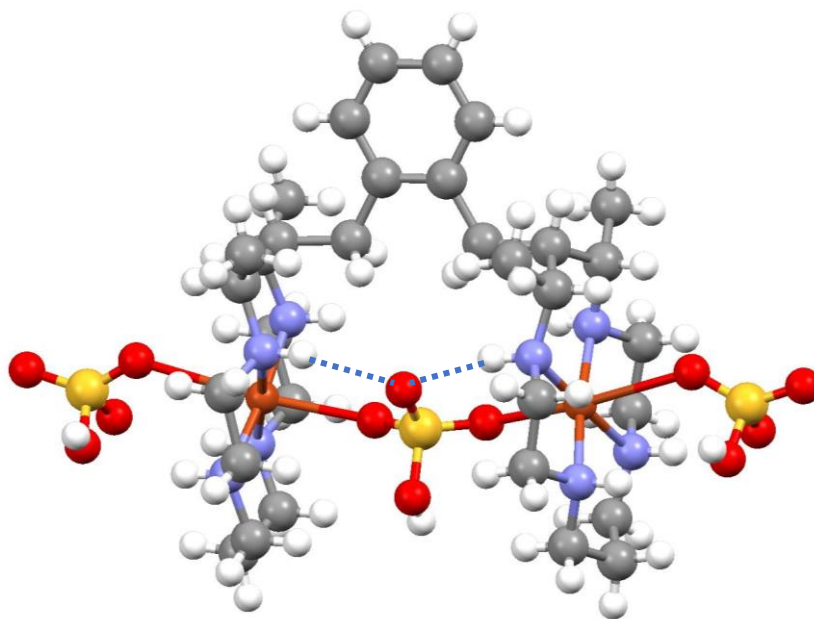
Figure 11. A simplified sketch of $[Cu^{II}_2(2)(\mu_2\text{-}HSO_4)(HSO_4)_2]^+$ molecular cations. The Cu^{II}-O distances are 2.38(1) Å inside the dimer and 2.74(1) Å outside; the Cu(II)-Cu(II) distance is 6.90(1) Å; the two hydrogen bonds distances, between the amine hydrogen and an oxygen atom of HSO_4^-, NH-HSO_4^-, represented with blue dotted line, are 2.23(1) Å.

ITC and UV-vis titration of DMSO solutions of $[Cu(1)](ClO_4)_2$ and $[Cu_2(2)](ClO_4)_4$ with TBAHSO4 were performed, using the same procedure carried out with the other investigated TBA salts. Figure 12 reports the thermograms corresponding to the to the ITC titration of receptors $[Cu(1)](ClO_4)_2$ and $[Cu_2(2)](ClO_4)_4$ with TBAHSO4 (for ITC profiles see Figure S11 in the Supporting Information).
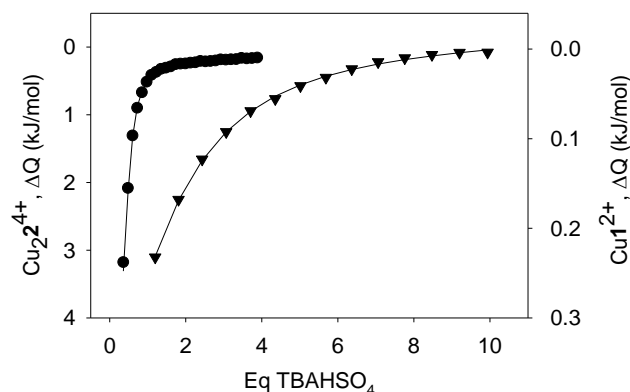
Figure 12. ITC profiles taken over the course of the titration of a solution of Cu1(ClO$_4$)$_2$ (5.13 mM) (black triangles) and a solution of [Cu$_2$(**2**)](ClO$_4$) (1mM) (black spheres) in DMSO with a solution respectively of TBAHSO$_4$ (100mM) and TBAHSO$_4$ (20mM).

The best fitting of the ITC data has been obtained by assuming the occurrence of one equilibrium, corresponding to the formation of 1:1 complex for the mononuclear receptor [Cu(**1**)]$^{2+}$ (equilibrium 5). For the receptor [Cu$_2$(**2**)]$^{4+}$, the binding constant is excessively high to be determined in these conditions, but the formation of a 1:1 complex is clearly visible from the titration curve, in accordance with (equilibrium 6). A similar trend was obtained from UV-vis titrations (for UV-vis absorption spectra and molar absorptivity vs added anion eq. see Figure S12 in the Supporting Information).

$$Cu(\mathbf{1})^{2+} + HSO_4^- \rightleftharpoons [Cu(\mathbf{1})(HSO_4)]^+ \tag{5}$$
$$Cu_2(\mathbf{2})^{4+} + HSO_4^- \rightleftharpoons [(Cu_2(\mathbf{2})(HSO_4)]^{3+} \tag{6}$$

Table **7** collects the thermodynamic parameters (log$K$, ΔH, -TΔS) at 25°C obtained from fitting of ITC and UV-vis titrations curves of receptors [Cu**1**](ClO$_4$)$_2$ and [Cu$_2$(**2**)](ClO$_4$)$_4$ with TBAHSO$_4$. As already seen for the ITC titration, also the UV-vis titration profiles confirmed that the [Cu$_2$(**2**)]$^{4+}$-HSO$_4^-$ association constant is excessively high and a reliable value cannot be obtained in these conditions (1 mM [Cu$_2$(**2**)]$^{4+}$). For this reason, we assigned a log $K_1 > 6$ to the [Cu$_2$(**2**)]$^{4+}$-HSO$_4^-$ interaction.[79]

76

Table 7. Thermodynamic parameters at 25°C obtained from fitting of ITC and UV-vis titrations curves of receptors [Cu(**1**)](ClO$_4$)$_2$ and [Cu$_2$(**2**)](ClO$_4$)$_4$ with TBAHSO$_4$ in DMSO. Numbers in parentheses are standard deviations.

Anion	Receptor	Fitting model	Log K_1 (ITC)	Log K_1 (UV-vis)	ΔH$_1$ [Kcal mol^{-1}]	-TΔS$_1$ [Kcal mol^{-1}]
HSO$_4^-$	Cu**1**$^{2+}$	1:1	2.03(1)	(a)	1.09(1)	-3.87
HSO$_4^-$	Cu$_2$**2**^{4}	1:1	> 6 (b)	> 6 (b)	/	/

^{a} no UV-vis spectrum changing. ^{b} estimated value on the base of the trend curve.

5.2.6 X-ray crystallography

Slow evaporation of an aqueous solution of [Cu$_2$(**2**)](ClO$_4$)$_4$ in the presence of excess NaBr provided crystals of the corresponding bromide salt of the di-nuclear complex. The molecular structure of the [Cu$_2$(**2**)(μ-Br)Br]$^{2+}$ cation occurring in the complex salt in shown in Figure 13; a plot showing thermal ellipsoids is drawn in Figure S9.
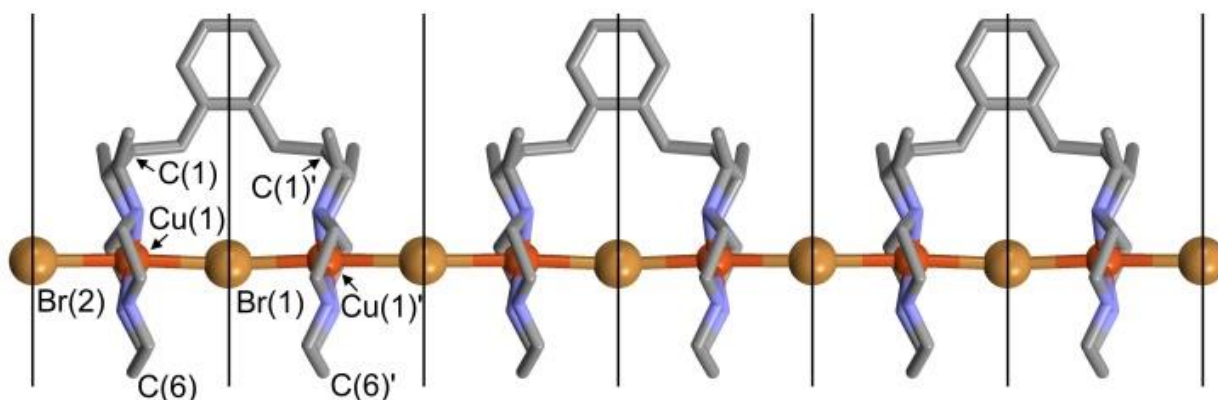
Figure 13. A simplified sketch of the [Cu$_2$(**2**)(μ-Br)Br]$^{2+}$ cations originating, at the solid state, molecular chains maintained by intermolecular Cu^{II}-Br$^-$ bond interactions (crystallographic mirror planes normal to the plane of projection of the figure are drawn with solid lines; atom names are reported only for selected atom positions). The Cu^{II}-Br- distances are 2.92(1) Å inside the dimer and 2.98(1) Å outside; the C(1)-C(1)', Cu(1)-Cu(1)' and C(6)-C(6)' separations are 5.91(1), 5.83(1), and 5.74(1) Å, respectively. Symmetry code: (') = x, 1-y, z.

The face-to-face bicyclam ligand exhibits a perfect C_s molecular symmetry, because a crystallographic mirror plane passes in the middle of the ortho-xylyl spacer. The two facing dimethyl-cyclam moieties result symmetrically equivalent and are arranged in a trans-III (RRSS) configuration. The metal centers are a bit displaced from the best plane of the chelate amines, being placed at 0.06(1) Å from the equatorial N4 plane and pointing inside the cavity formed by the two macrocyclic

subunits. The observed mean Cu^{II}-N distance of 2.03(1) Å corresponds to the expected value for a strain-free Cu-N bond in tetra-aza macrocycles.[80] The Cu^{II} coordination of each metal center is completed by two Br^- ions placed in the axial positions of a rather elongated octahedron. Being the Cu^{2+} ions slightly displaced towards the inside of the face-to-face bicyclam ligand, the two Cu^{II}-Br^- distances result asymmetric: a value of 2.92(1) Å occurs inside the cavity whereas a value of 2.98(1) Å occurs outside. $Cu^{II}\cdots Cu^{II}$ separation (5.83(1) Å) is in good agreement the distance determined by EPR measurements. Moreover, it is very similar to that observed for $Ni^{II}\cdots Ni^{II}$ (5.86 Å) in the crystallographic study performed at 100K on the analogous complex $[Ni_2(\mathbf{2})]^{4+}$, that contains both low-spin square planar and a high-spin axially elongated octahedral Ni^{II} coordination centers.[43] From the point of view of receptor ability, the di-copper complex should have an advantage compared to the di-nickel analogue, because the first one is able to coordinate the bridging anion simultaneously by the two metal centers, whereas the second one coordinates the bridging anion mainly by one high-spin nickel(II) ion.

Both the bromide ions placed in the inner and outer positions are placed on two crystallographic mirror planes and bridge two Cu^{II} metal centers, with almost linear two-fold coordination. The observed Cu^{II}-Br^- distance and the Cu^{II}-Br^--Cu^{II} angle and the $Cu^{II}\cdots Cu^{II}$ separation are 2.92(1) Å, 171.7(1)°, and 5.83(1) inside the dimer and 2.98(1) Å, 170.9(1)°, and 5.94(1) Å outside, respectively. At the solid state, these interactions originate infinite molecular chains of dinuclear complexes extending along the direction of the b crystallographic axis (Figure 13). Consequently, both the Cu^{II} centers of the bimacrocyclic complex $[Cu_2(\mathbf{2})(\mu\text{-}Br)Br]^{2+}$ display an octahedral coordination environment very similar to the one observed in the molecular structure of $[Cu^{II}(cyclam)Br_2]$ (mean equatorial Cu^{II}-N distance 2.02 Å, long axial Cu^{II}-Br^- distances of 2.95 Å).[81]

Due to the monoatomic nature of the bromide ion, the dinuclear complex maintains the two facing cyclam moieties close each other. This closed arrangement can be emphasized observing, for instance, the values for the C-C distance between the two symmetrically equivalent C(1) cyclam atoms (connected by the spacer), the Cu-Cu distance and the C-C distance between the two symmetrically equivalent distal C(6) cyclam atoms (Figure 13). These values are 5.91(1), 5.83(1), and 5.74(1) Å, respectively.

The crystal and molecular structure of the $[Cu^{II}_2(\mathbf{2})(\mu_2\text{-}HSO_4)(HSO_4)_2]^+$ molecular cation occurring in the $[Cu^{II}_2(\mathbf{2})(\mu_2\text{-}HSO_4)(HSO_4)_2]HSO_4 \cdot EtOH \cdot H_2O$ crystal is shown in Figure 14. A plot showing thermal ellipsoids is drawn in Figure S14. The crystals of $[Cu^{II}_2(\mathbf{2})](HSO_4)_4$ were obtained by slow diffusion of EtOH in a solution of $[Cu^{II}_2(\mathbf{2})](ClO_4)_4$ in MeCN with an excess of TBAHSO$_4$. Also in

this case, the bicyclam ligand exhibits a perfect C_s molecular symmetry, with the two facing cyclam moieties symmetrically equivalent and arranged in a *trans-III* (RRSS) configuration. The metal centers remain a bit displaced from the best plane of the chelate amines (being placed at 0.08(1) Å from the equatorial N_4 plane and pointing inside the dimer), and the observed mean Cu^{II}-N distance of 2.02(1) Å does not significantly differ from the strain-free value observed in the bromide compound.

However, in the bisulfate compound, the facing cyclam moieties of the dimetallic ligand are strongly divergent: the C-C distance between the two symmetrically equivalent C(1) cyclam atoms connected by the spacer remains the same as in the bromide compound [5.91(1) Å], whereas the Cu-Cu distance and the C-C distance between the two symmetrically equivalent distal C(6) cyclam atoms increase from the values of 5.83(1) and 5.74(1) Å in the bromide compound to the values of 6.90(1) and 8.22(1) Å in the bisulfate compound. This opened arrangement emphasizes the great flexibility of the dimetallic ligand (**2**), that results able to increase the space between the facing cyclam units in order to accommodate a polyatomic bisulfate ion. This latter bridges the two metal centers *via* two O atoms, originating two equivalent Cu-O bonds of 2.38(1) Å. The asymmetrically elongated octahedral coordinations of the two metal centers are completed by two O atoms of two bisulfate ions placed in the outer positions of the bicyclam ligand, bonded through long Cu-O bonds of 2.74(1) Å.

At the solid state, the bisulfate ions outside the ligand do not connect directly two metal centers and the supramolecular chains observed for the bromide compound do not occur. Connections between adjacent ligands are provided by supramolecular OH···O interaction occurring between the OH groups of bisulfate ions (H-donor) and the O atoms of adjacent bisulfate ions or of methanol solvent molecules (H-acceptor). Further connections are provided by NH···O interactions involving the secondary amines (H-donor) and the O atoms of adjacent bisulfate ions (H-acceptor). A possible H-bond motif, resulting from the assigned positions of H atoms belonging to bisulfate ions and ethanol molecules, is shown in Figure S15.
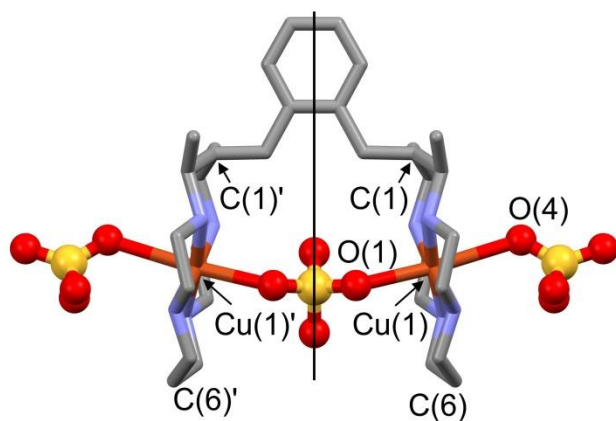
Figure 14. A simplified sketch of $[Cu^{II}_2(2)(\mu_2\text{-}HSO_4)(HSO_4)_2]^+$ molecular cations (crystallographic mirror plane normal to the plane of projection of the figure is drawn with solid lines; H atoms and additional $(HSO_4)^-$ ion, EtOH and water solvent molecules were omitted for clarity; atom names are reported only for selected atom positions). The $Cu^{II}\text{-}O$ distances are 2.38(1) Å inside the dimer and 2.74(1) Å outside; the C(1)-C(1)', Cu(1)-Cu(1)' and C(6)-C(6)' separations are 5.91(1), 6.90(1), and 8.22(1) Å, respectively. Symmetry code: (') $= x, y, {}^3/_2\text{-}z$.

5.2.7 Conclusion

Dimetallic complex $[Cu_2(2)](ClO_4)_4$ can coordinate anions in two ways, as demonstrated by EPR, inside the cavity and outside the cavity. The interaction between the dimetallic complex $[Cu_2(2)](ClO_4)_4$ and "bridged anions" is characterized by an advantage in term of binding constant compared to the interaction with the related monometallic complex $[Cu(1)](ClO_4)_2$, thanks to the bismacrocyclic effect, which is refers to the anion advantage of occupying the room between the two macrocyclic subunits. Especially, the first association constants between dimetallic complex $[Cu_2(2)]^{4+}$ and halides are about two logarithmic units higher than the corresponding $[Cu(1)]^{2+}$ association constants. Even more surprisingly, receptor $[Cu_2(2)]^{4+}$ strongly interacts with bisulfate, a poorly coordinating anion, with an at least four logarithmic units higher association constant than $[Cu(1)]^{2+}$. Only with cyanate and acetate the two receptors show similar binding constants due to the inability of these anion to assume a bridged coordination between the two metal centers. As a result, the affinity sequence of the mononuclear receptor for the considered anions ($Cl^- > CH_3COO^- > NCO^- > Br^- > N_3^- > I^- \sim HSO_4^-$) is strongly different from that observed for the dinuclear receptor ($HSO_4^- > Cl^- > Br^- > I^- \sim NCO^- \sim CH_3COO^- > N_3^-$), shown in figure 15. It proves that the affinity for $[Cu_2 2](ClO_4)_4$ is not simply dictated by donor proprieties of the anion, but is also controlled by the geometrical and steric complementary of the receptor and the anion.

The nature of the bismacrocyclic effect is both enthalpic and entropic, with a major contribute of

entropy, as can be seen from ITC results, indeed when the anion enters inside the cavity its solvation molecules are released (entropic effect) and it is coordinated by two metal centers at the same time, which is less solvated than outside (enthalpic effect). A further enthalpic effect could come from the hydrogen bonds between the amine hydrogens pointed toward the inside of the cavity and adequate oxoanions, as observed for HSO_4^-.

Apparently, cyanate and acetate don't profit from the bismacrocylic effect. They are more likely coordinated outside the cavity as suggested by EPR experiments. Their small advantage in term of binding constant (compared to the related monometallic complex) is probably due to the higher total charge and larger number of binding sites.

Even though its much more endothermic interaction with $[Cu_2(2)](ClO_4)_4$ compared to $[Cu(1)](ClO_4)_2$, azide is able to assume a bridged coordination inside the dimetallic receptor cavity, thanks to the entropic contribution of the bismacrocyclic effect.

Figure 15. Receptor – anion $LogK_1$ trend comparison between $[Cu_2(2)](ClO_4)_4$ and $[Cu(1)](ClO_4)_2$. Black circles: $LogK_1$ for $[Cu(1)X]^+$ complexes, X = Cl⁻, Br⁻, I⁻, N_3^-, NCO⁻, CH_3COO^-, HSO_4^-; black circles: $LogK_1$ for $[Cu_2(2)X]^{3+}$ complexes, X = Cl⁻, Br⁻, I⁻, N_3^-, NCO⁻, CH_3COO^- and HSO_4^-.

Unlike the monometallic complex $[Cu(1)](ClO_4)_2$, the dimetallic complex $[Cu_2(2)](ClO_4)_4$, is still able to coordinate some anions in water, with a binding constant high enough to be measured by ITC titrations, thanks to the bismacrocyclic effect, higher total charge, and statistical advantage. The nature of the $[Cu_2(2)]^{4+}$-anion interaction in water depends on the anion hydration enthalpy, the lower it is the more negative is the enthalpy change, with a maximum exothermicity for iodide and a maximum endothermicity for sulfate.

Thanks to the particular ability of $[Cu_2(\mathbf{2})](ClO_4)_4$ to coordinate anions in two different ways, either inside or outside its cavity, it is possible to easily switch on and off the metal-metal interaction, simply by changing the anion used. With perchlorate as a counter ion, there is no metal-metal interaction as can be seen from EPR spectra, while with halides, bisulfate and azide the two unpaired electrons are delocalized on both metal centers. With cyanate and acetate the spin-spin coupling remains off. Thanks to the particular magnetic proprieties and high affinity for specific anions of $[Cu_2(\mathbf{2})](ClO_4)_4$, further investigations of its use as molecular magnet and catalyst are under way in our laboratory.

5.3 Experimental section

5.3.1 General Procedures and Materials

All reagents and solvents were supplied by Aldrich and used as received. TBA^+ salts were all greater than 98% pure and dried in vacuo overnight before use. DMSO (ACS reagent, ≥ 99.9 %) and aqueous solution of Hepes 0.05M have been degassed under vacuum before use. Mass spectra were acquired on a Thermo-Finnigan ion-trap LCQ Advantage Max instrument equipped with an ESI source.

5.3.2 Synthesis

Both $[Cu^{II}(\mathbf{1})](ClO_4)_2$ and $[Cu^{II}_2(\mathbf{2})](ClO_4)_4$ were prepared through 3 steps:

- Synthesis of the $[Ni^{II}(\mathbf{1})](ClO_4)_2$ and $[Ni^{II}_2(\mathbf{2})](ClO_4)_4$;

- demetallation of $[Ni^{II}(\mathbf{1})](ClO_4)_2$ and $[Ni^{II}_2(\mathbf{2})](ClO_4)_4$ in order to obtain the free ligands $\mathbf{1}$ and $\mathbf{2}$;

- metalation of free ligands $\mathbf{1}$ and $\mathbf{2}$ with $Cu(ClO_4)_2 \cdot 6H_2O$ to obtain $[Cu^{II}(\mathbf{1})](ClO_4)_2$ and $[Cu^{II}_2(\mathbf{2})](ClO_4)_4$.

[(5,7-Dimethyl-6-benzyl-1,4,8,11-tetraazacyclotetradecane), ($\mathbf{1}$*).* The ligand was prepared according to a previously described procedure.[65]

α,α'-Bis[(5,7-dimethyl-1,4,8,11- tetraazacyclotetradecan-6-yl)-o-xylene, (*$\mathbf{2}$*).* $[Ni^{II}_2(\mathbf{2})](ClO_4)_4$ (0.4 g, 0.37 mmol) was dissolved in a solution of NaOH 1M (3.5 mL) and DMSO (3.5 mL), and 100 equiv of NaCN (1.81 g, 37mmol) was added slowly. The solution was refluxed for 3 h, during which time it became firstly pink and then yellow. The solution was then cooled to room temperature and placed in a refrigerator overnight. White crystals were collected by filtration from the pale-yellow solution

and recrystallized in NaOH 1M. Yeld: 0.1 g (50%). MS (CH$_3$OH, ESI): *m/z* 280.24 (100 %, [(**2** + 2H$^+$)]$^{2+}$).
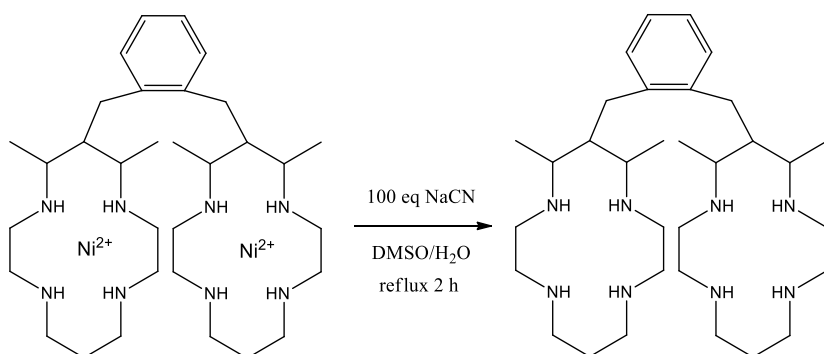
[(5,7-Dimethyl-6-benzyl-1,4,8,11-tetraazacyclotetradecane)-copper(II)] *Perchlorate*, [(Cu^{II}(**1**)](ClO$_4$)$_2$. Free ligand **1** (0.06 g, 0,19 mmol) was partially dissolved in MeOH (10 mL) HClO$_4$ 3M (1 mL) and an excess of Cu(ClO$_4$)$_2$·6H$_2$O (0.8 g, 2.2 mmol) was added. The solution was refluxed for 2 h. A purple-colored precipitate formed. The solution was then cooled to room temperature. The purple powder was collected by filtration and recrystallized in MeOH. Yield: 0.11 g (~100 %). MS (CH$_3$OH, ESI): *m/z* 190.69 (100 %, [Cu^{II}(**1**)]$^{2+}$), 380.35 (20 %, [Cu^{II}(**1**) - H$^+$]$^+$). UV−vis [DMSO, λ_{max} nm (ε, M^{-1} cm^{-1})]: 535 (98).

α,α'-Bis[(5,7-dimethyl-1,4,8,11-tetraazacyclotetradecan-6-yl)-copper(II)]-o-xylene *Perchlorate*, [(Cu$^{II}_2$(**2**)](ClO$_4$)$_4$. Free ligand **2** (0.1 g, 0,18 mmol) was partially dissolved in MeOH (20 mL) HClO$_4$ 3M (1 mL) and an excess of Cu(ClO$_4$)$_2$·6H$_2$O (1.5 g, 0.4 mmol) was added. The solution was refluxed for 2 h. A purple-colored precipitate formed. The solution was then cooled to room temperature. The purple powder was collected by filtration and recrystallized in MeOH. Yield: 0.19 g (~100 %). MS (CH$_3$OH, ESI): *m/z* 391.19 (100 %, [Cu$_2^{II}$(**2**) - H$^+$ + ClO$_4^-$]$^{2+}$. UV−vis [DMSO, λ_{max} nm (ε, M^{-1} cm^{-1})]: 535 (231).

5.3.3 Isothermal titration calorimetry (ITC)

ITC titrations were performed by using a Nano ITC Low Volume isothermal titration calorimeter (from TA instrument). All titrations were performed at 25°C. The results reported in Table 2 correspond to ITC experiment performed in DMSO by adding the solution of TBA$^+$ salt to the solution of receptor, placed in the instrument sample cell. The results reported in Table 6 correspond to ITC experiment performed in Hepes 0.05M by adding the solution of Na$^+$ salt to the solution of receptor,

placed in the instrument sample cell. The association parameters (K, ΔH, and ΔS), as well as the interaction stoichiometry, were determined by the fitting procedure using the software Affinimeter. Blank titrations in DMSO and Hepes 0.05M were performed and subtracted from the corresponding titrations to remove the effect of dilution.

5.3.4 UV-vis spectrophotometry

UV−vis spectra were recorded on a Varian CARY 50 spectrophotometer with quartz cuvette of 1 cm path length. UV−vis titrations were performed at 25 °C on 1×10^{-3} M solutions of $[Cu^{II}(\mathbf{1})](ClO_4)_2$ and $[Cu^{II}_2(\mathbf{2})](ClO_4)_4$ in DMSO, by adding aliquots of freshly prepared standard solutions (in DMSO) of $[Bu4N]X$ (X = Cl, Br, I, NCO, NCS, N_3, NO_3, HSO_4, and CH_3COO). Titration data were processed with the Hyperquad software to determine the equilibrium constants.[49] Best fitting of titration data was evaluated on the basis of the χ^2 value: accepted models showed a χ^2 value less than 10; rejected models showed $\chi^2 > 50$. HySS program was used to obtain the distribution diagrams of the species.[64]

5.3.5 Potentiometric titrations

All potentiometric titrations were performed at 25°C by using carbonate-free NaOH. Acidic dissociation constants of receptors $[Cu^{II}(\mathbf{1})](ClO_4)_2$ and $[Cu^{II}_2(\mathbf{2})](ClO_4)_4$ were determined in pure water. Titrations were performed under a nitrogen atmosphere. In a typical experiment, a 5×10^{-4} M solution of the receptor (15mL) was treated with an excess of a 1.0 M standard solution of HNO_3. Titrations were run by the addition of 10 uL portions of a standard 0.1 M solution of NaOH and collecting 80–100 points for each titration. Prior to each potentiometric titration, the standard electrochemical potential ($E°$) of the glass electrode was determined in pure water, by a titration experiment according to the Gran method. Protonation and complexation titration data (emf vs. mL of NaOH) were processed with the Hyperquad package to determine the equilibrium constants.[49]

5.3.6 X-ray Crystallographic Studies

Adiffraction data for $[Cu^{II}_2(\mathbf{2})(\mu_2\text{-}Br)_2]Br_2$ (violet, prismatic, 0.07 x 0.07 x 0.15 mm^3) and for $[Cu^{II}_2(\mathbf{2})(\mu_2\text{-}HSO_4)(HSO_4)_2]HSO_4 \cdot EtOH \cdot H_2O$ (pale red, lamellar, 0.02 x 0.32 x 0.50 mm^3) crystals have been collected by means of a Bruker-Axs CCD-based three circle diffractometer, working at ambient temperature with graphite-monochromatized Mo Kα X-radiation (λ = 0.7107 Å). Crystal data are reported in Table **6**. Data reductions were performed with the *SAINT* software and intensities were corrected for Lorentz and polarization effects. Absorption effects were empirically evaluated by

the *SADABS* software[82] and absorption corrections were applied to the data. Crystal structures were solved by direct methods (*SIR 97*)[66] and refined by full-matrix least-square procedures on F^2 using all reflections (*SHELXL 2014/7*).[83]

As for the $[Cu^{II}_2(\mathbf{2})(\mu_2\text{-Br})_2]Br_2$ crystal, all hydrogen atoms were placed at calculated positions with the appropriate AFIX instructions and refined using a riding model. Anisotropic displacement parameters were refined for all non-hydrogen atoms belonging to the dimetallic bicyclam ligand and for the Br^- ions interacting with the metal centers. The remaining two Br^- counterions exhibited positional disorder and resulted placed in mutually exclusive and partly populated atom sites. Atom occupancies for these atom sites were refined restraining their sum to the value imposed by stoichiometry, and only the most populated Br(3)a and Br(4)a atom sites were refined with anisotropic atom displacement parameters. The remaining alternative bromide positions occurring around these atom sites were refined with isotropic atom displacement parameters (constrained to be identical).

As for the $[Cu^{II}_2(\mathbf{2})(\mu_2\text{-HSO}_4)(HSO_4)_2]HSO_4 \cdot EtOH \cdot H_2O$ crystal, hydrogens bonded to C atoms were placed at calculated positions with the appropriate AFIX instructions and refined using a riding model, whereas positions for hydrogens belonging to the secondary amines were located in the final ΔF maps. These H atom positions were refined in the final least-square refinement cycles, restraining the N-H distances to be 0.9 ± 0.01 Å. Positions for hydrogens belonging to the bisulfate counterions did not appear in the final ΔF maps. These missing H atoms were placed at the staggered calculated positions bonded to the O(2), O(5) and O(9) atom sites, identified as plausible H-donor groups for supramolecular OH···O interactions based on the D···A distances. The O(9) H-donor group resulted with two alternative, symmetrically equivalent and half populated positions for the hydrogen. H atom belonging to the OH group of the ethanol solvent molecule was placed at the calculated position for an anti-ethanol isomer. All the calculated H atom positions were refined using a riding model. Water solvent molecules occurred in two symmetrically equivalent positions, half populated and mutually exclusive. Positions for H atoms belonging to water solvent molecules remained undetermined.

Table 6. Crystal data for the studied compounds.

	$[Cu^{II}_2(\mathbf{2})(\mu_2\text{-}Br)_2]Br_2$	$[Cu^{II}_2(\mathbf{2})(\mu_2\text{-}HSO_4)(HSO_4)_2]HSO_4 \cdot EtOH \cdot H_2O$
Formula	$C_{32}H_{62}Br_4Cu_2N_8$	$C_{34}H_{74}Cu_2N_8O_{18}S_4$
M	1005.52	1138.34
crystal system	orthorhombic	orthorhombic
space group	$Pcm2_1$ (no. 26)	$Pbcm$ (no. 57)
a (Å)	9.3657(7)	9.2823(5)
b (Å)	11.7713(8) Å	20.8029(10)
c (Å)	20.1233(14)Å	26.4431(13)
V (Å³)	2218.5(3) Å³	5106.1(4)
Z	2	4
ρ_{calcd} (gcm-3)	1.505	1.481
θ range (°)	2-25	2-25
measured reflections	22828	46486
unique reflections	4130	4622
R_{int}	0.032	0.049
strong data [$I_O > 2\sigma(I_O)$]	3383	3348
$R1$, $wR2$ strong data	0.0584, 0.1837	0.0747, 0.2142
$R1$ $wR2$ all data	0.0712, 0.1992	0.0958, 0.2404
max/min resid. (eÅ⁻³)	1.20/-0.45	1.04/-0.58

5.3.7 EPR studies

EPR measurements were made on a Bruker X-band EMX/12 spectrometer, equipped with a data station and temperature control. The spectral simulations were made using the Bruker Sinfonia package by adopting an Hamiltonian including the electronic and nuclear Zeeman and dipolar interaction terms with anisotropic g- and hf-tensors.

5.4 Supporting information
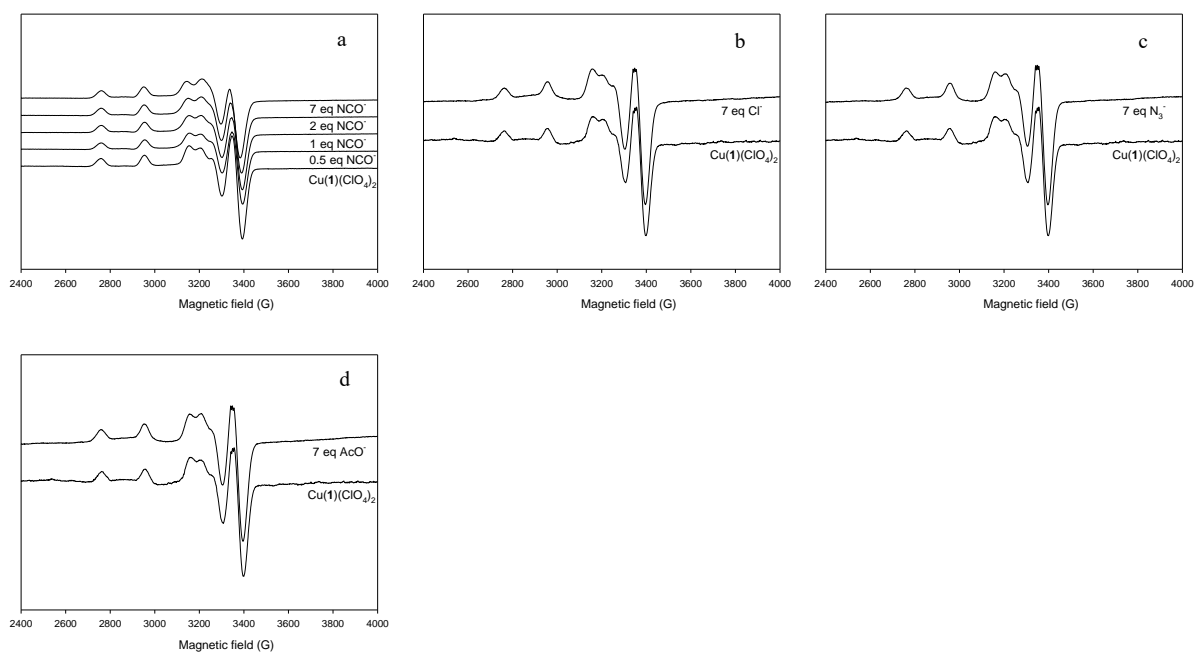
Figure S1. EPR spectra of a solution of $[Cu(1)](ClO_4)_2$ (5×10^{-4} M) in the presence of increasing amounts of cyanate (a), and in the presence of excess chloride (b), azide (c), and acetate (d).
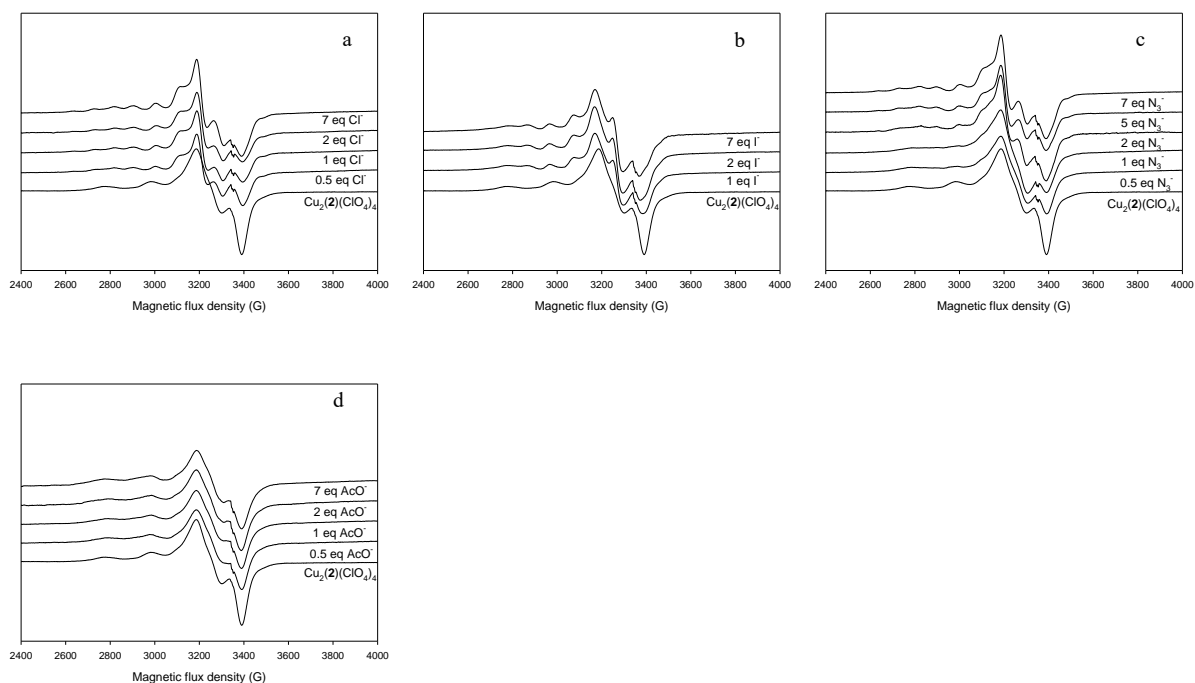
Figure S2. EPR spectra of a solution of $[Cu_2(2)](ClO_4)_4$ (5×10^{-4} M) in the presence of increasing amounts of chloride (a), iodide (b), azide (c), and acetate (d).
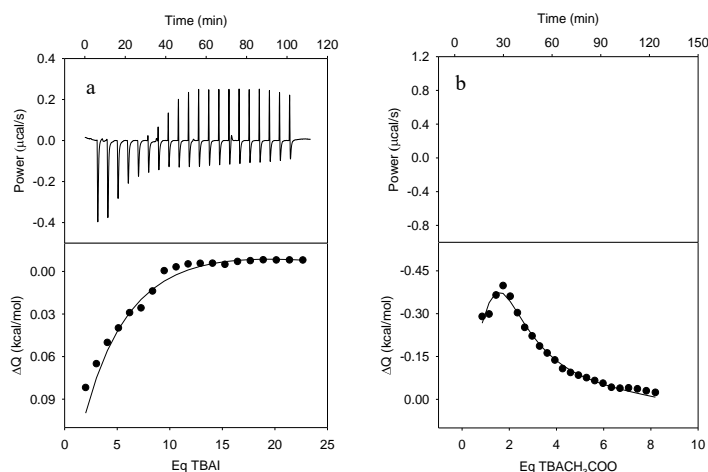
Figure S3. Thermograms and corresponding ITC profiles taken over the course of the titration experiments in DMSO: a) $[Cu(\mathbf{1})](ClO_4)_2$ (1.0 mM) titrated with (TBA)I (67.18 mM); b) $[Cu(\mathbf{1})](ClO_4)_2$ (5.13 mM) titrated with (TBA)CH_3COO (120 mM). Circles: experimental data; line: fitting profile (sequential two site models for a, b, d and e; one site model for c; "receptor" complex in the cell); T = 25°C.
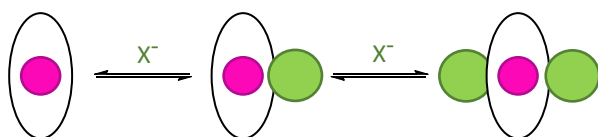
Figure S4. Schematic representation of equilibria taking place over the course of the titrations of $[Cu(\mathbf{1})]^{2+}$ with different anions (X⁻, green spheres = Cl^-, Br^-, I^-, NCO^-, N_3^-, CH_3COO^-).
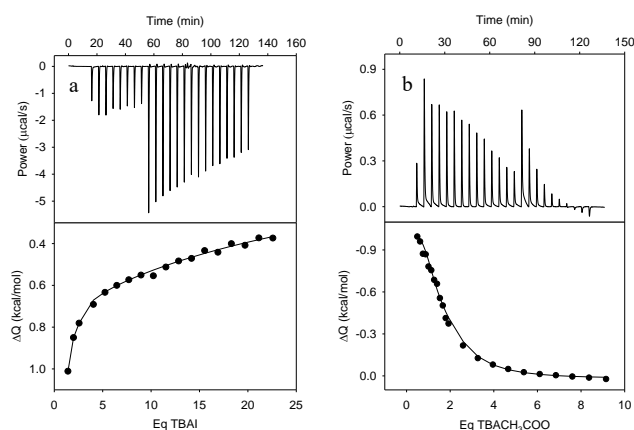
Figure S5. Thermograms and ITC profiles taken over the course of the titration of a solution of $[Cu_2(\mathbf{2})](ClO_4)_4$ (1 mM) in DMSO with a solution of: a) (TBA)I (67.18 mM); b) (TBA)CH_3COO (30 mM). Circles: experimental data; line: fitting profile (sequential two site models; "receptor" complex in the cell); T = 25°C.
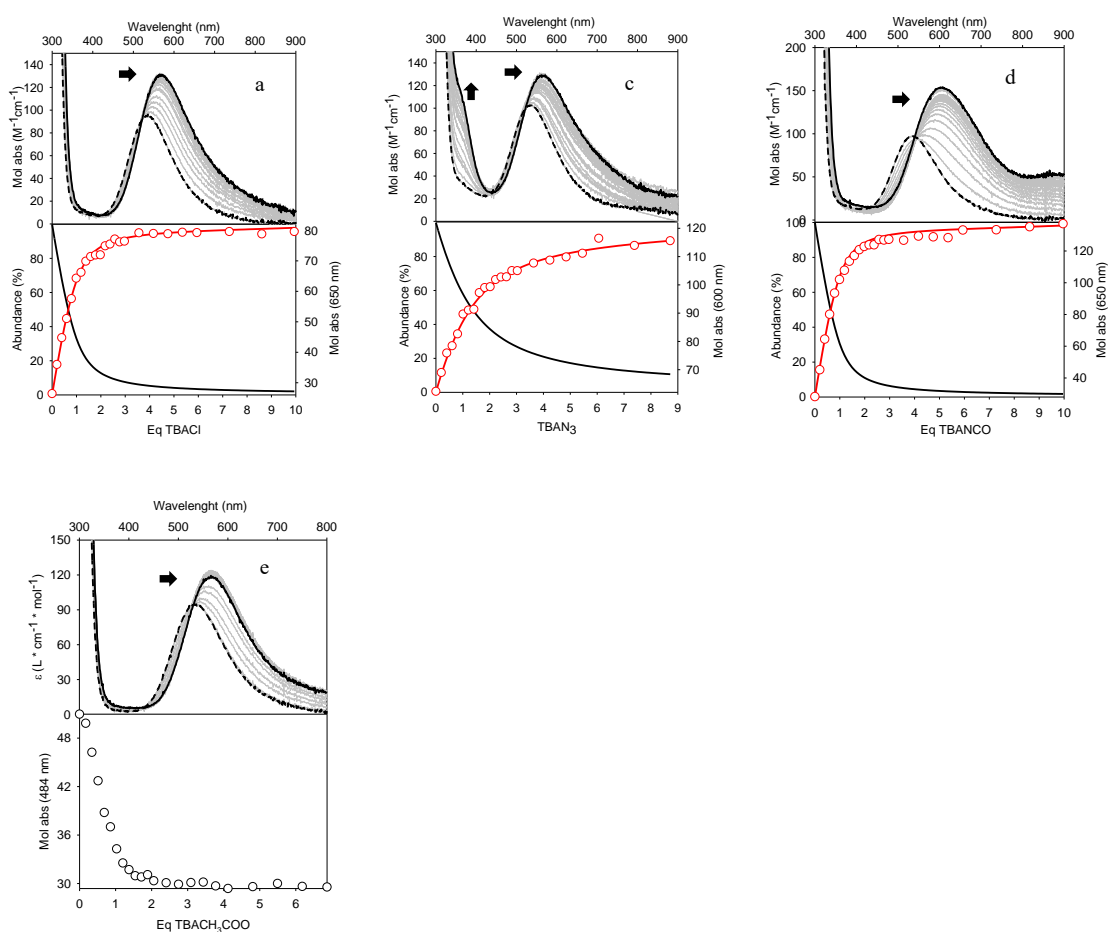
Figure S6. Absorption spectra taken over the course of the titration of $[Cu(\mathbf{1})](ClO_4)_2$ (1.02 mM in DMSO) with a DMSO solution of (TBA)Cl (50 mM, a), (TBA)I (50 mM, b), (TBA)N_3 (51,5 mM, b), (TBA)NCO (46,6 mM, c), and (TBA)CH_3COO (51, 5 mM, d), and the related distribution diagrams of species present at the equilibrium (black line: free $[Cu(\mathbf{1})]^{2+}$; red line: $[Cu(\mathbf{1})X]^+$; red circles: superimposed plots of molar absorptivity versus the equivalent ratio X^-/complex, X = Cl, NCO, N_3, T = 25°C). In the case of acetate the plot of molar absorptivity versus the equivalent ratio CH_3COO^-/complex is reported (black circles).
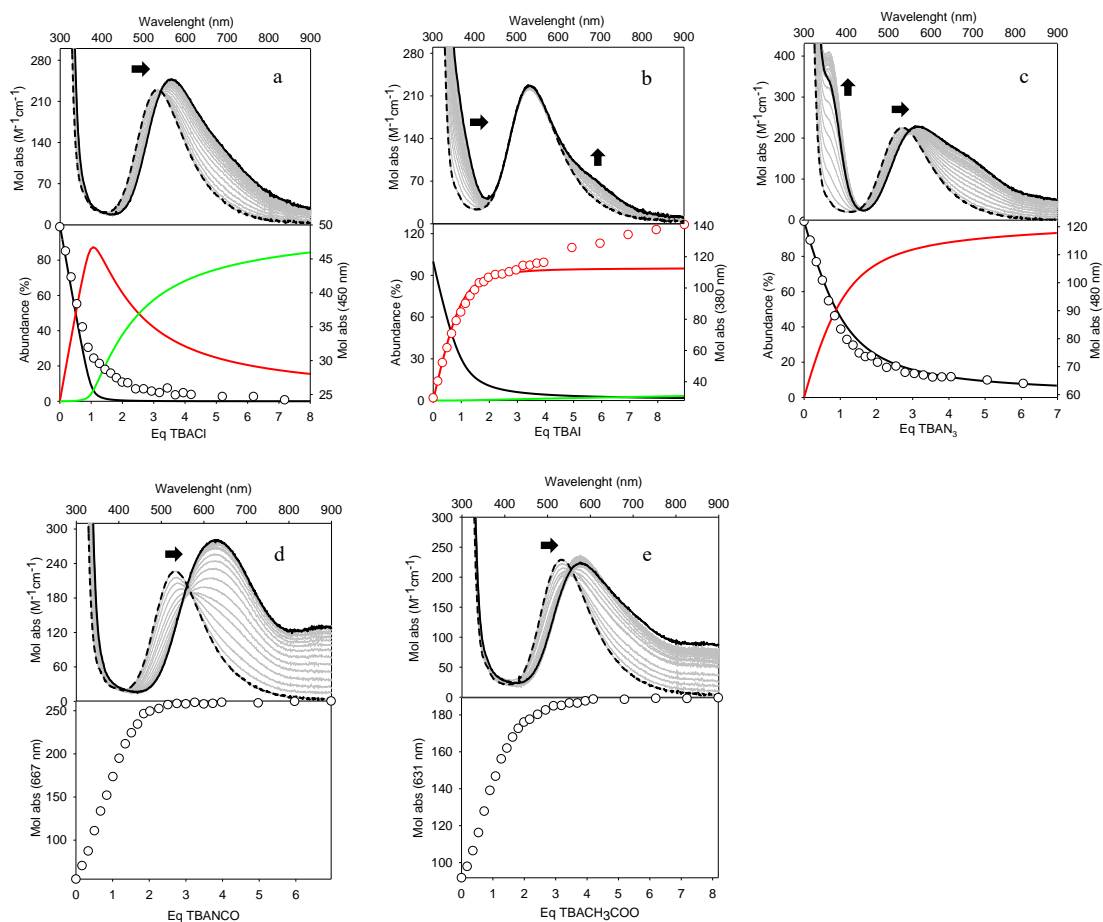
Figure S7. Absorption spectra taken over the course of the titration of $[Cu_2(\mathbf{2})](ClO_4)_4$ (1.015 mM in DMSO) with a DMSO solution of (TBA)Cl (55.1 mM, a), (TBA)I (50 mM, b), (TBA)N_3 (51,5 mM, c), (TBA)NCO (46,6 mM, d), and (TBA)CH$_3$COO (51,7 mM, e), and the related distribution diagram of species present at the equilibrium (black line: free $[Cu_2(\mathbf{2})]^{4+}$; red line: $[Cu_2(\mathbf{2})X]^{3+}$; green line: $[Cu_2(\mathbf{2})X_2]^{2+}$; circles: superimposed plots of molar absorptivity versus the equivalent ratio X^-/complex, X=Cl, I, N_3, T = 25°C). In the case cyanate and acetate, the plots of molar absorptivity versus the equivalent ratio anion/complex are reported (black circles).
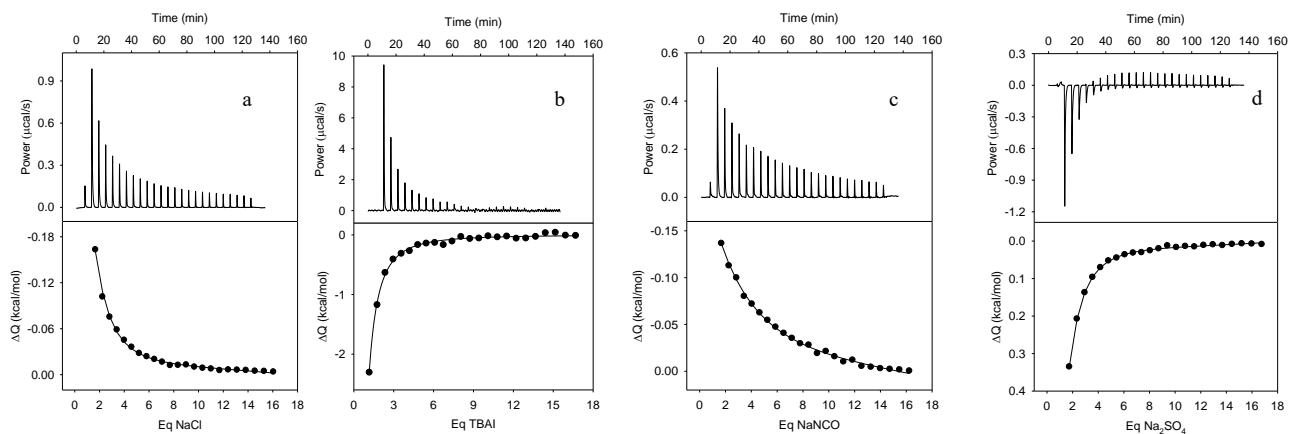
Figure S8. ITC profiles taken over the course of the titration of $[Cu_2(\mathbf{2})](ClO_4)_4$ (1.043 mM) in aqueous solution (HEPES 0.5 M) with aqueous solutions of: (a) NaCl (47.82 mM); (b) NaI (50 mM); (c) NaNCO (48,38 mM); (d) Na_2SO_4 (50mM). Circles: experimental data; line: fitting profile (one site model); receptor in the cell; T = 25°C.
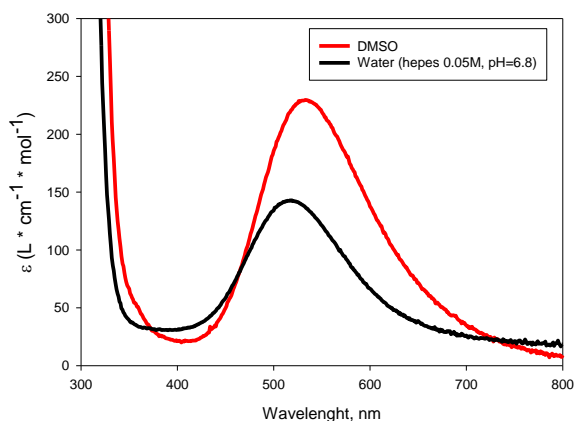
Figure S9. UV-Vis spectra of $[Cu_2\mathbf{2}]^{4+}$ in DMSO (red line) and water (Hepes 0.05M, pH = 6.8) (black line); λ_{max} in DMSO and in water are 533 and 518 nm, respectively.
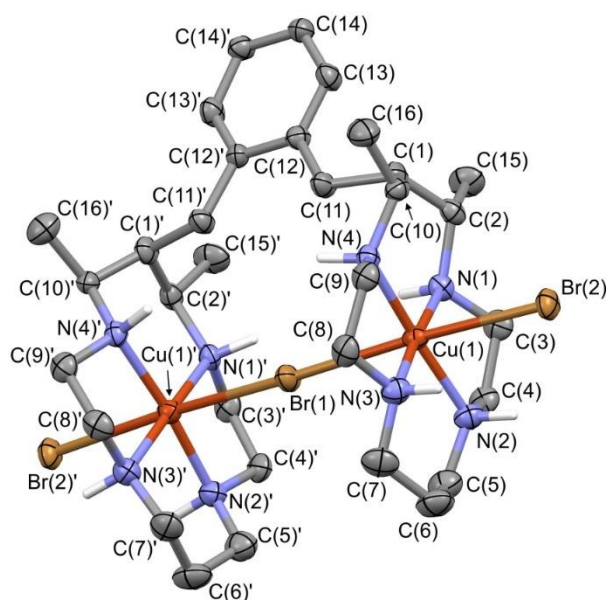
Figure S10. Plot showing thermal ellipsoids of the $[Cu^{II}_2(\mathbf{2})(\mu_2\text{-}Br)_2]^{2+}$ molecular cations occurring in the $[Cu^{II}_2(\mathbf{2})(\mu_2\text{-}Br)_2]Br_2$ crystal (ellipsoids are drawn at the 30% probability level; only H atom belonging to the secondary amines are shown; additional disordered bromide counterions are not reported). Symmetry code: (') = x, 1-y, z.
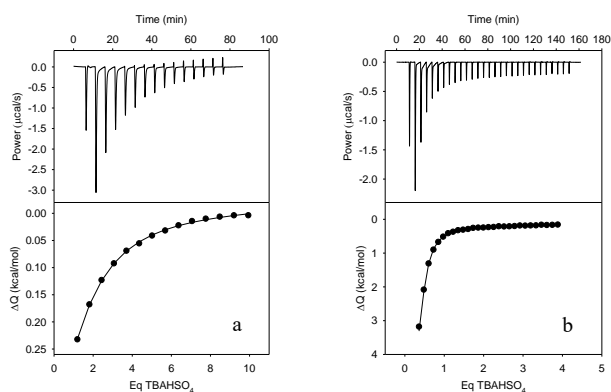
Figure S11. ITC profiles taken over the course of the titration of **a)** a solution of Cu**1**(ClO$_4$)$_2$ (5.13 mM) and **b)** a solution of Cu$_2$**2**(ClO$_4$)$_4$ (1mM) in DMSO with a solution respectively of TBAHSO$_4$ (100mM) and TBAHSO$_4$ (20mM).
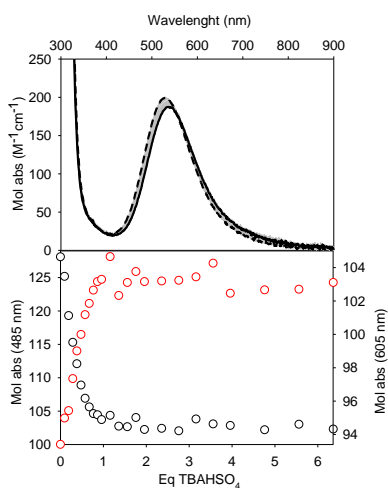
Figure S12. Absorption spectra taken over the course of the titration of a solution of [Cu$_2$**2**](ClO$_4$)$_4$ (1 mM) in DMSO with a solution of the TBAHSO$_4$ (20 mM). With black and red circles are reported the plots of molar absorptivity at two different wavelengths versus the equivalent ratio anion/complex. Absorption spectra taken over the course of the titration of a solution of [Cu**1**](ClO$_4$)$_2$ (1 mM) in DMSO with a solution of the TBAHSO$_4$ (53 mM) shows no UV-vis absorption spectra changing.
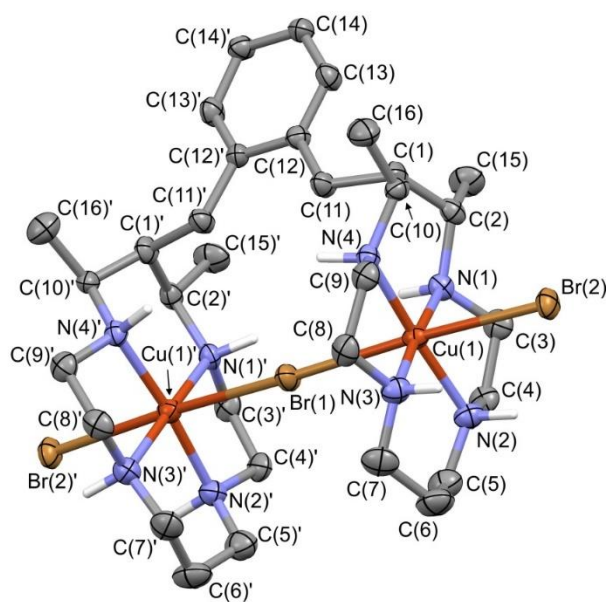
Figure S13. Plot showing thermal ellipsoids of the $[Cu^{II}_2(2)(\mu_2\text{-}Br)_2]^{2+}$ molecular cations occurring in the $[Cu^{II}_2(2)(\mu_2\text{-}Br)_2]Br_2$ crystal (ellipsoids are drawn at the 30% probability level; only H atom belonging to the secondary amines are shown; additional disordered bromide counterions are not reported). Symmetry code: (') = x, 1-y, z.
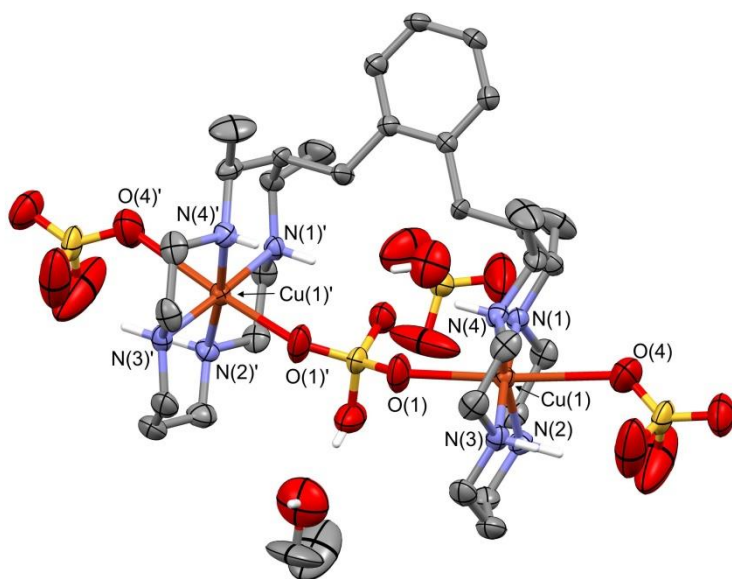
Figure S14. Plot showing thermal ellipsoids of the $[Cu^{II}_2(2)(\mu_2\text{-}HSO_4)(HSO_4)_2](HSO_4) \cdot EtOH$ compound occurring in the hydrate $[Cu^{II}_2(2)(\mu_2\text{-}HSO_4)(HSO_4)_2]HSO_4 \cdot EtOH \cdot H_2O$ crystal (ellipsoids are drawn at the 30% probability level; only H atom belonging to the secondary amines, bisulfate ions and ethanol solvent molecule are shown; disordered water solvent molecule are not reported; atom name are shown only for atom connected to the metal centers). Symmetry code: (') = x, y, $^3/_2$-z.
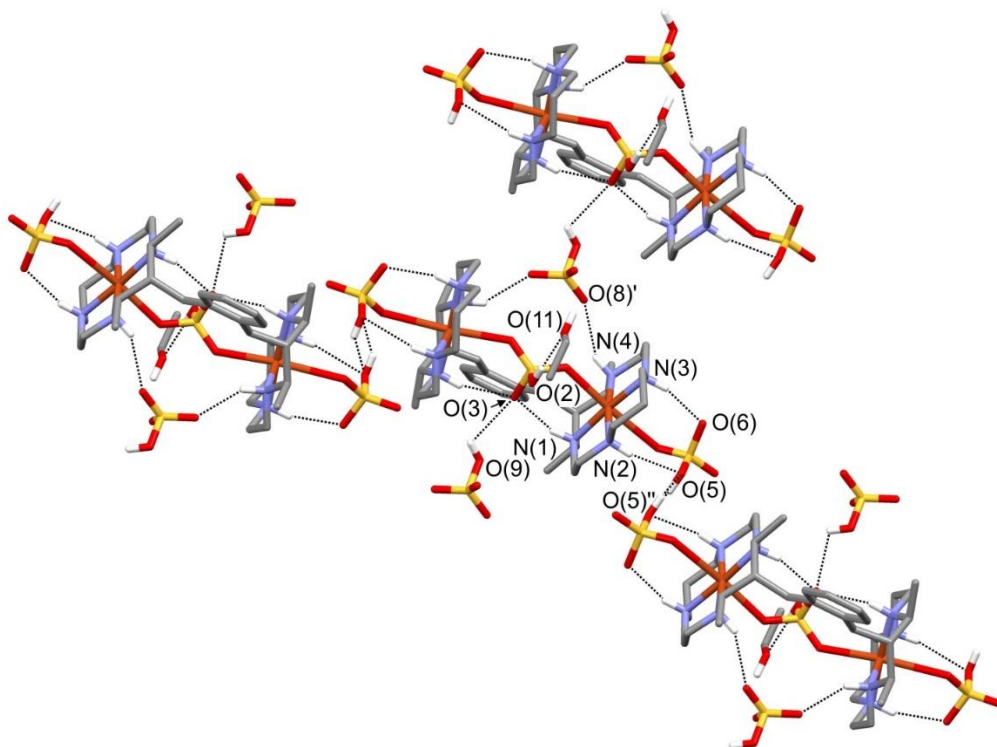
Figure S15. A simplified sketch showing a possible hydrogen bond motif in the $[Cu^{II}_2(\mathbf{2})(\mu_2\text{-}HSO_4)(HSO_4)_2]HSO_4 \cdot EtOH \cdot H_2O$ crystal, resulting from the H-atom positions assigned to the OH group of bisulfate ions and EtOH solvent molecules. Atom names are shown only for the atom species defining the not-symmetrically equivalent interactions. H-bonds are drawn with dashed lines and their geometrical features are reported in the following table:

D donor group	D···A [Å]	H···A [Å]	D-H···A [°]	A acceptor atom
N(1)-H(1N)	3.072(4)	2.23(2)	157.9(11)	O(3)
N(2)-H(2N)	3.246(10)	2.38(2)	161.9(12)	O(5)
N(3)-H(3N)	3.018(8)	2.15(2)	160.7(11)	O(6)
N(4)-H(4N)	3.137(9)	2.34(4)	147(2)	O(8)'
O(2)-H(2O)	2.78(2)	1.96(2)	177.6(7)	O(11)
O(5)-H(5O)	2.92(2)	2.58(2)	106.1(10)	O(5)"
O(9)-H(9O)a	2.89(2)	2.50(2)	110.6(2)	O(3)

Symmetry code:(') = 1+x, y, $^3/_2$-z; (") = 1-x, 1-y, 1-z

6 Catalytic CO$_2$ reduction

6.1 Introduction

Forty years ago, one of the biggest environmental issue was the ozone depletion and only in the 1987 thanks to the Montreal Protocol the international community made a series of regulations against the chlorofluorocarbons and only recently the ozone layer has started to recover. Currently one of the biggest environmental issue is the global warming, and one of the causes is the increment of CO_2 concentration in the atmosphere. In 2005, the Kyoto Protocol, and in 2016, the Paris Agreement, were made with the aim to reduce greenhouse gas emissions. Thus, the scientific challenge is to find a way to reduce the concentration of CO_2 in the atmosphere. The different proposed technologies follow one of two major approaches: to capture and geologically sequestrate CO_2, or to convert CO_2 into useful low-carbon fuels.[84–87]. In today's world of high energy demands, CO_2 conversion and utilization seems to be a more attractive and promising solution. Since CO_2 is an inert molecule both in thermodynamic and kinetic terms, CO_2 conversion is a very challenging task. Normally, CO_2 conversion can be achieved by chemical methods,[88–94] by photocatalytic and electrocatalytic reduction,[95–102] and by a few other means.[103–105] The present thesis is focused on CO_2 conversion by electrocatalytic approach.

6.2 Electrocatalysis[97]

An electrocatalyst both participates in an electron transfer reaction (at an electrode) and facilitates acceleration of a chemical reaction. Both the electron transfer and chemical kinetics must be fast for an efficient electrocatalyst. Additionally, an optimal electrocatalyst must display a good thermodynamic match between the redox potential (E^0) for the electron transfer reaction and the chemical reaction that is being catalyzed (e.g. reduction of CO_2 to CO). These factors can be optimized by chemical tuning of the electrocatalyst metal centers via appropriate ligand design. Electrocatalysts are typically screened for their redox potentials, current efficiencies, electron transfer rate and chemical kinetics in order to determine the best overall catalysts. In the general sense, electrocatalysts are electron transfer agents that ideally operate near the thermodynamic potential of the reaction to be driven, E^0(products/substrates). Direct electrochemical reduction of carbon dioxide on most electrode surfaces requires large overvoltages which consequently lowers the conversion efficiency. The overvoltage can be

considered to be the difference between the applied electrode potential, $V_{applied}$, and E^0(products/substrates), at a given current density. Both thermodynamic and kinetic considerations are important here. Clearly, in order to minimize overvoltages, catalysts need to be developed that have formal potentials, $E^0(Cat^{n+/0})$ well matched to E^0(products/substrates), and appreciable rate constants, k_{cat}, for the chemical reduction of substrates to products at this potential. In addition, the heterogeneous rate constant, k_h, for reduction of the electrocatalyst at the electrode must be high for $V_{applied}$ near $E^0(Cat^{n+/0})$. A general approach for an electrocatalytic system is given in Scheme 1. Reaction rates for these processes can be estimated from the steady-state limiting current in cyclic voltammetry, or by rotating disk voltammetry studies of the heterogeneous electron transfer kinetics. Electrocatalytic activity can be easily identified by cyclic voltammetry (CV).
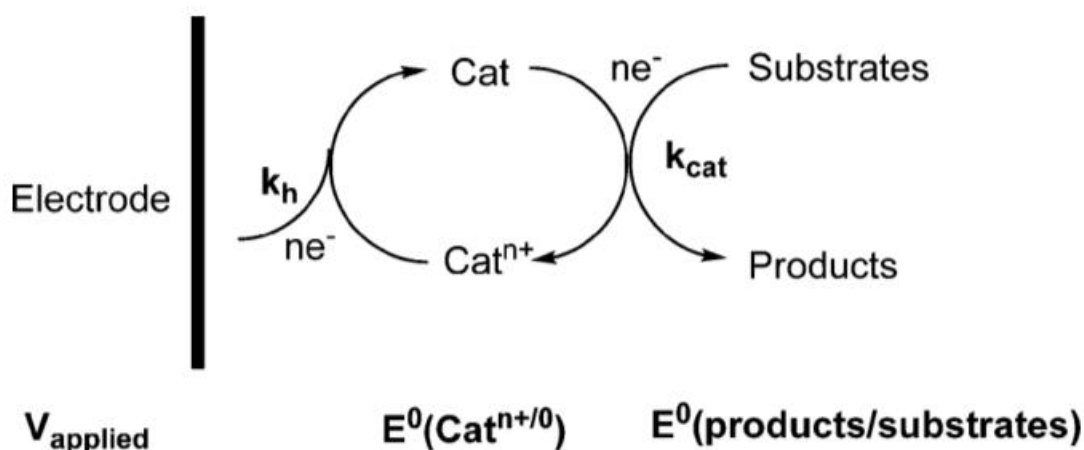
Scheme 1. Electrocatalysis with electron source.

In a CV under a dry inert atmosphere, an electrocatalyst should show a reversible redox couple. Upon addition of CO_2, the diffusion limited current should increase significantly, while the potential shifts anodically, and the reversibility in the return oxidation wave is lost due to the chemical reaction between CO_2 and the electrocatalyst. Electrocatalysts offer critical solutions to lowering the overpotentials, improving selectivity, and increasing the reaction kinetics of carbon dioxide conversion.

6.3 Mononuclear azamacrocycle complexes as catalysts for CO_2 reduction

The first reported transition metal catalysts with high current efficiencies and turnover numbers were demonstrated by Eisenberg and co-workers in 1980.[106] In this work, tetraazomacrocyclic complexes of cobalt and nickel were employed (1–5). These complexes were able to reduce carbon dioxide to carbon monoxide or a combination of CO and molecular hydrogen at potentials ranging from -1.3 to -1.6 V vs. SCE. These catalysts were also able to provide high current efficiencies, up to 98% (complex 3), but displayed low turnover frequencies between 2 and 9 per hour at 23 °C. Sauvage and co-workers have extensively studied the reaction of CO_2 with Ni^{II}(cyclam) complexes.[107–109] The Sauvage complexes are extremely stable, highly selective, and can show faradaic efficiencies up to 96% in the production of CO at -0.86 V vs. SCE, even under aqueous conditions, where the reduction of water to hydrogen is a strongly competitive reaction. The nickel macrocycle complexes were shown to be very sensitive to the pH and required an Hg electrode surface. A study of the reduction mechanism on mercury, using CV, polarography, and electrocapillarity, indicated that the adsorbed complex Ni(I)-cyclam on Hg was the active catalyst.[110]

Tetraaza open chain ligands or macrocyclic ligands other than cyclam (14 atoms in the ring) show poor stability during the electroreductive process.
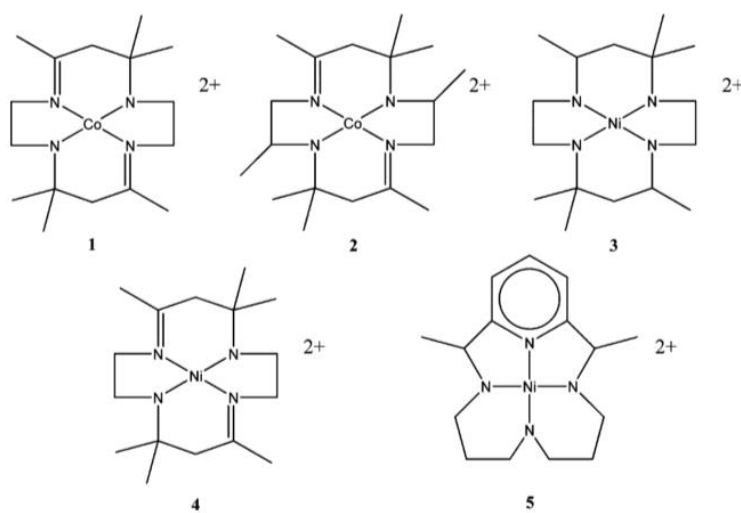
Interestingly, steric factors seem to play an important role. Introduction of methyl groups at the periphery of the complex drastically decreases the CO to H_2 ratio in the gas produced, being the coordination of the larger substrate (CO_2) unfavored than the much smaller H^+.[111] In addition to the accessibility of Ni(I), the presence of N-H functions in Ni(cyclam)$^{2+}$ could favor the formation of a CO_2 complex. It was shown that the CO_2 reduction activity diminishes with an

increasing degree of N-alkylation.[112] On the other hand, certain C substitutions of the tetraazacyclotetradecane ring have resulted in enhanced activities. The Ni(II) complex of N-hydroxyethylazacyclam (i.e. 3-(20-hydroxyethyl)-1,3,5,8,12-penta-azacyclotetradecane nickel(II) perchlorate) appeared to be more active than unsubstituted $Ni(cyclam)^{2+}$.[113] Recently, Schneider et al. explored a series of materials that are structurally similar to $[Ni(cyclam)]^{2+}$ to test them as electrocatalysts for CO_2 reduction at a mercury pool working electrode in aqueous solution.[114] Both $[Ni(HTIM)]^{2+}$ (HTIM = C-RRSS-2,3,9,10-tetramethyl-1,4,8,11-tetraazacyclotetradecane) and $[Ni(DMC)]^{2+}$ (DMC = C-meso-5,12-dimethyl-1,4,8,11tetraazacyclotetradecane) showed better electrocatalytic activities than $Ni(cyclam)^{2+}$. Schneider et al. suggested that (1) the catalyst's geometry should be suitable for its adsorption onto the mercury electrode surface and (2) there should be electronic effects of methyl groups or cyclohexane rings on the cyclam backbone. Additional observations have also been made about the influence of methyl substitution on these catalysts' activities.[115] Abba et al. found that the structural features of the cyclam and azacyclam framework played an important role in the enhanced catalytic efficiency of Ni-cyclam derivatives for CO_2 electroreduction. Even small deviations from such a geometrical arrangement caused the electrocatalytic effect to be drastically reduced or completely lost.[116]

Ni(II) and Co(II) are by far the most used metal centers. Nickel macrocycle complexes result better and more selective CO_2 reduction catalysts in aqueous solution than the cobalt analogues. They operate at a wide pH range and maintain selectivity, producing CO as opposed to H_2 even at low pH. This is probably due to the higher affinity of cobalt complexes for H^+, thereby making them more suited for proton reduction to H_2.[101]

6.4 Multinuclear azamacrocycle complexes as catalysts for CO_2 reduction

The presence of two or more co-ordination sites that might both be close enough to interact simultaneously with small molecules (CO_2) or the products of their redox transformation (for example CO or HCOOH) can lead to potentially different reaction pathways than for the mononuclear complex itself, favoring a higher catalytic activity or resulting in the reduction of CO_2 beyond CO (for example HCHO, CH_3OH, CH_4).

Lee et al.[117] studied the electrocatalytic activity of a multinuclear nickel(II) complex, towards CO_2 reduction and compared these results with those from catalysis by a mono- nuclear

complex, such as $[Ni(cyclam)]^{2+}$, in $CH_3CN–H_2O$ (9 : 1, v/v). Unfortunately, the catalytic efficiencies (TON) of $[Ni_3(L)]^{6+}$ were both lower than those of $[Ni(cyclam)]^{2+}$ and monometallic complex.

The catalytic activity of the dinickel complex of **0** was compared with that of $Ni^{II}(cyclam)$.[118] They discovered that as far as CO_2 electroreduction is concerned, $Ni_2(\mathbf{0})^{4+}$ shows no particular proprieties as compared to $Ni^{II}(cyclam)$. On the other hand, the electroreduction of water is markedly more efficiently catalyzed by the dinuclear complex than $Ni^{II}(cyclam)$. The involvement of dihydride intermediates of the type Ni(H)-Ni(H) might account for this result.

0
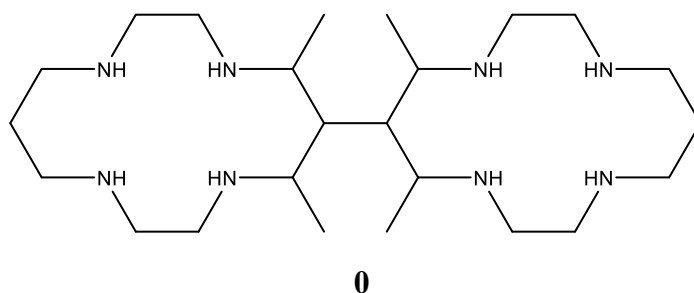
The catalytic reduction of CO_2 with the surface-confined dinickel complexes of ligands **1**–**9** was evaluated using a mercury coated silver electrode under CO_2 gas. Interestingly, the dinuclear pentaaza complexes' catalytic currents were only about half of the value for a mononuclear analogue. The conclusion from this result is that only one nickel site per dimer is adsorbing on the electrode, and is thus able to maintain catalytic activity. The more rigid, planar **5** complex had the largest catalytic current, likely because its structure most favored both nickel centers achieving planarity on the electrode.

The catalytic current for the complexes of **1**–**4** increased with the length of the linker, which was attributed to greater flexibility allowing both nickel sites better interaction with the electrode surface. Bulk CO_2 electrolysis and product analysis was carried out only on the complex of **3**. CO and H_2 were the major products detected. After about 10% of the available CO_2 was reduced to CO, changes in current and product distribution corresponded with deactivation of the catalyst due to nickel deposition. The dinickel complex of **6** was a poor catalyst for CO_2 reduction having a catalytic current about 15% of the pentaaza complexes, perhaps due to the additional steric hindrance. The tetraazabicyclononane fragment of ligands **7**–**9** occupies the same space around Ni^{2+} as ethylenediamine. Therefore, these ligands can be thought of as acting as 13-membered macrocycles around Ni^{2+}. These sterically hindered **7**–**9**

complexes were also relatively poor catalysts, with catalytic currents only about 10% of the pentaaza complexes. As was the case for **1–4**, the catalytic current did increase with chain length (i.e. flexibility) for the complexes of **7–9**.

1 X = $(CH_2)_2$
2 X = $(CH_2)_3$
3 X = $(CH_2)_4$
4 X = $(CH_2)_6$
5 X = *p*-xylyl

6

7 X = $(CH_2)_2$
8 X = $(CH_2)_3$
9 X = $(CH_2)_5$
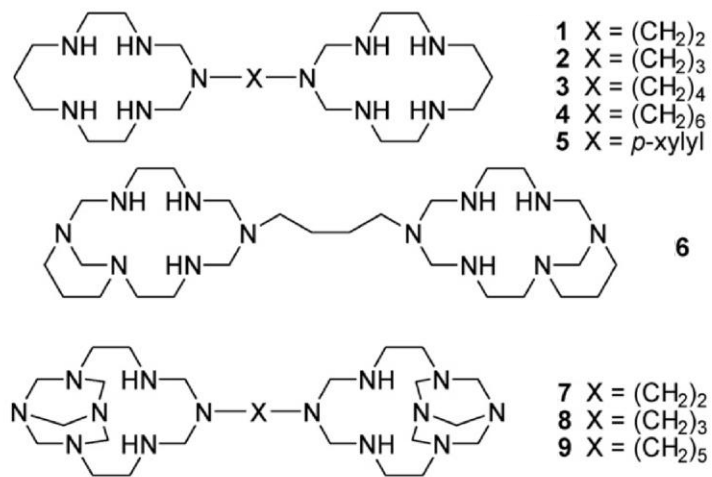
7 CO₂ electrocatalysis in water by cyclam-like nickel and copper complexes, using environment-friendly electrodes

7.1 Introduction

Electrochemical reduction of CO_2 to give reduced carbon fuel sources has been extensively studied over the last decades as a possible route to a renewable carbon fuel cycle. The reduction potentials for various CO_2 reductions can be seen in Equations 1–6 (pH 7 in aqueous solution versus a normal hydrogen electrode (NHE), 25∘C, 1 atm gas pressure, and 1 M for other solutes):[97]

$$CO_2 + e^- \rightarrow CO_2^{\bullet-} \quad E° = -1.90V \tag{1}$$

$$CO_2 + 2H^+ + 2e^- \rightarrow CO + H_2O \quad E° = -0.53V \tag{2}$$

$$CO_2 + 2H^+ + 2e^- \rightarrow HCO_2H \quad E° = -0.61V \tag{3}$$

$$CO_2 + 4H^+ + 4e^- \rightarrow HCHO + H_2O \quad E° = -0.48V \tag{4}$$

$$CO_2 + 6H^+ + 6e^- \rightarrow CH_3OH + H_2O \quad E° = -0.38V \tag{5}$$

$$CO_2 + 8H^+ + 8e^- \rightarrow CH_4 + 2H_2O \quad E° = -0.24V \tag{6}$$

The first step of CO_2 reduction is supposed to be the addition of one electron to form the radical anion, but it requires 1.9 eV of free energy (Equation 1), thus a proton coupled electron transfer mechanism (in other words the simultaneous reaction of protons and electrons) lowers the thermodynamic barrier, as we can see from the reduction potential shown in Equations 2–6. Fig. 1 shows a Latimer–Frost diagram[119] for the multi-electron, multi-proton reduction of CO_2 in homogeneous aqueous solution at pH 7. From a thermodynamic point of view the "two electron reductions" that forms either carbon monoxide or formate are much easier to achieve

than multi-electron reductions, indeed molecular systems that are capable of catalyzing the reduction of CO_2 typically give the products CO and/or formic acid (HCO_2H), while examples that reduce CO_2 to higher energy products such as methanol and methane are rare, typically inefficient, and not selective.
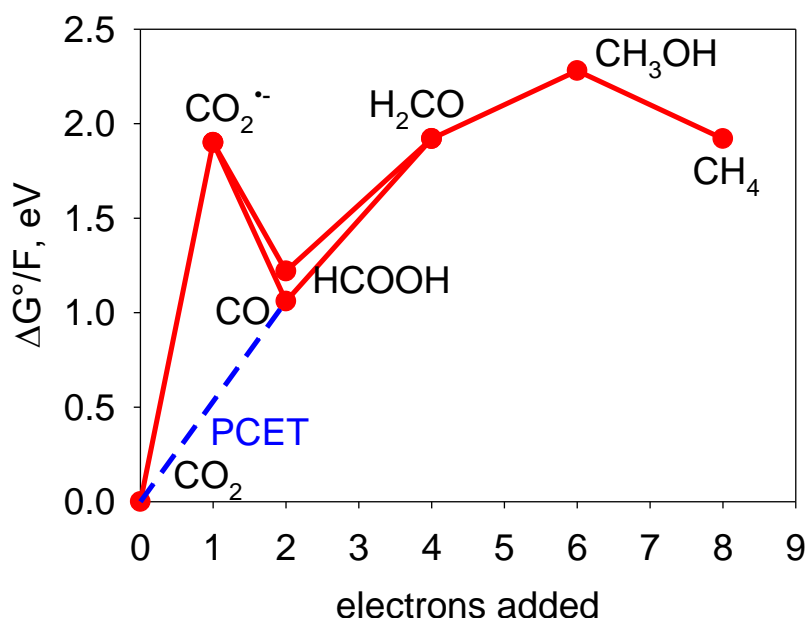
Figure 1. Latimer–Frost diagram for the multi-electron, multi-proton reduction of CO_2 in homogeneous aqueous solution at pH 7 based on the potentials in eqn 1–6.[119] Any species lying above the straight line joining two adjacent points (e.g., $CO_2^{\bullet-}$ between CO_2 and HCOOH) is thermodynamically unstable with respect to disproportionation.

From a kinetic point of view, all the CO_2 reductions are characterized by an overpotential that, in absence of an appropriate catalyst, impedes their success. Another complication for the CO_2 reduction is the presence of the competitive reaction of H^+ to hydrogen, which occurs at a similar potential of CO_2 reduction (Eq. 7).

$$2H^+ + 2e^- \rightarrow H_2 \quad E = -0.41 \text{ V} \quad (pH = 7) \tag{7}$$

The heterogeneous reduction of CO_2 by metallic electrodes has been explored;[120] however, the mechanisms of these systems can be difficult to study and often suffer from poisoning of the electrode by the intermediates or products of catalysis.[121] Transition metal molecular catalysts can be used in a homogeneous fashion by acting as an electron shuttle between an electrode and CO_2 in solution. The molecular catalyst serves to stabilize intermediate species allowing for less negative potentials to be used in the reduction of CO_2.

One of the most famous homogeneous catalyst for the CO_2 reduction is the macrocyclic complex $[Ni(cyclam)]^{2+}$ (cyclam = 1,4,8,11tetraazacyclotetradecane). Its popularity in this field is due to its ability to reduce CO_2 to CO in water with high efficiency at low over-potential (-1.00 V vs. NHE) and high stability (the catalytic activity remains intact after 800 cycles). Furthermore, mercury appears to be indispensable for CO_2 reduction by $[Ni(cyclam)]^{2+}$, as the reaction has been identified to take place predominantly at the mercury surface, indeed the influence of the catalyst concentration on the velocity of CO generation is not very important, increasing the $[Ni(cyclam)]^{2+}$ concentration 100-fold leads to an increase in rate of CO formation by a factor of only 3.[108] In search for more environmentally benign catalysts, Kubiak and co-workers recently reported that this reaction can proceed in a homogeneous fashion using an inert glassy carbon electrode. At −1.21 V versus the normal hydrogen electrode (NHE), the primary product was found to be CO with 90% Faraday efficiency, and no H_2 or formate was detected.[115] In 2014, Shengfa Ye and coworkers[122] proposed the reaction mechanism of CO_2 to CO reduction catalyzed by $[Ni(cyclam)]^{2+}$, here represented in the form of catalytic cycle in figure 2.
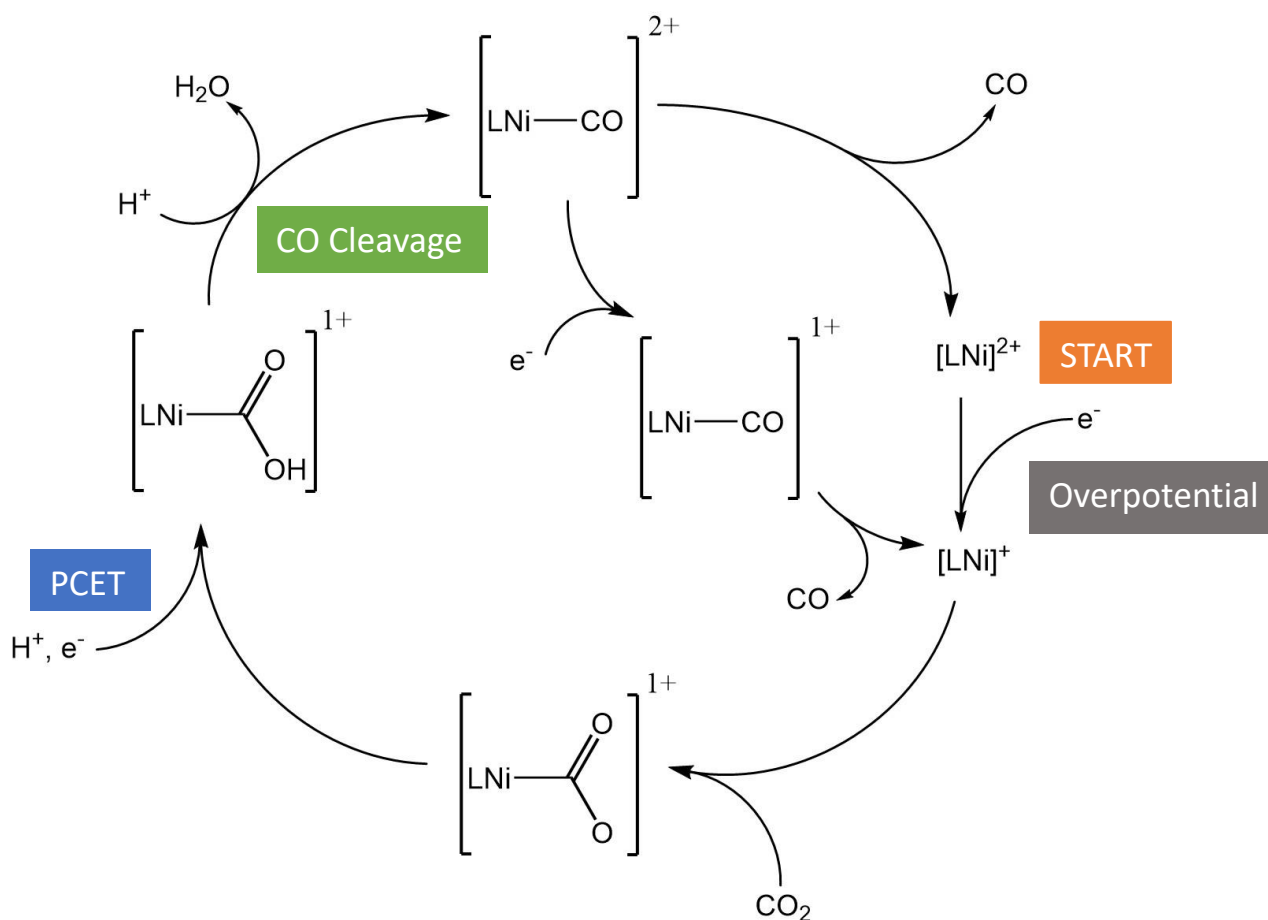
Figure 2. Catalytic cycle of CO_2 to CO reduction catalyzed by nickel complexes of cyclam-like ligand (L).[122]

The involved steps can be summarized as follows:

0) Ni(II) is reduced to Ni(I). This step determines the overpotential of the entire catalytic cycle.

1) Ni(I) coordinate CO_2. Here occurs a partial reduction of CO_2, thanks to the metal-to-ligand. electron transfer (π backdonation from d_z^2 metal orbital to π^* CO_2 orbital).

2) Then there is a proton coupled electron transfer. In this step the 2 electrons reduction of CO_2 is almost completed.

3) The next step consists of breaking the C–O single bond to generate the final product, CO, here the presence of a good proton donor is required.

4) The Ni^{II}–CO adduct can directly release CO regenerating the Ni(II) catalyst (ΔG = -5.8 Kcal/mol), but another way is possible, where the Ni^{II}–CO adduct is first reduced to Ni^{I}–CO and then occurs the CO release. The latter way is more difficult because of the stronger

interaction between Ni(I) and CO (ΔG = 8.6 Kcal/mol). In this step the working electrode comes into play, indeed it can speed up the CO release by adsorbing the catalyst and change its conformation. So far, the best electrode for this purpose is Hg electrode.[110,115,123]

An alternative approach to accelerate the CO release is the introduction of a molecular scavenger able to bind CO with a binding constant higher than that developed by the catalyst.[124]
Our goal is to find an electrode able to enhance the catalyst efficiency as Hg does but more environment-friendly than Hg. Bismuth and glassy carbon are the candidate working electrodes, thanks to their high overpotential for H_2 evolution and their nontoxic nature.
Since there are two steps of the CO_2 catalytic cycle where H^+ is involved and considering that the major competitive reaction is the H^+ reduction to H_2 where the macrocyclic complexes act as catalysts (H^+ catalytic cycle is represented in Fig. 4), the effect of pH for the CO_2 catalysis have been investigated.[101]

Figure 3. Catalytic cycle of H^+ to H_2 reduction catalyzed by nickel complexes of cyclam-like ligand (L)

Moreover, CO_2 is a Lewis acid, taking part of the Acid-Base equilibria involving HCO_3^- and CO_3^{2-} species (eq. 2 and 3), which must be considered as possible reducible species.

$$CO_2 + H_2O \rightarrow HCO_3^- + H^+ \qquad pK_a(1) = 6.37 \tag{8}$$

$$HCO_3^- + H_2O \rightarrow CO_3^{2-} + H^+ \qquad pK_a(2) = 10.37 \tag{9}$$

In the preset work we studied the reduction of CO_2 catalyzed by bimacrocyclic complexes, consist of two M(II)-Me_2cyclam unit (M(II) = Cu(II) or Ni(II)) linked by different types of bridge: *ortho*-xylil, *meta*-xylil, and *para*-xylil (**3**, **4** and **5** are respectively the related ligands).[43]

1   **2**   **3: *ortho*-xylil**
                                        4: *meta*-xylil
                                        5: *para*-xylil

We compared the catalytic property of these dimetallic complexes with the corresponding monometallic complexes consist of one M(II)-Me$_2$cyclam unit (M(II) = Cu(II) or Ni(II)) functionalized with a benzyl group on the carbon backbone (**2** is the related ligand),[65] and with the [M(II)cyclam]$^{2+}$ complexes (M(II) = Cu(II) or Ni(II)) (**1** is the related ligand). The decision to use copper as metal center in addition to nickel was taken in view of its catalytic property in the CO$_2$ reduction as reported recently by Hochun Lee and coworkers.[125]

Their catalytic activity for the CO$_2$ reduction in water, using different electrode (Hg, Bi and GC) and different values of pH, have been investigated.

All the experiments, included the investigation of the catalytic activity of the catalysts combined with the three different working electrode at different value of pH has been performed by using the cyclic voltammetry technique.

We focused on bismacrocyclic complexes because in many ways they could behave very differently compared to the analogous monomacrocyclic complexes,[118] and the idea is that they could improve the CO$_2$ catalysis by undertaking one of the two following ways:

1) coordinating the substrate in the form of CO$_2$ or HCO$_3^-$ or CO$_3^{2-}$ (at different values of pH), inside their cavity, between the two macrocyclic units in a "bridged" conformation. Bringing could introduce advantages, both in term of overpotential and catalytic activity, for instance, by directly donating two electrons from the same chelating catalyst or causing the reduction beyond

CO. The most promising catalyst for this purpose are the dicopper and dinickel complexes $[M^{II}_2(3)]^{4+}$ due to their ability to bind small anions inside their cavity thanks to their chelate effect as we saw in the anion recognition section of the present thesis.

2) Coordinating one molecule of CO_2 for each metal centers, this could favor coupling reactions, forming C-C products, such as oxalate.[126,127]

The effect of the benzyl group and the two methyl groups on the carbon backbone of $[M^{II}(2)]^{2+}$ is another object of our work and basing on the studies carried out by Froehlich and Kubiak, where the functionalization of the cyclam carbon backbone have led to an improvement in term of selectivity and catalytic efficiency.[128]

Summarizing, this work has the aim to:

- test current efficiency and overpotentials involved with mercury and alternative working electrodes (bismuth and glassy carbon),
- study the pH effect in the CO_2 reduction and investigate if HCO_3^- and CO_3^{2-} are involved in the catalysis at different value of pH,
- investigate the catalytic efficiency of the macrocyclic complexes under study, focusing on the effect of the functionalization of the cyclam carbon backbone with a benzyl group and linking a second macrocyclic subunit.

7.2 Results and discussion

7.2.1 Electrocatalysis by mercury electrode

Mercury electrode is the most used working electrode to study the reduction of CO_2 catalyzed by macrocyclic complexes in a homogeneous phase. It is so popular thanks to its capacity to absorb the macrocyclic catalysts, improving the catalytic current and the selectivity for the electrochemical reduction of CO_2 at a potential much less negative than that required for the uncatalyzed reduction and even more positive than the reduction potential of the macrocyclic catalyst in solution.[129] The reason of the catalyst activity improvement once the catalyst is adsorbed on the Hg surface is still unclear, the most likely involved effects are:

- Hg could improve the affinity of the catalyst for CO_2, modifying its conformation (from trans-III to trans-I). An increased CO_2 binding constant for the adsorbed species would lead to a higher TOF because CO_2 could better compete with CO for binding to the Ni(I) metal.[124]

- The DFT calculations of the $[Ni(cyclam)(CO)]^+$ structure showed the necessity for the bending out of square planar geometry to achieve a highly stable CO adduct. Hg surface could prevent such a distortion of the square planar cyclam ligand, favoring the CO release from the catalyst.[122]

7.2.1.1 Solution voltammetry of Nickel complexes

The cyclic voltammograms of the nickel complexes of the ligands 1–3 are shown in figure 4. The monometallic complexes, $[Ni^{II}(1)](ClO_4)_2$ and $[Ni^{II}(2)](ClO_4)_2$, display a single one-electron cathodic peak. These waves are assigned as the $Ni^{II/I}$ couple, and they are all reversible. The dimetallic complex, $[Ni^{II}_2(3)](ClO_4)_4$, display a reversible two-electron cathodic peak, which is considered the convolution of two distinct peaks corresponding to the two stepwise one-electron reduction processes:

$$[Ni^{II} - Ni^{II}(3)]^{4+} + e^- \rightarrow [Ni^I - Ni^{II}(3)]^{3+} \tag{1}$$

$$[Ni^I - Ni^{II}(3)]^{3+} + e^- \rightarrow [Ni^I - Ni^I(3)]^{2+} \tag{2}$$
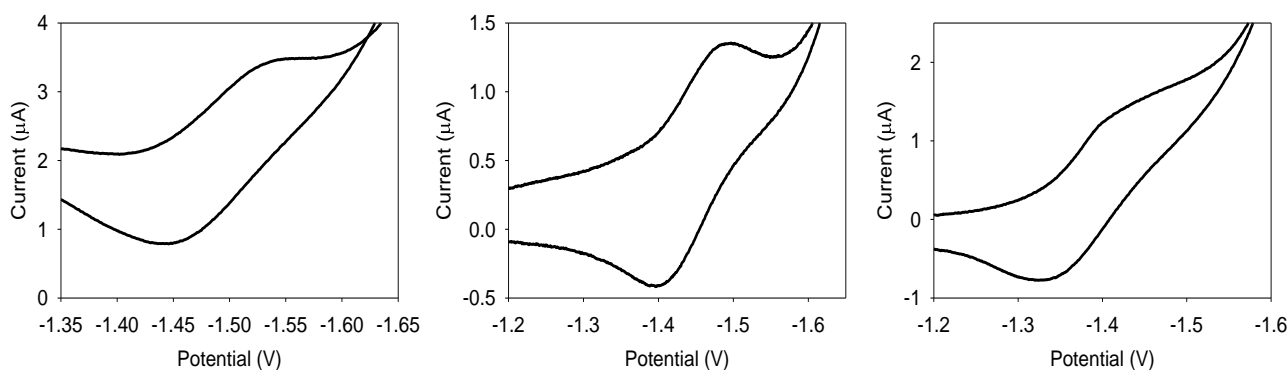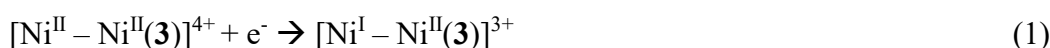
Figure 4. Cyclic voltammograms of 1.0 mM solutions of: (a) $[Ni^{II}(1)](ClO_4)_2$, (b) $[Ni^{II}(2)](ClO_4)_2$ and (c) $[Ni^{II}_2(3)](ClO_4)_4$ in a 0.05M solution of NaCl in water at pH = 7, purged with N_2. (For more details on experimental conditions see experimental section).

The reduction potential, $E_{1/2}$, of the complexes $[Ni^{II}(1)](ClO_4)_2$, $[Ni^{II}(2)](ClO_4)_2$ and $[Ni^{II}_2(3)](ClO_4)_4$ are respectively -1.5 V, -1.4 V and -1.35 V. The difference of 100 mV between $[Ni^{II}(1)](ClO_4)_2$ and $[Ni^{II}(2)](ClO_4)_2$ is due to the presence of two methyl groups on the carbon backbone, which act as electron-donor groups. The explanation could seem counterintuitive if we consider the electron-deficiency of the metal center as the only factor governing these $Ni^{II/I}$ reduction potentials. Another important factor is involved, namely the strength of the axial ligand coordination to the metal center.

These ligands could potentially be chloride (from NaCl and HCl) or H_2O under this condition. The presence of electron-donor groups on the carbon backbone weaken the interaction with the axial ligand, decreasing the e_g orbital energy of the octahedral macrocyclic complex, favoring the reduction of Ni(II) to Ni(I) at less negative potential. Tong Ren and coworkers found a similar behavior for some nickel complexes of C-substituited cyclams.[128] A proof of the weaker Ni(II)-Cl axial interactions involved in $[Ni^{II}(2)](Cl)_2$ than those in $[Ni^{II}(1)](Cl)_2$[11] are shown in figure 5. The molecular crystal structure $[Ni^{II}(2)](Cl)_2$ consist of two Ni(II)-Cl interactions of different length: 2.52 Å and 2.56 Å, whereas $[Ni^{II}(2)](Cl)_2$ consist of two identical Ni(II)-Cl interactions of length 2.51 Å, which are shorter than those of $[Ni^{II}(2)](Cl)_2$.

The dimetallic complex $[Ni^{II}_2(3)](ClO_4)_4$ has a reduction potential ($E_{1/2}$) further less negative by 50 mV (-1.35 V). This is explainable by assuming a moderate electrostatic repulsion between the two positively charged metal centers and the higher total charge of the molecule (4 + vs 2 +), which make easier the addition of electrons.
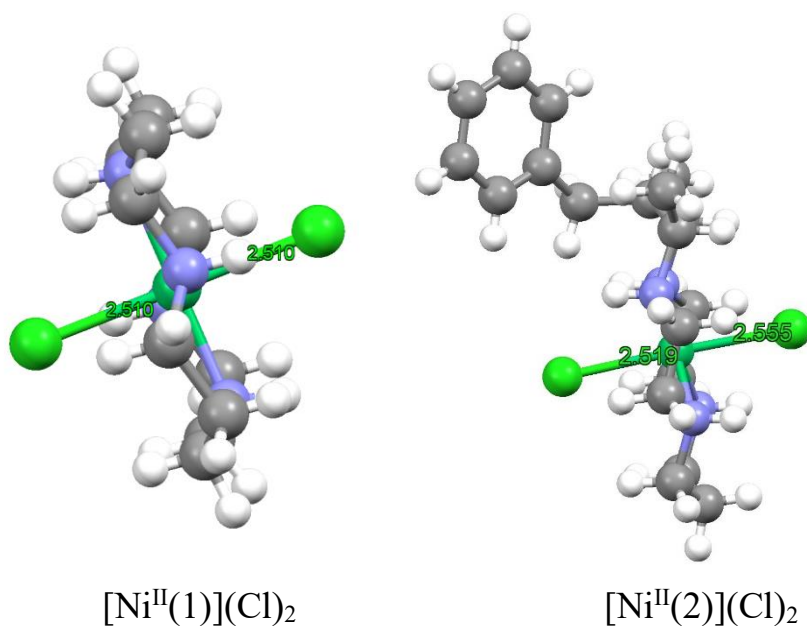
$$[Ni^{II}(1)](Cl)_2 \qquad [Ni^{II}(2)](Cl)_2$$

Figure 5. Lateral view of the molecular crystal structures of $[Ni^{II}(1)](Cl)_2$[11] and $[Ni^{II}(2)](Cl)_2$. $[Ni^{II}(1)]^{2+}$-Cl bond length: 2.51 Å. $[Ni^{II}(2)]^{2+}$-Cl bond length: 2.52 Å and 2.56 Å.

7.2.1.2 Solution voltammetry of Copper complexes

No waves have been observed using 1.0 mM of copper complexes in a 0.05M solution of NaCl in water, purged with N_2.

7.2.1.3   CO₂ electrocatalysis by nickel macrocyclic complexes

Figure 6 show the cyclic voltammograms recorded at different value of pH (from pH = 11 to pH = 5, decreasing the pH with a 6 M solution of HCl), of a 1×10^{-4} M solution of catalyst in water and 0.1 M of substrate Na_2CO_3 (for more details see experimental section).
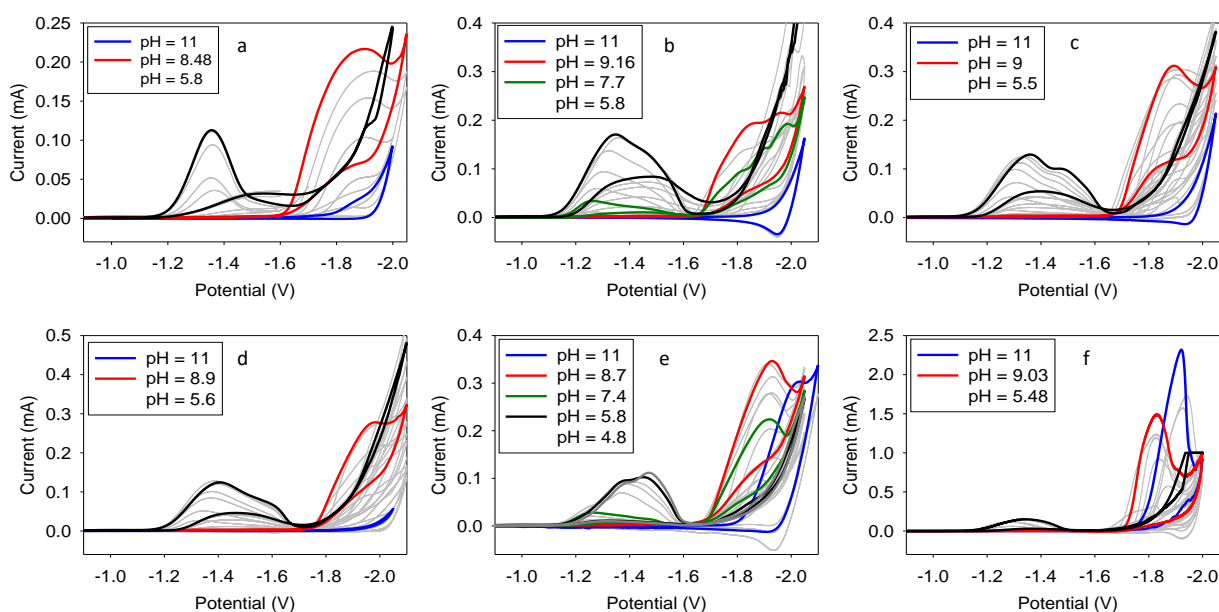
Figure 6. Cyclic voltammograms recorded at different values of pH (from pH = 11 to pH = 5) of a solution containing 0.1 M of Na_2CO_3 in water and $1e^{-4}$ M of: (a) $[Ni^{II}(1)](ClO_4)_2$, (b) $[Ni^{II}(2)](ClO_4)_2$, (c) $[Ni_2^{II}(5)](ClO_4)_4$, (d) $[Ni^{II}_2(4)](ClO_4)_4$ (e) $[Ni^{II}_2(3)](ClO_4)_4$. (f) cyclic voltammograms recorded at different values of pH of a solution containing 1M of Na_2CO_3 and $1e^{-4}$ M of $[Ni^{II}_2(3)](ClO_4)_4$.

From pH = 8 to pH = 5, all catalysts produce an irreversible peak. The potential of the peak maximum varies in a range between -1250 mV and -1450 mV vs Ag/AgCl (saturated NaCl), varying the value of pH. From pH = 10.5 to pH = 6, all catalyst develops an irreversible peak at -1850 mV. Over pH = 10.5, only $[Ni^{II}(3)](ClO_4)_4$ develop an irreversible peak at -1900 mV before the H_2O reduction, as observable in fig 6-e and in figure 6-f where the Na_2CO_3 concentration is 1 M. In order to better understand which species are involved in the reduction at different value of pH, the current peak area versus pH graphs are illustrated in figure 7. The figure 7-a represent the pH distribution diagram of CO_2. The current peaks area at -1350 mV, -1850 mV and -1900 mV at different value of pH are illustrated respectively with black, red and blue circles in Figure 7. Interestingly, as we can see from the superimposition of the graph 7-a with the other graphs in figure

7, the CO_2, HCO_3^- and CO_3^{2-} abundance follow the same trend of the current peak areas respectively at -1350 mV, -1850 mV and -1900 mV. This behavior could be explained by the assumption that the catalyst under study are able to catalyze the reduction of CO_2, HCO_3^- and CO_3^{2-}. CO_2 is reduced at a potential less negative than HCO_3^- and CO_3^2. This wide difference in the substrate reduction potential is due to different mechanism of reduction. CO_2 is reduced via a proton coupled electron transfer (PCET), which is favored by the acidic pH for the presence of H_3O^+ and H_2CO_3 species, which are great proton donors. Whereas, considering the low concentration of good proton donors at basic pH, HCO_3^- and CO_3^{2-} could be reduced via a direct one electron transfer mechanism, which increase the thermodynamic barrier compared to the PCET mechanism, alternatively they could be reduced via a PCET using water as a weak proton donor.[122]
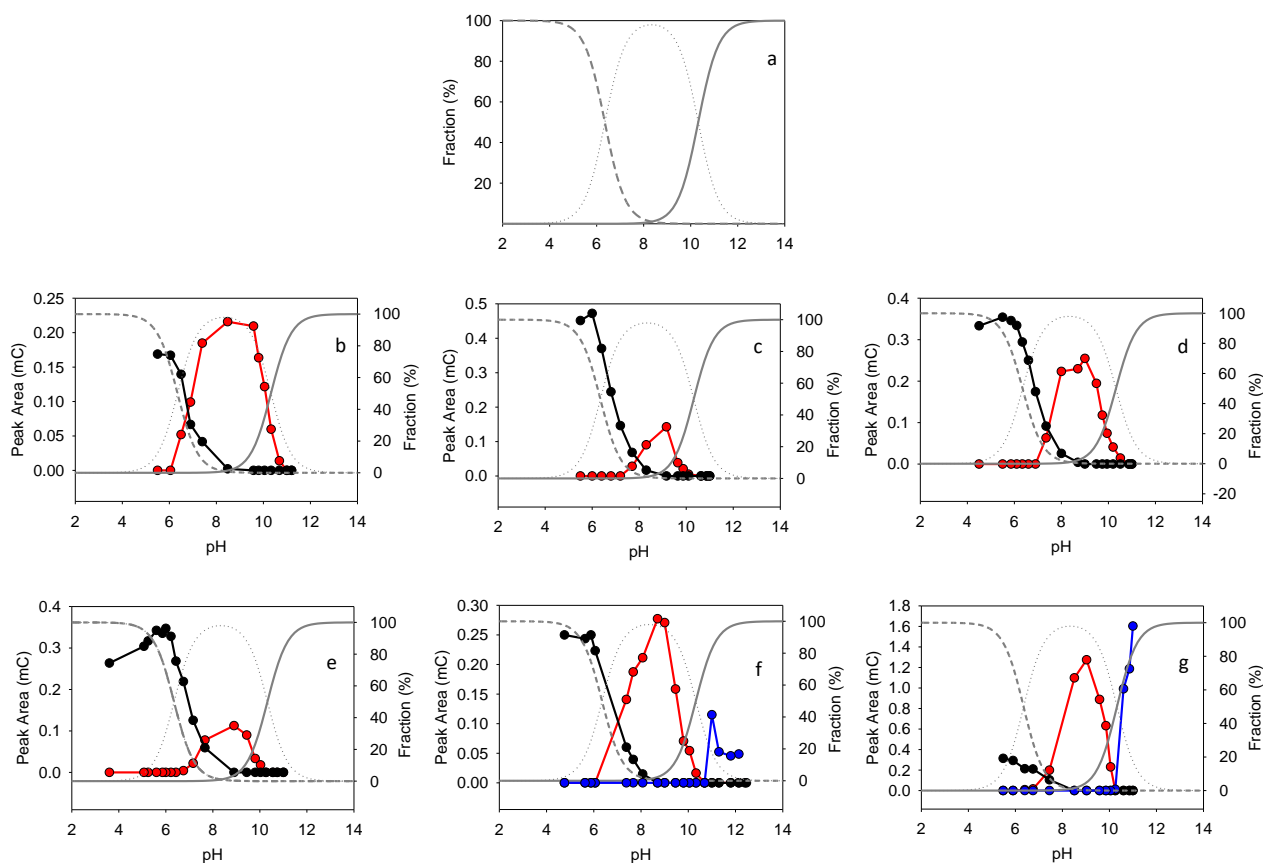
Figure 7. Current peak area versus pH graphs related to the $CO_2/HCO_3^-/CO_3^{2-}$ reduction, catalyzed by: (b) $[Ni^{II}(1)](ClO_4)_2$, (c) $[Ni^{II}(2)](ClO_4)_2$, (d) $[Ni_2^{II}(5)](ClO_4)_4$, (e) $[Ni^{II}_2(4)](ClO_4)_4$, (f) $[Ni^{II}_2(3)](ClO_4)_4$, (g) $[Ni^{II}_2(3)](ClO_4)_4$. All the starting solution contain $1e^{-4}$ M of catalyst and 0.1 M of Na_2CO_3 in water, except for (g) that contain 1 M of Na_2CO_3. (a) distribution diagram of CO_2 varying the value of pH. Solid grey line: fraction (%) of CO_3^{2-} varying the pH; dotted line: fraction (%) of HCO_3^- varying the pH; dashed grey line: fraction (%) of CO_2 varying the pH. Blue line and circles: current peak area at -1.9 V varying the pH; red line and circles: current peak area at -1.85 V varying the pH; black line and circles: current peak area at -1.35 V varying the pH.

At pH = 5.8, when the substrate is prevalently present in solution as CO_2, the catalysts develop the major catalytic effect toward the reduction of CO_2. As shown in Fig. p-e, decreasing the pH under 5.8, the catalytic peak at -1350 mV decrease because the concentration of H^+ increase and the catalyzed reduction of H^+ to H_2 became more competitive.

The catalyst activity of the macrocyclic complexes at pH = 5.8 follow the order: $[Ni^{II}(2)]^{2+} >$ $[Ni^{II}_2(4)]^{4+} = [Ni^{II}_2(5)]^{4+} > [Ni^{II}_2(3)]^{4+} > [Ni^{II}(1)]^{2+}$.

$[Ni^{II}(2)]^{2+}$ seems to be the most active catalyst for the CO_2 reduction, indeed it develop a current peak area of 0.45 mC at -1.35 V and pH = 5.8 versus 0.17 mC developed by $[Ni^{II}(1)]^{2+}$ at the same potential and pH, almost 3 times higher. Figure 8 might help to understand the exceptionally high catalytic activity of the macrocyclic complex $[Ni^{II}(2)]^{2+}$, which highlight the distances chloride – Ni^{II}. $[Ni^{II}(2)]^{2+}$ develop two interactions with two chlorides in axial position, with different bond length, 2.55 Å and 2.519 Å. The second one is shorter thanks to the additional hydrogen bond formed between chloride and a benzylic hydrogen with a bond length of 2.87 Å. We think that a similar interaction could occur between the oxygen donor atom of CO_2 and the benzyl hydrogen, as represented by the molecular structure $[Ni^{II}(2)(CO_2)]^{2+}$ in figure 8. Moreover, as I said previously, the two methyl groups on the carbon backbone act as electron-donor groups, which induce weaker metal/hard-anion interactions, such as with chloride (see figure 5), but stronger metal/soft-anion interactions (π backdonation), such as with carbon dioxide.

The additional hydrogen bond and the presence of the two methyl groups on the carbon backbone, increase the Ni(I) ability to coordinate CO_2.
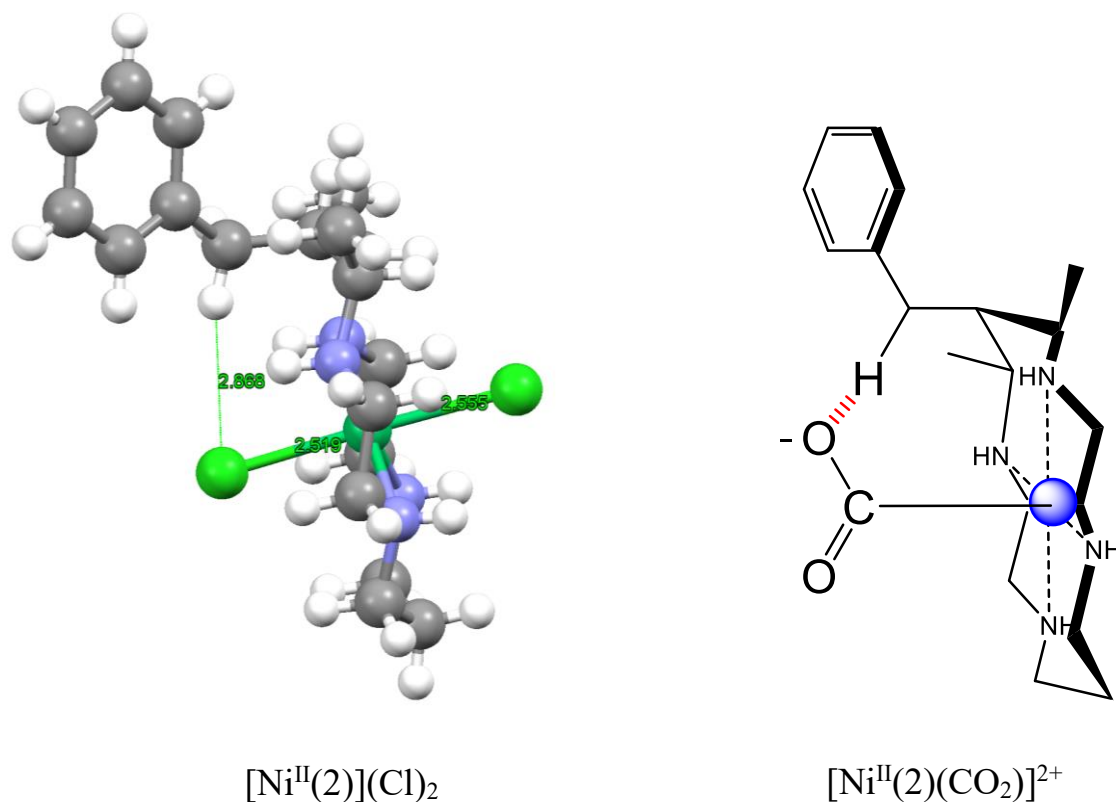
$$[Ni^{II}(2)](Cl)_2 \qquad\qquad [Ni^{II}(2)(CO_2)]^{2+}$$

Figure 8. Lateral view of the molecular crystal structures of $[Ni^{II}(2)](Cl)_2$ and the hypnotized structure of $[Ni^{II}(2)(CO_2)]^{2+}$.

The bismacrocyclic complexes of the ligands 3, 4 and 5 develop a current peak area at pH = 5.8 respectively of 0.25 mC, 0.35 mC, 0.35 mC. They are less active than the equivalent monometallic complex $[Ni^{II}(2)]^{2+}$ but more active than $[Ni^{II}(1)]^{2+}$. This lower activity compare to the related monomer has been found in other bismacrocyclic complex by Crayston and coworkers.[118] We know from many studies that the catalysis takes place predominantly at adsorbed nickel complex sites, thus the most likely explanation is that steric constraints permit strong interaction of only one nickel center of the binuclear complex on the surface. The weaker activity of $[Ni^{II}_2(3)]^{4+}$ is probably due to its face-to-face conformation, which cause the adsorption of only one metal center on the Hg electrode surface and the macrocycle subunit unabsorbed act as an obstacle for the CO_2 coordination by the adsorbed nickel, or there could be a competition for the substrate coordination between the two subunits, the adsorbed one (strongly active) and the unabsorbed one (weakly active).

Noteworthy, $[Ni^{II}(1)]^{2+}$ develop a single catalytic peak, whereas the other catalysts seems to develop 2 partially overlapped catalytic peaks. It could be explained in different ways:

- In the case of $[Ni^{II}(1)]^{2+}$ the CO_2 reduction process can occur only when the $[Ni^{II}(1)]^{2+}$ catalyst is adsorbed on the Hg surface, whereas with the other catalysts under study, the CO_2 reduction process can occur both when the nickel-catalyst is adsorbed on the Hg surface and when the nickel-catalyst is in solution.

- $[Ni^{II}(2)]^{2+}$, $[Ni^{II}_2(4)]^{4+}$, $[Ni^{II}_2(5)]^{4+}$ and $[Ni^{II}_2(3)]^{4+}$ exist in solution as an equilibrium mixture of two species able to catalyze the CO_2 reduction at different potentials. The two species could be a high-spin complex of octahedral elongated geometry and a low-spin complex of square planar geometry.

- All our catalysts, except for $[Ni^{II}(1)]^{2+}$, are capable of reducing other species (e.g. H^+) in addition to CO_2, at a potential similar of that used for CO_2 reduction.

- All our catalysts, except for $[Ni^{II}(1)]^{2+}$, are able to reduce CO_2 to different products, such as formate and CO, or by different catalytic pathway.

- The second peak at -1.45 mV developed by $[Ni^{II}(2)]^{2+}$, $[Ni^{II}_2(4)]^{4+}$, $[Ni^{II}_2(5)]^{4+}$ and $[Ni^{II}_2(3)]^{4+}$ might be due to the reduction of the Ni^I to Ni^0 (favored by the coordination of CO, produced by the CO_2 reduction), which is also active for the CO_2 reduction.

Other authors have reported this "second peak" in similar systems, but its origin is still not completely understood.[128]

All catalyst under exam are able to catalyze the reduction of HCO_3^- at a potential of -1850 mV. At pH = 9, where the concentration of HCO_3^- in solution is maximum, the catalysts exhibit the highest activity. $[Ni^{II}(1)]^{2+}$ seems to be the most active catalyst for the HCO_3^- reduction, however it is difficult to quantify the peak area because of the poor quality of the data in this region.

The reduction of CO_3^{2-} is observed only when using the catalyst $[Ni^{II}_2(3)]^{4+}$, probability because it is able to coordinate CO_3^{2-} better than the other catalyst, thanks to its bismacrocyclic effect,[34] where CO_3^{2-} is coordinated by both metal centers. The molecular crystal structure represented in figure 9 of $[Ni^{II}_2(3)(CO_3)]^{2+}$ reinforce the hypothesis,[130] showing the ability of $[Ni^{II}_2(3)]^{4+}$ to coordinate the CO_3^{2-} preferentially inside the cavity, between the two Ni^{II} centers rather than outside coordinated by only one Ni^{II}.
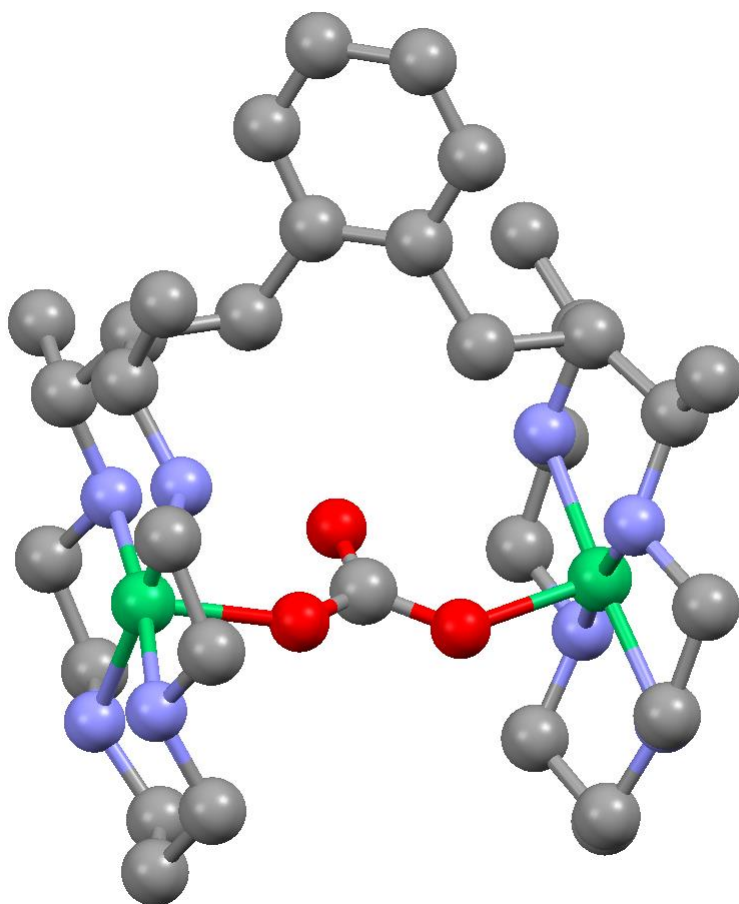
Figure 9. molecular crystal structure of $[Ni^{II}(3)(CO_3)]^{2+}$.[130] The perchlorate anions outside the cavity and the hydrogens have been omitted for clarity.

The figure 7-f show that increasing ten times the concentration of Na_2CO_3, the catalytic current peak area increases ten times.

It's also noteworthy that when the pH is over 11 (values reached by NaOH addition), the current peak area at -1900 mV, referred to the CO_3^{2-} catalyzed reduction, decrease, as we can see from the blue trend in figure 7-f. We can explain this behavior taking into account that increasing the pH the concentration of OH^- in solution increases. The competition between CO_3^{2-} and the coordinating anion hydroxide for the available binding sites results in a lower CO_3^{2-} reduction rate. Additional information could be extrapolated from another difference between $[Ni^{II}(1)]^{2+}$ and the other catalysts is the trend of the CO_2 reduction peak, changing the pH value. $[Ni^{II}(1)]^{2+}$ has no shift of the peak potential decreasing the pH from 11 to 5, the current is increased but the potential maintains the value of -1350 mV. The other catalysts present a shift of the CO_2 reduction peak from -1250 mV at pH = 8 to -1350 mV at pH = 5. Unfortunately, this particular behavior is difficult to be

interpreted on the base of the available data.

In general, the CO_2 reduction compared to HCO_3^- and CO_3^{2-} reduction is favored thanks for the less negative applied potential required to reduce the substrate. On the other hand, bicarbonate and carbonate are more soluble in water than carbon dioxide, permitting to improve the catalysis process by increase the concentration of the substrate in solution.

7.2.1.4   CO₂ electrocatalysis by copper macrocyclic complexes

The Figure 10 shows the cyclic voltammograms recorded at different value of pH (from pH = 11 to pH = 5, decreasing the pH with a 6 M solution of HCl), of a 1e^{-4} M solution of catalyst in water and 0.1 M of substrate Na_2CO_3.
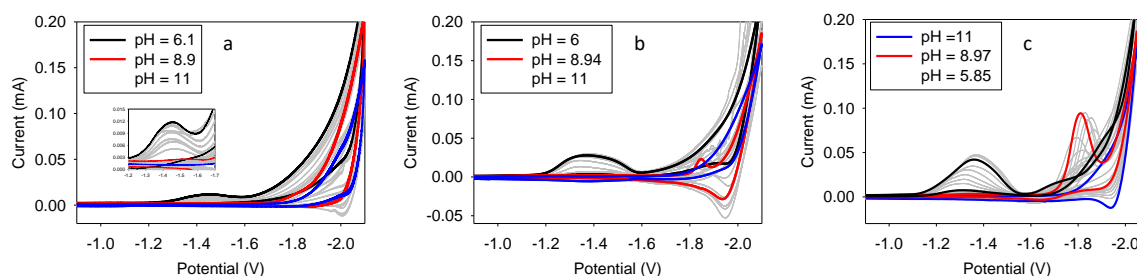
Figure 10. Cyclic voltammograms recorded at different values of pH (from pH = 11 to pH = 5) of a solution containing 0.1 M of Na_2CO_3 in water and 1e^{-4} M of: (a) $[Cu^{II}(1)](ClO_4)_2$, (b) $[Cu^{II}(2)](ClO_4)_2$, (c) $[Cu_2^{II}(3)](ClO_4)_4$.

From pH = 8 to pH = 5, all catalyst produces an irreversible peak. The potential of the peak maximum varies in a range between -1300 mV and -1450 mV vs Ag/AgCl (sat'd NaCl). From pH = 10.5 to pH = 6, the $[Cu^{II}(2)](ClO_4)_2$ and $[Cu^{II}_2(3)](ClO_4)_2$ develop an irreversible peak at -1800 mV. Over pH = 10.5, no peaks are observable.
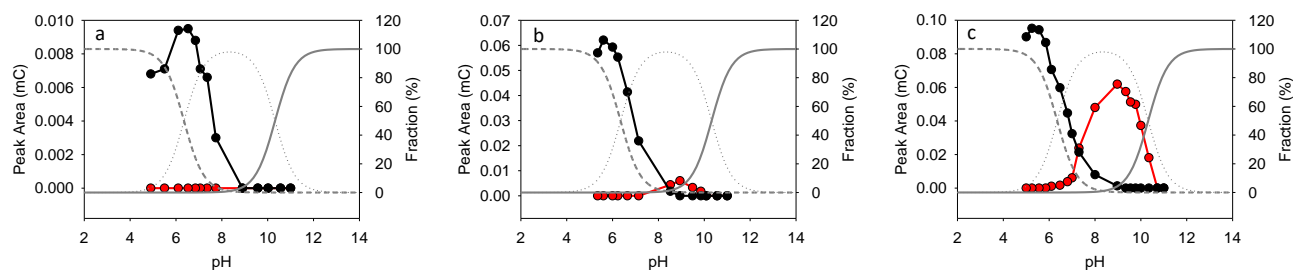
Figure 11. Current peak area versus pH graphs related to the CO_2/HCO_3^- reduction, catalyzed by: (a) $[Cu^{II}(1)](ClO_4)_2$, (b) $[Cu^{II}(2)](ClO_4)_2$, (c) $[Cu_2^{II}(3)](ClO_4)_4$. All the starting solution contain 1e^{-4} M of catalyst,

0.1 M of Na_2CO_3 in water. Solid grey line: fraction (%) of CO_3^{2-} varying the pH; dotted line: fraction (%) of HCO_3^- varying the pH; dashed grey line: fraction (%) of CO_2 varying the pH. Red line and scatter plot: current peak area at -1.80 V varying the pH; black line and scatter plot: current peak area at -1.35 V varying the pH.

The current peaks area at -1350 mV and -1800 mV at different value of pH are illustrated in figure 11, respectively with black and red circles and lines.

The superimposition of the CO_2 pH distribution, follows the current peak area at -1350 mV against pH. This behavior could be explained by the assumption that the catalyst under study are able to catalyze the reduction of CO_2, where the reaction rate is controlled by the CO_2 concentration. At pH = 5.8, when the substrate is prevalently present in solution as CO_2, the catalysts are able to reduce larger amounts of CO_2. Under 5.8 the activity toward CO_2 slightly decreases because the competition with the H^+ reduction became more important. The catalyst activity of the macrocyclic complexes at pH = 5.8 follow the order: $[Cu^{II}_2(3)]^{2+} > [Cu^{II}_2(2)]^{4+} >> [Cu^{II}(1)]^{2+}$. The reason for the higher catalytic activity of $[Cu^{II}(2)]^{2+}$ than $[Cu^{II}(1)]^{2+}$ is in line with what we explained for the nickel complexes: the two methyl groups on the carbon backbone act as electron donor, increasing the Cu(I) ability to coordinate CO_2 and for the presence of the additional hydrogen bond between the oxygen donor atom of CO_2 and the benzyl hydrogen. $[Cu^{II}_2(3)]^{2+}$ is more active than $[Cu^{II}_2(2)]^{4+}$, showing a different situation compared to the related nickel complexes.

The HCO_3^- reduction occurs mainly at pH = 9, because at this value of pH there is the maximum concentration of this species. $[Cu^{II}_2(3)]^{4+}$ is the most active catalyst with a peak area of 0.06 mC at pH = 9, while $[Cu^{II}(2)]^{2+}$ is only slightly active with a peak area of 0.006 mC at pH = 9, ten times less active than the related binuclear complex. $[Cu^{II}(1)]^{2+}$ shows no activity toward HCO_3^- reduction. Probably, $[Cu^{II}_2(3)]^{4+}$ is able to chelate HCO_3^- inside the cavity, increasing its ability to reduce this anion.

$[Cu^{II}(1)]^{2+}$ has no shift of the peak potential related to the CO_2 reduction, the peak current becomes higher while decreasing the pH from 11 to 5 but the potential maintains the value of -1450 mV. The other catalysts present a shift of the CO_2 reduction peak from -1250 mV at pH = 8 to -1450 mV at pH = 5.

The reason for the $[Cu^{II}(2)]^{2+}$ catalytic peak falling at less negative potential than $[Cu^{II}(1)]^{2+}$ is in line with what we explained for the nickel complexes: the presence of the two methyl groups on the carbon backbone lower the e_g energy level favoring the Cu(II) reduction, and the presence of the additional hydrogen bond could improve the CO_2 binding, stabilizing the Cu(I) species.

Noteworthy, $[Cu^{II}_2(3)]^{4+}$ has a more defined peak at 1800mV (at pH = 9) than the related Nickel

117

complex.

Compared to the related Nickel macrocyclic complexes, the Copper macrocyclic complexes seem less active both toward CO_2 and HCO_3^-, and inactive toward CO_3^{2-}. The reason might be attributed to the tendency of Cu(II) to disproportionate in Cu(I) and Cu(0). By mercury electrode is not possible to verify if copper complexes undergo demetallation caused by the disproportion of Cu(II), because the oxidation of mercury occur to potential more negative than the typical anodic peak of Cu(0) to Cu(II), which occur at around 0 mV vs Ag/AgCl with glassy carbon working electrode.[125]

7.2.2 Electrocatalysis by environment-friendly electrodes

For nearly two decades, the CO_2 reduction capabilities of $Ni^{II}(cyclam)^{2+}$ and its analogues were almost exclusively studied with a Hg working electrode, because of the large negative potential window possible with mercury in aqueous solutions and its ability to enhance the catalytic activity of the catalysts.

Glassy carbon working electrodes were tested by Fujihira and co-workers in 1990 and recently used by Froehlich and Kubiak to measure the faradaic efficiency of several nickel cyclam complexes.[115] They found that the activity on mercury is much greater than that on glassy carbon and explained this difference on the base of the "self-poisoning" behavior that involved Ni^{II}cyclam and simil-Ni^{II}cyclam complexes during the catalyzed CO_2 reduction, which consist in the formation of the species $[Ni^{I}(cyclam)(CO)]^+$ and $Ni^0(CO)_4$ between the reduced catalyst Ni(I) and Ni(0) respectively and the main product CO, a schematic representation is shown in figure 12.[124] This self-poisoning behavior is presumed to be minimized by interaction of the complex with the Hg surface, because of the stabilization of a more planar geometry of cyclam complexes that more readily releases CO.[122,124] The acceleration of CO release is one of the most important property that catalysts must have in order to develop a high catalytic current, since this could be the rate determining step of the CO_2 to CO reduction (see figure 1).
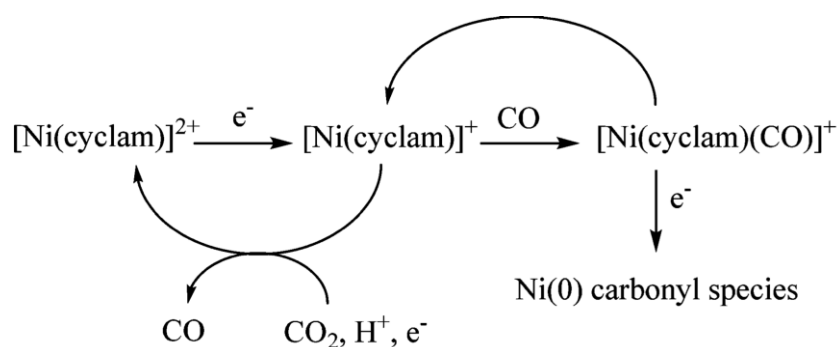
Figure 12. Proposed Degradation Pathway of $[Ni(cyclam)]^{2+}$.[124]

We studied the CO_2 reduction catalyzed by nickel and copper complexes of the ligands 1, 2, and 3, using bismuth working electrode (Bi), with the idea to find an electrode more environmentally benign than mercury and more efficient than glassy carbon (GC). Glassy carbon was also used as working electrode, in order to compare the results with those obtained with Hg and Bi electrodes.

7.2.2.1 Choice of the catalyst concentration

Figure 13 represent the cyclic voltammograms of a 0.05 M solution of NaCl, CO_2 saturated (pH = 4.2), and recorded at different concentration of the catalyst $[Ni^{II}(1)](ClO_4)_2$, using glassy carbon (fig. 13-a) and bismuth (fig. 13-b) as a working electrode, Ag/AgCl, NaCl (saturated) electrode as reference electrode, and a Pt wire as auxiliary electrode. When the catalyst is absent (dashed black line) there are no reduction peaks, whereas in presence of the catalyst, an irreversible peak occurs. Using GC and Bi working electrode, increasing the catalyst concentration results in an increase of the peak current and the related reduction potential falls to increasingly more negative values. Using glassy carbon working electrode (figure 13-a) the solvent discharge starts at a less negative potential when increasing the concentration of the catalyst, partially hiding the CO_2 reduction peak. This behavior could be explained by taking into account the mechanism by which H^+ is reduced to H_2 (see figure 3). The second electron is provided to $[LNi-H]^{2+}$ by another reduced catalyst molecule, $[LNi]^+$, thus the higher the concentration of catalyst the more likely is the second electron transfer step, favoring the H^+ catalysis (H+ reduction Bologna). Bi electrode doesn't have such a behavior probably due to its ability to absorb the catalyst.

Taking into account all these aspect, we decided to use a catalyst concentration of $1 \cdot 10^{-3}$ M, a good compromise between the peak catalytic current, the peak potential and the solvent discharge level. Noteworthy, figure 13-a shows an anodic peak at -0.5 V (catalyst concentration = $5 \cdot 10^{-3}$ M) and one at 0 V (catalyst concentration = $1 \cdot 10^{-2}$ M), possibly due to the presence of Ni(0) carbonyl species.[124]
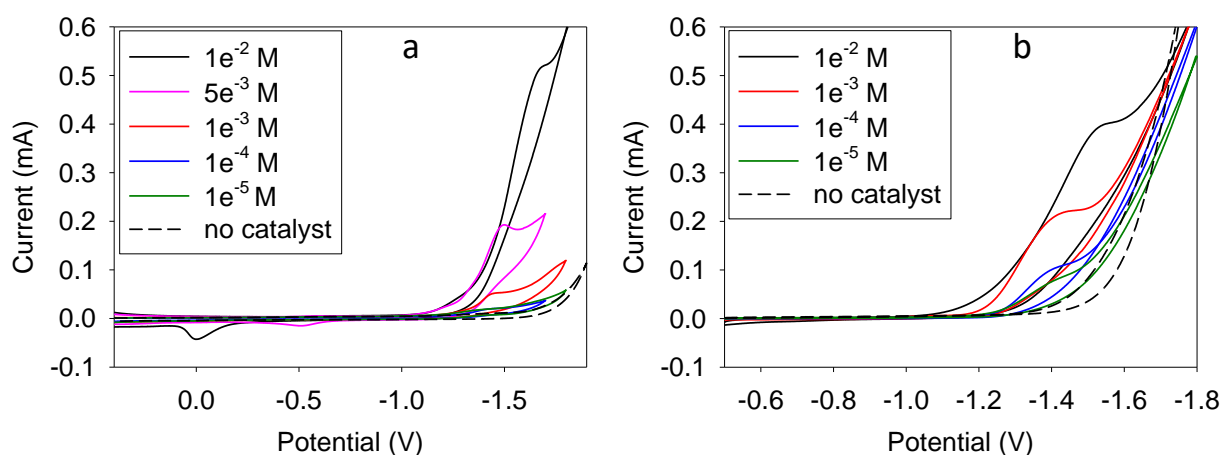
Figure 13. Cyclic voltammograms of a 0.05 M solution of NaCl, CO_2 saturated (pH = 4.2), and recorded at different concentration of the catalyst $[Ni^{II}(1)](ClO_4)_2$, using (a) glassy carbon (GC) and (b) bismuth (Bi) as a working electrode, Ag/AgCl, NaCl (sat'd) electrode as reference electrode, and a Pt wire as auxiliary electrode.

7.2.2.2 GC and Bi electrode behavior for H^+ and CO_2 reduction

In order to distinguish the macrocylic complexes catalytic activity from the working electrode catalytic activity toward CO_2 reduction, we performed cyclic voltammograms in the absence of macrocyclic catalyst but in presence of the substrate (CO_2) at different value of pH, starting with a 0.1 M solution of $NaHCO_3$ (pH = 8.2), and decreasing the pH by adding HCl 6M (Figure 14). As we can see from the figure 14-a, GC electrode doesn't develop peaks from pH = 8.2 to pH = 3.8 but at pH = 3 it develops a defined peak at -1.65 V, considering the high concentration of H^+ a that pH, the peak is probably due to the H^+ reduction to H_2. Bi electrode (fig. 14-b) doesn't develop peaks from pH = 8.2 to pH = 3 but at pH = 2.6 there is a well-defined peak at -1.24 V, due to the H^+ reduction.
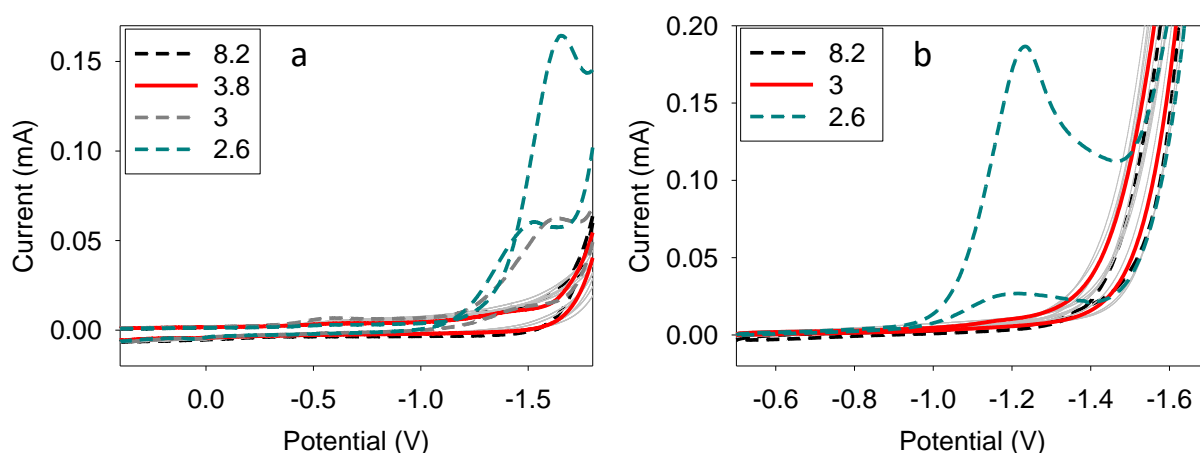
Figure 14. Cyclic voltammograms recorded in 0.1 M solution of $NaHCO_3$, 0.05 M of NaCl at differente value

of pH, using Ag/AgCl, NaCl (sat'd) reference electrode, Pt auxiliary electrode, (a) GC working electrode and (b) Bi working electrode.

Figure 15 shows a series of voltammograms in the absence of macrocyclic catalyst and substrate at different value of pH. The developed peaks are very similar to those develop in presence of the substrate, both in term of peak reduction potential and current, confirming that the peaks are produced by the H^+ reduction and not by the CO_2 reduction. We can conclude that the GC and Bi electrode, under this experimental condition, are not able to reduce CO_2, but at acid pH (< 4), they can reduce H^+ to H_2. Noteworthy, GC electrode, in presence of CO_2, start to reduce H^+ at pH less acid than Bi electrode, on the other hand, GC need a potential more negative (-1.64 V) than that needed to Bi electrode (-1.24 V).
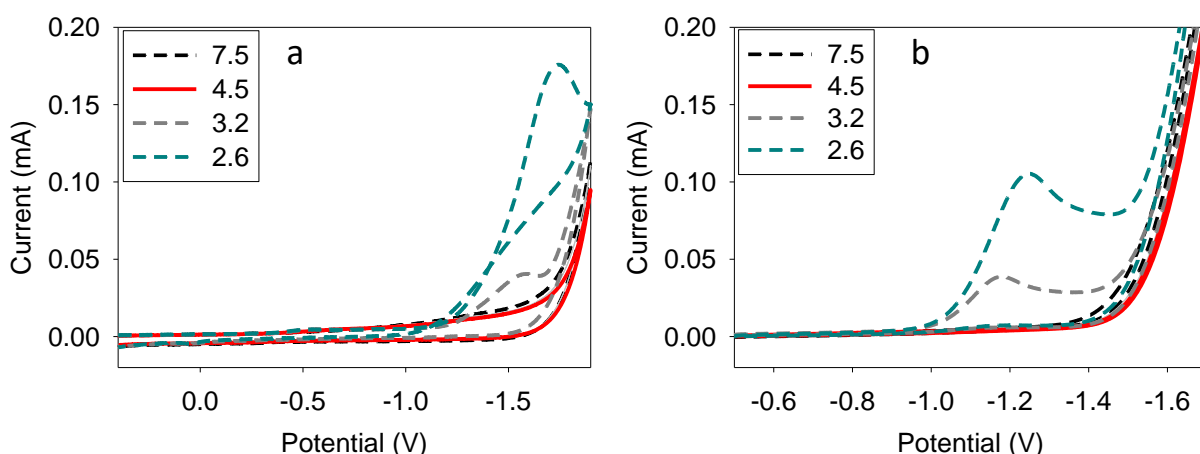
Figure 15. Cyclic voltammograms recorded in 0.05 M of NaCl at differente value of pH, using Ag/AgCl, NaCl (sat'd) reference electrode, Pt auxiliary electrode, (a) GC working electrode and (b) Bi working electrode.

7.2.3   Nickel complexes catalytic activity for H^+ reduction

In order to distinguish the macrocylic complexes catalytic activity toward CO_2 reduction from their catalytic activity toward H^+ reduction we performed cyclic voltammograms in the absence of CO_2 sources but in presence of the catalyst, at different values of pH by adding diluted HCl and NaOH solutions.

As we can see from the figure 16, all the macrocyclic catalysts, using either GC or Bi electrode, don't develop peaks from pH = 8.2 to pH = 3.5 but at pH < 3.5 they develop a peak, due to the H^+ reduction

to H₂. Comparing the peak cathodic potentials (E$_{pc}$) related to H$^+$ reduction in the presence and in absence of catalysts (see table 1) we observe that, with a GC working electrode all of the considered catalysts make the potential slightly less negative than the value observed in the absence of any catalyst, differently, when working with a Bi electrode, [Ni^{II}(1)]$^{2+}$ don't influence the potential, whereas the presence of [Ni^{II}(2)]$^{2+}$ or [Ni$_2^{II}$(3)]$^{4+}$ makes more difficult the H$^+$ reduction, moving the potential to a 190 mV more negative value (from -1.24 V to -1.43 V).
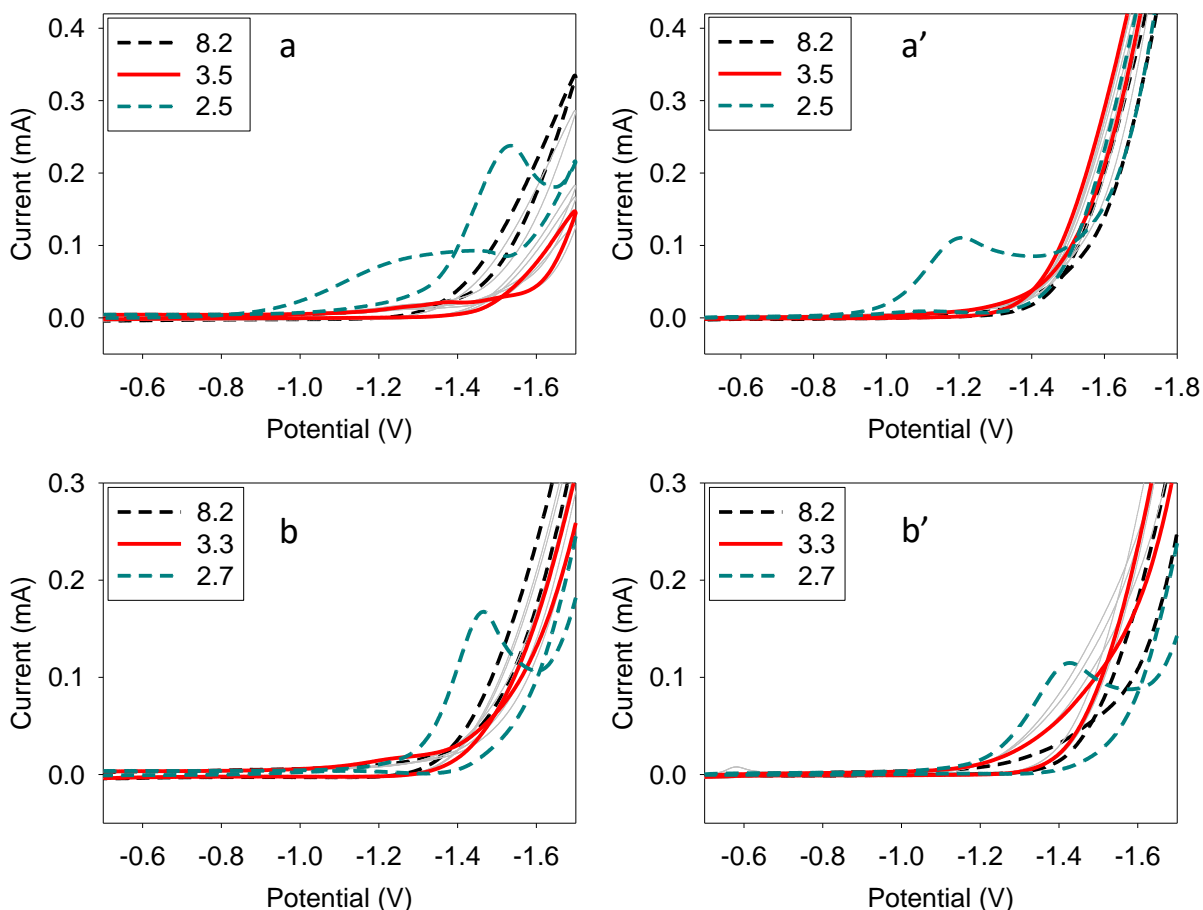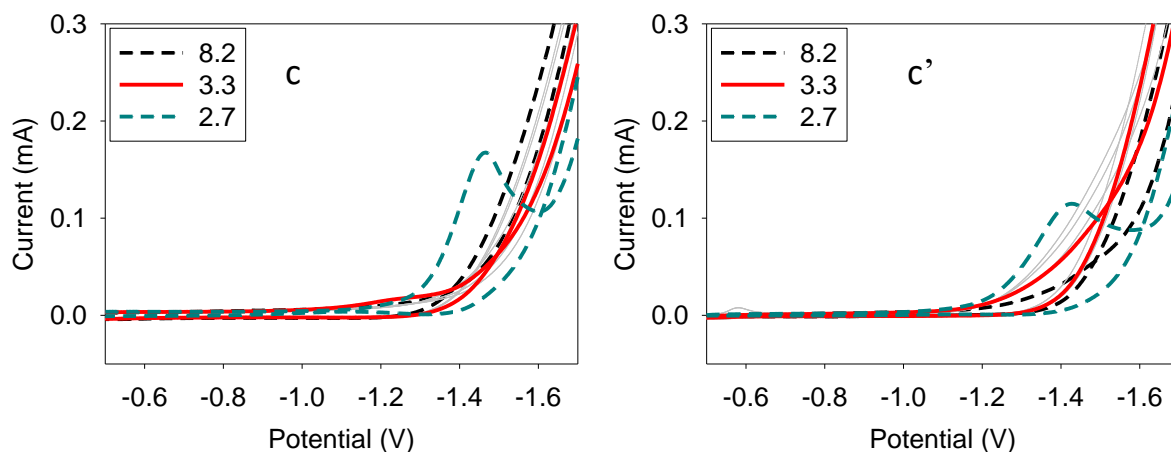
Figure 16. Cyclic voltammograms recorded in 0.05 M solution of NaCl and $1e^{-3}$M of (a) $[Ni^{II}(1)]^{2+}$, GC electrode; (a') $[Ni^{II}(1)]^{2+}$, Bi electrode; (c) $[Ni^{II}(2)]^{2+}$, GC electrode; (d) $[Ni^{II}(2)]^{2+}$, Bi electrode; at different value of pH.

The behavior of $[Ni^{II}(2)]^{2+}$ and $[Ni_2^{II}(3)]^{4+}$, which move the reduction potential of the H^+ to more negative values, is a great advantage in terms of selectivity, since it could favor the CO_2 reduction over that of H^+.

Table 1. Peak cathodic potentials (E_{pc}) related to H^+ reduction to H_2 in presence of catalyst and in absence of catalyst.

Catalyst	E_{pc}, GC (V)	E_{pc}, Bi (V)
$[Ni^{II}(1)]^{2+}$	-1.53	-1.2
$[Ni^{II}(2)]^{2+}$	-1.47	-1.43
$[Ni_2^{II}(3)]^{4+}$	-1.47	-1.43
No catalyst	-1.64	-1.24

7.2.3.1 Nickel complexes catalytic activity for CO_2 reduction

Thanks to the performed cyclic voltammetry experiments, we know that the CO_2 reduction does not occur in the absence of the catalysts and the H^+ reduction occur only setting a pH < 4, also in absence of catalysts.

Thus, at pH > 4, the concomitant presence of the catalyst and the substrate imply that the only reducible specie is the CO_2 and its equilibrium species (HCO_3^- and CO_3^{2-}). The cyclic voltammograms represented in figure 17 are recorded on a 0.1 M solution of $NaHCO_3$, 0.05 M of NaCl and $1 \cdot 10^{-3}$ M of catalyst (17-a, 17-b and 17-c respectively in presence of $[Ni^{II}(1)]^{2+}$, $[Ni^{II}(2)]^{2+}$ and $[Ni^{II}(3)]^{4+}$) from

pH = 8.2 to pH = 4 (adding HCl 6 M) using glassy carbon working electrode. As we can see from the figures 17-a', 17-b' and 17-c', which show the peak areas at different value of pH respectively related to the collected cyclic voltammograms of 17-a, 17-b and 17-c, the three catalysts start to show CO_2 reduction peaks at pH < 8, where the concentration of CO_2 becomes significative (see CO_2 distribution diagram in figure 7-a). From pH = 8 to pH = 4 we can assign the peaks to the CO_2 reduction (considering the pH and the reduction potential we can exclude the reduction of HCO_3^- and CO_3^{2-}), at pH < 4 the observed peaks are the combination of two reductive process: the CO_2 and the H^+ reductions. $[Ni^{II}(2)]^{2+}$ and $[Ni^{II}_2(3)]^{4+}$ reach their maximum activity for CO_2 reduction at pH = 5.9 (figure 17-b' and 17-c'), whereas $[Ni^{II}(1)]^{2+}$ reach the maximum at pH = 7.2 and its activity remains stable decreasing the pH to 4.9. This means that $[Ni^{II}(1)]^{2+}$ requires a lower concentration of proton donor to explicate its maximum catalytic activity for CO_2 reduction. The optimal pH for the CO_2 reduction must take into account three factors: CO_2 concentration, H^+ - CO_2 competition and the two steps of the CO_2 catalytic cycle that involve H^+ (PCET and C-O cleavage).

Comparing the catalytic peak area at pH = 5.9 of the three catalysts $[Ni^{II}(1)]^{2+}$ (17-a'), $[Ni^{II}(2)]^{2+}$ (17-b') and $[Ni_2^{II}(3)]^{4+}$ (17-c'), $[Ni^{II}(2)]^{2+}$ seem to be the most active, with a peak area of 0.058 mC, which is 5 times greater than that of $[Ni^{II}(1)]^{2+}$ (peak area: 0.012 mC) and 1.5 times greater than that of $[Ni_2^{II}(3)]^{4+}$ (peak area: 0.039 mC). Thus, the catalytic activity of the macrocyclic complexes, using GC electrode, at pH = 5.9 follow the order: $[Ni^{II}(2)]^{2+}$ > $[Ni^{II}_2(3)]^{4+}$ > $[Ni^{II}(1)]^{2+}$. $[Ni^{II}(2)]^{2+}$ develop a peak larger than those developed by the other two catalyst because it consist in two overlapped peaks, the first falls at -1.37 V and the second falls at -1.62 V (blue solid line in figure 17-b). Others have reported this splitted peak in similar systems, but its origin is still not completely understood some hypothesis are described in the chapter 7.2.1.3. Noteworthy, at pH = 5.9, $[Ni^{II}(1)]^{2+}$ and $[Ni^{II}_2(3)]^{4+}$ develop a peak falling at the same potential of -1.44 V (Figure 17-a and 17-c). $[Ni^{II}_2(3)]^{4+}$ is less active than the equivalent monometallic complex, but comparing its activity with that of $[Ni^{II}(1)]^{2+}$ we can suppose it is able to catalyze CO_2 reduction with both macrocyclic units in a similar way of $[Ni^{II}(1)]^{2+}$ (presumably coordinating CO_2 externally its cavity) but without the extra activity of the related monometallic complex $[Ni^{II}(2)]^{2+}$. At acid pH (pH < 2.5), an intense peak occurs (cyan dashed line in figure 17-a, 17-b, 17-c), which is ascribable to the H^+ reduction for the similarity with the peaks recorded in absence of either catalyst or the substrate. At pH = 2.3, $[Ni^{II}(1)]^{2+}$ develops a peaks at -1.43 V, falling at a very close potential to that of CO_2 reduction (-1.44 V), preventing the selective reduction of CO_2 at acidic pH. $[Ni^{II}(2)]^{2+}$ and $[Ni^{II}(3)]^{4+}$ present two overlapped peaks at pH

= 2.5, one falling at more negative potential (-1.6 V), which is referred to the H^+ reduction, the other one falling at a similar potential of the CO_2 reduction peaks observed at pH > 4, thus related to the CO_2 reduction. This behavior is a great advantage in term of selective reduction of CO_2 at acidic p. Thus, $Ni^{II}(2)]^{2+}$ and $[Ni^{II}(3)]^{4+}$, permit to have a versatile system, able to reduce CO_2 in a large window pH.

Figure 17. (a), (b), (c) represent the cyclic voltammograms recorded on a solution consist on 0.01M of NaHCO$_3$, 0.05 M of NaCl and, respectively 1e^{-3} M of $[Ni^{II}(1)]^{2+}$, $[Ni^{II}(2)]^{2+}$, $[Ni^{II}(3)]^{4+}$, from pH = 8.2 to pH = 2.3 (adding HCl 6 M), using glassy carbon working electrode. (a'), (b'), (c'), represent the peak areas at different value of pH respectively related to the collected cyclic voltammograms (a), (b), (c). Red circles: peak areas related to the CO_2 reduction peaks, blue circles: peak areas related to the H^+ reduction peaks.

Figure 18 shows the CVs obtained using a Bismuth electrode (Bi). As already observed with GC electrode, all the catalysts, start to be active toward CO_2 reduction at pH < 8. $[Ni^{II}(1)]^{2+}$, $[Ni^{II}(2)]^{2+}$ and $[Ni^{II}_2(3)]^{4+}$ reach their maximum activity for CO_2 reduction at pH = 5.9 (figure 18-a', 18-b' and 18-c').

The catalyst activity of the macrocyclic complexes, using Bi electrode, at pH = 5.9 follow the order: $[Ni^{II}(2)]^{2+} > [Ni^{II}(1)]^{2+} >> [Ni^{II}_2(3)]^{4+}$. The $[Ni^{II}_2(3)]^{4+}$ activity is much lower than the other two

catalysts, its peak area at pH = 5.9 (figure 18-c') is at least 10 times smaller than the other two catalysts. This might be explained by considering the involvement of adsorptive phenomena. We suppose that only one macrocyclic unit of $[Ni^{II}_2(3)]^{2+}$ is adsorbed on the Bi electrode (the more active for CO_2 reduction), whereas the other macrocyclcic subunit (the less active) act as an hindering group, which limit the CO_2 coordination by the active site, becoming itself the site for CO_2 reduction, indeed, it shows a peak area similar to that developed by $[Ni^{II}(1)]^{2+}$ with GC electrode (0.01 mC), where the reductive process is not adsorptive.

Noteworthy, at pH = 5.9, $[Ni^{II}(1)]^{2+}$ develop a peak falling at -1.38 V (Figure 18-a), whereas, $[Ni^{II}(2)]^{2+}$ and $[Ni^{II}_2(3)]^{4+}$ develop a peak at -1.31 V, showing an advantage in term of less negative potential, that results in a more efficient catalysis. Interestingly, at approximately pH = 2.5 (gray solid line in figure 18-a, 18-b and 18-c) on the base of the reduction potential, it seems to selectively occur the CO_2 reduction, while the H^+ reduction peak is not observed, in contrast with the experiments performed in presence of catalyst and in absence of substrate, where the H^+ reduction was clearly visible catalytic peaks developed at pH = 2.5 fell at different reduction potentials than those developed in presence of substrate. This is probably due to the competition between CO_2 and H^+ coordination to the Ni(I) center, which imposes to have a higher H^+ concentration in order to carry out its reduction to H_2.

At more acidic pH (pH = 2.1), an intense peak occurs (cyan dashed line in figure 18-a, 18-b, 18-c), which is ascribable to the H^+ reduction for the similarity, both in term of reduction potential and peak current, with the peaks recorded in absence of either catalyst or the substrate. $[Ni^{II}(1)]^{2+}$ develops a peaks at -1.31 V, falling at a less negative potential than that of CO_2 reduction (-1.38 V), impeding the selective reduction of CO_2 at strongly acidic pH. Instead, $[Ni^{II}(2)]^{2+}$ and $[Ni^{II}_2(3)]^{4+}$ develop two overlapped peaks at pH = 2.1, one falls at more negative potential (-1.47 V), which is referred to the H^+ reduction, the other one falls at a similar potential of the CO_2 reduction peaks at pH > 4 (-1.25 V), thus related to the CO_2 reduction. Thus, the selective reduction of CO_2 is still possible at strongly acidic pH.

In general, the catalysts are more active using Bi electrode than GC electrode. $[Ni^{II}(2)]^{2+}$ is almost 3 times more active with Bi than with GC, $[Ni^{II}(1)]^{2+}$ is 7 times more active with Bi than with GC. Moreover, they catalyze the CO_2 reduction at less negative potentials, as shown in table f. These two effects are probably due to the ability of Bismuth to absorb the catalyst on its surface, which accelerate the CO release, improving the catalyst efficiency, and modify the catalyst conformation, lowering the overpotential.

Using Bi electrode, both $[Ni^{II}(2)]^{2+}$ and $[Ni^{II}_2(3)]^{4+}$, have the advantage to reduce CO_2 at less negative potential than $[Ni^{II}(1)]^{2+}$ (figure 18).
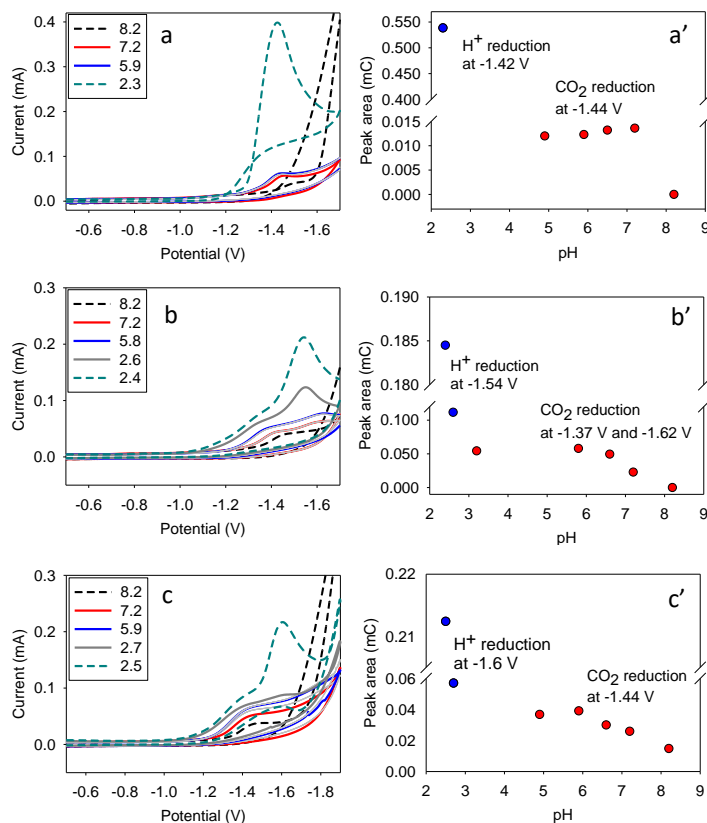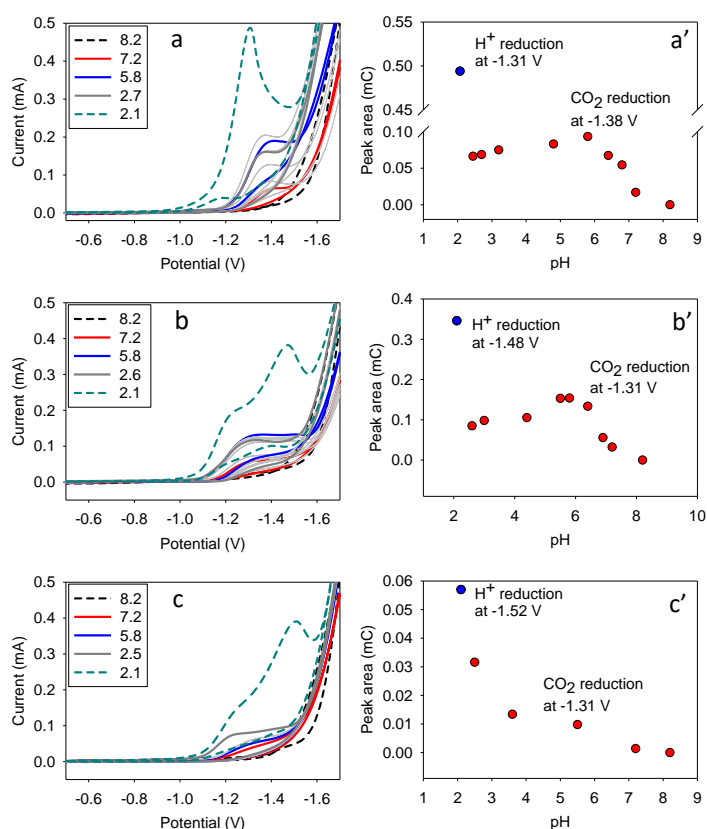

Figure 18. (a), (b), (c) represent the cyclic voltammograms recorded on a solution consist on 0.01M of $NaHCO_3$, 0.05 M of NaCl and, respectively $1e^{-3}$ M of $[Ni^{II}(1)]^{2+}$, $[Ni^{II}(2)]^{2+}$, $[Ni^{II}(3)]^{4+}$, from pH = 8.2 to pH = 2.1 (adding HCl 6 M), using bismuth working electrode. (a'), (b'), (c'), represent the peak areas at different value of pH respectively related to the collected cyclic voltammograms (a), (b), (c). Red circles: peak areas related to the CO_2 reduction peaks, blue circles: peak areas related to the H^+ reduction peaks.

7.2.3.2 Copper complexes catalytic activity for CO_2 reduction

No catalytic activity has been observed by using copper macrocyclic complexes represented in figure s. This is possibly due to the disproportion of the reduced Cu(I) forms to Cu(0) and Cu(II).[125]

7.3 Conclusion

With the present work we investigated three factors that influence the efficiency of the CO_2 reduction in water: type of catalyst, pH and type of working electrode. The nickel complexes under studies have

shown a higher catalytic activity compared to the equivalent copper complexes, since the latter suffer of disproportion of Cu(I). The functionalization of the cyclam carbon backbone with two methyl groups and a benzyl group results in an improvement of the catalyst, both in term of lower overpotential and higher efficiency, the reasons are summarize as following:

- The benzyl hydrogen might improve the affinity for CO_2 and decrease the affinity for H^+ thanks to the additional hydrogen bond with the CO_2 oxygen atoms.
- The two methyl groups, acting as electron donor groups, lower the e_g energy level of the macrocyclic complex and consequently also the overpotential, and improve the CO_2 coordination, favoring the π backdonation (for a more detailed explanation see results and discussion section).

Compared to the analogous monomacrocyclic complex, the bimacrocyclic complexes don't have an advantage in the CO_2 reduction since they have only one active macrocyclic unit, which is the one adsorbed on the electrode surface. With Hg electrode the catalysts can reduce CO_2, HCO_3^- and CO_3^{2}, where the latter can be reduced only by $[Ni_2(3)]^{4+}$, thanks to its ability to coordinate anions between the two metal centers.

The optimal pH for CO_2 reduction was found to be around pH $= 5.9$ whereas for HCO_3^- higher values were attained with pH $= 8.5$.

Moreover, $[Ni^{II}_2(3)]^{4+}$ and $[Ni^{II}(1)]^{2+}$ showed to selectively reduce CO_2 even at acidic pH, where the competition with the parallel H^+ reduction is higher.

Using more environmental-friendly working electrode, bismuth and glassy carbon, the CO_2 catalysis is still achievable. Bismuth proved to be better working electrode than glassy carbon, both in term of improvement of the catalyst efficiency and lowering of the overpotential. Hg remain the best electrode to enhance the catalytic proprieties of the macrocyclic complexes, but considering the lower toxicity of Bi, it could still be a good alternative to Hg.

7.4   Experimental section

7.4.1   General Procedures and Materials

All reagents and solvents were supplied by Aldrich and used as received. The water employed was triply distilled. All electrochemical measurements and characterizations were carried out with a BASI PWR-3 power module and a standard three-electrode EF-1085 C-3 cell, using a platinum wire as auxiliary electrode and a Ag/AgCl/NaCl (sat'd) electrode as reference electrode (see figure 19). The

working electrode was either a Hanging Mercury Drop Electrode (HDME) (area = 0.92 mm^2), a bismuth electrode (Bi) (area = 7.065 mm^2) or a Glassy Carbon electrode (GC) (BAS MF-2012, area = 7.065 mm^2).

Electrochemical potentials are referred to Ag/AgCl/NaCl (sat'd).

An Orion SA 520 pH meter was used for pH measurements.
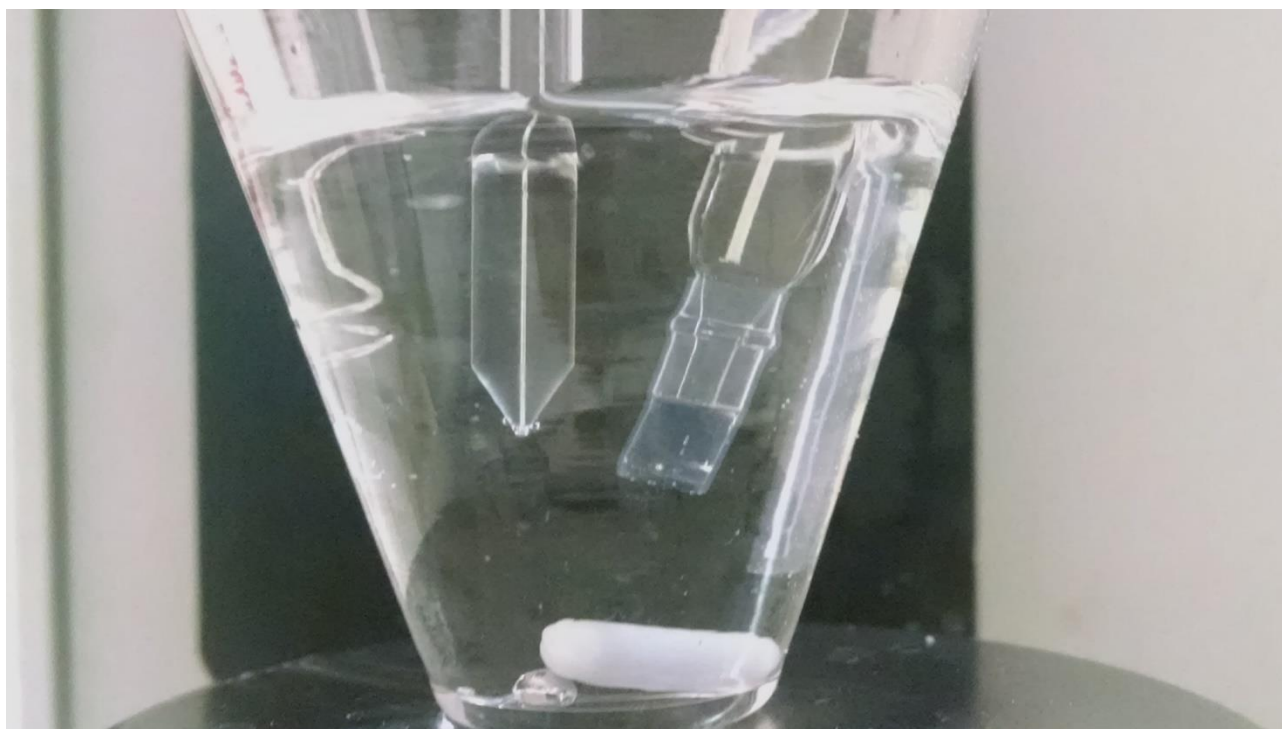
Figure 19. Three-electrode cell used for the experiments. On the left the platinum auxiliary electrode, in the middle the hanging mercury drop electrode, on the right the Ag/AgCl, NaCl (sat'd) reference electrode.

7.4.2 Electrochemistry

Measurements in cyclic voltammetry (CV) to evaluate the reduction potential of the macrocyclic complexes were performed on an aqueous solution consist of 0.05 M of NaCl (supporting electrolyte) at pH = 7 and $1e^{-3}$ M of macrocyclic complex, in the potential range from -1200 mV to -1700 mV and with a scan rate of 100 mV s^{-1}. HDME was used as working electrode, with GC and Bi the water discharge covered the macrocyclic complexes' redox waves.

In order to study the catalytic reduction of the neutral species CO_2 and anionic species HCO_3^- and CO_3^{2-}, CV experiments have been performed as following, slightly changing on the base of the working electrode: **HDME.** In order to study the catalytic reduction of the neutral species CO_2 and

anionic species HCO_3^- and CO_3^{2-}, cyclic voltammetry experiments have been conducted on an aqueous solution consist of 0.1 M of sodium carbonate (CO_2 source), 0.05 M of NaCl (supporting electrolyte) and $1e^{-4}$ M of catalyst in the potential range from -800 mV to -2100 mV and with a scan rate of 100 mV s^{-1}. The voltammograms have been recorded using different value of pH from 11 to 5 by adding a 6 M solution of hydrogen chloride. **GC.** Cyclic voltammetry experiments have been conducted on an aqueous solution consist of 0.1 M of sodium bicarbonate (CO_2 source), 0.05 M of NaCl (supporting electrolyte) and $1e^{-3}$ M of catalyst in the potential range from -500 mV to -1900 mV and with a scan rate of 100 mV s^{-1}. The voltammograms have been recorded using different value of pH from 8.2 to 2 by adding a 6 M solution of hydrogen chloride. **Bi.** Cyclic voltammetry experiments have been conducted on an aqueous solution consist of 0.1 M of sodium bicarbonate (CO_2 source), 0.05 M of NaCl (supporting electrolyte) and $1e^{-3}$ M of catalyst in the potential range from -500 mV to -1900 mV and with a scan rate of 100 mV s^{-1}. The voltammograms have been recorded using different value of pH from 8.2 to 2 by adding a 6 M solution of hydrogen chloride. The same experimental condition is used for CV experiments performed in absence of catalyst and/or substrate.

Before each CV experiments, the solutions are bubbled for 5 min with N_2 to ensure the absence of O_2 in solution.

7.4.3   Synthesis

Ligand 1 (cyclam = 1,4,8,11-tetrazazcyclotetradecane) and $[Ni^{II}(1)](ClO_4)_2$ were synthesized according to the literature procedure.[13]

$[Cu^{II}(1)](ClO_4)_2$ was synthesized based on the similar method to $[Ni^{II}(1)](ClO_4)_2$.

Ligand 2 and $[Ni^{II}(2)](ClO_4)_2$ was prepared according to a previously described procedure.[65] Anal. Calcd for $C_{19}H_{34}Cl_2N_4NiO_8$ (PM = 576.09): C, 39.6; H, 5.9; N, 9.7. Found: C, 39.4; H, 6.0; N, 9.6%. MS (CH_3OH, ESI): m/z 188.2 (100%; $[Ni^{II}(2)]^{2+}$), 475.4 (20% $[Ni^{II}(2) + ClO_4^-]^+$). UV−vis [acetone, λ_{max} nm (ε, M^{-1} cm^{-1})]: 468 (62).

$[Ni^{II}_2(3)](ClO_4)_4$ was prepared according to a previously described procedure.[43] Anal. Calcd for $C_{32}H_{62}Cl_4N_8Ni2O_{16}$ (PM = 1074.08): C, 35.8; H, 5.8; N, 10.4. Found: C, 35.6; H, 5.7; N, 10.1%. MS

(CH₃OH, ESI): m/z 336.4 (40%; $[Ni^{II}_2(3) - 2H^+]^{2+}$), 386.3 (100%, $[Ni^{II}_2(3) - H^+ + ClO_4^-]^{2+}$). UV−vis [acetone], λ_{max} nm (ε, M^{-1} cm^{-1})]: 468 (124).

$[Ni^{II}_2(4)](ClO_4)_4$ and $[Ni^{II}_2(5)](ClO_4)_4$ was synthesized based on the similar method to $[Ni^{II}(3)](ClO_4)_2$.

Ligand 3 was prepared according with the following procedure: $Ni^{II}_2(3)(ClO_4)_4$ (0.4 g, 0.37 mmol) was dissolved in a solution of NaOH 1M (3.5 mL) and DMSO (3.5 mL), and 100 equiv of NaCN (1.81 g, 37mmol) was added slowly. The solution was refluxed for 2 h, during which time it became firstly pink and then yellow. The solution was then cooled to room temperature and placed in a refrigerator overnight. White crystals were collected by filtration from the pale-yellow solution and recrystallized in NaOH 1M. Yield: 0.1 g (50%).
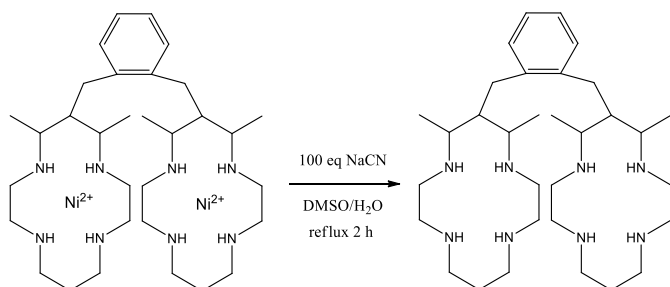
Ligand 4 and 5 were synthesized based on the similar method to ligand 3.

$[Cu^{II}(2)](ClO_4)$ was prepared according with the following procedure:
Free ligand 2 (0.06 g, 0,19 mmol) was partially dissolved in MeOH (10 mL) and an excess of Cu(ClO₄)₂·6H₂O (0.8 g, 2.2 mmol) was added. The solution was refluxed for 2 h. A purple-colored precipitate formed. The solution was then cooled to room temperature. The purple powder was collected by filtration and recrystallized in MeOH. Yield: 0.11 g (~100 %). MS (CH₃OH, ESI): *m/z* 190.69 (100 %, $[Cu^{II}(1)]^{2+}$), 380.35 (20 %, $[Cu^{II}(2) - H^+]^+$). UV−vis [DMSO, λ_{max} nm (ε, M^{-1} cm^{-1})]: 535 (98).

$[Cu^{II}_2(3)](ClO_4)_4$ was prepared according with the following procedure:
Free ligand 3 (0.1 g, 0,18 mmol) was partially dissolved in MeOH (20 mL) HClO₄ 3M (1 mL) and an excess of Cu(ClO₄)₂·6H₂O (1.5 g, 0.4 mmol) was added. The solution was refluxed for 2 h. A purple-colored precipitate formed. The solution was then cooled to room temperature. The purple

powder was collected by filtration and recrystallized in MeOH. Yeld: 0.19 g (~100 %). MS (CH$_3$OH, ESI): *m/z* 391.19 (100 %, [Cu$_2^{II}$(3) - H$^+$ + ClO$_4^-$]$^{2+}$. UV−vis [DMSO, λ_{max} nm (ε, M^{-1} cm^{-1})]: 535 (231).

8 Bibliography

(1)   Melson, G. *Coordination Chemistry of Macrocyclic Compounds*; Springer Science & Business Media, 2012.

(2)   Lindoy, L. F. *The Chemistry of Macrocyclic Ligand Complexes*; Cambridge University Press, 1990.

(3)   Goedken, V. L. Natural-Product Model Systems. In *Coordination Chemistry of Macrocyclic Compounds*; Springer, Boston, MA, 1979; pp 603–654.

(4)   Pedersen, C. J. Cyclic Polyethers and Their Complexes with Metal Salts. *J. Am. Chem. Soc.* **1967**, *89* (10), 2495–2496 DOI: 10.1021/ja00986a052.

(5)   K. Yudin, A. Macrocycles: Lessons from the Distant Past, Recent Developments, and Future Directions. *Chem. Sci.* **2015**, *6* (1), 30–49 DOI: 10.1039/C4SC03089C.

(6)   Lindoy, L. F.; Park, K.-M.; Lee, S. S. Metals, Macrocycles and Molecular Assemblies – Macrocyclic Complexes in Metallo-Supramolecular Chemistry. *Chem Soc Rev* **2013**, *42* (4), 1713–1727 DOI: 10.1039/C2CS35218D.

(7)   Curtis, N. F. Macrocyclic Coordination Compounds Formed by Condensation of Metal-Amine Complexes with Aliphatic Carbonyl Compounds. *Coord. Chem. Rev.* **1968**, *3* (1), 3–47 DOI: 10.1016/S0010-8545(00)80104-6.

(8)   Bosnich, B.; Poon, C. K.; Tobe, M. L. Complexes of Cobalt(III) with a Cyclic Tetradentate Secondary Amine. *Inorg. Chem.* **1965**, *4* (8), 1102–1108 DOI: 10.1021/ic50030a003.

(9)   van Alphen, J. On Aliphatic Polyamines III. *Recl. Trav. Chim. Pays-Bas* **1936**, *55* (10), 835–840 DOI: 10.1002/recl.19360551004.

(10)   van Alphen, J. On Aliphatic Polyamines IV. *Recl. Trav. Chim. Pays-Bas* **1937**, *56* (4), 343–350 DOI: 10.1002/recl.19370560405.

(11)   Bosnich, B.; Mason, R.; Pauling, P. J.; Robertson, G. B.; Tobe, M. L. The Molecular Structure of Dichloro-1, 4, 8, 11-Tetra-Azacyclotetradecanenickel (II). *Chem. Commun. Lond.* **1965**, No. 6, 97–98.

(12)   Kent Barefield, E. Coordination Chemistry of N-Tetraalkylated Cyclam Ligands—A Status Report. *Coord. Chem. Rev.* **2010**, *254* (15), 1607–1627 DOI: 10.1016/j.ccr.2010.03.007.

(13)   Barefield, E. K. New Synthesis of 1, 4, 8, 11-Tetraazacyclotetradecane (Cyclam) via the Nickel (II) Complex. *Inorg. Chem.* **1972**, *11* (9), 2273–2274.

(14)   Cabbiness, D. K.; Margerum, D. W. Macrocyclic Effect on the Stability of Copper(II) Tetramine Complexes. *J. Am. Chem. Soc.* **1969**, *91* (23), 6540–6541 DOI: 10.1021/ja01051a091.

(15)   Izatt, R. M.; Bradshaw, J. S.; Nielsen, S. A.; Lamb, J. D.; Christensen, J. J.; Sen, D. Thermodynamic and Kinetic Data for Cation-Macrocycle Interaction. *Chem. Rev.* **1985**, *85* (4), 271–339 DOI: 10.1021/cr00068a003.

(16)   Izatt, R. M.; Pawlak, K.; Bradshaw, J. S.; Bruening, R. L. Thermodynamic and Kinetic Data for Macrocycle Interactions with Cations and Anions. *Chem. Rev.* **1991**, *91* (8), 1721–2085 DOI: 10.1021/cr00008a003.

(17)   Clay, R. M.; Corr, S.; Micheloni, M.; Paoletti, P. Non-Cyclic Reference Ligands for Tetraaza Macrocycles. Synthesis and Thermodynamic Properties of a Series of. Alpha.,. Omega.-Di-N-Methylated Tetraaza Ligands and Their Copper (II) Complexes. *Inorg. Chem.* **1985**, *24* (21), 3330–3336.

(18)   Frensdorff, H. K. Stability Constants of Cyclic Polyether Complexes with Univalent Cations. *J. Am. Chem. Soc.* **1971**, *93* (3), 600–606 DOI: 10.1021/ja00732a007.

(19)   Sokol, L. S.; Ochrymowycz, L. A.; Rorabacher, D. B. Macrocyclic, Ring Size, and Anion Effects as Manifested in the Equilibrium Constants and Thermodynamic Parameters of Copper (II)-Cyclic Polythia Ether Complexes. *Inorg. Chem.* **1981**, *20* (10), 3189–3195.

(20)   Paoletti, P.; Fabbrizzi, L.; Barbucci, R. Linear Relation between the Enthalpy of Formation and the Frequency of the Maximum in the Electronic Absorption Spectra of the Copper (II)-Tetramine Complexes. *Inorg. Chem.* **1973**, *12* (8), 1961–1962.

(21)   Anichini, A.; Fabbrizzi, L.; Paoletti, P.; M. Clay, R. A Microcalorimetric Study of the Macrocyclic Effect. Enthalpies of Formation of Copper(II) and Zinc(II) Complexes with Some Tetra-Aza Macrocyclic Ligands in Aqueous Solution. *J. Chem. Soc. Dalton Trans.* **1978**, *0* (6), 577–583 DOI: 10.1039/DT9780000577.

(22)   Fabbrizzi, L.; Micheloni, M.; Paoletti, P. Enthalpy of Formation of Copper(II) Complexes with 14-Membered Tetra-Aza Macrocycles. *J. Chem. Soc. Chem. Commun.* **1978**, *0* (19), 833–834 DOI: 10.1039/C39780000833.

(23)   Tasker, P. A.; Sklar, L. Crystal and Molecular Structure of Di(Perchlorato)(1,4,8,11-Tetraazacyclotetradecane)Copper (II). Cu(Cyclam) (ClO4)2. *J. Cryst. Mol. Struct.* **1975**, *5* (5), 329–344 DOI: 10.1007/BF01270621.

(24)   Panneerselvam, K.; Lu, T.-H.; Tung, S.-F.; Chi, T.-Y.; Chung, C.-S. Crystal Structure of (Diperchlorato-*O,O′*)(1,4,7,11-Tetraazacyclotetradecane-*N,N′,N″,N‴*)Copper(II). *Anal. Sci.* **1998**, *14* (5), 1029–1030 DOI: 10.2116/analsci.14.1029.

(25)   Airey, S.; Drljaca, A.; Hardie, M. J.; Raston, C. L. Cyclam as a Supramolecular Synthon: Infinite Stacked Arrays to Encapsulation in Superanions. *Chem. Commun.* **1999**, *0* (12), 1137–1138 DOI: 10.1039/A902124H.

(26)   Timmons, J. C.; Hubin, T. J. Preparations and Applications of Synthetic Linked Azamacrocycle Ligands and Complexes. *Coord. Chem. Rev.* **2010**, *254* (15–16), 1661–1685 DOI: 10.1016/j.ccr.2009.09.018.

(27)   McAuley, A.; Subramanian, S. Formation of Multinuclear Complexes: New Developments from Cyclam Derivatives. *Coord. Chem. Rev.* **2000**, *200*, 75–103.

(28)   Evans, N. H.; Beer, P. D. Advances in Anion Supramolecular Chemistry: From Recognition to Chemical Applications. *Angew. Chem. Int. Ed.* **2014**, *53* (44), 11716–11754 DOI: 10.1002/anie.201309937.

(29)   Amendola, V.; Fabbrizzi, L.; Mangano, C.; Pallavicini, P.; Poggi, A.; Taglietti, A. Anion Recognition by Dimetallic Cryptates. *Coord. Chem. Rev.* **2001**, *219–221* (Supplement C), 821–837 DOI: 10.1016/S0010-8545(01)00368-X.

(30)   Fabbrizzi, L.; Poggi, A. Anion Recognition by Coordinative Interactions: Metal–amine Complexes as Receptors. *Chem Soc Rev* **2013**, *42* (4), 1681–1699 DOI: 10.1039/C2CS35290G.

(31)   O'Neil, E. J.; Smith, B. D. Anion Recognition Using Dimetallic Coordination Complexes. *Coord. Chem. Rev.* **2006**, *250* (23–24), 3068–3080 DOI: 10.1016/j.ccr.2006.04.006.

(32)   Kimura, E.; Aoki, S.; Koike, T.; Shiro, M. A Tris(ZnII−1,4,7,10-Tetraazacyclododecane) Complex as a New Receptor for Phosphate Dianions in Aqueous Solution. *J. Am. Chem. Soc.* **1997**, *119* (13), 3068–3076 DOI: 10.1021/ja9640408.

(33)   Fabbrizzi, L.; Foti, F.; Taglietti, A. Metal-Containing Trifurcate Receptor That Recognizes and Senses Citrate in Water. *Org. Lett.* **2005**, *7* (13), 2603–2606 DOI: 10.1021/ol0507064.

(34)   Boiocchi, M.; Fabbrizzi, L.; Fusco, N.; Invernici, M.; Licchelli, M.; Poggi, A. Anion Binding by Dimetallic Nickel(II) and Nickel(III) Complexes of a Face-to-Face Bicyclam: Looking for a Bimacrocyclic Effect. *Inorg. Chem.* **2016**, *55* (6), 2946–2959 DOI: 10.1021/acs.inorgchem.5b02826.

(35)   Bowman-James, K.; Bianchi, A.; García-Espana, E. *Anion Coordination Chemistry*; John Wiley & Sons, 2012.

(36)   Schmidtchen, F. P.; Berger, M. Artificial Organic Host Molecules for Anions. *Chem. Rev.* **1997**, *97* (5), 1609–1646 DOI: 10.1021/cr9603845.

(37)   Amendola, V.; Fabbrizzi, L. Anion Receptors That Contain Metals as Structural Units. *Chem. Commun.* **2009**, *0* (5), 513–531 DOI: 10.1039/B808264M.

(38)   Alibrandi, G.; Amendola, V.; Bergamaschi, G.; Fabbrizzi, L.; Licchelli, M. Bistren Cryptands and Cryptates: Versatile Receptors for Anion Inclusion and Recognition in Water. *Org. Biomol. Chem.* **2015**, *13* (12), 3510–3524 DOI: 10.1039/C4OB02618G.

(39)   Fabbrizzi, L.; Leone, A.; Taglietti, A. A Chemosensing Ensemble for Selective Carbonate Detection in Water Based on Metal–Ligand Interactions. *Angew. Chem. Int. Ed.* **2001**, *40* (16), 3066–3069 DOI: 10.1002/1521-3773(20010817)40:16<3066::AID-ANIE3066>3.0.CO;2-0.

(40)   Asato, E.; Toftlund, H.; Kida, S.; Mikuriya, M.; Murray, K. S. Preparation and Characterization of Copper(II) Complexes with 1,4,8,11-Tetrakis(2-Pyridylmethyl)-1,4,8,11-Tetraazacyclotetradecane. *Inorganica Chim. Acta* **1989**, *165* (2), 207–214 DOI: 10.1016/S0020-1693(00)83241-7.

(41)   Fabbrizzi, L.; Montagna, L.; Poggi, A.; Kaden, T. A.; Siegfried, L. C. Ditopic Receptors for Transition-Metal Ions: A Heterobimetallic Nickel (II)-Copper (II) Bis (Macrocyclic) Complex and Its Stepwise Oxidation to the Tervalent State. *Inorg. Chem.* **1986**, *25* (16), 2671–2672.

(42)   Kajiwara, T.; Yamaguchi, T.; Kido, H.; Kawabata, S.; Kuroda, R.; Ito, T. A Dinucleating Bis (Dimethylcyclam) Ligand and Its Dinickel (II) and Dizinc (II) Complexes with the Face-to-Face Ring Arrangement. *Inorg. Chem.* **1993**, *32* (23), 4990–4991.

(43)   Szacilowski, K. T.; Xie, P.; Malkhasian, A. Y. S.; Heeg, M. J.; Udugala-Ganehenege, M. Y.; Wenger, L. E.; Endicott, J. F. Solid-State Structures and Magnetic Properties of Halide-Bridged, Face-to-Face Bis-Nickel(II)-Macrocyclic Ligand Complexes: Ligand-Mediated Interchanges of Electronic Configuration. *Inorg. Chem.* **2005**, *44* (17), 6019–6033 DOI: 10.1021/ic050147x.

(44)   Anichini, A.; Fabbrizzi, L.; Paoletti, P.; Clay, R. M. Does a Macrocyclic Effect Exist in the Blue-to-Yellow Conversion of Nickel(II) Complexes with Tetra-Aza Ligands? *Inorganica Chim. Acta* **1977**, *24* (Supplement C), L21–L23 DOI: 10.1016/S0020-1693(00)93812-X.

(45)   Sabatini, L.; Fabbrizzi, L. Fitting of Nickel (II) Ion into Two 14-Membered Tetraaza Macrocycles. Blue-to-Yellow Conversion and the Oxidation and Reduction Behavior. *Inorg. Chem.* **1979**, *18* (2), 438–444.

(46)   Liang, X.; J. Sadler, P. Cyclam Complexes and Their Applications in Medicine. *Chem. Soc. Rev.* **2004**, *33* (4), 246–266 DOI: 10.1039/B313659K.

(47)   R. Adam, K.; Antolovich, M.; G. Brigden, L.; J. Leong, A.; F. Lindoy, L.; J. Baillie, P.; K. Uppal, D.; McPartlin, M.; Shah, B.; Proserpio, D.; Fabbrizzi, L.; A. Tasker, P. Macrocyclic Ligand Ring Size Effects. Part 2. Synthetic, Structural and Electrochemical Studies of the Interaction of Ni II with 14-Membered Tetraaza Macrocycles Containing Fused Dibenzo Substituents. *J. Chem. Soc. Dalton Trans.* **1991**, *0* (10), 2493–2501 DOI: 10.1039/DT9910002493.

(48)   Valach, F.; Dunaj-Jurčo, M. Bis(3-Amino-Pyridine)Copper Cyanate Monohydrate. *Acta Crystallogr. B* **1982**, *38* (8), 2145–2148 DOI: 10.1107/S0567740882008206.

(49)   Gans, P.; Sabatini, A.; Vacca, A. Investigation of Equilibria in Solution. Determination of Equilibrium Constants with the HYPERQUAD Suite of Programs. *Talanta* **1996**, *43* (10), 1739–1753 DOI: 10.1016/0039-9140(96)01958-3.

(50)   Hinz, F. P.; Margerum, D. W. Ligand Solvation and the Macrocyclic Effect. Nickel (II)-Tetramine Complexes. *Inorg. Chem.* **1974**, *13* (12), 2941–2949.

(51)   Olson, D. C.; Vasilevskis, J. Cyclic Amine Complexes of Nickel (I),-(II), and-(III). Electrochemistry, Preparation, and Properties. *Inorg. Chem.* **1969**, *8* (8), 1611–1621.

(52)   Bencini, A.; Fabbrizzi, L.; Poggi, A. Formation of Nickel (III) Complexes with n-Dentate Amine Macrocycles (N= 4, 5, 6). ESR and Electrochemical Studies. *Inorg. Chem.* **1981**, *20* (8), 2544–2549.

(53)   Olson, D. C.; Vasilevskis, J. Cyclic Amine Complexes of Copper (I),-(II), and-(III). Electrochemistry, Preparation, and Properties. *Inorg. Chem.* **1971**, *10* (3), 463–470.

(54)   Bisi Castellani, C.; Fabbrizzi, L.; Licchelli, M.; Perotti, A.; Poggi, A. Stablization by a Strongly Acidic Medium of Trivalent Copper Tetra-Aza Macrocyclic Complexes. *J. Chem. Soc. Chem. Commun.* **1984**, *0* (12), 806–808 DOI: 10.1039/C39840000806.

(55)   Barefield, E. K.; Mocella, M. T. Complexes of Silver (II) and Silver (III) with Macrocyclic Tetraaza Ligands. *Inorg. Chem.* **1973**, *12* (12), 2829–2832.

(56)   Pesavento, M.; Profumo, A.; Soldi, T.; Fabbrizzi, L. Formation of a Trivalent Silver Tetraaza Macrocyclic Complex in Aqueous Solution: Hydrolytic Tendencies and Interaction with the Sulfate Ion. *Inorg. Chem.* **1985**, *24* (23), 3873–3875.

(57) Lovecchio, F. V.; Gore, E. S.; Busch, D. H. Oxidation and Reduction Behavior of Macrocyclic Complexes of Nickel. Electrochemical and Electron Spin Resonance Studies. *J. Am. Chem. Soc.* **1974**, *96* (10), 3109–3118.

(58) Nishigaki, J.; Matsumoto, T.; Tatsumi, K. Coordination of Methyl Coenzyme M and Coenzyme M at Divalent and Trivalent Nickel Cyclams: Model Studies of Methyl Coenzyme M Reductase Active Site. *Inorg. Chem.* **2012**, *51* (6), 3690–3697 DOI: 10.1021/ic202686x.

(59) Richardson, D. E.; Taube, H. Determination of E20-E10 in Multistep Charge Transfer by Stationary-Electrode Pulse and Cyclic Voltammetry: Application to Binuclear Ruthenium Ammines. *Inorg. Chem.* **1981**, *20* (4), 1278–1285 DOI: 10.1021/ic50218a062.

(60) Amendola, V.; Fabbrizzi, L.; Mosca, L. Anion Recognition by Hydrogen Bonding: Urea -Based Receptors. *Chem. Soc. Rev.* **2010**, *39* (10), 3889–3915 DOI: 10.1039/B822552B.

(61) Miller, S. R.; Gustowski, D. A.; Chen, Z. H.; Gokel, G. W.; Echegoyen, L.; Kaifer, A. E. Rationalization of the Unusual Electrochemical Behavior Observed in Lariat Ethers and Other Reducible Macrocyclic Systems. *Anal. Chem.* **1988**, *60* (19), 2021–2024.

(62) Amendola, V.; Boiocchi, M.; Colasson, B.; Fabbrizzi, L.; Monzani, E.; Douton-Rodriguez, M. J.; Spadini, C. Redox Active Cage for the Electrochemical Sensing of Anions. *Inorg. Chem.* **2008**, *47* (11), 4808–4816 DOI: 10.1021/ic800099j.

(63) Irving, H.; Williams, Rjp. 637. The Stability of Transition-Metal Complexes. *J. Chem. Soc. Resumed* **1953**, 3192–3210.

(64) Alderighi, L.; Gans, P.; Ienco, A.; Peters, D.; Sabatini, A.; Vacca, A. Hyperquad Simulation and Speciation (HySS): A Utility Program for the Investigation of Equilibria Involving Soluble and Partially Soluble Species. *Coord. Chem. Rev.* **1999**, *184* (1), 311–318 DOI: 10.1016/S0010-8545(98)00260-4.

(65) DeRosa, F.; Bu, X.; Pohaku, K.; Ford, P. C. Synthesis and Luminescence Properties of Cr(III) Complexes with Cyclam-Type Ligands Having Pendant Chromophores, Trans-[Cr(L)Cl2]Cl1. *Inorg. Chem.* **2005**, *44* (12), 4166–4174 DOI: 10.1021/ic048312g.

(66) Altomare, A.; Burla, M. C.; Camalli, M.; Cascarano, G. L.; Giacovazzo, C.; Guagliardi, A.; Moliterni, A. G. G.; Polidori, G.; Spagna, R. SIR97: A New Tool for Crystal Structure Determination and Refinement. *J. Appl. Crystallogr.* **1999**, *32* (1), 115–119 DOI: 10.1107/S0021889898007717.

(67) Sheldrick, G. M. A Short History of SHELX. *Acta Crystallogr. A* **2008**, *64* (1), 112–122 DOI: 10.1107/S0108767307043930.

(68) Guerriero, P.; Tarnburini, S.; Vigato, P. A. From Mononuclear to Polynuclear Macrocyclic or Macroacyclic Complexes. *Coord. Chem. Rev.* **1995**, *139* (Supplement C), 17–243 DOI: 10.1016/0010-8545(93)01105-7.

(69) Mochizuki, K.; Manaka, S.; Takeda, I.; Kondo, T. Synthesis and Structure of [6,6'-Bi(5,7-Dimethyl-1,4,8,11-Tetraazacyclotetradecane)]Dinickel(II) Triflate and Its Catalytic Activity for Photochemical CO2 Reduction. *Inorg. Chem.* **1996**, *35* (18), 5132–5136 DOI: 10.1021/ic960208e.

(70) Fukuzumi, S.; Okamoto, K.; Gros, C. P.; Guilard, R. Mechanism of Four-Electron Reduction of Dioxygen to Water by Ferrocene Derivatives in the Presence of Perchloric Acid in Benzonitrile, Catalyzed by Cofacial Dicobalt Porphyrins. *J. Am. Chem. Soc.* **2004**, *126* (33), 10441–10449 DOI: 10.1021/ja048403c.

(71) Schneider, R.; Riesen, A.; Kaden, T. A. Metal Complexes with Macrocyclic Ligands. Part XXII. Synthesis Two of Bis-Tetraaza-Macrocycles and Study of the Structures, Electrochemistry, VIS and EPR Spectra of Their Binuclear Cu2+ and Ni2+ Complexes. *Helv. Chim. Acta* **1986**, *69* (1), 53–61 DOI: 10.1002/hlca.19860690108.

(72) El Ghachtouli, S.; Cadiou, C.; Déchamps-Olivier, I.; Chuburu, F.; Aplincourt, M.; Turcry, V.; Le Baccon, M.; Handel, H. Spectroscopy and Redox Behaviour of Dicopper(II) and Dinickel(II) Complexes of Bis(Cyclen) and Bis(Cyclam) Ligands. *Eur. J. Inorg. Chem.* **2005**, *2005* (13), 2658–2668 DOI: 10.1002/ejic.200500120.

(73) V. Rosokha, S.; D. Lampeka, Y.; M. Maloshtan, I. Synthesis and Properties of a New Series of Bis(Macrocyclic) Dicopper(II , II), Dinickel(II , II) and Dinickel(III , III) Complexes Based on

the 14-Membered Pentaaza Unit. *J. Chem. Soc. Dalton Trans.* **1993**, *0* (4), 631–636 DOI: 10.1039/DT9930000631.

(74) Lachkar, M.; Guilard, R.; Atmani, A.; De Cian, A.; Fischer, J.; Weiss, R. Synthesis of New Binucleating Cylindrical Macrotricyclic Ligands Where Two Cyclam Rings Are in a Face-to-Face Conformation. Characterization of Their Dicopper(II) and Dinickel(II) Complexes. *Inorg. Chem.* **1998**, *37* (7), 1575–1584 DOI: 10.1021/ic9708327.

(75) Soibinet, M.; Déchamps-Olivier, I.; Guillon, E.; Barbier, J.-P.; Aplincourt, M.; Chuburu, F.; Le Baccon, M.; Handel, H. XAS, ESR and Potentiometric Studies of Three Dinuclear N,N′-Para-Xylylenebis(Tetraazamacrocycle)Copper(II) Complexes − X-Ray Crystal Structure of [N,N′-p-Xylylenebis(Cyclen)]Copper(II). *Eur. J. Inorg. Chem.* **2003**, *2003* (10), 1984–1994 DOI: 10.1002/ejic.200200517.

(76) Buttafava, A.; Fabbrizzi, L.; Perotti, A.; Seghi, B. Dicopper(II) and Dicopper(III) Complexes with a Double-Ring Octa-Aza Macrocycle. *J. Chem. Soc. Chem. Commun.* **1982**, *0* (20), 1166–1167 DOI: 10.1039/C39820001166.

(77) Brandès, S.; Gros, C.; Denat, F.; Pullumbi, P.; Guilard, R. New Facile and Convenient Synthesis of Bispolyazamacrocycles Using Boc Protection. Determination of Geometric Parameters of Dinuclear Copper(II) Complexes Using ESR Spectroscopy and Molecular Mechanics Calculations. *Bull. Soc. Chim. Fr.* **1996**, *1* (133), 65–73.

(78) Smith, D. W. Ionic Hydration Enthalpies. *J Chem Educ* **1977**, *54* (9), 540.

(79) Thordarson, P. Determining Association Constants from Titration Experiments in Supramolecular Chemistry. *Chem. Soc. Rev.* **2011**, *40* (3), 1305–1323 DOI: 10.1039/C0CS00062K.

(80) Thoem, V. J.; Boeyens, J. C.; McDougall, G. J.; Hancock, R. D. Origin of the High Ligand Field Strength and Macrocyclic Enthalpy in Complexes of Nitrogen-Donor Macrocycles. *J. Am. Chem. Soc.* **1984**, *106* (11), 3198–3207.

(81) Chen, X.; Long, G.; Willett, R. D.; Hawks, T.; Molnar, S.; Brewer, K. Three Metal (1,4,8,11-Tetraazacyclotetradecane) Halide Salts. *Acta Crystallogr. C* **1996**, *52* (8), 1924–1928 DOI: 10.1107/S0108270195016829.

(82) Krause, L.; Herbst-Irmer, R.; Sheldrick, G. M.; Stalke, D. Comparison of Silver and Molybdenum Microfocus X-Ray Sources for Single-Crystal Structure Determination. *J. Appl. Crystallogr.* **2015**, *48* (1), 3–10 DOI: 10.1107/S1600576714022985.

(83) Sheldrick, G. M. SHELXT – Integrated Space-Group and Crystal-Structure Determination. *Acta Crystallogr. Sect. Found. Adv.* **2015**, *71* (1), 3–8 DOI: 10.1107/S2053273314026370.

(84) Schrag, D. P. Preparing to Capture Carbon. *Science* **2007**, *315* (5813), 812–813 DOI: 10.1126/science.1137632.

(85) Yuan, D.; Yan, C.; Lu, B.; Wang, H.; Zhong, C.; Cai, Q. Electrochemical Activation of Carbon Dioxide for Synthesis of Dimethyl Carbonate in an Ionic Liquid. *Electrochimica Acta* **2009**, *54* (10), 2912–2915 DOI: 10.1016/j.electacta.2008.11.006.

(86) Whipple, D. T.; Kenis, P. J. A. Prospects of CO2 Utilization via Direct Heterogeneous Electrochemical Reduction. *J. Phys. Chem. Lett.* **2010**, *1* (24), 3451–3458 DOI: 10.1021/jz1012627.

(87) Agarwal, A. S.; Zhai, Y.; Hill, D.; Sridhar, N. The Electrochemical Reduction of Carbon Dioxide to Formate/Formic Acid: Engineering and Economic Feasibility. *ChemSusChem* **2011**, *4* (9), 1301–1310 DOI: 10.1002/cssc.201100220.

(88) Meyer, T. J. Chemical Approaches to Artificial Photosynthesis. *Acc. Chem. Res.* **1989**, *22* (5), 163–170.

(89) Leitner, W. The Coordination Chemistry of Carbon Dioxide and Its Relevance for Catalysis: A Critical Survey. *Coord. Chem. Rev.* **1996**, *153* (Supplement C), 257–284 DOI: 10.1016/0010-8545(95)01226-5.

(90) Cheng, M.; Lobkovsky, E. B.; Coates, G. W. Catalytic Reactions Involving C 1 Feedstocks: New High-Activity Zn(II)-Based Catalysts for the Alternating Copolymerization of Carbon Dioxide and Epoxides. *J. Am. Chem. Soc.* **1998**, *120* (42), 11018–11019 DOI: 10.1021/ja982601k.

(91) Alstrum-Acevedo, J. H.; Brennaman, M. K.; Meyer, T. J. Chemical Approaches to Artificial Photosynthesis. 2. *Inorg. Chem.* **2005**, *44* (20), 6802–6827 DOI: 10.1021/ic050904r.

(92) Aresta, M.; Dibenedetto, A. Utilisation of CO 2 as a Chemical Feedstock: Opportunities and Challenges. *Dalton Trans.* **2007**, *0* (28), 2975–2992 DOI: 10.1039/B700658F.

(93) Centi, G.; Perathoner, S. Opportunities and Prospects in the Chemical Recycling of Carbon Dioxide to Fuels. *Catal. Today* **2009**, *148* (3), 191–205 DOI: 10.1016/j.cattod.2009.07.075.

(94) Concepcion, J. J.; House, R. L.; Papanikolas, J. M.; Meyer, T. J. Chemical Approaches to Artificial Photosynthesis. *Proc. Natl. Acad. Sci.* **2012**, *109* (39), 15560–15564 DOI: 10.1073/pnas.1212254109.

(95) Sakakura, T.; Choi, J.-C.; Yasuda, H. Transformation of Carbon Dioxide. *Chem. Rev.* **2007**, *107* (6), 2365–2387 DOI: 10.1021/cr068357u.

(96) Oloman, C.; Li, H. Electrochemical Processing of Carbon Dioxide. *ChemSusChem* **2008**, *1* (5), 385–391 DOI: 10.1002/cssc.200800015.

(97) E. Benson, E.; P. Kubiak, C.; J. Sathrum, A.; M. Smieja, J. Electrocatalytic and Homogeneous Approaches to Conversion of CO 2 to Liquid Fuels. *Chem. Soc. Rev.* **2009**, *38* (1), 89–99 DOI: 10.1039/B804323J.

(98) Lee, J.; Kwon, Y.; Machunda, R. L.; Lee, H. J. Electrocatalytic Recycling of CO2 and Small Organic Molecules. *Chem. – Asian J.* **2009**, *4* (10), 1516–1523 DOI: 10.1002/asia.200900055.

(99) Windle, C. D.; Perutz, R. N. Advances in Molecular Photocatalytic and Electrocatalytic CO2 Reduction. *Coord. Chem. Rev.* **2012**, *256* (21), 2562–2570 DOI: 10.1016/j.ccr.2012.03.010.

(100) Inglis, J. L.; MacLean, B. J.; Pryce, M. T.; Vos, J. G. Electrocatalytic Pathways towards Sustainable Fuel Production from Water and CO2. *Coord. Chem. Rev.* **2012**, *256* (21), 2571–2600 DOI: 10.1016/j.ccr.2012.05.002.

(101) Schneider, J.; Jia, H.; Muckerman, J. T.; Fujita, E. Thermodynamics and Kinetics of CO2, CO, and H+ Binding to the Metal Centre of CO2reductioncatalysts. *Chem Soc Rev* **2012**, *41* (6), 2036–2051 DOI: 10.1039/C1CS15278E.

(102) Mori, K.; Yamashita, H.; Anpo, M. Photocatalytic Reduction of CO 2 with H2O on Various Titanium Oxide Photocatalysts. *RSC Adv.* **2012**, *2* (8), 3165–3172 DOI: 10.1039/C2RA01332K.

(103) Aresta, M. *Carbon Dioxide Recovery and Utilization*; Springer Science & Business Media, 2013.

(104) Halmann, M. M. *Chemical Fixation of Carbon DioxideMethods for Recycling CO2 into Useful Products*; CRC Press, 1993.

(105) Sullivan, B. P.; Krist, K.; Guard, H. E. *Electrochemical and Electrocatalytic Reactions of Carbon Dioxide*; Elsevier, 2012.

(106) Fisher, B. J.; Eisenberg, R. Electrocatalytic Reduction of Carbon Dioxide by Using Macrocycles of Nickel and Cobalt. *J. Am. Chem. Soc.* **1980**, *102* (24), 7361–7363.

(107) Beley, M.; Collin, J.-P.; Ruppert, R.; Sauvage, J.-P. Nickel(II)-Cyclam: An Extremely Selective Electrocatalyst for Reduction of CO 2 in Water. *J. Chem. Soc. Chem. Commun.* **1984**, *0* (19), 1315–1316 DOI: 10.1039/C39840001315.

(108) Beley, M.; Collin, J. P.; Ruppert, R.; Sauvage, J. P. Electrocatalytic Reduction of Carbon Dioxide by Nickel Cyclam2+ in Water: Study of the Factors Affecting the Efficiency and the Selectivity of the Process. *J. Am. Chem. Soc.* **1986**, *108* (24), 7461–7467.

(109) Collin, J. P.; Jouaiti, A.; Sauvage, J. P. Electrocatalytic Properties of (Tetraazacyclotetradecane) Nickel (2+) and Ni2 (Biscyclam) 4+ with Respect to Carbon Dioxide and Water Reduction. *Inorg. Chem.* **1988**, *27* (11), 1986–1990.

(110) Fujihira, M.; Hirata, Y.; Suga, K. Electrocatalytic Reduction of CO2 by Nickel(II) Cyclam: Study of the Reduction Mechanism on Mercury by Cyclic Voltammetry, Polarography and Electrocapillarity. *J. Electroanal. Chem. Interfacial Electrochem.* **1990**, *292* (1), 199–215 DOI: 10.1016/0022-0728(90)87336-I.

(111) Fujita, E.; Creutz, C.; Sutin, N.; Szalda, D. J. (Brookhaven N. L. Carbon Dioxide Activation by Cobalt(i) Macrocycles: Factors Affecting Co Sub 2 and Co Binding. *J. Am. Chem. Soc. U. S.* **1991**, *113:1* DOI: 10.1021/ja00001a048.

(112) Bujno, K.; Bilewicz, R.; Siegfried, L.; Kaden, T. A. Effects of Ligand Structure on the Adsorption of Nickel Tetraazamacrocyclic Complexes and Electrocatalytic CO2 Reduction. *J. Electroanal. Chem.* **1998**, *445* (1), 47–53 DOI: 10.1016/S0022-0728(97)00603-7.

(113)   Hay, R. W.; Crayston, J. A.; Cromie, T. J.; Lightfoot, P.; de Alwis, D. C. L. The Preparation, Chemistry and Crystal Structure of the Nickel(II) Complex of N-Hydroxyethylazacyclam [3-(2′-Hydroxyethyl)-1,3,5,8,12-Penta-Azacyclotetradecane Nickel(II) Perchlorate]. A New Electrocatalyst for CO2 Reduction. *Polyhedron* **1997**, *16* (20), 3557–3563 DOI: 10.1016/S0277-5387(97)00113-7.

(114)   Schneider, J.; Jia, H.; Kobiro, K.; E. Cabelli, D.; T. Muckerman, J.; Fujita, E. Nickel(Ii) Macrocycles: Highly Efficient Electrocatalysts for the Selective Reduction of CO 2 to CO. *Energy Environ. Sci.* **2012**, *5* (11), 9502–9510 DOI: 10.1039/C2EE22528J.

(115)   Froehlich, J. D.; Kubiak, C. P. Homogeneous CO2 Reduction by Ni(Cyclam) at a Glassy Carbon Electrode. *Inorg. Chem.* **2012**, *51* (7), 3932–3934 DOI: 10.1021/ic3001619.

(116)   Abba, F.; De Santis, G.; Fabbrizzi, L.; Licchelli, M.; Manotti Lanfredi, A. M.; Pallavicini, P.; Poggi, A.; Ugozzoli, F. Nickel (II) Complexes of Azacyclams: Oxidation and Reduction Behavior and Catalytic Effects in the Electroreduction of Carbon Dioxide. *Inorg. Chem.* **1994**, *33* (7), 1366–1375.

(117)   Lee, E. Y.; Hong, D.; Park, H. W.; Suh, M. P. Synthesis, Properties, and Reactions of Trinuclear Macrocyclic Nickel(II) and Nickel(I) Complexes: Electrocatalytic Reduction of CO2 by Nickel(II) Complex. *Eur. J. Inorg. Chem.* **2003**, *2003* (17), 3242–3249 DOI: 10.1002/ejic.200200543.

(118)   de Alwis, C.; Crayston, J. A.; Cromie, T.; Eisenblätter, T.; Hay, R. W.; Lampeka, Y. D.; Tsymbal, L. V. Cyclic Voltammetry Study of the Electrocatalysis of Carbon Dioxide Reduction by Bis(Polyazamacrocyclic) Nickel Complexes. *Electrochimica Acta* **2000**, *45* (13), 2061–2074 DOI: 10.1016/S0013-4686(99)00427-2.

(119)   Weller, M.; Overton, T.; Rourke, J.; Armstrong, F. *Inorganic Chemistry*; OUP Oxford, 2014.

(120)   Hori, Y.; Wakebe, H.; Tsukamoto, T.; Koga, O. Electrocatalytic Process of CO Selectivity in Electrochemical Reduction of CO2 at Metal Electrodes in Aqueous Media. *Electrochimica Acta* **1994**, *39* (11), 1833–1839 DOI: 10.1016/0013-4686(94)85172-7.

(121)   Kedzierzawski, P.; Augustynski, J. Poisoning and Activation of the Gold Cathode during Electroreduction of CO 2. *J. Electrochem. Soc.* **1994**, *141* (5), L58–L60 DOI: 10.1149/1.2054936.

(122)   Song, J.; Klein, E. L.; Neese, F.; Ye, S. The Mechanism of Homogeneous CO 2 Reduction by Ni(Cyclam): Product Selectivity, Concerted Proton–Electron Transfer and C–O Bond Cleavage. *Inorg. Chem.* **2014**, *53* (14), 7500–7507 DOI: 10.1021/ic500829p.

(123)   Jacquinot, P.; Hauser, P. C. Ni(II)Cyclam Catalyzed Reduction of CO2 – Towards a Voltammetric Sensor for the Gas Phase. *Electroanalysis* **2003**, *15* (18), 1437–1444 DOI: 10.1002/elan.200302743.

(124)   Froehlich, J. D.; Kubiak, C. P. The Homogeneous Reduction of CO 2 by [Ni(Cyclam)] + : Increased Catalytic Rates with the Addition of a CO Scavenger. *J. Am. Chem. Soc.* **2015**, *137* (10), 3565–3573 DOI: 10.1021/ja512575v.

(125)   Kang, S.-J.; Dale, A.; Sarkar, S.; Yoo, J.; Lee, H. Electrocatalytic Reduction of CO 2 by Copper (II) Cyclam Derivatives. *J. Electrochem. Sci. Technol.* **2015**, *6* (3), 106–110 DOI: 10.5229/JECST.2015.6.3.106.

(126)   Angamuthu, R.; Byers, P.; Lutz, M.; Spek, A. L.; Bouwman, E. Electrocatalytic CO2 Conversion to Oxalate by a Copper Complex. *Science* **2010**, *327* (5963), 313–315.

(127)   Rudolph, M.; Dautz, S.; Jäger, E.-G. Macrocyclic [N 4 2 -] Coordinated Nickel Complexes as Catalysts for the Formation of Oxalate by Electrochemical Reduction of Carbon Dioxide. *J. Am. Chem. Soc.* **2000**, *122* (44), 10821–10830 DOI: 10.1021/ja001254n.

(128)   Cook, T. D.; Tyler, S. F.; McGuire, C. M.; Zeller, M.; Fanwick, P. E.; Evans, D. H.; Peters, D. G.; Ren, T. Nickel Complexes of C-Substituted Cyclams and Their Activity for CO 2 and H + Reduction. *ACS Omega* **2017**, *2* (7), 3966–3976 DOI: 10.1021/acsomega.7b00714.

(129)   Balazs, G. B.; Anson, F. C. The Adsorption of Ni(Cyclam)+ at Mercury Electrodes and Its Relation to the Electrocatalytic Reduction of CO2. *J. Electroanal. Chem.* **1992**, *322* (1), 325–345 DOI: 10.1016/0022-0728(92)80086-J.

(130)   Newell, R.; Appel, A.; DuBois, D. L.; Rakowski DuBois, M. Studies of Bicarbonate Binding by Dinuclear and Mononuclear Ni(II) Complexes. *Inorg. Chem.* **2005**, *44* (2), 365–373 DOI: 10.1021/ic049202c.